GEOLOGICA ULTRAIECTINA

Mededelingen van de
Faculteit Aardwetenschappen
Universiteit Utrecht

No. 174

Mass transfer processes in crystalline aggregates containing a fluid phase

H.J.M. Visser

GEOLOGICA ULTRAIECTINA

Mededelingen van de
Faculteit Aardwetenschappen
Universiteit Utrecht

No. 174

Mass transfer processes in crystalline aggregates containing a fluid phase

H.J.M. Visser

ISBN: 90-57-44-032-6

Mass transfer processes in crystalline aggregates containing a fluid phase

massatransport in kristallijne aggregaten
in aanwezigheid van een vloeibare fase

(met een samenvatting in het Nederlands)

PROEFSCHRIFT

TER VERKRIJGING VAN DE GRAAD VAN DOCTOR
AAN DE UNIVERSITEIT TE UTRECHT, OP GEZAG VAN DE
RECTOR MAGNIFICUS, PROF. DR. H.O. VOORMA,
INGEVOLGE HET BESLUIT VAN HET COLLEGE VOOR PROMOTIES
IN HET OPENBAAR TE VERDEDIGEN OP
WOENSDAG 2 JUNI 1999 DES NAMIDDAGS TE 14.00 UUR

DOOR

HENDRICA JOHANNA MARIA VISSER

GEBOREN OP 9 NOVEMBER 1964 TE GODENSTEDT

PROMOTOR: PROF. DR. C.J. SPIERS
FACULTEIT AARDWETENSCHAPPEN
UNIVERSITEIT UTRECHT

EXAMINING COMMITTEE:

PROF. DR. H.W. GREEN II
University of California, USA
PROF. DR. B.H.W.S. DE JONG
Utrecht University, the Netherlands
PROF. DR. B. STÖCKHERT
Ruhr-Universität Bochum, Germany
DR. G. HIRTH
Woods Hole Oceanographic Institute, USA

The research described in this thesis has been funded by Koninklijke Hoogovens Groep, Ceramic Research Centre, Hoogovens R&D, IJmuiden, the Netherlands.

CONTENTS

SUMMARY 1

1 INTRODUCTION
1.1 Scope and Motivation 5
1.2 Background 5
1.2.1 Partial melting at mid-ocean ridges and constraints on natural conditions 5
1.2.2 Constraints on rheological behaviour and melt distribution 9
1.3 Problem definition 12
1.4 Present aims 14

2 SOLUTION/PRECIPITATION PROCESSES IN STRESSED SOLID/LIQUID SYSTEMS: THEORETICAL ASPECTS

2.1 Introduction 15
2.2 Thermodynamic Preliminaries 18
2.2.1 Surface Thermodynamics 18
2.2.2 The Interfacial Free Energy 26
2.2.3 Equilibrium Considerations 29
2.2.4 Non-equilibrium Thermodynamic Considerations 36
2.3 Behaviour of solid/liquid systems under hydrostatic conditions: a model for neck growth by solution/ precipitation transfer 42
2.3.1 General 42
2.3.2 New Models for Neck Growth 44
2.4 Behaviour of solid/liquid systems under stress: extended models for densification by solution/ precipitation creep and neck growth under stress 51
2.4.1 General 51
2.4.2 An Extended Model for Densification by Solution/ Precipitation Creep 53
2.4.3 An extended model for neck growth under stress 55
2.5 Conditions for neck growth / undercutting versus solution/precipitation creep 59
2.5.1 Condition of zero driving force for solution/precipitation creep and related behavioural fields 60
2.5.2 Condition of Zero Driving Force for Neck Growth and Related Behavioural Fields 61
2.5.3 Grain Boundary Healing Versus a Dynamically Wetted Island-Channel Structure 63
2.5.4 The mass transport mechanism maps: NaCl as an example 67
2.6 Summary and conclusions 74

3 DENSIFICATION OF $NaNO_3$ AGGREGATES PLUS SATURATED SOLUTION: AN ANALOGUE FOR PARTIALLY MOLTEN SYSTEMS

3.1 Introduction 77
3.2 Background data on $NaNO_3$ **78**
3.2.1 $NaNO_3$ plus saturated solution as an analogue system 78
3.2.2 Physical properties of $NaNO_3$ 78
3.3 Models to be tested **80**
3.4 Experimental aspects **82**
3.4.1 Starting Material 82
3.4.2 Experimental Apparatus and Testing Procedure 83
3.4.3 Friction Tests 85
3.4.4 Data processing 88
3.5 Results **88**
3.5.1 Mechanical data 88
3.5.2 Microstructural observations 94
3.6 Discussion **106**
3.6.1 The high stress regime: low and high stress fields 106
3.6.2 Determining the kinetic coefficient governing creep in the high stress regime 108
3.6.3 The low stress regime 109
3.6.4 Comparison with criteria for pressure solution versus contact healing processes 110
3.7 Summary and conclusions **117**

4 DENSIFICATION OF FORSTERITE AGGREGATES AT LOW STRESSES

4.1 Introduction **119**
4.2 Theoretical background **122**
4.2.1. Driving force and mass transfer paths at high temperature 122
4.2.2. Models 125
4.3 Experimental aspects **129**
4.3.1 Starting material and sample preparation 129
4.3.2 Experimental apparatus 130
4.3.3 Testing procedure and data processing 132
4.3.4 Microstructural analysis 133
4.4 Results **136**
4.4.1 Mechanical data 136
4.4.2 Microstructural observations 144
4.5 Discussion **150**
4.5.1 Regime A (average grain size $\geq$ 5 μm) 150
4.5.2 Kinetic coefficient in regime A 151
4.5.3 Regime B (average grain size < 5 μm) 153

4.5.4 Determining the surface energy related contribution 154
4.5.5 Comparison with previous work on olivine aggregates 156
4.6 Summary and conclusions **161**

5 DENSIFICATION OF PARTIALLY MOLTEN FORSTERITE AGGREGATES AT LOW STRESSES

5.1 Introduction **163**
5.2 Theoretical considerations **165**
5.2.1 Driving forces and mass transfer paths in partially molten aggregates 165
5.2.2 Models 168
5.3 Experimental methodology **172**
5.3.1 Starting material and sample preparation 172
5.3.2 High temperature densification apparatus 178
5.3.3 Testing procedure and data processing 180
5.3.4 Grain growth experiments and grain size estimation 181
5.3.5 Microstructural analyses 184
5.4 Experimental results **185**
5.4.1 Mechanical data 185
5.4.2 Microstructural observations and chemical analyses 190
5.5 Discussion **199**
5.5.1 Grain growth and mechanical behaviour 199
5.5.2 Microstructural and chemical analyses 202
5.5.3 Comparison with models 204
5.5.4 Comparison of forsterite experiments with and without melt 207
5.6 Conclusions **212**

6 GENERAL CONCLUSIONS AND SUGGESTIONS FOR FURTHER RESEARCH

6.1 Theoretical developments **215**
6.2 Densification behaviour at relatively high stresses **217**
6.3 Densification behaviour at low stresses **219**
6.4 Conclusions regarding the influence of a liquid phase on densification creep **221**
6.5 Implications for large scale modelling of melt segregation/migration **222**
6.6 Suggestions for further research **225**

7 REFERENCES **227**

SAMENVATTING **241**

NAWOORD **243**

CURRICULUM VITAE **244**

SUMMARY

Understanding mass transfer processes in porous crystalline aggregates containing a fluid phase is of major importance for modelling partially molten regions of the Earth's mantle, such as those under mid-ocean spreading ridges. Despite the fact that mid-ocean ridges can be considered the simplest large scale setting where partial melting occurs, many processes at depth beneath the ridges, such as segregation and migration of the melt phase, remain poorly understood. For example, essential input information for large scale modelling, such as the melt distribution on the grain scale, whether or not a continuous network of (grain-scale) melt channels exists and the associated transport properties, are poorly constrained. Also poorly constrained is the effect of melt on the rheological behaviour of mantle rock. When trying to combine information from equilibrium (hydrostatic) melt distribution studies and densification or deformation studies on partially molten samples, the difficulty arises that little or no information is available under conditions where both stress-related and surface-energy-related driving forces for grain scale diffusive mass transfer are comparable in magnitude. Such conditions may, however, be important in partially molten regions of the earth. This thesis reports a theoretical and experimental study of grain scale mass transfer processes in solid/fluid systems under the low effective stress conditions where surface energy related forces are expected to become significant.

In Chapter 1, the problems adressed are introduced and the aims of the present study are identified. In Chapter 2, a theoretical background is provided concerning the thermodynamic description of interfaces and on driving forces for grain scale diffusive transport in solid/liquid aggregates, taking both stress and interfacial energy related terms into account. Building on this basis, models are developed for 1) purely hydrostatic conditions, describing mass transfer towards grain contacts (neck growth), and 2) for densification under an applied effective stress, resulting in mass transfer away from grain contacts (solution/precipitation or pressure solution creep). The neck growth models for the first time allow for the effect of grain boundary energy as well as solid/liquid interfacial energy. The densification models predict that densification by solution/precipitation creep will slow down towards fine grain size, as opposing surface energy driving forces become more important compared with the applied stress. The new expression for the thermodynamic force driving transport from grain contacts to pore walls during densification is $\Delta\mu=(\sigma_n\Omega^s-4\gamma/d)$, where $\Delta\mu$ is the difference in chemical potential, σ_n is the

effective normal stress at the contact, Ω^s is the molecular volume of the solid, γ is the interfacial energy and d is grain size. The normal stress σ_n can also be described as $a\sigma_e/e_v$, where σ_e is the effective applied stress on the aggregate, a is an aggregate packing constant and e_v is volumetric strain. Accordingly, densification is predicted to come to a halt below a strain and grain size dependent "yield stress". The various models derived are subsequently used to obtain criteria defining the conditions under which densification and neck growth/undercutting can be expected to occur in granular solid/liquid systems. Mass transfer mechanism maps defining the corresponding fields in stress versus surface force space are drawn using material specific data for the NaCl/brine system. Finally, experimental data for this system are superimposed on the maps, as a first test of the models.

In Chapter 3, uniaxial compaction creep or densification tests are reported for fine grained NaNO3 aggregates flooded with pre-saturated $NaNO_3$ solution. This system is used as a simple analogue for a solid plus partial melt system. Experiments can be performed on such a salt/solution system under ambient conditions, enabling large quantities high quality data to be obtained more easily than for silicate/melt systems. In particular, these experiments were performed to investigate the possible effects of the solid/liquid interfacial energy as a driving force for grain scale mass transfer and the occurrence of the predicted "yield stress" for solution/precipitation creep due to surface energy forces opposing the effect of applied stress. The results of the $NaNO_3$/brine experiments show that rapid creep of the aggregate occurs in the presence of saturated solution, while no significant creep occurs when the material is dry or flooded with silicon oil. At volumetric strains of 10-20 %, grain sizes $d > 20$ μm and effective applied stresses $\sigma_e > 3\ 10^4$ Pa, the wet-compacted samples showed densification behaviour roughly consistent with a conventional solution/precipitation creep model, developed for the case of grain boundary diffusion control when surface energy effects are negligible. Estimation of the effective grain boundary diffusivity associated with the observed behaviour, gives a value of 6.10^{-19} m^3/s. However, at low applied stresses ($\sigma_e < 3.10^4$ Pa) and fine grain sizes (< 20 μm), microstructural observations and decreasing strain rates with decreasing grain size indicate that surface energy related driving forces become important. An anomalous dependence of strain rate on grain size can be observed for these low stress experiments, with a positive slope (strain rate decreasing with decreasing grain size) instead of the negative dependence predicted by the conventional grain boundary diffusion creep model. Experiments which reach unmeasurably slow strain rates, as well as stress versus strain

rate data extrapolated to zero strain rate, demonstrate a yield stress effect which is broadly consistent the predictions of the densification model for the case when the driving force for solution/precipitation approaches zero due to an opposing surface energy force.

In Chapter 4, uniaxial stress densification experiments are reported for fine grained (1.5-20 μm) forsterite (Fo_{100}) aggregates compacted with only a vapour phase in the pores at temperatures of 1390-1470 °C. At volumetric strains $e_v < 20\%$, applied stresses > 1 MPa, grain sizes > 5 μm and temperatures of 1470 °C, compaction rates at constant e_v are approximately proportional to the applied stress and to one over the grain size cubed, which is consistent with Coble or grain boundary diffusion controlled creep. Fitting the data to a Coble creep equation, the effective grain boundary diffusivity δD_{gb} was determined to be 2 $10^{-20} m^3/s$, which is broadly consistent with literature data for the diffusion of Mg in grain boundaries. The apparent activation energies determined are in the range 570-730 kJ/mol which is high compared to reported activation energies for lattice diffusion. However the values obtained were consistent with values recalculated from previous studies on densification of fine grained forsterite aggregates for which grain boundary diffusion was found to be the dominant mass transfer mechanism. Microstructural study of the samples showed very low dislocation densities, no grain flattening and few fractures to be present. These features plus tightly fitting grains and reduced porosity support the dominance of diffusion creep as the main densification mechanism. At grain sizes < 5 μm however, the grain size dependence of the strain rate is reversed, showing a significant reduction in densification rate compared with the Coble creep behaviour seen at coarser grain sizes. By comparison with theory and with the results obtained for $NaNO_3$, it is suggested that this effect is due to the action of surface energy related forces, and data plotted in linear stress versus strain rate diagrams are again broadly consistent with the existence of a "yield stress" which has to be overcome before densification occurs.

In Chapter 5, stress densification experiments are reported for fine grained (1.5-20 μm) forsterite (Fo_{100}) aggregates compacted uniaxially in the presence of a simulated basaltic melt (51% SiO_2, 29% MgO and 20% Al_2O_3). At volumetric strains of 7.5%-12.5%, applied effective stresses > 1 MPa, grain sizes > 8 μm and temperatures of 1470 °C, compaction rates at constant strains are approximately proportional to the applied stress and to one over the grain size cubed. This is again consistent with Coble or grain boundary diffusion controlled creep. Microstructural study of the samples shows very low dislocation densities, no grain flattening and only very minor amount of grain fracturing.

Tightly fitting grains and reduced porosity support diffusion creep as the main densification mechanism. Both triple junction networks of melt as well as melt-wetted grain boundaries were observed. However comparison of glass compositions measured under the SEM and microprobe with the compositions expected from the appropriate phase diagram shows that samples were not sufficiently rapidly quenched to preserve the melt composition, i.e. crystallisation occurred during cooling of the samples. Fitting the data for grain sizes > 8 μm to the Coble creep equation, the effective grain boundary diffusivity was determined to be 8.10^{-21} m^3/s. Based on the strain rates of the 20 μm experiments with and without melt, the experiments with melt are a factor 3 faster, while based on the kinetic factors determined, the experiment without melt would be roughly a factor 2 ½ faster under otherwise similar conditions. In view of the limited accuracy of the data and the small differences observed, it is concluded that porous forsterite aggregates compacted in the presence of only a vapour phase, and forsterite aggregates with melt-filled porosity, densify at similar compaction rates under similar conditions. The presence of porosity, either vapour-filled or melt-filled seems of significant importance when comparing the results of densification experiments with those of deformation experiments on dense material. The faster rates seen in densification are believed to be due to a shorter diffusion path length through the grain boundary when porosity is present. The similarity in densification rates obtained when the porosity is melt-filled versus can be explained by the fact that in both cases the grain boundary diffusion path length is reduced in comparison to dense samples and by rapid transport in the pores (by surface diffusion or diffusion through the melt). The fact that the melt-bearing samples densify slightly faster can be explained by a number of possibilities, including chemical gradient effects due to impurities in the melt, a lower solid/fluid interfacial energy and hence dihedral angle for the melt-bearing material (futher reducing the diffusion path length within the solid/solid grain boundaries) or fully wetting of a certain fraction of the grain boundaries in the melt-bearing samples.

In Chapter 6, the results are drawn together, general conclusions are presented, and suggestions made for further work.

CHAPTER 1

INTRODUCTION

1.1 Scope and Motivation

The research reported in this thesis is concerned with gaining a fundamental understanding of the deformation behaviour of porous, crystalline aggregates containing a fluid phase, i.e. a solution, vapour or partial melt phase. Ultimately, it is aimed at contributing to a general understanding of large scale deformation and melt expulsion phenomena in partially molten regions of the Earth's mantle, such as those beneath mid-ocean spreading ridges. The approach adopted involves the development of microphysical models for densification and other mass re-distribution mechanisms, as well as systematic experimental work designed to test these models. The experimental materials and conditions chosen are simple, especially chemically, in order to limit the number of variables involved and thus to gain a basic understanding of mass-transport processes in solid-liquid systems, under fully hydrostatic and non-hydrostatic (densification) conditions. In the models developed, both stress and interfacial energy are taken into account as possible driving forces for grain scale mass transport during densification. The models are tested and refined where necessary, by comparison with experimental results obtained on three different material systems, namely sodium nitrate with saturated solution, forsterite/vapour and forsterite with a synthetic basaltic melt.

1.2 Background

1.2.1 Partial melting at mid-ocean ridges and constraints on natural conditions.

Partial melting is believed to have played a major role in the dynamic evolution of the Earth and other terrestrial planets since the earliest stages of their existence. Throughout the history of the Earth, partial melting has been an active process in separation and redistribution of materials. Chemical fractionation of the crust and mantle being the integrated result of ongoing magmatic transport via partial melting through

geological history (Waff, 1986, Vlaar et al., 1994 and de Smet, 1999). Volcanic eruptions at the Earth's surface today, indicate that dynamic processes involving melts continue to take place, and apart from their role in chemical fractionation, the presence of melts in specific geological environments represents an integral part of plate tectonics and mantle convection.

At mid-ocean spreading ridges, the oceanic crust is continuously renewed, with the cooling crust moving laterally away from the ridge as melt ascents from the mantle. Except in the vicinity of fracture zones and mantle plumes, the crust formed is uniform in thickness (7 ± 1 km) and composition (mid-ocean ridge basalts-MORB). Mantle material ascends along an adiabat beneath the spreading centre, characterised by a thermal gradient with depth of about 0.5 °/km, while the pressure dependence of the fertile mantle solidus beneath a ridge is about 4 °/km. Upwelling mantle material passes through the solidus at ~ 50-120 km depth (depending on the temperature of the rising mantle material) and partial melting results. This process of decompression melting is widely accepted as the mechanism by which melts are generated beneath ridges (Turcotte and Morgan, 1992 and White and McKenzie, 1995).

Let us consider now the parameters required to describe the processes of melt generation, segregation and migration, making use of the uniform mantle composition and phase relations established by both experimental work and studies of natural rocks.

The major mineral constituents of the upper mantle are believed to be olivine (~Fo 90), ortho/clinopyroxene plus an additional aluminous phase (plagioclase, spinel or garnet) (Ringwood 1975). Geochemical and petrological studies constrain the depth where most basaltic melt is generated from mantle rocks with this composition. Most melting beneath mid-ocean ridges is thus calculated to occur in the 20-65 km depth range, in the spinel peridotite stability field. Similarly, smaller amounts of melting are expected to take place at depths < 20 km in the plagioclase lherzolite stability field and at depths > 65 km in the garnet lherzolite field (Salters and Hart, 1989; Klein, 1991 and Turcotte and Morgan, 1992).

Mid-ocean ridge basalts are thought to be generated by an average of 10-15 vol% partial melting of the sub-ridge mantle with a maximum total melt extraction of 20-30%. The above compositions and melt volumes are consistent with a temperature of around 1350 °C for the rising mantle material at the onset of decompression melting (Turcotte and Morgan, 1992 and White and McKenzie, 1995). For the cases where a mantle plume interacts with a spreading ridge, e.g. beneath Iceland, the temperature of the mantle is

thought to be 150°-250 °C higher and hence melting may start at depths of 120 km or more (White and McKenzie, 1995). For the hottest adiabat directly underneath the spreading centre, Hess (1992) assumed the maximum amount of melt to be 25% and the melting process to be largely stopped at pressures < 0.5- 1.0 GPa, where all calcic clinopyroxene is thought to have gone in the melt phase. Taking a mean heat of fusion to be 43.10^{-3} J/kg and a heat capacity of 7.2 10^{-5} J/kg °C (both values are averages for forsterite, enstatite and diopside), an excess temperature of 150 °C is required to melt 25% of the mantle and as a result the onset of melting is placed at 1470-1530 °C at 2.7-3.2 GPa (spinel lherzolite- garnet-lherzolite) (Hess, 1992; Turcotte and Schubert, 1982).

The very low water content of water-undersaturated ocean floor basalts, implies that the H_2O content of the mantle is 100-200 ppm and consequently the amount of melt produced above the dry solidus will not deviate noticeably from that in totally H_2O- free mantle (Hess, 1992).

In contrast to the high hydrostatic pressures, differential stresses in the upper mantle are thought to be very low. Independent estimates of upper mantle differential stresses obtained from earthquake and gravitational data (see Stocker and Ashby, 1973) and from microstructural studies (Mercier, 1980) give global values which fall between 0.1 and 20 MPa. Stocker and Ashby (1973) propose that local stresses could be higher, up to 50 MPa, and Mercier's microstructural estimates include some higher stresses (up to 45 MPa) associated with specific tectonic settings, e.g. the uppermost mantle beneath continental extension regions (Mercier,1980). However for the bulk of the upper mantle 0.1-20 MPa is considered the best estimate (Stocker and Ashby, 1973).

The distribution of a melt phase in a volume of rock, on the grain scale, is known to effect material properties such as rheological behaviour and the electrical- and accoustic properties of rocks (Waff, 1986). These changes provide another source of data in addition to geochemical and petrological data and can be used in locating and characterising (large-scale) partially molten zones at depth in the Earth (Shankland et al, 1981). Sato et al. (1989) considered such changes in the neighbourhood of the mid-Atlantic ridge near Iceland. Assuming the melt to be distributed in a tube-like system of connected triple junctions at the grain boundaries, and using a combination of seismic, electrical conductivity, heat flow and experimental data, Sato et al inferred about 5% of melt to be present at depths above 65-105 km.

The width of the partial melting zone at the above depth is for the Mid-Atlantic ridge estimated to be ~ 100 km on either side of the ridge. For the East Pacific Rise (EPR)

a lower volume percentage of melt (2-3%) is indicated, but over a much wider range from the ridge (Sato et al, 1989). Figure 1.1 illustrates a schematic drawing for the EPR situation (following Levy, 1998). Forsyth (1992) gives an average of 3-6% melt beneath young sea floor of the Pacific (< 4 Ma) at 30-80 km depth based on the same melt geometry. If the melt is assumed to be distributed as thin films perfectly wetting the grain boundaries, then the estimated melt fractions would be smaller, i.e. < 1% (Sato et al, 1989; Forsyth, 1992). From recent seismic data on the EPR (Forsyth et al., 1998; Levi, 1998), it is suggested that the indicated region of hundreds of kilometres width would have 1-2% melt. However, based on detailed conductivity measurements, less than 1% of melt is expected to be interconnected (Forsyth et al, 1998; Toomey et al., 1998 and Levi, 1998). Perhaps the strongest observational constraint on melt occurrence at mid-ocean ridges is the fact that the neovolcanic zone (melt emplacement at the surface) is restricted to only a 2-3 km wide zone, independent of axial morphology or spreading rate (Macdonald, 1982).

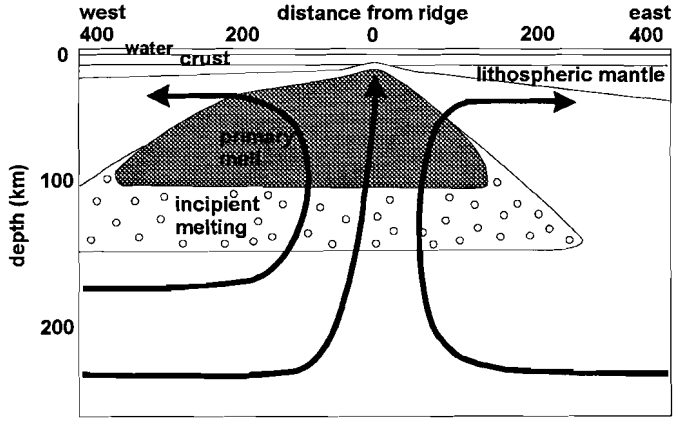

Figure 1.1 Schematic drawing of the partially molten mantle underneath the EPR as a function of depth and distance from the ridge axis (After Forsyth et al., 1988 and Levi, 1998). Note the primary melt zone extends laterally several hundreds of kilometers from the axis going down to around 100 km depths. Smaller amount of partial melting may extend to ~150 km depth and to a larger lateral distance from the axis.

Combining all data above, a consistent picture emerges of the amount and depth of melt occurrences associated with ocean spreading ridges. Together with the physical/chemical parameters of mineral combinations representing mantle composition, a useful framework for modelling large scale processes in mid-ocean partially molten

systems is established. However, combining available data on melt percentages at depth with the amount of material emplaced at the ridge axis, a major problems arises, namely, a mechanism is required to focus melt from the wide source region to the very narrow mid-ocean ridge axis (see Figure 1.1). Melt migration due simply to the difference in buoyancy between the solid matrix and the melt fraction can account only for vertical movement. No focusing mechanism can be directly derived from any of the above data sources. Also, episodicity in melt emplacement, in the absence of geophysical evidence for the presence of continuous magma chambers under slow spreading ridges, places constraints on melt-migration processes, i.e. requiring variations of permeability and/or melt fraction/ melt generation with time (Hess, 1992).

1.2.2 Constraints on rheological behaviour and melt distribution

Two basic scenarios have been proposed for the focusing of melt to the ridge axis in the last few decades. The main differences in these large scale models, are on the meso-to-grain scale distributions of the melt phase and on the driving force for melt migration.

The first scenario involves a number of models proposed for the development of veins, channels or conduits in which melt can flow very rapidly (Sleep, 1988; Stevenson, 1989; Kelemen et al, 1995; Aharonov et al, 1995 and Richardson et al, 1996). These channels are assumed to be either completely open (e.g. Kelemen et al, 1995) or to be zones of increased porosity or higher melt content compared to the adjacent matrix (Richardson et al, 1996). Note that when more melt per unit time flows from deep regions of the mantle to the ridge axis, lateral melt focusing towards the ridge axis is not required. However, in models for channelized flow, melt generation and initial segregation are not taken into account. With respect to the highly porous conduits proposed by Richardson et al. (1996), the authors state that they do not examine the question of channel formation, but simply assume the channels to exist and with a continuous supply of melt to keep them open. The idea of channelized flow thus restricted and requires a fast melting, presumably at the grain boundaries, and effective segregation of the first melt from the grain boundaries into a channelized system. However, a large pressure gradient is needed to obtain rapid flow of the melt phase in the conduits and the continuous feed of melt at the lower end of the channel-system.

Data supporting the channelized flow model come from field studies on peridotites which demonstrate dike formation and flow of melt under shallow mantle conditions (< 30

km) with focussing along actively deforming shear zones (e.g. Kelemen and Dick, 1995). However, the occurrence of shear zones probably requires relatively large deviatoric stresses (microstructural studies indicate tens to several hundred MPa - Ceulenaar and Rabinowicz, 1992), not thought to exist below the shallow upper mantle (Stocker and Ashby, 1973; Mercier, 1980). Hence, it must be concluded that while the conduit-flow models provide a possible explanation for the processes of melt transfer in the shallow upper mantle, and maybe under conditions of exceptionally rapid and short lived melt flow (such as flood basalt production related to an upwelling mantle plume - White and McKenzie, 1995), they do not provide a suitable explanation for melt segregation and migration phenomena occuring in the partially molten mantle under mid-oceanic ridges, where most melt is thought to be generated.

The second scenario for melt focussing at ocean ridges involves models addressing flow of the melt phase through a porous, compacting (deformable) solid matrix. Most of these models consider only vertical movement due to buoyancy. An exception however, is the model by Sparks and Parmentier (1991). They propose a sloping P-T solidus, similar to the near ridge isotherms, away from the ridge axis (see Figure 1.2). Melt freezing will occur at the solidus and a pressure gradient will develop that drives ascending melt away from the relative high-pressure freezing region to the lower-pressure ridge axis. Underneath the freezing boundary, a layer of higher porosity/larger melt volume then develops by de-compaction. Hence an additional driving force for melt migration due to a pressure gradient is present compared to buoyancy alone.

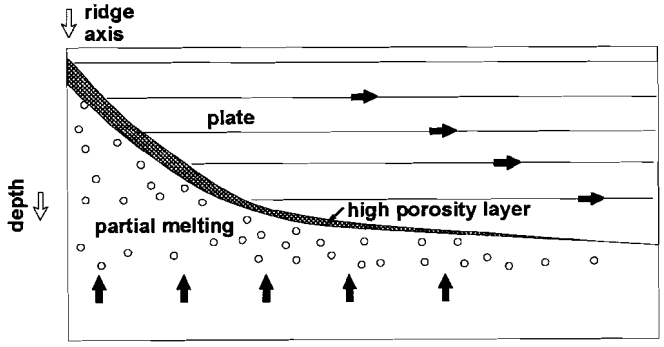

Figure 1.2 Simplified two-dimensional ridge model (After Sparks and Parmentier, 1991). A high porosity layer (grey area) directly underneath and parallel to the sloping p-T solidus (near ridge isotherm) is indicated above the melt production region (dots). In the melt production region matrix compaction occurs and melt flow is buoyancy driven.

One of the main assumption in the latter scenario of porous flow models in general, is that of a fully interconnected fluid network along grain boundaries, through which melt flow under the influence of a pressure gradient (Richardson et al, 1996). The existence of such a fluid network is based on theoretical considerations in which the equilibrium dihedral wetting angle is calculated from solid/solid and solid/liquid interfacial energies, assuming (mechanical and chemical) equilibrium conditions and a homogenous, isotropic matrix material. Although the idea of porous flow is compatible with the predominantly small differential stresses thought to prevail at depth of more than 30 km under mid-ocean ridges, and also with the idea of partial melting occurring first at the grain boundaries, some difficulties remain for the porous flow scenario. The first is that a connected fluid network would be of very limited height (10-100m) under equilibrium conditions because a partially molten column exceeding this height would collapse under its own weight (Ahern and Turcotte, 1979 and Turcotte and Morgan, 1992). However, even if such a connected network extended over considerable vertical distances, extraction due to buoyancy forces alone through the narrow grain boundary tubule-network would be very slow and it is generally believed that the melt would equilibrate with the matrix through which is passes (Richardson et al, 1996). Nonetheless, the latter flow mechanism contribute under the bulk mantle conditions (below 25-30 km depth), though additional driving forces (such as in the model by Sparks and Parmentier, 1991) must be considered.

Brown et al (1995) have summarised a number of possible additional driving forces. Apart from the buoyancy force, melt segregation can be driven by gradients in surface energy. Models for this consider expulsion of melt in excess of the equilibrium melt fraction, so as to achieve lower interfacial energy per unit volume (Jurewicz and Watson, 1985). A second additional driving force can be an applied differential stress. This is addressed in models which consider the melt expulsion from layers or zones of compaction as a result of melt buoyancy coupled with deformation of the matrix under its own weight, either during melting (McKenzie, 1984; 1987) or during crystallisation (Petford, 1993). Other additional driving forces for melt segregation could be convection driven by thermal effects, or convection driven by volume changes during mineral phase changes (Brown et al, 1995).

1.3 Problem definition

From the above, it can be concluded that despite the fact that mid-ocean ridges are the simplest large scale setting where partial melting occurs, many processes at depth, such as segregation and migration of the melt phase, remain poorly understood. Essential input parameters for large scale modelling, such as the melt distribution on the grain scale and whether or not a continuous network of (grain-scale) melt channels exists, are poorly constrained. Also poorly constraint is the effect of melt on the rheological behaviour of the mantle rock.

In order to establish the solid/liquid phase distribution under controlled conditions, many experimental studies have already been performed (Waff and Bulau, 1979; 1982; von Bargen and Waff, 1986; Cooper and Kohlstedt, 1982; Riley and Kohlstedt, 1992; Faul et al., 1994; Jin et al, 1994 and Faul, 1997). However, recently Faul and co-workers (1994 and 1997) and Hirth and Kohlstedt (1995) found that anisotropy of interfacial energy has a large effect on the melt topology. Instead of equilibrium dihedral wetting angles in the range 30-47° (Waff amd Bulau, 1979 and 1982), which determine that for olivine/basalt the melt is present in triple junction networks only, many wetted grain boundaries were found. Jin et al. (1994) found wetted grain boundaries thought to result from non-equilibrium melt spreading. If indeed melt is present on grain boundaries at depth, it will have major implications for seismic velocities and other geopysical parameters, but also for the rheological behaviour of the partially molten rock as diffusive mass transfer will presumably occur through the grain boundary melt phase.

An important contribution to understanding the behaviour of partially molten regions of the earth is provided by experimental densification and deformation studies on olivine plus basaltic melt samples. Cooper and Kohlstedt (1984 and 1986) and Hirth and Kohlstedt (1995 and 1996) studied the dependence of densification rates on stress and melt content, comparing the results with the rheological behaviour of olivine rock in the absence of a melt phase. It was found that for applied stresses in the range 10- ~100 MPa and grain sizes < 20 μm both densification (Cooper and Kohlstedt, 1982, 1984) and deformation (Hirth and Kohlstedt, 1995, 1996) were dominated by grain boundary diffusion at temperatures in the range ~1100-1400 °C. Samples with medium/high porosities (> 10%) show only a modest difference in densification rate between vapour filled and melt-filled pores, the latter densifying faster by a factor 2. A possible explanation for the minor difference in densification rate is that the solid/solid grain boundary diffusion step of the mass transfer process is rate limiting in both cases, only the solid/solid diffusion

path becomes shorter due to partial penetration (i.e. penetration of an outer contact rim) of the melt phase into the grain boundaries (Cooper and Kohlstedt, 1982 and 1984). However, the studies by Hirth and Kohlstedt (1995, 1996) indicate that when comparing dense samples with samples containing varying amounts of melt, then at melt fractions > 5% the effect of the melt phase becomes increasingly more important and the above explanation would significantly underestimate the effect of melt fraction on strain rate (Hirth and Kohlstedt, 1995). The authors state that the viscosity of the mantle can be reduced more than an order of magnitude if the retained melt fraction is greater than 5%. Further, it was observed that with an increase of melt above 5%, the number of completely wetted two-grain boundaries increased (Hirth and Kohlstedt, 1995). Note that complete wetting of grain boundaries by the melt phase deviates from the average equilibrium wetting angle of 38° measured under hydrostatic conditions.

When trying to combine information from equilibrium (hydrostatic) melt distribution studies and densification or deformation studies on partially molten samples, the difficulty arises that little or no information is available under conditions where both stress-related and surface-energy-related driving forces for diffusive mass transfer are comparable in magnitude. Rather, in work on solid/melt geometries in partially molten mantle rocks, small differential stresses are neglected and interfacial energies are considered to determine the melt distribution (Faul et al., 1994 and Waff and Bulau, 1982). Similarly, no systematic densification studies have been performed on partially molten aggregates under the low stress conditions where surface energy forces become significant. In all previously reported deformation and densification studies of olivine/melt samples, surface energy was, when considered at all, found to be negligible compared to stress-related driving forces. However, applied stresses are usually > 10 MPa in the experiments reported (except for a few individual experiments excluded from curves and/or conclusions), which is high compared with stresses expected in the mantle.

Although surface forces are small and usually neglected, order of magnitude calculations indicate they could become significant in the differential stress range from 0.1 - 10 MPa, which is the differential stress range thought to prevail under bulk mantle conditions (Stocker and Ashby, 1973). Therefore, taking both interfacial energy and low stresses into account in trying to understand diffusive mass transfer processes is a necessary step in investigating the rheological behaviour and solid/melt topology of partially molten systems under low stress conditions.

1.4 Present aims

In view of the problems identified above, the aims of the thesis can be specified as follows:

1) To provide a theoretical framework for treating grain scale mass transfer processes in partially molten systems, taking both surface energy related driving forces and intergranular stresses into account.
2) To derive microphysical models, based on fundamental thermodynamic arguments, for neck growth and densification via solution/precipitation mass transfer processes in solid/liquid systems under purely hydrostatic and stressed (non-hydrostatic) conditions.
3) To test the models derived by performing experiments on solid/fluid systems and to establish the relative importance of surface energy related driving forces compared to an applied stress. Emphasis in the experimental work will first be placed on solution/precipitation processes in an inorganic salt/brine analogue system at room temperature.
4) To expand the theoretical models to high temperature systems taking solid state diffusion processes into account alongside solution-precipitation transfer, and to test the applicability of these models to forsterite at high temperature.
5) To elucidate the effect of the presence of a melt phase in the pores by comparing the results obtained from the high temperature experiments on forsterite/melt and on forsterite/vapour systems.
6) To consider the implications of the results for modelling large scale processes.

CHAPTER 2

SOLUTION/PRECIPITATION PROCESSES IN STRESSED SOLID/LIQUID SYSTEMS: THEORETICAL ASPECTS

2.1 Introduction

An understanding of the physical and microstructural properties of aggregates containing a fluid phase is of major importance to earth-scientists, in relation to topics ranging from near-surface compaction and lithification of sediments, to situations encountered in partially molten regions of the Earth's mantle. In particular, the presence of an intergranular fluid phase has important implications for rock rheology, transport properties and response to seismic waves (Waff, 1986; Andersen and Spetzler, 1970; Bulau et al., 1979; Toramaru and Fujii, 1986; Daines and Richter, 1988; Drury and Roermund, 1989; Goetze, 1977; McKenzie, 1984, 1989; Shankland et al., 1981; Mavko, 1980; Nur, 1987; Sato et al., 1989 and Scott and Stevenson, 1989). Moreover, changes in fluid content and fluid-filled pore configuration directly influence these properties. In the case of partially molten regions of the mantle, for example, the rheological and permeability properties of the rock material in question will determine rates of both melt segregation and melt-migration processes which play a crucial role in controlling magmatic and volcanic activity within the Earth. In order to understand how, and to quantify at what rate, changes in total porosity, pore geometry and pore connectivity occur, one has to understand the underlying grain-scale processes that can operate in fluid-bearing systems under both hydrostatic and deviatoric stress conditions.

Pressure solution or solution/precipitation creep processes are known to be important in solid/fluid aggregates under relatively low stresses where dislocation creep mechanisms are negligibly slow (Rutter, 1976; Robin, 1978; Raj, 1982, Pharr and Ashby, 1983; Lehner and Bataille, 1984; Watson and Brenan, 1987; Lehner, 1990 and Spiers and Schutjens, 1990). Due to an increased solubility at grain to grain contacts under stress, compared to pore-wall regions, material is transported from contacts to pores resulting in deformation/compaction of the aggregate and porosity reduction. Stress-driven solution/precipitation creep processes of this type have been extensively studied both theoretically and experimentally (e.g. Rutter, 1976; Robin, 1978; Raj and Chuyng, 1981;

Cooper and Kohlstedt, 1984; Green, 1984; Lehner, 1990; Spiers and Schutjens, 1990; Spiers et al., 1990 and de Meer and Spiers, 1995). However, although the intergranular stresses considered in these investigations were generally low, the effect of interfacial forces was disregarded or assumed to be negligible. On the other hand, numerous studies which have concentrated on pore geometries (e.g. dihedral angles) resulting from balanced interfacial forces under hydrostatic stress conditions, neglect small differential stresses acting at grain contacts. Studies considering solely interfacial energies have been performed on granites with melt (Jurewicz and Watson, 1985), on mafic (olivine) rocks with basaltic melt (Bulau et al., 1979; Vaughan et al., 1982; Waff and Faul, 1992 and Faul, 1997), and on limestone with water (Hay and Evans, 1988).

Thus, despite the fact that they may often be of comparable magnitude under natural conditions, only a few studies have considered both surface energy and differential stress as competing driving forces for material transport and porosity/permeability change in fluid or vapour bearing aggregates (Coble, 1967, 1970; German, 1985 and Heidug, 1992). Moreover, there is a great deal of disagreement in the literature regarding the relative importance of the two possible driving forces. This is examplified by the contradictory interpretation of the results and microstructures obtained in the NaCl bi-crystal experiments of Hickman and Evans (1991) and Schutjens (1991). In the experiments by Hickman and Evans (See Figure 2.1a), stresses transmitted across grain contacts were found to be unimportant compared to interfacial energies, the latter resulting simply in transport of material from the pores towards the grain contact leading to so called "neck-growth", i.e. growth of the grain contact due to material being added to its margin. These findings seem inconsistent with the results of similar experiments under comparable conditions (See Figure 2.1b) presented by Schutjens (1991). In his bi-crystal experiments, Schutjens observed fluid penetrating the grain boundaries between the NaCl crystals. Furthermore, ongoing intergranular pressure solution occurred which could be explained in terms of stress-related driving forces. In summary, there has been little attempt to present a complete picture of the thermodynamic driving forces which can operate in a solid/liquid system, and competition between surface energy and stress-induced driving forces has been largely neglected despite experimental evidence that both are important (Coble, 1967; Swinkels et al., 1983; Watson and Brenan, 1987; Hickman and Evans, 1991 and Schutjens, 1991).

It is the aim of this chapter to provide a theoretical framework for the description of solution/precipitation processes in solid/liquid systems taking both surface energy related driving forces and intergranular stresses into account. As a starting point, fundamental thermodynamic arguments are used to define equilibrium conditions for a liquid bearing crystalline aggregate and to identify the physically possible driving forces for mass transport when such an aggregate is removed from a state of equilibrium. This provides a basis for considering the various processes which can occur under both "unstressed" (purely hydrostatic) and stressed (non-hydrostatic) conditions. Models for neck-growth and densification by solution/precipitation processes, taking into account the competition between stress-related and interfacial-energy-related driving forces, are thus derived. Existing experimental data on the NaCl/brine system are subsequently inserted into the models to get a first idea of their characteristics and applicability. In addition, a basis is established for the design of appropriate experiments aimed at more rigorously testing the applicability of the models obtained, on both analogue and geological systems.

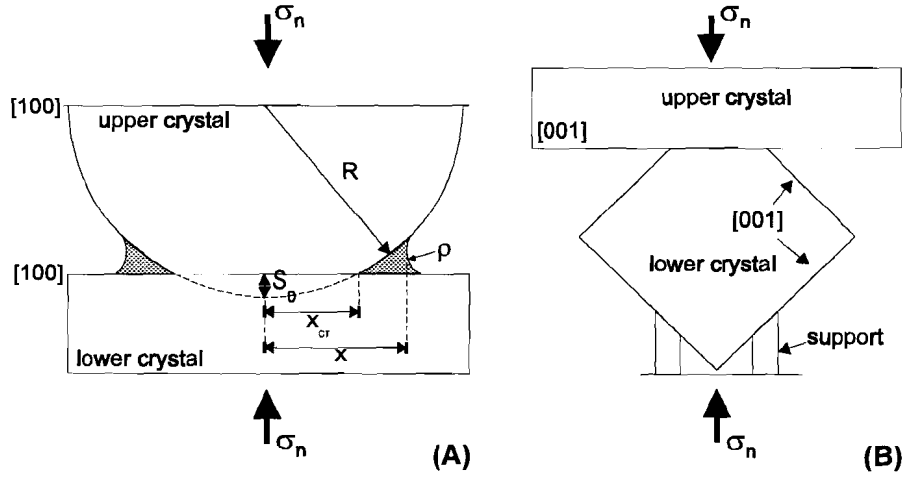

Figure 2.1. A) Schematic ball-and-plate geometry employed in the Hickman and Evans (1991) experiments. A spherical lens (radius of curvature R) and a flat plate of NaCl are pressed together in the presence of a saturated brine. Material has precipitated at the highly curved neck region. B) Schematic diagram of the bi-crystal geometry used by Schutjens (1991). When a stress is applied to the crystals in the presence of a brine, a time dependent convergence is observed. Applied stresses in the experiments of A) and B) are in the same range.

2.2 Thermodynamic Preliminaries

In the following, a number of important thermodynamic background concepts are drawn together from the literature where comprehensive reviews are lacking. Throughout the chapter, attention is restricted to a granular solid plus liquid only, i.e. with no vapour phase. For now, all solid state deformation processes are assumed to be negligibly slow insofar as they contribute to strain accumulation and/or porosity change. The arguments and results which will be presented apply both to solid plus saturated solution and solid plus partial melt systems. In chapters 4 and 5, some extensions of the models are made to include solid state diffusion processes.

2.2.1 Surface Thermodynamics

2.2.1.1 Definition of a surface; The Gibbs dividing surface

In order to describe surface phenomena and thermodynamics a good definition of a surface is essential. In general, the vicinity of surfaces of discontinuity are associated with variations in the densities of the component substances and of energy and entropy. Gibbs (1906) showed that when two homogeneous phases are separated by a surface of discontinuity, thermodynamic potentials for the system (i.e. internal energy, entropy or Helmholz free energy) can be unambiguously divided into contributions from the phases present (e.g. phase (1) and phase (2)) and from the dividing surface. Gibbs (1906) chose a geometrical surface which is coincident with the physical surface of discontinuity to within the accuracy with which the latter is localizable but which has a precisely determined position: it is chosen to pass through "all points which are similarly situated with respect to the condition of the adjacent matter". This geometrical surface, defined with respect to matter, is called the Gibbs dividing surface. With respect to the physical surface, the position of the dividing surface is to some extent arbitrary, but the directions of its normals are everywhere determined, so all definable dividing surfaces are parallel to each other. The most important consequence of the chosen surface definition for a thermodynamic description is the introduction of excess quantities associated with a surface. To illustrate the excess quantities of a system containing a dividing surface, a simple example is given here for excess energy. An energy E(1) is assigned to phase (1) equal to the volume of the phase on one side of the dividing surface times the average energy density for bulk phase

(1). Doing the same for phase (2) and letting both phases be homogeneous up to the dividing surface, the total energy of the system can be defined by

$$E_{syst} = E(1) + E(2) + E(surface) \qquad (2.1)$$

where E (surface) can be regarded as an excess value of E for the real system compared to a system consisting of two bulk phases (without taking a surface into account), the "excess" being positive or negative depending on the system under consideration. The same concept can be applied to all extensive thermodynamic quantities and mechanical forces.

Strictly, the value of any surface property depends on the location of the dividing surface, if the boundary is not flat, as moving the boundary parallel to itself would increase/decrease the total surface area and radii of curvature, and therefore surface mass, energy and/or entropy density. This effect will be disregarded here because the effect for the grain sizes considered (> 100 nm) is negligible.

Two main approaches for thermodynamic modelling of surfaces can be found in literature. The first uses the Gibbs dividing surface, as just described. The other is the Guggenheim approach (Guggenheim, 1952, 1967), in which the excess quantities due to the presence of a surface are assigned to a layer of finite thickness. However, surface properties are usually associated with a layer so thin, that it is below the acceptable scale for using macroscopic thermodynamics and a molecular/atomic description is required when the surface is considered as a layer. Therefore, the Gibbs dividing surface concept will be used in this thesis to describe surface phenomena using surface thermodynamics.

In summary, the introduction of the Gibbs dividing surface can be described as assigning the excess quantities of a real 3-dimensional interfacial region to a mathematical 2-dimensional interface. This can be compared to the jump condition treatment of an interface in the continuum theory used, for example, by Chadwick (1976) and Lehner (1990), in which a finite jump in the relevant variable is described across a "singular surface".

2.2.1.2 Surface Tension and Work to Create Unit Surface

Gibbs was the first to distinguish between

1) the work γ, required to create unit surface, (i.e. adding atoms at the surface at constant p, T and surface density of the substance components) and
2) the surface tension, γ_{tens}, being the work done in extending the surface so as to increase the area by a combination of (elastic) stretching and adding material to the surface.

For a surface between two liquid phases, γ and γ_{tens} are the same because the molecules or atoms are mobile and accommodate themselves to the new situation and no stresses can be built up to (elastically) stretch the surface. The surface between two liquid phases thus, behaves mechanically, as was pointed out by Young (1805), as a membrane stretched uniformly and isotropically by a constant force per unit length which is the same at all points and for all directions in the surface and which is independent of surface displacement (unlike an elastic membrane). For a curved surface, γ relates the pressure difference, Δp, across the interface to its principle radii of curvature (r_1, r_2). The pressure difference is given by the Gibbs-Thomson relation

$$\Delta p = \gamma \left(\frac{1}{r_1} + \frac{1}{r_2} \right) \qquad (2.2)$$

and is directly measurable for example by capillary methods (Defay et al., 1966, Balmer, 1975).

However, when one or more of the phases is a solid, γ and γ_{tens} are not necessarily the same, because of surface strain. In this case, the definition of γ as the work to create unit surface remains the same, but the definition of γ_{tens} has to be changed. When a scalar quantity is preferred, e.g. to make an order of magnitude calculation, the surface tension definition of Shuttleworth (1950) can be used. He defined "surface tension" as 1/2 the trace of the 2D surface stress tensor (i.e. the mean surface stress). However, when one or more solids are involved, the surface stress tensor allows a more complete and general description compared to the scalar surface tension. Therefore the use of term mean surface stress is preferred here for solids. The use of the term surface tension, when solids are involved, is largely historical and due to the early work on fluid/fluid systems. One should be aware that very different use of terminology has lead to much confusion in literature, especially regarding "surface tension" which is often associated with the definition of surface free energy (Herring, 1952; Defay et al, 1966; Benson et al, 1967; Balmer, 1975).

2.2.1.3. Surface free energy

Let us now take γ, the work involved in creating unit area of new surface at constant p, T and surface density of the component substances, as a basic parameter for further analysis. This work done, γ, is equal to the change in Helmholz free energy of the whole system, when the system consists of two bulk phases seperated by an interface. The work per unit area is defined as

$$\gamma = f^{surf} - \Sigma \Gamma_i \mu_i \qquad (2.3)$$

where f^{surf} is the specific surface (Helmholz) free energy, which is the Helmholz free energy per unit surface, μ_i is the chemical potential of the bulk phase i, and Γ_i is the excess number of moles per unit surface of the ith substance (Herring, 1952 following Gibbs, 1906). The excess value here is defined, in accordance with the Gibbs dividing surface concept, as the total number of moles of the component(s) in the system minus the bulk values. If the dividing surface were re-located, translating it parallel to itself, by convention making $\Sigma \mu\Gamma_i = 0$ (no excess of components associated with the interface), the term specific surface free energy, f^{surf}, could be used to denote γ. This is only convenient and feasible for systems without absorbable components (Herring, 1952), as an adsorbed component will cause a true physical/chemical effect in decreasing γ (as $\Sigma \mu_i \Gamma_i$ increases) which cannot be neglected. Also, in the case of a solid/liquid system with 1 or more components adsorbed at the surface, it would be questionable whether the dividing surface still coincides with the physical surface.

When taking $\Sigma \mu_i \Gamma_i = 0$, the product of γ times the area of surface, may be regarded as the available energy of the system due to the presence of surface(s), i.e. the excess energy, when the temperature and the chemical potentials are maintained constant (Gibbs, 1906).

Not only the equality or non-equality between γ and γ_{tens} is an important difference in surface characteristics between solids and fluids, but also the fact that γ is isotropic for fluids, while for crystalline solids it varies, in general, with crystallographic direction in the surface. The existence of relatively close-packed crystallographic orientations results in a number of sharply defined minima in the work to create unit surface (Gibbs, 1906). If the anisotropy of γ is sufficiently marked, these sharply defined minima (called cusps) lead to the development of low energy crystallographic facets, generally parallel to low index planes (e.g. {100} for cubic minerals). When considering solid/solvent interfaces, for

anisotropic polyhedral grains, different γ_i for the different crystal faces have to be taken into account. For a constant volume of crystal, the product of surface free energy times the associated surface area, $\Sigma\ \gamma_i A_i$, has a minimum value at equilibrium (Gibbs, 1906), and represents the work required to form the surfaces (faces) of the crystal. Note that only if γ were isotropic, would the equilibrium condition be satisfied at the minimum area of surface for the total volume of material, i.e. the crystal would reconfigure to a sphere (ΣA_i = minimum). Other euhedral shapes would lead to $\Sigma\gamma_i A_i$ being minimum. The variation of γ with orientation, $\gamma(n)$ is most conveniently represented in a polar diagram, called the Wulff or γ-plot (Herring, 1950 and Tiller, 1991), as shown in Figure 2.2.

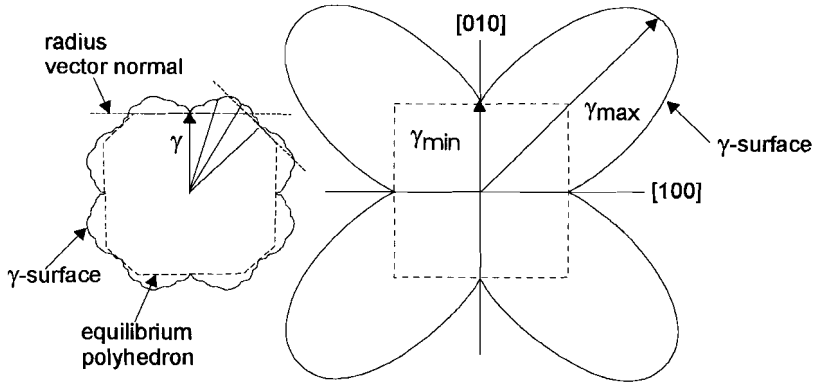

Figure 2.2. Schematic diagram of two Wulff- or γ-plots. The surface free energy, of which the relative magnitude is represented by a radius vector, is shown as a function of orientation. The 2-D equilibrium crystal habit is then given by the inner surface described by the radius vector normals. It follows from the γ-plot that due to the occurrence of sharp cusps, the equilibrium form has a polygonal shape. If γ would be isotropic, the equilibrium shape would have been a circle (in 2 D). The ratio of $\gamma_{max}/\gamma_{min}$ can be used as a measure of anisotropy. If for example, in A) the 0 and 45 degree cusps would be less distinct, the intersections of the normals would be outside the γ-surface and the corners would be rounded (Tiller, 1991 following Herring 1950). Only a very small measure of anisotropy, i.e. for $\gamma_{max}/\gamma_{min} > 1.3$, determines that the crystal habit is completely polyhedral (Herring, 1950). By comparing A) and B) it is easily shown that for polyhedral crystal shapes $\gamma_{max}/\gamma_{min}$ is a better measure of anisotropy than e.g. crystal habit. Note that for B) γ_{max} could be substantially smaller and the crystal habit would still remain cubic.

Lastly, only small particles have any hope of reaching an equilibrium shape, since for larger particles the mass that has to be transported to achieve an appreciable change of shape is so large compared with the lowering of $\Sigma\gamma_i A_i$ that the rate of equilibration

becomes negligible. The shape of the larger particles is likely to be determined by the kinetics of growth or dissolution rather then by a minimum of $\Sigma\gamma_i A_i$ (Herring, 1952). For unconfined solid/liquid interfaces this results in low energy (crystallographic low index) surfaces (facets) without a necessary smallest possible area (Gibbs, 1906).

2.2.1.3. Surface stress

Two sources of surface stress can be identified in solids. First, Gibbs (1906) envisaged that the surface region of a solid may be in a state of stress, even if no pressure or stress are applied. The outermost two or three atomic layers, if left to themselves, would have lattice parameters (e.g., nearest neighbour atom distances) different from those in the bulk. Smaller lattice parameters would lead to a compressive surface stress, larger values to a tensile surface stress. In the actual situation they are balanced by a bulk stress parallel to the surface and extending a few μm inside the crystal. One can imagine, following Gibbs, that when applying a hypothetical force at the edges of the surface the bulk stress can vanish. These surface forces may be of either sign and may be of the same order of magnitude as γ (Sparnaay, 1985).

In the second situation, the solid material is strained due to an applied pressure or stress. Gibbs (1906) states that the rigidity of solids is in general so great, that any tendency of the surfaces of discontinuity to vary in area or form may be neglected in comparison with the forces which are produced in the interior of the solids by any strains, so that it is not generally necessary to take account of the nature of the surfaces of discontinuity in determining the state of strain of the solid masses. However, a state of surface stress will have direct influence on the equilibrium solubility of the (surface) solid in solution when considering a solid/liquid system and therefore on dissolution and precipitation processes, even if the stress is not high enough to cause bulk dislocation motion or elastic deformation. Therefore surface stress can not be neglected in dissolution/precipitation creep.

In general, the surface of a solid can be described as a region where the stress tensor differs from the average tensor in the bulk of the solid, as the stress tensor is no exception to the general rule that the division can be made into bulk and surface (i.e. excess) contributions. These tensor components at the solid surface, σ_{ij}^{surf}, will in general depend on the reference directions chosen in the surface (Defay et al, 1966).

2.2.1.4 The relation between surface free energy and surface stress

So far, surface stress and surface free energy have been described as the two most important parameters in surface thermodynamics. The relation between surface stress, σ_{ij}^{surf}, and the work to create unit surface area, γ, was described by Shuttleworth (1950) and Herring (1952). Recall that changes in area can be achieved by adding new atoms to the surface as well as by stretching the existing surface. The reversible work done ON the system as a result of a surface strain increment, associated with the surface area change, is given

$$\delta W = \delta(\gamma A) = \gamma \delta A + A \delta \gamma \tag{2.4}$$

where W is surface work. The surface work term can be expressed as a function of the 2-D strain tensor, with

$$\delta \gamma = \frac{\delta \gamma}{\delta \varepsilon_{ij}} \delta \varepsilon_{ij} \tag{2.5}$$

so that

$$W = A \left[\gamma \sum_{i=1,2} \varepsilon_{ii} + \sum_{i,j} \frac{\delta \gamma}{\delta \varepsilon_{ij}} \varepsilon_{ij} \right] \tag{2.6}$$

where ε_{ij} is the incremental strain tensor of the surface deformation. The total mechanical work done on the system can be expressed as,

$$W^{mech} = A \Sigma \sigma_{ij}^{surf} \varepsilon_{ij} \tag{2.7}$$

When assuming $\Sigma \Gamma_i \mu_i = 0$ and therefore γ being equal to the surface free energy, then by equating equation (2.7) with equation (2.6) a relation between the surface stress, surface strain and surface free energy can be written, defined by Herring (1952) as

$$\sigma_{ij}^{surf} = \gamma \delta_{ij} + \frac{\delta \gamma}{\delta \varepsilon_{ij}} \tag{2.8}$$

where σ_{ij}^{surf} is the surface stress tensor. The last term will vanish in general for liquids, since the state of the surface of separation between two liquids is not changed by any shear

strains, new atoms are freely supplied to an expanding surface and volume strains in the fluid are negligible. For an isotropic strain (no shear components) the surface stress reduces to

$$\sigma^{surf} = \gamma + A\frac{\delta\gamma}{\delta A} \qquad (2.9)$$

which illustrates very clearly the distinction first made by Gibbs between the energy needed to create new area ($\gamma\delta A$) by definition of γ and the mechanical work ($\sigma^{surf}\,\delta A$) needed to stretch the area. Equation 2.9 is known as Shuttleworth's equation (Herring, 1952 and Shuttleworth, 1950).

Although isotropic strain is not in general observed for crystalline solids, one can question whether the surface stress can be approximated by $\gamma\delta_{ij}$ at high temperatures. This depends on the relaxation time required for the surface to regain its original state by atomic migration. In glasses and melts, both solid-like behaviour ($\delta\gamma/\delta\varepsilon_{ij}\neq 0$) and liquid-like ($\delta\gamma/\delta\varepsilon_{ij}=0$) behaviour should be attainable by varying the temperature and strain rate. Even in ordinary liquids, sufficiently high strain rates can give rise to non-vanishing values of $\delta\gamma/\delta\varepsilon_{ij}$ (Tiller, 1991). For solids, Herring (1951), Benson and Yun (1967) and Tiller (1991) estimate the value of the last term in equation (2.8) for a crystal to be, of the same order as γ itself or a little larger. Since γ is almost invariably positive, the surface stress can be either tensile or compressive (negative) depending on the sign and magnitude of the last term of equation (2.8). The surface stress can therefore be estimated to be numerically in the range from (close to) zero to a few times γ or $-\gamma$. Although the use of a surface stress tensor would in many applications be more correct (complete) than the use of γ, the lack of any numerical estimates provides no improvement over γ when order of magnitude calculations are made. It also seriously complicates the derivation of models addressing surface effects. Therefore, surface free energy will be used in this work as a first approximation when considering surface-related phenomena, though where necessary qualitative use of surface stress will be made.

2.2.2 The Interfacial Free Energy

2.2.2.1 The physical nature of interfacial free energy

In the above a mathematical description of a surface was defined and its thermodynamic consequences described. Now surfaces will be described from a physical point of view because this offers an illustrative means to qualitatively describe the varies interfaces possible, e.g. phase boundaries and grain boundaries.

Consider a solid/vacuum surface. Each atom will have neighbours in the surface plane and in the plane beneath the surface, but the atoms in the plane above the surface are absent. Since each bond made lowers the energy of the atom, the surface atoms will have a higher energy by virtue of these broken bonds. This will be the extra (excess) internal energy of the surface, u^{surf}. Whether the interfacial free energy, f^{surf} , is higher requires knowledge of the excess entropy of the surface, s^{surf} at temperatures above 0 K ($f^{surf}=u^{surf}-Ts^{surf}$). The origin of the surface entropy is to be found in both vibrational and configurational effects. The configurational entropy increase (e.g. due to the formation of ad-atoms by atoms leaving the surface plane) can be neglected at low temperatures. The reduced binding energy for atoms at the surface, causes a lower vibration frequency of the surface atoms and this raises the vibrational entropy (Swalin, 1962; Martin and Doherty, 1976). However, the effect of increasing entropy is of limited value, especially at lower temperatures, therefore the total effect at the surface due to both an increase in internal free energy and entropy always has a finite (positive) excess surface free energy, as previously discussed (Martin and Doherty, 1976).

As an example of the described physical properties, consider the cleaving of a single crystal, which creates two new surfaces. This requires work to be done on the system, and the energy of the new (2 crystal) system is higher than that of the single crystal. However, the energy can not be directly calculated from the amount of work done, since after cleaving the outermost layers of the crystal will reconfigure or "reconstruct", which leads to a decrease of the surface free energy and tends to relax surface stresses. However, these relaxation phenomena do not completely annihilate surface free energy and surfaces stresses (Benson and Yun, 1967; Sparnaay, 1985). When considering theoretical values for surface free energy or surface stress, care must be taken to use values for (relaxed) reconstructed surfaces.

2.2.2.2 Approximations used to determine interfacial free energy values

In order to take the interfacial free energy into account in solution/precipitation models, an order of magnitude value is needed for the solid/liquid interfacial energy, γ_{sl}, and the grain boundary energy, γ_{gb}. Such values are not directly available. Interfacial energy data only exist for solid/vacuum, γ_s, liquid/vacuum, γ_l ,and liquid/vapour, γ_{lv} ,and even these are limited in number and reliability. Here some approximations are explained which will be used to get some order of magnitude values for γ_{sl} and γ_{gb}, based on γ_s, γ_l and γ_{lv} data and the general description of a physical surface given above.

At the dividing surface between a solid and a liquid phase, the energy at the interface is deceased in comparison with the total value of 1 solid/vacuum plus 1 liquid/vacuum surface. This is due to the interaction of solid and liquid atoms. The type of interaction depends the chemical components of the solid and liquid phase. An estimation of the solid/liquid interfacial energies, can be obtained using the simple (empirical) approximation suggested by Israelachvili (1985)

$$\gamma_{sl} \approx \gamma_s + \gamma_l - \sqrt{\gamma_s \gamma_l} \qquad (2.10)$$

where γ_s is the solid/vacuum value, γ_l is the liquid/vacuum value and $\sqrt{\gamma_s\gamma_l}$ represents the solid/liquid atom interaction. The interaction term must be considered a minimum, as it only represents the solid/liquid interaction due to van der Waals forces. If other interaction forces would be significant, e.g. hydration forces (due to the presence of an electrical double layer), the interaction term would be larger and hence the γ_{sl} value smaller (Israelachvili, 1985).

At a solid/solid interface, the surface free energy is also reduced due to the interaction of atoms across the interface compared to twice the solid/vacuum surface free energy value. When both solid phases are (chemically) the same and only differ in crystal orientation the interface is called a grain boundary. The nature, e.g. the surface free energy, of any given grain boundary depends on the misorientation of the boundary relative to the solid grains. The lattice of any two grains can be made to coincide by rotating one of them through a suitable angle ϑ about a single axis (Porter and Easterling, 1992). An important distinction can be made with respect to γ_{gb} between low angle and high angle grain boundaries. Low angle boundaries, with $\vartheta < 10\text{-}15^\circ$, can be considered as an array of dislocations, with the atoms in regions between the dislocations fitting almost

perfectly into both adjoining grains whereas the dislocation cores are regions of poor fit in which the crystal structure is highly distorted. The energy of low angle grain boundaries can simply be taken as the total energy of the dislocations within unit area of boundary (Ashby et al, 1978). At angles ϑ smaller than ~10-15°, γ_{gb} is approximately proportional to the angular misorientation (Porter and Easterling, 1992). However, when ϑ exceeds 10-15°, the boundary is known as a random high angle boundary and at this stage γ_{gb} becomes independent of misorientation (Porter and Easterling, 1992). This is schematically illustrated in Figure 2.3.

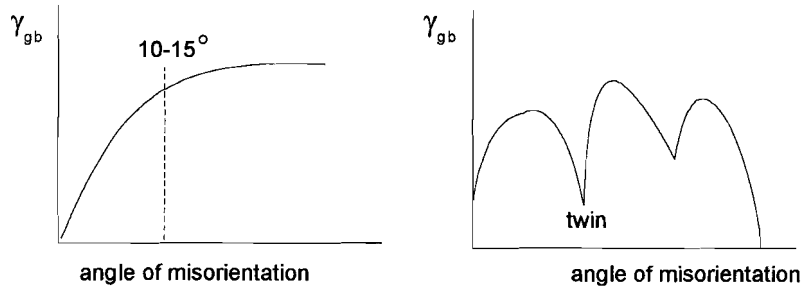

Figure 2.3. Schematic representation of the γ_{gb} variation with grain boundary orientation. A) in the general case the γ_{gb} energy increases roughly linear with the angle of misorientation until 10-15°. For larger angles of misorientation the grain boundary is called high angle grain boundary and γ_{gb} remains roughly the same. B) The grain boundary energy versus orientation shows sharp cusped minima at orientations for which the two adjoining lattices fir together with relatively little distortion. After Porter and Easterling (1992).

High angle boundaries contain large areas of poor fit and have a relatively open structure. The bonds between the atoms are broken or highly distorted and consequently, the boundary is associated with a relatively high energy (Porter and Easterling, 1992). For high angle boundaries it is often found that roughly

$$\gamma_{gb} \approx \frac{1}{3}\gamma_{sv} \qquad (2.11)$$

where γ_{gb} is the grain boundary energy (when $\Sigma\mu_i\Gamma_i=0$) and γ_{sv} is the solid-vacuum equilibrium interfacial energy.

With the Wulff plot (Figure 2.2), it was illustrated that for solids which do not have an isotropic surface free energy (i.e. an euhedral spherical shape) the surface free energy varies with orientation. For these solids (almost all solids) therefore the grain

boundary energy does not only depend on the angle of rotation ϑ, but it can also depend on the orientation of both adjacent crystals. In most cases, the grain boundary between two grains will be a random high angle grain boundary and its grain boundary energy can be approximated by equation (2.11). There are, however, some special high angle boundaries which have significantly lower energies than random boundaries. These boundaries occur when two adjoining lattices fit together with relatively little distortion of the atomic bonds. The simplest example of these special high angle boundaries is the boundary between the two crystals of twins (Porter and Easterling, 1992). For most minerals there are a limited number of special high angle boundaries associated with a good fit and therefore a relatively low γ_{gb} (Porter and Easterling, 1992). Grain boundaries in which the boundary plane is a lattice plane common to both crystals are usually referred to as coincident grain boundaries. If γ_{gb} is plotted as function of boundary orientation, a sharp cusped minimum is obtained at the coherent boundary position. Even for near-coincident boundaries, atoms are shared and boundary coherence is maximised (Porter and Easterling, 1992). Therefore, it can be expected that coincident and near-coincident boundaries are associated with a lower grain boundary energy than average random high angle grain boundaries.

2.2.3 Equilibrium Considerations

2.2.3.1 Global Equilibrium in Dense Crystalline Aggregates

When defining thermodynamic equilibrium as the state of minimum free energy, the question arises whether a polycrystalline aggregate can attain equilibrium at all. All boundaries in an annealed sample, irrespective of if they are grain boundaries, solid/vapour or solid/fluid interfaces, are high energy regions that increase the free energy of a polycrystal or porous aggregate relative to a single crystal of the same volume of material. The ultimate equilibrium state of a monomineralic polycrystalline sample under stress-free conditions would therefore be a single crystal. However, this conflicts with the observation that polycrystalline materials held at high temperatures for long (geological) times remain polycrystalline, and that mass transport processes have stopped (or become undetectably slow) long before the stage of a single crystal is achieved. Thus, although a true minimum free energy state cannot be attained in a polycrystalline aggregate, it will adjust itself, given

the possibility for mass transport, to a structure that reduces the total energy to a metastable condition, dependent on the space defined by a set of internal variables representing the microstructural state of the material (e.g. grain size, pore size, pore distribution). Porter and Easterling (1992) note that in moving towards equilibrium, polycrystalline samples evolve to a fixed microstructure with many local equilibria (force balances), e.g. at grain boundary intersections and grain boundary/ pore intersections (See Figure 2.4b). Such a state can be defined as a metastable equilibrium.

This type of metastable equilibrium, i.e. metastable equilibrium relating to local minima in total surface free energy, can be understood as follows. In order to decrease the total free energy of the aggregate, a number of local equilibria would first have to change to a higher (non-equilibrium) energy state simultaneously, before further geometrical changes could be achieved. This is in agreement with the definition of metastable equilibrium that an activation energy barrier must be overcome before true equilibrium can be obtained. Because true equilibrium is not feasible for polycrystalline aggregates, metastable and associated local equilibrium concepts will be used here, and will be further referred to simply as equilibrium.

In polycrystalline materials not in equilibrium, provided no pressure gradients or applied stresses need to be considered, surface energy related driving forces will thus induce mass transport, thereby moving the system towards a lower total interfacial energy resulting in the ultimate metastable equilibrium configuration. The surface energy driven microstructural change can be recognised in a sample as

1. A reduction in grain boundary curvature
2. Growth of low energy interfaces at the expense of higher energy interfaces (at grain boundaries, pore walls etc.)
3. An increase in the volume to surface ratio, by reduction of the total grain-surface area (e.g. via reduction of surface curvature or via grain growth).

In natural material and experimental samples, many of the mass transport processes observed in aggregates and related to a reduction in surface energy, are due to heterogeneities in the sample, e.g. due to a distribution in grain size or grain packing. For example to describe grain growth or Ostwald ripening, grain size distributions and grain size averages are required, to describe which grains will grow and which will decrease in size and eventually disappear. Such processes require a description only feasible on the aggregate scale, or a representative volume of it. Although related to a reduction in total surface free energy these processes cannot be described using the local equilibrium concept and are therefore omitted.

2.2.3.2. Local Equilibrium at a Solid/Solvent Interface

Gibbs (1906) derived the condition for chemical equilibrium between an isotropic soluble solid at a point on the interface with its saturated solution. This condition was generalized by Heidug (1992). Assuming that the surface stress can be approximated by γ, the condition can be described by

$$\mu_s^f = \mu_{eq} \equiv f^s + p_f \Omega^s + \gamma(1/r_1 + 1/r_2)\,\Omega^s \qquad (2.12)$$

where μ_s^f is the chemical potential of the solid dissolved in the fluid, μ_{eq} is the equilibrium value of μ_s^f (which is equivalent to the potential of the solid), f^s is the free energy of the solid phase, p_f is the fluid pressure, r are the principal radii of curvature which are defined as positive for a convex solid surface (from an origin within the solid grain) and Ω^s is the molecular volume of the solid phase. The term, $\gamma(1/r_1 + 1/r_2)$, can be viewed as the excess hydrostatic pressure in the interior of the solid (Gibbs, 1906) due to the effect of surface stress assumed to be numerically equal to γ and which will vanish when the surface is plane.

Worth emphasising at this point is that the solubility of the solid is dependent on the radius of curvature of the solid surface. As equation (2.12) shows, the equilibrium chemical potential is increased for a positively curved surface in comparison with a flat surface. Accordingly, since

$$\mu = \mu_0 + RT\ln C \qquad (2.13)$$

where C is the solubility of the solid into the liquid phase, then if a solution is saturated with respect to flat crystal faces it is undersaturated with respect to positively curved surfaces.

When dealing with curved interfaces, it is usually implicitly assumed that the value of γ is independent of the local radius of curvature of the surface. General agreement (Gibbs, 1906; Herring, 1952; Defay et al., 1966 and Blakely, 1973) exists on the fact that the changes of γ with the radius of a particle can be neglected for crystalline solids larger than the nucleus size. For fluid systems, for example, the deviation of γ becomes larger than 3% for drops or bubbles $\leq$ 10 nm (Defay et al 1966). Herring (1952) neglects the effect of changing γ with the radius of a particle, when the radius of curvature is large

compared with the (physical) thickness of the interface (usually atomic). Because particles > 100 nm are considered in this work, this effect will be neglected.

2.2.3.3. Solid/solid/liquid equilibria

The solid/solid/liquid distribution on the grain-scale, not just the presence of the liquid, is one of the most important factors in determining the extent to which the liquid (e.g. a melt phase) influences the pore microstructure and physical properties of the total aggregate or rock (Kohlstedt, 1992). Where a solid/solid grain boundary intersects the liquid phase, local equilibrium is characterized by a fixed angle (θ) between the two solid grains filled with liquid. This angle is called the dihedral wetting angle. When representing the surface (interfacial) free energies γ_{ab} ($\Gamma_i \mu_i = 0$) of the interfaces a-b by vectors having a direction parallel to the surface near the point of intersection and a length representing the relative value of γ_{ab}, a vector balance can be described for equilibrium at the point of intersection. For three phases, the general balance is described by (Porter and Easterling, 1992)

$$\frac{\gamma_{12}}{\sin\theta_3} = \frac{\gamma_{23}}{\sin\theta_1} = \frac{\gamma_{13}}{\sin\theta_2} \qquad (2.14)$$

where the angles are indicated in Figure 2.4a.

For the special case of two solid grains of the same material whose common boundary intersects a liquid phase, the equilibrium at the intersection point is described by the Young-Dupre' relation

$$\gamma_{ss} = 2\,\gamma_{sl}\,\cos\left(\frac{\theta_{eq}}{2}\right) \qquad (2.15)$$

with $\theta/2$ being the equilibrium dihedral angle (See Figure 4b.) From this equation, the following important and well-known microstructural consequences can be deduced (Kingery et al, 1976). If $\gamma_{sl} > \gamma_{ss}$,then the dihedral wetting angle is > 120° and the liquid forms isolated pockets of material at the grain intersections. If the ratio $\gamma_{ss} / \gamma_{sl}$ is between 1 and $\sqrt{3}$, the dihedral wetting angle is between 60° and 120° and the fluid partly penetrates along the grain intersections at corners of three grains. If the ratio is larger than $\sqrt{3}$, then the dihedral angle is less than 60° and the fluid phase is stable along any length of grain

edge forming triangular prisms at the intersection of three grains. When the ratio $\gamma_{ss} / \gamma_{sl} = 2$, the dihedral angle equals zero and at equilibrium the faces of all grains are seperated by fluid (Kingery et al. 1976).

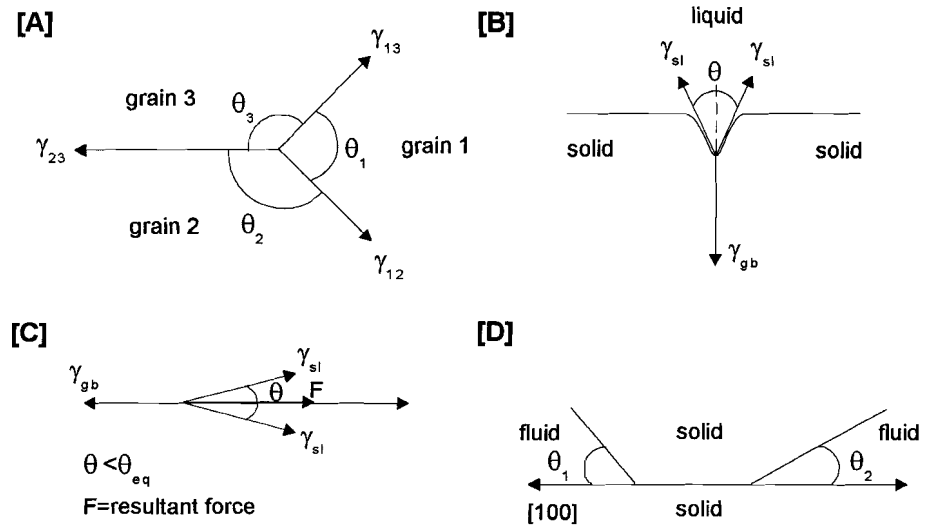

Figure 2.4. a) Schematic diagram of a vector balance of grain boundary energies for three phases in equilibrium. b) Schematic diagram of a vector balance for two solid phases of the same material whose common boundary contacts a liquid phase. The angle θ is the dihedral wetting angle. c) Schematic diagram of a vector representation of the interfacial energies when no equilibrium, i.e. when a resultant force exists. d) Schematic diagram of two asymmetric wetting angles resulting from surface energy anisotropy. For these and similar situations the dihedral wetting angle concept as illustrated in diagram b) can not be used.

Not only the distribution of the solid and fluid phases are important but also the relative amounts. The equilibrium solid/liquid fraction depends on the dihedral wetting angle as well as on the packing of grains, and it is defined as the minimum amount of fluid necessary to have the system adjusted to its minimum free energy situation for a fixed grain size when no solid mass transfer occurs (Park and Yoon, 1985; German, 1985). If more fluid is present than the equilibrium fraction then either the excess is expelled, or the system will adjust itself to the metastable configuration, i.e. the minimum energy configuration possible for the given amount of liquid.

2.2.3.4 When the dihedral wetting angle concept should NOT be used

A word of caution is needed on the concept of dihedral angles, since many restrictions to the use of dihedral wetting angles in determining γ and pore connectivity are often not fully appreciated. Notably, the dihedral wetting angle concept only applies to solid/liquid systems under purely hydrostatic equilibrium conditions, since non-hydrostatic stresses are likely to change the local solid/liquid equilibrium with reference to dissolution/precipitation and therefore the spreading tendencies of the fluid. For a non-equilibrium situation, an unbalanced (Young) force exists (See also Figure 2.4c),

$$F = 2\gamma_{sl} \left(\cos\frac{\theta}{2} - \cos\frac{\theta_{eq}}{2}\right) \qquad (2.16)$$

where θ_{eq} is the equilibrium angle and θ is the dynamic contact angle (De Gennes, 1990). De Gennes calls this the spreading force of the liquid phase (for $\theta_{eq} > \theta$ the fluid phase will be retreating). Measuring angles in an aggregate not representing the hydrostatic equilibrium situation, or under non-equilibrium conditions, will clearly give misleading (incorrect) information on interfacial energy (γ), values and on possible connectivity of the fluid phase at equilibrium. Similar errors in measuring γ from θ can be caused by measuring angles in grain geometries in which special low-energy interfaces (either solid/liquid or grain boundaries) occur. This could also lead to non-symmetrical θ with respect to the grain boundary, for which equation (2.15) cannot be used. This is illustrated in Figure 2.4d.

The use of the dihedral wetting angle concept is also dependent on chemical equilibrium. During chemical reactions, e.g. between a solid and liquid at an interface, a decrease in the corresponding interfacial free energy occurs, by an amount equal to the free energy change per unit area for the effective chemical reaction at the interface (Aksay et al, 1974). During the initial reaction an instantaneous lowering of the dihedral angle, i.e. spreading of the liquid can occur. After completion of the reaction at the surface, the dynamic wetting angle gradually increases to its static (equilibrium) value and the liquid will be pulled back to the equilibrium configuration (Aksay et al., 1974). This is illustrated in Figure 2.5.

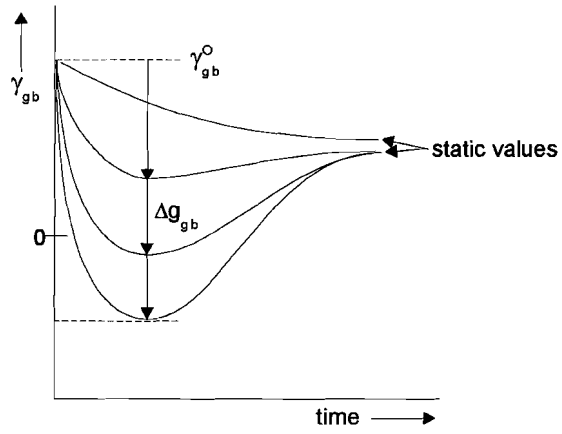

Figure 2.5. Schematic diagram showing the variation of the dynamic interfacial energy with time during a chemical reaction (e.g. dissolution or precipitation reactions due to a non-equilibrium concentration of the solid in solution). The initial value is indicated with γ_{gb}, while Δg_{gb} indicates a few examples of the free energy changes per unit area dependent on the chemical reaction. The dynamic interfacial energy could even become negative. Note that a process of pure adsorption can also reduce the initial γ_{gb} to a lower static value, but in this case no transient minimum is observed. After Aksay et al. (1974).

2.2.3.4 Limitations and assumptions for modelling applications

For the derivation of the models presented in this chapter, some assumptions are required. These assumptions will be motivated here.

First, mass transport processes due to heterogeneity in the sample (e.g. grain growth and Ostwald ripening), have to be neglected as well as heterogeneities due to different grain size or packing. Moreover, surface energy anisotropy in an aggregate would cause numerous different possible local equilibria dependent on the orientations at which grains touch, in which directions grain boundaries intersect and which grain boundary/pore intersection orientations and curvatures exist. It is impossible to describe every possible local equilibrium and its associated transport paths. Therefore, to be able to model mass transport processes due to the surface energy related driving forces (deviation from local equilibria), the starting aggregate is most conveniently described as a fixed geometry with a regular packing of regular grain shapes (e.g. spheres) of a uniform grain size and with average values for grain boundary energy γ_{gb}, as well as for γ_{sl}, the surface

free energy of solid/liquid surfaces in the pores.

With respect to the value of grain boundary energy, it is convenient to assume that all grain boundaries are random high angle (high energy) interfaces and that all grain boundaries are straight (not-curved) which excludes surface energy driven grain boundary migration as a possible mass transport process. The grain boundary energy, γ_{gb}, can be approximated by 1/3 γ_{sv}, as explained above, and this will then be a material specific value. The solid/liquid interfacial energy, γ_{sl}, is assumed to be isotropic and to have a value corresponding to the mean of non-faceted, high energy interfaces (based on high angle γ_s and γ_l values and the interaction described by equation (2.10)).

2.2.4 Non-equilibrium Thermodynamic Considerations.

2.2.4.1 Irreversible Processes and Dissipation

In classical equilibrium thermodynamics one considers homogeneous systems within which the thermodynamic parameters describe relations in bulk quantities for a finite volume V, e.g.

$$dU = TdS - pdV + \mu dM - \gamma dA \qquad (2.17)$$

where U is the total energy, T is temperature, S is the entropy, p is fluid pressure, μ is the chemical potential, M is the total mass, γ is the interfacial energy and A is the total area. Both the first and second law of thermodynamics apply as equalities for reversible systems. The condition of reversibility is exactly what the term implies. Such processes can be carried out backwards with everything being restored to its original state. For processes involving dissipation, reversibility is out of the question, as the energy dissipated is irrecoverable. A process can only be treated as reversible if the system is, at all times, very close to equilibrium. A spontaneously occurring process, however, is by nature irreversible. Such processes include spontaneous chemical reactions, deformation under traction of an applied stress, and mass transport processes due to reduction in internal or surface free energy (which also lead to permanent deformation and/or microstructural change). This illustrates the need for irreversible thermodynamics to describe the processes discussed in this chapter.

In the non-equilibrium thermodynamics of irreversible processes, the dissipation is

explicitly taken into account. Any spontaneous process implies an increase in entropy and the fundamental problem in irreversible thermodynamics is to determine the corresponding rate of entropy production ($dS > 0$). As with reversible processes, the first law of thermodynamics still applies in the non-equilibrium situation, so that

$$dU = q + w \quad \text{or} \quad \dot{U} = \dot{q} + \dot{w} \tag{2.18}$$

where U is internal energy, q the heat added to and w the work done on the system, and the equivalent symbols with a dot are the time derivatives.
However, the second law is now an inequality, indicating an entropy source in the volume considered, written

$$dS > \frac{q}{T} \quad \text{or} \quad \dot{S} > \frac{\dot{q}}{T} \tag{2.19}$$

compared with dS being equal to q/T for reversible systems. This inequality can be rewritten as

$$dS - \frac{q}{T} \equiv \frac{q'}{T} \tag{2.20}$$

with $q' = 0$ for reversible systems and $q'/T > 0$ being the entropy production for irreversible systems

Although time and/or spatial coordinates are not required to describe reversible thermodynamic processes, they are needed to describe most irreversible processes. Following de Groot and Mazur (1962) and Lehner and Bataille (1984), in treating irreversible processes such as the mass transfer processes involved in deformation or microstructural change, a continuum theory is set up in which the state parameters, internal energy, entropy, free energy and density (u, s, f and ρ_{dens}) are handled as field variables i.e. as continuous functions of space and time. Moreover, one would like to formulate the theory in the form of local equations, i.e. referring to a point in space and time. In order to calculate the entropy production (rate), it is assumed that the laws which are valid for macroscopic systems remain valid for infinitesimally small parts of it. It implies, on a microscopic scale, that the local macroscopic thermodynamic parameters are really measurements of the properties of the system, and contain still a large number of the constitutive particles. Such small parts of the system one might call physically infinitesimally small. With this in mind, it still makes sense to speak about local values of

such macroscopic quantities as entropy and entropy production (de Groot and Mazur, 1962). At equilibrium, under hydrostatic pressure, p, the total differential of the entropy per unit mass, s, is given by the Gibbs relation, in the form

$$Tds = du + pdv - \Sigma \mu_i dc_i + \frac{\gamma dA}{M} \qquad (2.21)$$

where M= mass, s= S/M, v= V/M (= $1/\rho_{dens}$), ρ_{dens} is the density, u=U/M, , c_i is the mass fraction species i, μ is the chemical potential of component i, and A is area.

It will now be assumed that, although the total system is not in equilibrium, there exists, within the small mass elements a state of "local" equilibrium, for which the local entropy is a function of u, v, c_i, and A/M (equation 2.21) as at (macroscopic) equilibrium. This justifies the use of equation (2.21) if deviations from equilibrium are not "too large", which is the case for most familiar transport phenomena (de Groot and Mazur, 1962, p 23). In agreement with the hypothesis of local equilibrium, equation (2.21) can be rewritten outside equilibrium as

$$T\frac{ds}{dt} = \frac{du}{dt} + p\frac{dv}{dt} - \Sigma\mu_i \frac{dc_i}{dt} + \frac{\gamma dA}{dtM} \qquad (2.22)$$

or, the dissipation Tds/dt can be written in the form of the first law of thermodynamics

$$T\dot{s} = \dot{u} - \dot{w} + \dot{q}' \qquad (2.23)$$

For generalisation to non-hydrostatic situations, the reader is referred to Lehner (1990).

2.2.4.2 Driving force for mass transfer in solid/liquid systems

Consider now an idealised granular aggregate consisting of a skeleton of solid grains with a saturated solution phase occupying the pores, and suppose that this is in equilibrium. For such a starting point, variations in the local surface value of μ_{eq} due to variations induced in any of the right hand terms in equation (2.12)

$$\mu_{eq} = f^s + p_f\Omega^s + \gamma\left(\frac{1}{r_1} + \frac{1}{r_2}\right)\Omega^s \qquad ((2.12))$$

will remove the system form equilibrium, providing a driving force for grain scale mass transport, i.e. for the dissipative processes of dissolution, diffusion and precipitation. Thus,

when neglecting pressure gradients in the fluid, physically possible driving forces for grain scale transport are seen to correspond to gradients in f^s, Ω^s and r at the solid surface. Gradients in r can be present in the initial microstructure of a solid/liquid system. However, gradients in all of the right hand side terms can be induced by an applied stress, as elastic and plastic deformation induce stored energy changes (elastic or defect-stored), density changes and distortion of the solid/liquid interface. These changes in f^s, Ω^s and r are not independent of each other as a gradient in one of right hand terms of equation (2.12) will generally be linked to gradients in the other terms, e.g. changes in defect-stored energy of the solid resulting from plastic strain could be coupled to changes in the interfacial radius of curvature.

When solid grain-to-grain contacts are also considered, additional driving force terms become apparent. Depending on the relative values of the grain boundary free energy (γ_{gb}), the interfacial solid/liquid free energy (γ_{sl}) and the solid/solid/fluid junction geometry, a driving force may exist for material transport to increase the relative area of lower energy boundaries. As already mentioned, the local equilibrium condition for a solid/solid/fluid a junction, when variations in f^s and Ω^s are negligible, is given by the force balance relation

$$\gamma_{gb} = 2\gamma_{sl} \cos\frac{\theta_{eq}}{2} \qquad ((2.15))$$

From Figure 2.4c it can be seen that any value of $\theta/2$ not equal to $\theta_{eq}/2$ would induce a local driving force for change in the contact geometry. Provided the boundary is not completely wetted at equilibrium ($\theta_{eq}/2 > 0$), then for a geometry of two touching spherical grains, if $\theta/2 < \theta_{eq}/2$, an outwardly directed resultant force on the solid/solid/fluid junction would lead to growth of the lower energy grain boundary. The opposite case where $\theta/2 > \theta_{eq}/2$, would lead to a retreating grain boundary, resulting in more solid/liquid surface. If the fields in f^s and $p\Omega^s$ and r are non-uniform, all of these variations will compete in driving a diffusive flux of solute from locations of relatively high surface potential μ_{eq} to locations of relatively low potential.

A case of particular interest and importance is if contacts are penetrated by a liquid phase either in an adsorbed film or island-channel network and transmit intergranular tractions. It has long been speculated that a continuous adsorbed fluid film could be present in grain boundaries thus sustaining a normal stress and allowing intergranular pressure solution to occur (Rutter, 1976, Hickman and Evans, 1991). On the other hand,

there is some experimental evidence for the existence of an island-channel structure is stressed salt/saturated solution systems (Spiers et al,, 1989; Schutjens, 1991 and Cox and Paterson, 1991). Models of the latter structure (See Figure 2.6), assume the grain boundary fluid to be interconnected by a fine-scale channel system, and the fluid pressure equals that in the pores (Lehner, 1990.). A compressive normal stress acts on the grain boundary and is transmitted across and concentrated at the solid/solid contacts or islands. Since stress and strain energy distribution are highly inhomogeneous on this scale, no chemical equilibrium can exist for the grain boundary between solid and solute in solution. Instead, provided the grain boundary is an open system, continuous dissipation of energy will occur as solid dissolves at highly stressed, high potential "islands", diffuses out of the boundary and reprecipitates at sited of relatively low stress and low chemical potential (such as pore walls). This will result in a net transport out of the contact region and a relative displacement of the grains towards each other leading to deformation and/or densification. To a first approximation, it has been shown by Lehner (1990) that regardless of the grain boundary structure, the average chemical potential at points on the solid surface within grain boundaries penetrated by a fluid is given

$$\mu_{gb} \approx f^s + \sigma_n \Omega^s \tag{2.24}$$

where all quantities are averaged over a representative element transmitting average normal stress σ_n (see Figure 2.6). For a detailed discussion on this equation, the reader is referred to Lehner and Bataille (1984), Lehner (1990, 1995) and Spiers and Schutjens (1990).

By comparison with equation (2.12) it can now be seen that even when there are no gradients in p, gradients in σ_n (stressed systems) can provide gradients in μ_{gb}, which will drive transport from contacts to pores. Numerous authors have shown that gradients in $\sigma_n\Omega^s$ between contacts and pores can be very significant compared with gradients in the other terms (Robin, 1978; Raj, 1982; Kwon and Messing, 1989, 1991), so that it is this which essentially drives intergranular pressure solution (solution/precipitation creep) in a closed system (i.e. $\Delta\mu \approx \Delta\sigma_n\Omega^s$).

A final point which arises in the present context, is the possible effect of applied stress on γ, on surface stresses (σ_{ij}^{surf}, equation 2.8) and hence on μ_{eq} at the pore walls and grain boundaries. The magnitude of this effect has received little attention. However, in the case of surface stress on free pore walls remote from grain contacts, contact mechanics arguments (Herz, 1882) suggest that the effect will generally be neglible. Surface stresses

and strains near or at the contact can be large. However, since no information is available on $\delta\gamma/\delta\varepsilon_{ij}$ (equation 2.8), no statement can be made on the magnitude of surface stress in the neighborhood of contacts. Unfortunately, for this reason $\delta\gamma/\delta\varepsilon_{ij}$ has to be neglected henceforth. Assuming material to be isotropic and adsorption at the solid surface to be negligible, γ is used instead of σ_{ij}^{surf}, as a first approximation.

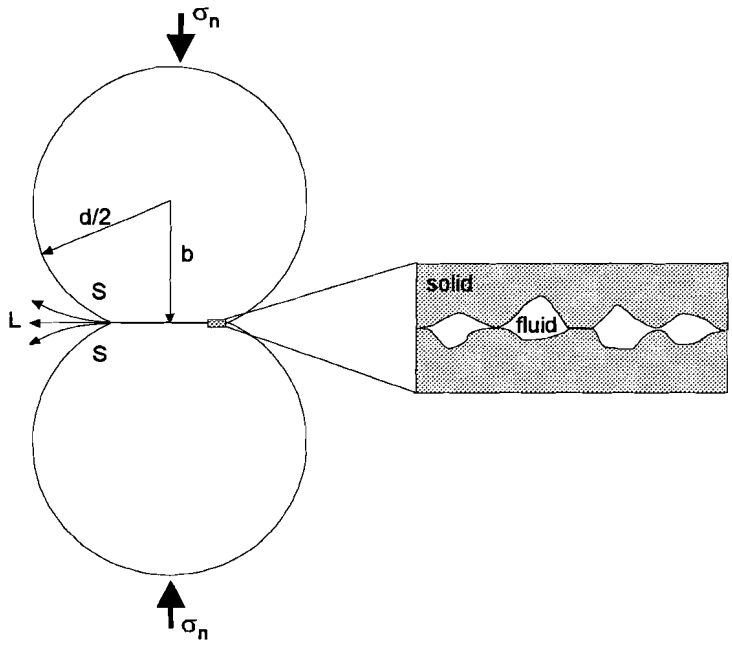

Figure 2.6 Schematic diagram of two grains undergoing stress induced solution/precipitation or pressure solution creep, with mass transfer through an island channel type grain-to-grain contact. The inset shows a section through a representative grain boundary element with an island-channel structure.

2.3 Behaviour of solid/liquid systems under hydrostatic conditions: a model for neck growth by solution/precipitation transfer

2.3.1 General

Consider a granular solid/solution system such as illustrated in Figure 6a. It follows from the above discussion of equation (2.11) that under fully hydrostatic conditions (solid and fluid at uniform hydrostatic pressure p), the stress and deformation fields in the solid grains will be uniform and p is uniform, so that the term ($f^s + p\Omega^s$) will also be uniform around all solid/liquid interfaces. Therefore, only surface energy driving forces will be significant (i.e. variations in r and total interfacial energy). These will drive the system towards an equilibrium microstructure, via a non-equilibrium neck growth process that will result finally in an equilibrium microstructure in which all pores are bounded by equipotential surfaces meeting grain boundaries at the equilibrium dihedral angle (See Section 2.2.3.3 and Figure 2.4b)

Neck growth in a solid/liquid system is similar to neck growth during sintering in a solid/vapour system as considered by Kuczinsky (1949), Coble (1961), Kingery (1959), Kingery et al. (1976) and Cannon and Carter (1989). The process can be understood by considering the following relations for the chemical potential and the concentration of solid in solution

$$\mu_s^f = \mu_{eq} \equiv f^s + p_f \Omega^s + \gamma(1/r_1 + 1/r_2)\,\Omega^s \qquad ((2.12))$$

$$\mu_{eq} = \mu_0 + RT\ln C_{eq} \qquad ((2.13))$$

Combining these equations shows that at the surface of a spherical solid particle, there is a positive radius of curvature so that the surface chemical potential and solubility (C_{eq}) is somewhat larger than would be observed for a flat surface. However, at the junction between two touching spherical particles there is a small negative radius of curvature (See Figure 2.7) with associated (local) lower potential and solubility. Following the classical sintering argument, in which γ_{ss} ($= \gamma_{gb}$) is neglected (Kingery et al 1976), the solubility and associated potential difference between the neck area (i.e. the junction between touching grains) and the free particle surface acts as a driving force to transfer material from the free

walls into the neck region. When solid state diffusion is slow, the only available transport path for material transport is via the liquid filled pores. Transfer of matter to the neck regions via the pores reduces curvature gradients as the neck area grows (the negative curvature getting less sharp due to precipitation). At the same time, the total free energy of the system decreases until an equilibrium microstructural configuration is established (note that for γ_{ss}=0 and $\theta = 180^0$ this would be a new single spherical grain, when starting with 2 spherical grains). Assuming a succession of steady states, the rate of the neck growth process, for a granular solid/liquid system, is controlled by the kinetics of the three serial steps of dissolution at the free surfaces, diffusion through the pore fluid and precipitation at the neck margin. The kinetics of dissolution and precipitation can in principle be specified in terms of crystal growth/dissolution laws and diffusion rates can be described by Ficks law. Hence, by coupling the driving force with the appropriate rate equations, constitutive equations for neck growth can be obtained.

Using this approach, constitutive models have been derived e.g. by Hickman and Evans (1991) for diffusion and precipitation controlled neck growth in a solid/liquid system, following the classical sintering approach (Kingery et al, 1976). In this approach the solid/solid interfacial energy (γ_{ss}=γ_{gb}) is neglected, i.e. assumed to be zero. This is equivalent to assuming an equilibrium dihedral wetting angle θ_{eq} of 180°, which is highly unrealistic as can be directly shown substituting values, for nearly any material and using random high energy interface values. The resulting dihedral wetting angle, calculated in accordance with the assumptions made in Section 2 will hardly ever be 180°. The neck growth models which Hickman and Evans derive, for the precipitation controlled case is derived for the geometry of Figure 2.7a and is given

$$\dot{x} = \frac{dx}{dt} = \frac{2\,(I_1\ \Omega^s)\ \gamma_{sl}\ \Omega^s\ d}{kT\,(x^2 - x_0^2)} \qquad (2.25)$$

where $\dot{x}$ is the velocity of neck growth, $(I_1\Omega^s)$ is a precipitation rate constant, d is the grain size (i.e. twice the radius of curvature of the solid grains), and x and x_0 are the instantaneous and initial neck radii as indicated in Figure 2.1a. The Hickman and Evans neck growth model for the diffusion controlled case is derived for a different geometry as illustrated in Figure 2.7b and is given

$$\dot{x} = \frac{dx}{dt} = \frac{2\pi DC\gamma_{sl}\Omega^s\ x\ d}{kT(x^2 - x_0^2)^2} \qquad (2.26)$$

This is derived assuming the source region of material to be a region confined to an annular region or "moat" around the neck between two grains, as a result of dissolution of the grain surfaces immediately adjacent to the neck. This also requires a different approximation for the radius of curvature ρ, see Table 2.1. The moat is approximated to be circular in cross section, so that the characteristic diffusion path for material transported to the neck is of the order of the moat radius (chosen is 2ρ).

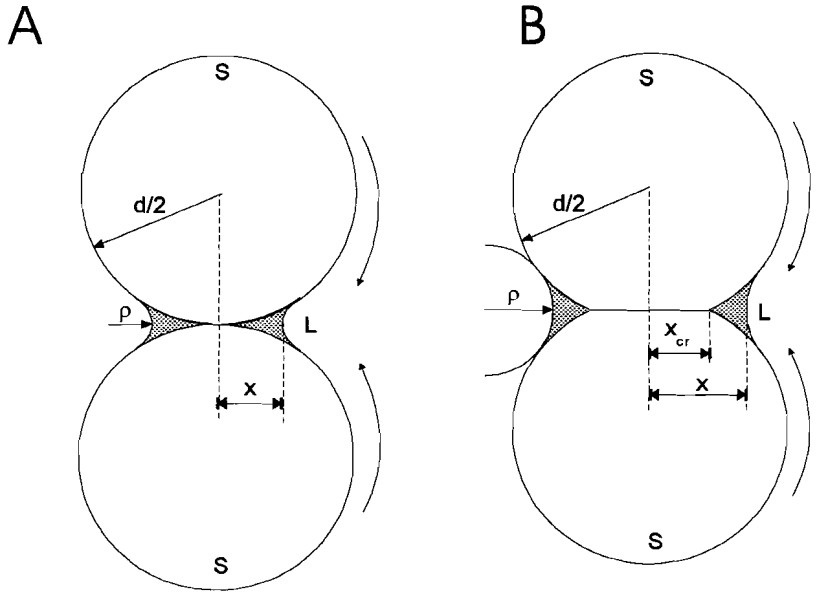

Figure 2.7. Schematic diagrams of 2-grain geometries undergoing neck growth due to material transfer from the positively curved, high potential, surfaces with a radius d/2 towards the grain contact area with a curvature ρ. a) shows a 2-grain geometry starting with point contacts. b) shows a 2-grain geometry with initial contact radius x_{cr} before neck growth started.

2.3.2 New Models for Neck Growth

A new model is now presented for neck growth in a granular solid/liquid system under purely hydrostatic conditions. The approach followed resembles that of Kuczinsky's (1949) evaporation/condensation model extended by Coble (1958) and followed by Kingery et al (1976) Raj (1982) and Hickman and Evans (1992; 1995). However, in contrast to previous models, the role of solid-solid interfaces (grain boundary) is taken into account here, i.e. γ_{ss} is not assumed zero but is assigned a finite constant value. The fact

that solid-solid-interfaces cannot to be neglected is clearly illustrated by the following experimental observations. First, many granular solid/liquid systems are known to evolve towards an equilibrium pore configuration with well-defined dihedral wetting angles $<180^{\circ}$. Second, grain boundaries separating grains of different misorientation and therefore having different grain boundary energies, have been shown to be characterised by different dihedral wetting angles (Faul and Waff, 1994). Thus previous models are incapable of predicting the equilibrium contact geometry and pore configuration in solid/liquid systems in a general sense.

Let us start by considering the two-grain configuration represented in Figure 2.7b, where $\gamma_{ss} < \gamma_{sl}$. For a hydrostatic situation, when no external work is done on the system, the first law of thermodynamics implies that the change of internal energy of the system, due to neck growth and concomitant change of area of solid/solid and solid/liquid surfaces (A_{ss} and A_{sl}), equals the rate of dissipation due to the transport of atoms through the fluid phase (see equations 2.3, 2.17 and 2.21), from surface points of relatively high chemical potential to surface points of relatively low potential. The sum $\Sigma\gamma_i A_i$ is therefore progressively reduced.

$$u^{surf} = \gamma_{ss} A_{ss} + \gamma_{sl} A_{sl} \tag{2.27}$$

The rate of change of internal energy (u) and hence of dissipation can accordingly be calculated from

$$\dot{u} = - \dot{q} = \gamma_{ss} \frac{dA_{ss}}{dt} + \gamma_{sl} \frac{dA_{sl}}{dt} \tag{2.28}$$

where $\dot{q}$ is the rate of dissipation (dq/dt) with t being time. Inserting geometrical expressions for A_{ss} and A_{sl} following Figure 2.7, and carrying out the appropriate differentiation with time leads to the result

$$\dot{u} = - \dot{q} = 2\pi x \dot{x} \gamma_{sl} \left(\cos\frac{\theta}{2} - \cos\frac{\theta_{eq}}{2}\right) \tag{2.29}$$

However, the rate of dissipation can also be described in terms of the volume of material (material flux) being transported times the average change in chemical potential ($\Delta\mu$) (thermodynamic force) per unit volume transferred from source to sink, i.e. from pore wall to neck surface. Using the geometrical variables shown in Figure 2.7b, the rate of dissipation can hence be written as

$$- \dot{q} \approx 2\rho\dot{x}\, 2\pi x \frac{\Delta\mu}{\Omega^s} \qquad (2.30)$$

where x is the neck radius, $\dot{x}$ is the neck growth rate and ρ is the smallest of the principle radius of curvature of the neck.

A third way of writing the rate of dissipation is in terms of surface forces times a material flux. It will be recalled that for equilibrium at a neck margin

$$2\gamma_{sl}\cos(\frac{\theta_{eq}}{2}) = \gamma_{ss} \qquad ((2.15))$$

When the angle θ is smaller than the equilibrium angle, (see Figure 2.4c), the forces acting on the neck junction are not in equilibrium (See Kuczinsky, 1949) and from the vector sum the resultant force can be seen to be directed outward. The force per unit length acting on the neck periphery then is

$$F = 2\gamma_{sl}(\cos\frac{\theta}{2} - \cos\frac{\theta_{eq}}{2}) \qquad ((2.16))$$

Hence, the resulting rate of dissipation for a neck growth rate $\dot{x}$ is

$$- \dot{q} = 2\pi x\, F\, \dot{x} = 2\pi x\, \dot{x}\, 2\gamma_{sl}(\cos\frac{\theta}{2} - \cos\frac{\theta_{eq}}{2}) \qquad (2.31)$$

Combining the resulting equations for the rate of dissipation, i.e., (2.29), (2.30) and (2.31) thus leads to the result,

$$\gamma_{sl}\frac{dA_{sl}}{dt} + \gamma_{ss}\frac{dA_{ss}}{dt} = 2\rho\dot{x}\, 2\pi x \frac{\Delta\mu}{\Omega^s} = 2\pi x\, \dot{x}\, 2\gamma_{sl}(\cos\frac{\theta}{2} - \cos\frac{\theta_{eq}}{2}) \qquad (2.32)$$

and therefore, from the right hand members,

$$\Delta\mu = \frac{\gamma_{sl}}{\rho}\,\Omega^s\,(\cos\frac{\theta}{2} - \cos\frac{\theta_{eq}}{2}) \qquad (2.33)$$

From this point on, essentially the same procedure is followed as in all papers describing models for neck growth and solution/precipitation creep (e.g. Coble, 1958; Rutter, 1976; Raj, 1982; Spiers et al, 1989; Hickman and Evans, 1991). Accordingly, the chemical potential drop ($\Delta\mu$) acting between source and sink sites is assumed to be associated with the slowest of the three serial steps of dissolution, diffusion and precipitation, while the other two are considered to be negligibly easy. When the diffusion step is fast compared to the interfacial kinetics, precipitation is assumed to be rate controlling due to the very small area of the neck region compared with the free grain surface the velocity of precipitation will be much higher than of dissolution, so the associated potential drop also much bigger. Thus, for interface (precipitation) controlled neck growth

$$\Delta\mu_{precip} = \Delta\mu \tag{2.34}$$

Assuming a linear growth law at the neck site, the velocity of precipitation can be described as

$$v_{precip} = \frac{I^{*}\Delta\mu}{kT} \tag{2.35}$$

where v is velocity, I^{*} is the precipitation velocity for a driving force of 1 kT, k is Boltzmann's constant and T is absolute temperature. Combining equations 2.33, 2.34 and 2.35 it thus emerges that the rate of neck growth, which is approximately equal to the velocity of precipitation on the neck surface, is given

$$\dot{x} = \frac{I^{*}\,\gamma_{sl}\Omega^{s}}{\rho\,kT}\left(\cos\frac{\theta}{2} - \cos\frac{\theta_{eq}}{2}\right) \tag{2.36}$$

A geometrical approximation for ρ can now be made following Coble (1958) such that $\rho \approx x^2/2d$ for small x. Thus the rate of neck growth with precipitation as rate controlling process can be written

$$\dot{x} = \frac{2I^{*}\,\gamma_{sl}\Omega^{s}\,d}{kT\,x^{2}}\left(\cos\frac{\theta}{2} - \cos\frac{\theta_{eq}}{2}\right) \tag{2.37}$$

In the diffusion controlled case, the chemical potential drop ($\Delta\mu$) between free grain surfaces and the neck margin is used in driving diffusion so that

$$\Delta\mu_{diff} = \Delta\mu \tag{2.38}$$

To a first approximation, in which the divergence of the diffusion flux is neglected, Fick's first law can be used assuming the average diffusion distance to be (πd/4-x). Hence the volume flux of material to the neck is

$$J_C = [\ \frac{(DC)}{kT}\Delta\mu\ /\ (\frac{\pi d}{4} - x)\ ]\ A_{flux} \tag{2.39}$$

where (DC) is the product of the diffusivity and solubility in the pore region, and A_{flux} is the average area through which the flux acts. The neck growth rate for the diffusion controlled case is thus

$$\dot{x} = \frac{J_C}{A_{precip}} \tag{2.40}$$

where $A_{precip} = \pi x.\pi\rho$ is the area of precipitation per grain. For small x, and $A_{flux} \approx A_{precip}$, the neck growth rate can therefore be described by

$$\dot{x} = \frac{4\ (DC)_{pore}}{\pi\ kT}\frac{\gamma_{sl}\Omega^s}{x^2}\ (\cos\frac{\theta}{2} - \cos\frac{\theta_{eq}}{2}) \tag{2.41}$$

These models are for two grains just touching (point contacts), whereas the models by Hickman and Evans (1995) are for two grains having already a finite contact surface before neck growth starts. The latter geometry could be a result of solution/precipitation or any other creep mechanism and therefore the finite radius contact before neck-growth starts will be indicated with x_{cr}, the radius of contact due to creep in general. To show the effect of the different geometries as well as to make a comparison with the Hickman and Evans models possible, the new models are given in Table 2.1 for both geometries. Details of the geometries, radius of curvature approximation and diffusion path lengths (depending on the choice of the source region) are indicated in the table as well.

From inspection of the table it is seen that the most general description of the new neck growth models is characterised by a driving force

$$\Delta\mu \approx \frac{\gamma_{sl}\Omega^s}{\rho}(\cos\frac{\theta}{2} - \cos\frac{\theta_{eq}}{2}) \qquad ((2.33))$$

and the rate equation,

$$\dot{x} = A(T)\ R\ \gamma_{sl}\ (\cos\frac{\theta}{2} - \cos\frac{\theta_{eq}}{2})^a\ \frac{d^b}{(x^2 - x_{cr}^{\ 2})^c} \qquad (2.42)$$

where A(T) is a temperature dependent term, describing the temperature dependence of solubility and of diffusivity or surface reaction rates, R is a constant incorporating molecular volume and geometry dependent constants. The exponents a is 1, b is either 0 or 1 and c is 1or 2 depending on the initial contact configuration and on the chosen diffusion path length. At zero initial contact x_{cr} is zero.

GEOMETRIES CONSIDERED		
A)	B)	C)
NO MOAT FORMATION	WITH MOAT FORMATION	POINT CONTACTS
Models by Hickman and Evans (1992) Finite initial contact radius ($x_{cr} > 0$)	New Models I) Finite initial contact radius ($x_{cr} > 0$)	New Models II) Initial point contacts ($x_{cr} = 0$)
Precipitation controlled case. Geometry A. $\dot{x} = \frac{2(I_1\Omega^s)\gamma_{sl}\Omega^s d}{kT(x^2 - x_{cr}^2)}$	Precipitation controlled case. Geometry A. $\dot{x} = \frac{2I^*\gamma_{sl}\Omega^s d}{kT(x^2 - x_{cr}^2)}(\cos\frac{\theta}{2} - \cos\frac{\theta_{eq}}{2})$	Precipitation controlled case. Geometry C. $\dot{x} = \frac{2I^*\gamma_{sl}\Omega^s d}{kTx^2}(\cos\frac{\theta}{2} - \cos\frac{\theta_{eq}}{2})$
Diffusion controlled case. Geometry B. Diffusion path length = 2ρ $\dot{x} = \frac{2\pi DC\ \gamma_{sl}\ \Omega^s\ x\ d}{kT(x^2 - x_{cr}^2)^2}$	Diffusion controlled case. Geometry B. Diffusion path length = 2ρ $\dot{x} = \frac{2\pi DC\ \gamma_{sl}\ \Omega^s\ x\ d}{kT(x^2 - x_{cr}^2)^2}(\cos\frac{\theta}{2} - \cos\frac{\theta_{eq}}{2})$ Geometry A. Diffusion path length = (πd/4 - x) $\dot{x} = \frac{4\,DC\ \gamma_{sl}\ \Omega^s}{\pi kT(x^2 - x_{cr}^2)}(\cos\frac{\theta}{2} - \cos\frac{\theta_{eq}}{2})$	Diffusion controlled case. Geometry C. Diffusion path length=(πd/4 - x) $\dot{x} = \frac{4\,DC\ \gamma_{sl}\ \Omega^s}{\pi kTx^2}(\cos\frac{\theta}{2} - \cos\frac{\theta_{eq}}{2})$

Table 2.1 Neck Growth Models. Radii of curvature are as follows Geometry A, $\rho = (x^2 - x_{cr}^2)/2d$. Geometry B, $\rho = (x^2 - x_{cr}^2)/\sqrt{(4\pi d)}$. Geometry C, $\rho = x^2/2d$.

2.4 Behaviour of solid/liquid systems under stress: extended models for densification by solution/precipitation creep and neck growth under stress.

2.4.1 General

When a granular solid plus intergranular liquid system such as that in Figure 2.6a is loaded, such that the solid framework supports hydrostatic stress, σ_{el}, grain contacts will become loaded supporting normal stresses σ_n, while pore walls experience the fluid pressure p. Accordingly, f^s, Ω^s, and r in the Gibbs equilibrium condition (2.12) will vary around grain surfaces as will σ_n vary in equation (2.24). As already discussed, f^s and Ω^s will be affected by elastic deformation and by the introduction of defects if plastic deformation occurs. In addition, r can also be changed, in particular by plastic deformation. Such effects will generally lead to an increase in the equilibrium chemical potential at grain contact margins, thus tending to reduce the driving force for neck growth or, if large enough, creating one for so-called "marginal dissolution" (negative neck-growth) (Pharr and Ashby, 1983; Spiers and Brzesowsky, 1993). With the exception of the preliminary work of Pharr and Ashby (1983) no models currently exist for this type of neck corrosion or coupled deformation effects (Spiers and Brzesowsky, 1993).

More importantly than marginal dissolution, provided grain contacts are penetrated by the fluid phase in thin film or island-channel form, are gradients in the term $\sigma_n\Omega^s$ between contacts and pores. These will lead to intergranular pressure solution or solution/precipitation creep involving dissolution within contacts, diffusion, and precipitation on pore walls (Rutter, 1983 and Raj, 1982). This will, of course, in turn lead to densification under the action of an effective applied stress. The rate of this densification process is (in steady state) controlled by the kinetics of the three serial steps of dissolution, diffusion and precipitation as described above for neck growth. Again the kinetics can be specified in terms of crystal growth/dissolution laws or Ficks law. By coupling the driving force for solution transfer (i.e. differences in the quantity $\sigma_n\Omega^s$ around grain surfaces), with kinetic rate equations, constitutive equations for densification by solution/precipitation creep can be obtained (Raj, 1982; Lehner and Bataille 1984, Spiers et al 1989).

Taking diffusion as the rate controlling step, constitutive models for densification by intergranular pressure solution have been developed by Spiers et al. (1990), Schutjens

(1991) and Spiers and Brzesowsky (1993). See also Rutter (1976), Raj (1982), Spiers et al (1989) and Lehner (1990). Assuming that the granular aggregate undergoes only small isotropic volumetric strains (< 20%), the resulting models for densification of a face centred cubic packing of grains take the form

$$\dot{\beta} = \frac{A\, a\, Z^* \sigma}{T\, d^3\, e_v^2} \tag{2.43}$$

where $\dot{\beta}$ is the rate of densification, e_v is volumetric strain, d is the aggregate grain size, a is a geometrical term dependent on the grain packing geometry (for FCC it is 0.675), A is a constant with value $A=144\Omega^s/k$ and Z^* is an effective grain boundary diffusivity parameter defined

$$Z^* = D_{gb} C S \tag{2.44}$$

where D_{gb} is the intrinsic grain boundary diffusion coefficient, C is the solubility of the solid in grain boundary solution (volume-fraction ≈ mole-fraction) and S is the average grain boundary fluid thickness. In the case of an "island and channel" model $S = \delta (1- \alpha)$ where δ is the grain boundary width and α is the volume fraction of the boundary occupied by solid material (islands). For an adsorbed grain boundary film, S=1, and the effect of adsorption on diffusion is accounted for in the different values of $D_{gb}C$.

When interfacial reactions are rate limiting in a solid/liquid system, Spiers et al. (1990) write the rate of densification as

$$\dot{\beta} \approx \frac{n\, a\, \Gamma^*\, \Omega^s\, \sigma}{kT\, d\, e_v^{\,b}} \tag{2.45}$$

where Γ^* is the rate coefficient for the dissolution or precipitation reaction depending which is rate controlling (see also de Meer and Spiers, 1995, 1997). Note that n = 6 and b = 1 for dissolution and n= 3 and b=2 for precipitation being rate controlling respectively.

2.4.2 An Extended Model for Densification by Solution/Precipitation Creep

In the following, the above models for densification by solution/precipitation creep under the action of an applied effective hydrostatic stress, are extended to take into account the effects of interfacial energy which have hitherto been neglected. Thus both stress-related and γ-related driving forces are taken into account.

2.4.2.1 Assumptions

In deriving the solution/precipitation creep models the following assumptions are made:

-Densification is assumed to occur by the solution/precipitation mechanism only; i.e. by intergranular pressure solution as described above.

-All mechanical work done is either dissipated by the solution/precipitation process or converted into interfacial energy.

-All dissipation is assumed to occur by one of the three serial steps of diffusion, dissolution or precipitation, each operating under conditions of a series of steady states.

-During compaction the grain to grain contacts are assumed to remain macroscopically flat while the free grain surfaces remain spherical.

-Grain to grain contacts are assumed to posses a "dynamically stable" island-channel structure (Raj, 1982 ; Lehner, 1990 and Spiers and Schutjens, 1990).

-Strains are assumed to be small (volumetric strain, e_v<20%), which simplifies the resulting geometry.

2.4.2.2 Model Formulation

As starting point, the idealised granular aggregate is assumed to have a face centred cubic (FCC) packing and is subjected to an applied effective stress, $\sigma_e=(\sigma-p)$ which is hydrostatic in nature. Individual grain contacts are treated as shown in Figure 2.7. Making use of equations (2.12) and (2.24), the chemical potentials at the free surfaces (pores) and the grain contact can be described by

$$\mu_p = f^s + p\Omega^s + \frac{2\gamma_{sl}\Omega^s}{d/2} \qquad \text{at the free surface} \qquad (2.46)$$

$$\mu_c \approx f^s + \sigma_n\Omega^s \qquad \text{within the contact area} \qquad (2.47)$$

The mean potential difference between the contact area and the free surface in the pores can hence be written

$$\Delta\mu = [(\sigma_n - p) - \frac{4\gamma_{sl}}{d}]\,\Omega^s \qquad (2.48)$$

assuming differences in f^s are negligible on the relevant scale and taking σ_n to be the mean normal stress at contacts. Now, from the geometry of an FCC packed array of particles, a consideration of the force balance of grain contacts (Spiers et al, 1989) shows that

$$\sigma_n \approx \frac{a\sigma_e}{e_v} + p \qquad (2.49)$$

where a is a geometrical factor ($3/\pi\sqrt{2}$ for an FCC packing). Thus

$$\Delta\mu = (\frac{a\sigma_e}{e_v} - \frac{4\gamma}{d})\Omega^s \qquad (2.50)$$

From here on, the procedure followed is the same as described in Section 2.4.1, i.e., one of three serial steps (dissolution, diffusion or precipitation) is assumed to be rate limiting, and the rate equations for crystal growth/dissolution or Fick's law are coupled with the driving force for solution transfer, so that constitutive equations for densification by solution/precipitation are obtained.

The resulting models are, for the diffusion controlled case

$$\dot{\beta}_{diff} = \frac{A\,Z^*}{T\,d^3\,e_v}(\frac{a\sigma_e}{e_v} - \frac{4\gamma_{sl}}{d}) \qquad (2.51)$$

and for the dissolution or precipitation controlled case

$$\dot{\beta}_{pr} = \frac{n\Gamma^*\Omega^s}{kTd\,e_v^{\,b}}(\frac{a\sigma_e}{e_v} - \frac{4\gamma_{sl}}{d}) \qquad (2.52)$$

where n= 6 and b=0 for dissolution and n=3 and b= 1for precipitation control.

To compare these models with those for neck growth, they can be rewritten in terms of the contact radius (x) growth rate due to solution/precipitation creep, expressed as $\dot{x}_{sp}$. Hence when diffusion is rate limiting, (2.51) modifies to

$$\dot{x}_{SP} = \frac{2d}{x^3} \frac{(CD)_{gb}\delta(1-\alpha)\Omega^s}{kT} \left(\frac{a\sigma_e}{e_v} - \frac{4\gamma_{sl}}{d}\right) \tag{2.53}$$

When the interfacial reactions are rate limiting, (2.52) yields

$$\dot{x}_{sp} = \frac{d}{x}\frac{I^*\Omega^s}{kT}\left(\frac{a\sigma}{e_v} - \frac{4\gamma_{sl}}{d}\right) \tag{2.54}$$

2.4.3 An extended model for neck growth under stress

In a granular solid/liquid system (Figure 2.6a) subjected to a state of positive effective hydrostatic stress $\sigma_e=(\sigma-p)$ and where grain contacts are <u>not</u> penetrated by fluid, neck growth or undercutting may occur depending on the magnitude of stress-induced changes in potential of the solid at the neck margin. In other words, both surface energy and stress-related driving forces may become important. While the possibility of neck growth (positive or negative) in the absence of stress has already been mentioned, here a simple model will be formulated for neck growth when grain contacts support an effective stress.

As starting point, consider the two-grain model of Figure 2.6 and 2.7, and assume that the contact is not penetrated by fluid. When no effective normal stress acts across the grain contact (i.e. when fields in f^s and Ω^s are uniform in the solid grain), pore wall sites ($_p$) posses an excess potential compared with contact margin ($_m$) given

$$\Delta\mu = \mu_p - \mu_m = +\frac{\gamma_{sl}}{\rho}\Omega^s\left(\cos\frac{\theta}{2} - \cos\frac{\theta_{eq}}{2}\right) \tag{2.55}$$

which is the driving force for neck growth. Here θ_{eq} is the equilibrium dihedral welting angle under <u>hydrostatic</u> reference conditions. Writing explicitly for μ_m and μ_p, the chemical potentials of the solid at neck margin and pore walls, this is equivalent to

$$\Delta\mu = [\, f_p^s + p\Omega_p^s + \frac{4\gamma_{sl}}{d}\Omega_p^s] - [\, f_m^s + p\Omega_m^s - \frac{\gamma_{sl}}{\rho}\Omega_m^s\,(\cos\frac{\theta}{2} - \cos\frac{\theta_{eq}}{2})] \quad (2.56)$$

in which $\Delta f^s = 0$ and $\Delta\Omega^s = 0$ since the fields corresponding are uniform, and where the term $4\gamma_{sl}\Omega_m{}^s/d$ is negligibly small since d is relatively large. When the grain scale fields in f^s and Ω^s are not uniform, however, due to non-hydrostatic stresses transmitted across grain contacts, then the driving force for neck growth becomes

$$\Delta\mu = \mu_p - \mu_m = \frac{\gamma_{sl}}{\rho}\Omega^s[\cos\frac{\theta}{2} - \cos\frac{\theta_{eq}}{2}] + (\Delta f^s + p\Delta\Omega^s) \quad (2.57)$$

in which the term $(\Delta f^s + p\Delta\Omega^s)$ may take positive or negative values. If $\Delta\mu > 0$, neck growth occurs. If $\Delta\mu < 0$, marginal dissolution occurs (negative neck growth). Note that here, Δf^s is the excess Helmholtz free energy at the neck margin due to elastic and defect stored energy, while $\Delta\Omega^s$ is the corresponding difference in molecular volume. In general $\Delta\Omega^s$ is small and, if p is also low, we can neglect $p\Delta\Omega^s$. Hence, the driving force for neck growth, in a system which is subjected to a positive effective stress σ_e, is given

$$\Delta\mu \approx \frac{\gamma_{sl}}{\rho}\Omega^s(\cos\frac{\theta}{2} - \cos\frac{\theta_{eq}}{2}) - \Delta f^s \quad (2.58)$$

When assuming the grains to be purely elastic (stiffness matrix C_{ij}) and the contact margin strains to be represented by the matrix ε_i, this becomes

$$\Delta\mu = \frac{\gamma_{sl}}{\rho}\Omega^s(\cos\frac{\theta}{2} - \cos\frac{\theta_{eq}}{2}) - \frac{\Omega^s}{2}C_{ij}\varepsilon_i\varepsilon_j \quad (2.59)$$

Alternatively, when dislocation stored energy is the dominant contribution to Δf^s, we may write

$$\Delta\mu = \frac{\gamma_{sl}}{\rho}\Omega^s(\cos\frac{\theta}{2} - \cos\frac{\theta_{eq}}{2}) - (\rho_{disloc} \cdot W)\Omega^s \quad (2.60)$$

where ρ_{disloc} is the local dislocation density at the neck margin and where W is the dislocation line energy.

To obtain the corresponding rate equation for neck growth/undercutting, it is only necessary to replace the driving force term ($\cos\theta/2 - \cos\theta_{eq}/2$) in Table 2.1 and equations (2.42) with the modified expression ($\cos\theta/2 - \cos\theta_{eq}/2 - (\rho/\gamma_{sl}\Omega^s)\Delta f^s$. For a 2-grain geometry with an initial contact radius x_{cr} this results in

$$\dot{x} = \frac{2I^* \gamma_{sl}\Omega^s d}{kT\,(x^2 - x_{cr}^2)} \left[\cos\left(\frac{\theta}{2}\right) - \cos\left(\frac{\theta_{eq}}{2}\right) - \left(\frac{\rho}{\gamma_{sl}\Omega^s}\right)\Delta f^s\right] \qquad (2.61)$$

when precipitation is rate controlling. For initial point contacts, x_{cr} =0. Note that Δf^s = (ρ_{disl}.W) Ω^s when dislocation density is the dominant contribution and Δf^s = ½ $\Omega^s C_{ij}\varepsilon_i\,\varepsilon_j$ when the elastic stored energy is the dominant contribution to Δf^s, as described in equations 2.59 and 2.60.

When diffusion is rate controlling, then from Table 2.2 for geometry II,

$$\dot{x} = \frac{4(DC)_{pore}\,\gamma_{sl}\Omega^s}{\pi kT\,(x^2 - x_{cr}^2)} \left[\cos\left(\frac{\theta}{2}\right) - \cos\left(\frac{\theta_{eq}}{2}\right) - \left(\frac{\rho}{\gamma_{sl}\Omega^s}\right)\Delta f^s\right] \qquad (2.62)$$

Accordingly, the general equation described by equation 2.42 modifies to

$$\dot{x} = A(T)\,R\,\gamma_{sl}\left[\cos\left(\frac{\theta}{2}\right) - \cos\left(\frac{\theta_{eq}}{2}\right) - \left(\frac{\rho}{\gamma_{sl}\Omega^s}\right)\Delta f^s\right] \frac{d^b}{(x^2 - x_{cr}^2)^c} \qquad (2.63)$$

An overview of the resulting models under stress is given in Table 2.2.

Table 2.2 Overview of the neck-growth and densification models under stress

GEOMETRIES CONSIDERED		
(I) FLUID PENETRATED ISLAND/CHANNEL GRAIN BOUNDARY		(II) SOLID/SOLID GRAIN BOUNDARY
Models by Spiers et al., 1990 Geometry (I) Surface energy neglected	New Models for rate of densification ($\dot{\beta}$)/ Growth rate of the contact ($\dot{x}$); Geometry (I) Surface energy taken into account	New Models for neck growth under stress Geometry (II) Initial grain contacts (x_{cr})
Precipitation controlled case. $\dot{\beta} = \frac{3aI^* \sigma_e \Omega^s}{kTde_v^2}$	Precipitation controlled case $\dot{\beta} = \frac{3I^* \Omega^s}{kTde_v}(\frac{a\sigma_e}{e_v} - \frac{4\gamma_{sl}}{d})$ $\dot{x} = \frac{d}{x}\frac{I^* \Omega^s}{kT}(\frac{a\sigma_e}{e_v} - \frac{4\gamma_{sl}}{d})$	Precipitation controlled case. $\dot{x} = \frac{2I^* \gamma_{sl} \Omega^s d}{kT(x^2 - x_{cr}^2)}(\cos\frac{\theta}{2} - \cos\frac{\theta_{eq}}{2} - \frac{\rho\gamma_{sl}\Delta f^s}{\Omega^s})$ with $\Delta f^s = -(\rho_{disl} x w)\Omega^s$ for dislocation stored energy and $\Delta f^s = -\frac{1}{2}\Omega^s C_{ij}\varepsilon_i\varepsilon_j$ for elastic stored energy
Diffusion controlled case. $\dot{\beta} = \frac{144aZ^* \sigma_e \Omega^s}{kTd^3 e_v}$ with $Z^* = D_{gb} C\delta(1-\alpha)$	Diffusion controlled case. $\dot{\beta} = \frac{144Z^* \Omega^s}{kTd^3 e_v}(\frac{a\sigma_e}{e_v} - \frac{4\gamma_{sl}}{d})$ $\dot{x} = \frac{2d}{x^3}\frac{Z^* \Omega^s}{kT}(\frac{a\sigma_e}{e_v} - \frac{4\gamma_{sl}}{d})$	Diffusion controlled case $\dot{x} = \frac{4\,DC\,\gamma_{sl}\,\Omega^s}{\pi kT(x^2 - x_{cr}^2)}(\cos\frac{\theta}{2} - \cos\frac{\theta_{eq}}{2} - \frac{\rho\gamma_{sl}\Delta f^s}{\Omega^s})$ with $\Delta f^s = -(\rho_{disl} x w)\Omega^s$ for dislocation stored energy and $\Delta f^s = -\frac{1}{2}\Omega^s C_{ij}\varepsilon_i\varepsilon_j$ for elastic stored energy

2.5 Conditions for neck growth / undercutting versus solution/precipitation creep

Inspection of the new models derived above, leads to a number of interesting and important observations on their characteristics.

The models for neck growth under hydrostatic conditions (table 2.2) show that γ-driven neck growth rates are increased by increasing γ_{sl}, solubility and diffusivity / reaction rate constants and decreased by increasing neck diameter, grain size and decreasing difference between the current and equilibrium dihedral angle (which occurs with the approach to equilibrium). When sufficient intergranular stress is transmitted across contacts, equations 2.61 and 2.62 indicate that neck growth can be inhibited or even reversed, leading to undercutting and dynamic grain boundary wetting, under the action of stress-related driving forces. When grain boundaries are penetrated by a fluid phase, solution/precipitation can occur in stressed aggregates (Rutter, 1976; Spiers et al 1990). The rate of this process tends to increase with decreasing grain size (d), decreasing volumetric strain (e_v) and increasing applied stress. The rate also increases with increasing diffusivity or reaction rate, or increasing solubility and grain boundary thickness. However if d is small enough, equations (2.51) and (2.52) show that surface energy driving forces may decelerate pressure solution creep or even stop it completely, after which neck growth can occur (again). Neck growth arguments may also be applicable within grain boundaries with an island-channel structure, describing the growth of islands and hence grain boundary healing.

From the entire assembly of the models given above, it is thus clear that the relative driving forces for and rates of neck growth versus solution/precipitation creep will vary strongly, depending on factors such as d, σ, γ and so on. This implies that fields of conditions will exist where stress-driven solution/precipitation creep is possible and dominant, and other fields where γ-driven neck growth and healing processes dominate, pulling the system towards equilibrium, expelling fluid from the contact or sealing the rim and hence preventing creep.

In the following, an attempt will be made to delineate these fields in stressed systems by deriving relevant criteria describing competition between the driving forces for neck growth type processes and solution/precipitation creep.

2.5.1 Condition of zero driving force for solution/precipitation creep and related behavioural fields.

The driving force term for solution/precipitation creep in the new models derived in Section 2.4.2 takes the form ($a\sigma_e/e_v$ - $4\gamma_{sl}/d$) and thus contains a surface energy related driving force term which is opposed to the driving force term due to the applied stress. The solution/precipitation models therefore predict three different conditions in a stressed solid/liquid system, depending on the relative magnitude of the terms $a\sigma/e_v$ and 4 γ_{sl}/d. These are considered below.

Case 1: When $a\sigma_e/e_v > 4\gamma_{sl}/d$, the stress related driving force term driving transport from grain contacts to pores exceeds the surface energy term. Densification will hence proceed under non-equilibrium conditions, i.e. matter dissolves at the contacts and is transported to the pore walls. Provided $a\sigma_e/e_v >> 4\gamma_{sl}/d$, solution/precipitation creep will proceed according to conventional models (e.g. Spiers et al., 1990, see Table 2.2) with surface energy exerting no influence. However, as $4\gamma_{sl}/d \rightarrow a\sigma_e/e_v$ the driving force for solution/precipitation is reduced and therefore the rate at which densification occurs will decrease.

Case 2: When $a\sigma_e/e_v = 4\gamma_{sl}/d$ the stress related driving force and the surface energy related driving force balance each other and the resulting strain rate will be zero. This condition of zero driving force is the limiting condition for solution/precipitation creep and can be viewed as expressing a surface-energy-controlled yield stress ($\sigma_c = 4\gamma_{sl}e_v/ad$) for solution/precipitation creep.

Case 3: When $a\sigma_e/e_v < 4\gamma_{sl}/d$, the surface energy related driving force term tending to drive transport from the free surfaces to the contact region exceeds the stress related term which acts in the opposite sense. The interfacial energy term will therefore dominate, cementing-up the contact and driving the microstructure towards an equilibrium configuration. Hence, the corresponding field can be called the equilibrium field (no deformation). Note that this field corresponds exactly to the grain boundary-healing field proposed to exist by Lehner (1990, 1995) when the potential of solid dissolved in the pore fluid exceeds the grain boundary potential.

In order to visualise these effects the following criteria can be defined delineating the fields described:

Criterion 1

When the driving force for solution/precipitation creep goes to zero, then the strain rate is zero and as described in case 2,

$$\frac{a\sigma_e}{e_v} = \frac{4\gamma_{sl}}{d} \quad \text{or} \quad \sigma_e = \frac{4\gamma_{sl}e_v}{a\,d} \tag{2.64}$$

Thus, when the surface energy term is significant, a yield stress must be overcome to make solution/precipitation possible at a finite rate. The yield stress, σ_e (in equation 2.64), is dependent on strain, on the value of γ_{sl}, and inversely dependent on the packing constant and grain size. Note that replacing the grain size, d, by 2ρ, where in this case ρ expresses the radius of curvature of the grains at the pore walls, and substituting σ_n for $a\sigma_e/e_v$, the criterion can be written in (dimensionless) log form as

$$\ln\left(\frac{\sigma_n\Omega^s}{kT}\right) = \ln\left(\frac{\gamma_{sl}\Omega^s}{\rho kT}\right) + \ln 2 \tag{2.65}$$

2.5.2 Condition of Zero Driving Force for Neck Growth and Related Behavioural Fields

In determining the conditions where solution/precipitation creep versus neck growth are dominant in a stressed solid/liquid system, it is important to realise that not only can the driving force for solution/precipitation creep be decreased due to surface energy effects (as described in criterion 1), but that the driving force for neck growth can also be reduced due to the effect of stress. A model for neck growth under stress was derived in Section 4.3, and the driving force determined to be

$$\Delta\mu \approx \frac{\gamma_{sl}}{\rho}\Omega^s\left(\cos\frac{\theta}{2} - \cos\frac{\theta_{eq}}{2}\right) - \Delta f^s \tag{(2.58)}$$

where ρ is now the radius of curvature at the contact margin. Recall that here θ_{eq} is the equilibrium dihedral angle under hydrostatic reference conditions. Again the driving force

consists of two terms and therefore three conditions can be recognised depending on competition between the γ and σ driving forces. These are

Case 1: When $(\cos \theta/2 - \cos \theta_{eq}/2) > (\rho/\gamma_{sl}\Omega^s)\Delta f^s$. This represents normal neck growth with reduced driving force as the right hand side nears the value of the left hand side in the approach to equilibrium.

Case 2: When $(\cos \theta/2 - \cos \theta_{eq}/2) = (\rho/\gamma_{sl}\Omega^s)\Delta f^s$. This represents the equilibrium condition when no neck growth will occur. When $\Delta f^s = 0$, the normal dihedral wetting condition will result. Important to note is that when $\Delta f^s > 0$, the wetting angle shows reduced values, because the equilibrium condition is no longer described by $\theta = \theta_{eq}$, but by $\cos \theta/2 = \cos \theta_{eq}/2 + (\rho/\gamma_{sl}\Omega^s)\Delta f^s$. For all $\Delta f^s > 0$, θ is therefore always smaller than θ_{eq}. Note that the formation of an equilibrium state with $\theta < \theta_{eq}$ assumes that Δf is relatively uniform in the contact margin area.

Case 3: When $(\cos \theta/2 - \cos \theta_{eq}/2) < (\rho/\gamma_{sl}\Omega^s)\Delta f^s$. Here, marginal dissolution will take place until a stable situation is reached at angle $\theta < \theta_{eq}$ or until the grain contact is completely undercut and the boundary becomes dynamically wetted.

Criterion 2:

In Section 2.4.3, Δf^s was specified for two extreme case, namely for purely elastic strain at the contact margin and alternatively for dislocation stored energy being dominant. From case 2 above, the zero driving force condition for neck growth is written

$$\frac{\gamma_{sl}}{\rho kT}\Omega^s\left(\cos\frac{\theta}{2} - \cos\frac{\theta_{eq}}{2}\right) = \frac{\Delta f^s}{kT} \tag{2.66}$$

When Δf^s is assumed to reflect purely elastic strain energy at the contact margin, then

$$\Delta f^s = \frac{\sigma_n^2}{2E}\Omega^s \tag{2.67}$$

where E is the Youngs modulus. Criterion 2a for the elastic case can hence be written

$$\ln\left(\frac{\sigma_n\Omega^s}{kT}\right) = \frac{1}{2}\ln\left(\frac{\gamma_{sl}\Omega^s}{\rho kT}\right) + \frac{1}{2}\left[\ln\left(\frac{2E\Omega^s}{kT}\right) + \ln\left(\cos\frac{\theta}{2} - \cos\frac{\theta_{eq}}{2}\right)\right] \tag{2.68}$$

For dislocation stored energy being the dominant contribution to Δf^s,

$$\Delta f^s = (\rho_{disl} . W)\Omega^s \tag{2.69}$$

with

$$\rho_{disl} \approx \frac{2\sigma_n^{\,2}}{b^2 G^2} \tag{2.70}$$

and

$$W = \frac{1}{2} G b^2 \tag{2.71}$$

where b is the burgers vector, and G the shear modulus (Humphreys and Hatherly, 1995; Hull, 1975 and Poirier, 1985). Hence, Δf^s can be described as

$$\Delta f^s = \frac{\sigma_n^{\,2}}{G} \frac{(\Omega^s)^2}{k\,T} \frac{kT}{\Omega^s} \tag{2.72}$$

and Criterion 2b for the dislocation case can be rewritten as

$$\ln\frac{\sigma_n \Omega^s}{kT} = \frac{1}{2}\ln\frac{\gamma_{sl}\Omega^s}{\rho kT} + \frac{1}{2}[\ln\frac{G\Omega^s}{kT} + \ln(\cos\frac{\theta}{2} - \cos\frac{\theta_{eq}}{2})] \tag{2.73}$$

2.5.3 Grain Boundary Healing Versus a Dynamically Wetted Island-Channel Structure

Consider now a grain boundary with an island-channel structure, where the solid/solid contacts support the applied stress and fluid penetrates the boundary in channel-like structures which constantly change position. One cannot describe such a contact as purely solid/solid nor as two solid/liquid surfaces. Such a contact could only consist under non-equilibrium conditions. Following the arguments of Lehner (1990) discussed earlier, the existence of such an irregular island-channel structure is thought to be dependent on the uneven distribution of stress and stress-induced irregularities in free energy density (f^s) at the grain boundary surface, leading to an irregular pattern of dissolution which results in

a channel structure migrating continuously within the grain contact area and thus allowing dynamic wetting.

If the solid/solid/liquid contact would have a finite dihedral angle under hydrostatic equilibrium conditions, the minimum energy configuration for grain contacts would be solid/solid contact with fluid only in triple junctions. Therefore an island-channel grain boundary structure represents a higher surface free energy situation then the equilibrium geometry of grain boundary surfaces. As pointed out by Lehner (1990), to maintain such an island-channel structure, local stress-induced forces must overcome γ-effects. If the stress on the contact would be released, i.e. under non-stressed but also non-equilibrium conditions, a resultant surface energy related force would exist which would lead to a spreading of the lower energy solid/solid grain contacts, e.g. by growth of the islands and shrinking of the channels. This shows that cementing-up of the grain contact is not necessarily caused by material being transported from the pores to the contact region. It could also be caused by growing "islands" and occlusion of the "channels" under the influence of γ_{sl}, once the applied stress gets below a critical value and is unable to create enough irregularities and fluctuations in f^s to keep the boundary open. This should mean that there exists a yield stress below which the boundary will seal by internal redistribution of solid and fluid within the grain contact area.

An attempt is now made to derive a criterion for the internal healing of an island-channel structured grain boundary, separating fields in which solution/precipitation creep in such a system is possible or not possible. Consider two spherical grains touching each other and sharing a macroscopically flat grain boundary having an island-channel structure, as shown in Figure 2.6. When a mean effective normal stress (σ_n-p) is applied, the force acting across the circular contact is σ_n A, where the area $A = \pi x^2$ and x is the radius of the contact. Describing this in terms of an effective hydrostatic stress applied to the aggregate, the force transmitted across the contact is given (using equation 2.49)

$$F_{stress} = (\sigma_n - p)A \approx \frac{a\sigma_e}{e_v} \pi x^2 \qquad (2.74)$$

The approximation of $\sigma_n = a\sigma_e/e_v$ is valid for small e_v only.

The island/island contacts within the grain boundary contact are now treated as "small necks" occupying an area fraction α. The chemical potential at the solid/liquid interface within the channel (ch) locations is given

$$\mu_{ch} = f^s_{ch} + p\Omega^s_{ch} \tag{2.75}$$

where the solid/liquid interfaces are assumed to be macroscopically flat. On the other hand, the potential at the islands (isl) margins is given

$$\mu_{isl} = f^s_{isl} + p\Omega^s_{isl} - \frac{\gamma_{sl}\Omega^s_{isl}}{\rho_{isl}}\left(\cos\frac{\theta}{2} - \cos\frac{\theta_{eq}}{2}\right) \tag{2.76}$$

where ρ_{isl} is the smallest of the principle radii of curvature at the island margin (cf. the equations for neck growth). Due to the convention that radii of curvature are taken positive for the convex outward interfaces from an origin within the solid grains, ρ_{isl} is negative. This is already accounted for in the equation above, and therefore values for ρ_{isl} to be substituted must be positive. The driving force for island growth is thus given,

$$\Delta\mu = \mu_{ch} - \mu_{isl} = -\Delta f^s - p\Delta\Omega^s + \frac{\gamma_{sl}\Omega^s_{isl}}{\rho_{isl}}\left(\cos\frac{\theta}{2} - \cos\frac{\theta_{eq}}{2}\right) \tag{2.77}$$

where Δf^s and $p\Delta\Omega^s$ are defined as excess quantities at the island margin. For $\Delta\mu > 0$, the islands will grow and produce a healed or partially healed contact, with every island growing in the same way as described by the foregoing neck growth models. For $\Delta\mu < 0$, island dissolution will occur, potentially maintaining an active grain boundary structure. Note that the sign of $\Delta\mu$ will be determined by the relative magnitudes of the term (Δf^s-$p\Delta\Omega^s$) versus the last term on the right hand side of equation (2.77). In general (Δf^s-$p\Delta\Omega^s$) will be influenced by the applied stress through elastic deformation and/or defect generation at the islands within contacts.

Consider further the driving force for island growth derived above. The term $p\Delta\Omega^s$ is expected to be negligibly small, due to the small compressibility of solids and the low applied stresses considered. Therefore,

$$\Delta\mu \approx -\Delta f^s + \frac{\gamma_{sl}\Omega^s_{sl}}{\rho_{isl}}\left(\cos\frac{\theta}{2} - \cos\frac{\theta_{eq}}{2}\right) \tag{2.78}$$

Note that equation (2.78) is similar to equation (2.58). The only difference is that ρ is not the radius of curvature of the grain boundary margin, but ρ_{isl}, the radius of curvature of an

island margin. At the grain boundary margin, however, these need not be different.

Again three cases can be recognised, considering the two driving force terms.

Case 1: When $(\cos\theta/2 - \cos\theta_{eq}/2) > (\rho_{isl}/\gamma_{sl}\Omega^s)\Delta f^s$,grain boundary healing will occur in an attempt to approach equilibrium.

Case 2: When $(\cos\theta/2 - \cos\theta_{eq}/2) = (\rho_{isl}/\gamma_{sl}\Omega^s)\Delta f^s$,this represents the equilibrium condition .

Case 3: When $(\cos\theta/2 - \cos\theta_{eq}/2) < (\rho_{isl}/\gamma_{sl}\Omega^s)\Delta f^s$. In this case, dissolution of the islands will occur. If the Δf^s term always dominates, an actively dissolving rough (island-channel) structure will be maintained.

Criterion 3

A criterion can now be derived defining the conditions for grain boundary healing, equilibrium, or dissolution, assuming the solid is purely elastic or plastic. Δf^s is again assumed to be either due to elastic strain related to the elastic stored energy or due to defect stored energy. Treating each island as a purely elastic column carrying a stress σ_n/α, substituted for σ_n in equation (2.67), then following the same arguments as for Criterion 2a, Criterion 3a becomes

$$\ln\left(\frac{\sigma_n\Omega^s}{\alpha kT}\right) = \frac{1}{2}\ln\left(\frac{\gamma_{sl}\Omega^s}{\rho_{isl}kT}\right) + \frac{1}{2}\left[\ln\left(\frac{2E\Omega^s}{kT}\right) + \ln\left(\cos\frac{\theta}{2} - \cos\frac{\theta_{eq}}{2}\right)\right] \quad (2.79)$$

When the dislocation stored energy is the dominant contribution to Δf^s, equation (2.67) is used with the modified contact stress σ_n/α, and following the derivation of Criterion 2b, Criterion 3b can be written

$$\ln\frac{\sigma_n\Omega^s}{\alpha kT} = \frac{1}{2}\ln\frac{\gamma_{sl}\Omega^s}{\rho kT} + \frac{1}{2}\left[\ln\left(\frac{G\Omega^s}{kT}\right) + \ln\left(\cos\frac{\theta}{2} - \cos\frac{\theta_{eq}}{2}\right)\right] \quad (2.80)$$

However, the stress distribution on the grain-to-grain contact is likely to vary with the radius (x) of the contact, such that σ_n/α reaches a maximum at the centre of the

contact and is near zero at the margin. This parabolic stress distribution would be consistent with diffusion controlled removal of mass from the contact by solution/precipitation creep (Rutter, 1976) and with static contact mechanics (Johnson, 1987). Assuming that the elastic or plastic stored energy is largely related to the normal stress component, σ_n, this implies that Δf^s will be a maximum at the centre of the contact and a minimum at the margins. Therefore the criterion for island-growth is more likely to be satisfied at the contact margin, rather than for islands well within the contact. This would lead to circumferential growth of the islands near the contact rim, sealing the grain-to-grain contact and preventing further transport in or out of the boundary, trapping fluid inclusions.

2.5.4 Mass transport mechanism maps: NaCl as an example

With the dimensionless equations 2.65, 2.68, 2.73, 2.79 and 2.80, it is now possible to construct maps of transport mechanism fields in stress versus "surface pressure" (γ_{sl}/ρ) space. Each equation defines the boundary between the fields of active solution/precipitation transport on one side and a field of neck growth or contact healing on the other. The relative position of the boundaries is largely determined by the constant terms in the equations. Of these, some are constants which can be calculated or approximated, while others are system specific or universal constants. In the following, system specific maps will be made for NaCl plus saturated solution as an example. The results are then compared with existing experimental data for the system.

In constructing transport mechanism maps for a given solid/liquid system, data are needed on G, E, γ_{sl} and Ω^s. The values of these constants, as employed in the present treatment of the NaCl brine system, are given in Table 2.3. Using these values and assuming that the term $(\cos\theta/2 - \cos\theta_{eq}/2) \approx 0.5$, Criteria 1, 2 a + b and 3 a + b have been plotted for the NaCl-brine system in σ_n versus ρ space (Figures 2.8, 2.9 and 2.10). The choice of $(\cos\theta/2 - \cos\theta_{eq}/2) \approx 0.5$ is considered justified since the equilibrium dihedral angle, $\theta_{eq}/2$, is known to be "quite blunt" (Hickman and Evans, 1991). Indications from micrographs suggest ~ 80-90°, hence the cosine difference term is expected to be positive and the range of possible values to be dominated by $\theta/2$, for which an average value of 0.5 is chosen.

Material specific data for NaCl/ brine system at room temperature		
$\gamma_{s,vac}$	0.163 J/m^2 for {100} 0.354 J/m^2 for {110}	Benson and Yun (1967)
$\gamma_{l,vac}$	0.082 J/m^2	Gel' perin et al.(1969)
γ_{sl}	0.129 J/m^2 for {100}/ brine 0.269 J/m^2 for {110}/ brine	calculated using equation (2.10) and $\gamma_{l,vac}$ and $\gamma_{s,vac}$
Order of facet disappearing during grow from sphere to cube crystal shape in brine {110}, {211} and {111} then {100} remain (Spangenberg, 1923)		
Approximation of γ_{sl} for random high energy solid/liquid interfaces = 0.27 J/m^2		
Shear modulus Bulk modulus Youngs modulus	14.7 GPa 24.9 GPa 36.9 GPa	Bass (1995) Bass (1995) calculated using Shear and Bulk modulus
molecular volume	$1.8 \cdot 10^{-28}$ m^3	Weast (1970)

Table 2.3 Material specific data for NaCl/brine system at room temperature. The calculation of γ_{sl} is performed using the approximation by Israelachvili (1985). The γ_{sl} value for spherical and other randomly oriented solid/liquid interfaces, is approximated by the value for {110} surfaces.

From the plotted criteria in Figures 2.8, 2.9 and 2.10, it is clear that active pressure solution, contact dissolution and undercutting processes are favoured at high contact stresses and high values of ρ. Conversely, neck growth and contact healing processes are favoured at low stresses and low values of ρ. Now, experiments on solution/transfer processes in the NaCl-brine system have revealed four important results which can be compared with the predictions of Criteria 1-3 (Figures 2.8-2.10). First Hickmann and Evans (1991) have shown that when lenses of halite (radius ~ 10 cm) are pressed against halite plates (see Figure 2.1a) at T $\approx$ 50 °C, σ_n=1-14 MPa, the dominant process is neck growth. Second, Schutjens (1991) pressed NaCl crystal edges against cleaved plates (see Figure 2.1b), at room temperature and contact stresses of 1-7 MPa, obtaining convergence by pressure solution. Third, Spiers et al. (1990) compacted NaCl powder at 20-90 °C, applied stresses up to 4 MPa and volumetric strains up to 20% and observed compaction by pressure solution. Lastly, Spiers and Brzesowsky (1993) compacted NaCl powder at room temperature at applied stresses up to 8.0 MPa. Above applied stresses of ~ 4 MPa, they observed compaction involving plastic/brittle deformation of contacts and contact

undercutting. Below 4 MPa applied stress the results are the same as Spiers et al (1990).

For the aggregate compaction experiments by Spiers et al (1990) and Spiers and Brzesowsky (1993), the contact stresses were calculated using equation (2.49). Further for Criterion 1, $\rho = 1/2\ d$, for Criterion 2, ρ is approximated by $x^2/2d$ as described in Section 2.3.2 and for Criterion 3, ρ is approximated by the grain boundary width. The contact radius, x, for the aggregate densification studies is approximated by $d^2e_v/6$ for $e_v \leq 20\%$. The σ_n versus ρ data, characterising the 4 studies are directly compared with criteria 1, 2a + b and 3 a + b by superposition in Figures 2.8-2.10

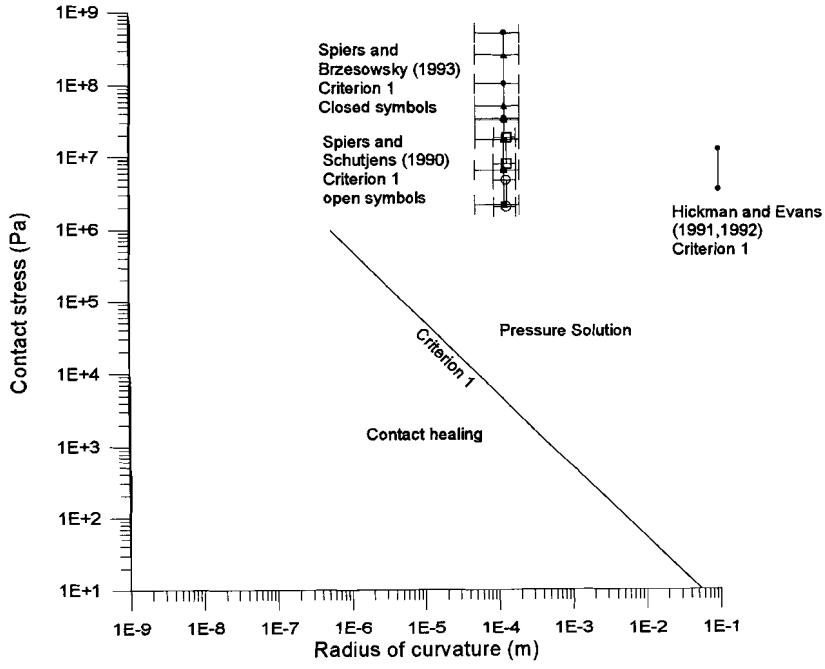

Figure 2.8 The map of material transport mechanism fields as indicated by Criterion 1 for the NaCl /brine system. Superimposed are the experimental data from Hickman and Evans (1991,1992), Spiers et al. (1990), and Spiers and Brzesowsky (1993). For the aggregate compaction experiments of the latter two studies, contact stresses are calculated for volumetric strains of 1%, 5% and 15% for the average grain size investigated. The total range of grain sizes investigated is indicated by the error bars. Note that all experimental data plot in the pressure solution field as defined by Criterion 1.

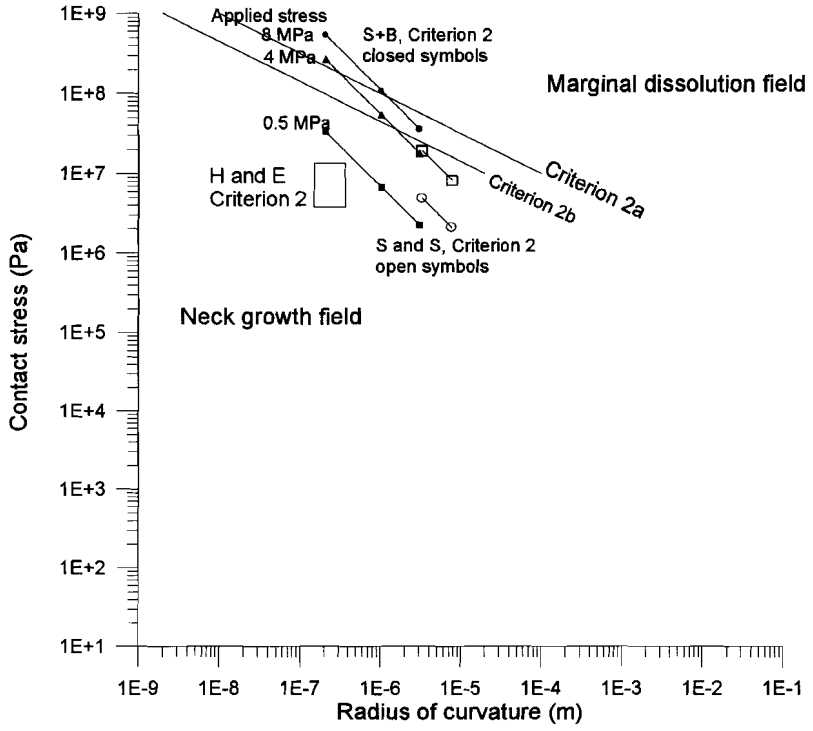

Figure 2.9 The map of material transport mechanism fields as indicated by Criterion 2a and2 b for the NaCl /brine system. Superimposed are the experimental data from Hickman and Evans (1991,1992), Spiers and Schutjens (1990), Spiers et al. (1990), and Spiers and Brzesowsky (1993). For the aggregate compaction experiments of the latter two studies, contact stresses are calculated for volumetric strains of 1%, 5% and 15% for the average grain size investigated for applied stresses of 0.5 MPa, 4 MPa and 8 MPa. For the data of Hickman and Evans, the rectangular box indicates the maximum stress of all individual experiments and ρ calculated as indicated using the reported contact radius, x, at the onset of neck growth (after some instantaneous convergence). Note that the experimental data of Spiers and Brzesowsky (1993) cross the boundary indicated from marginal dissolution to neck growth.

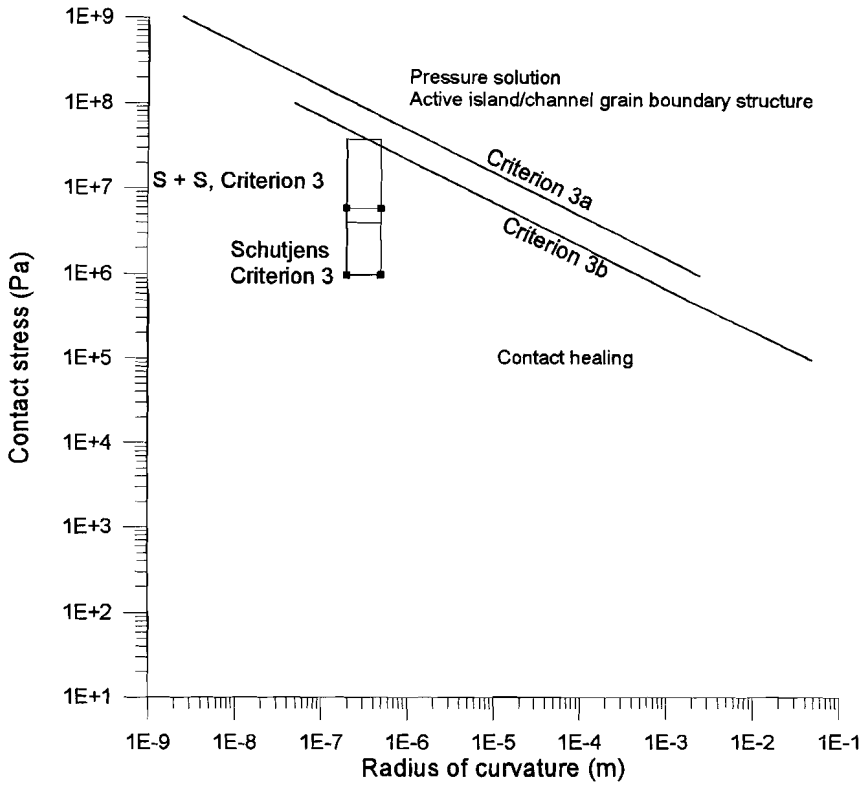

Figure 2.10 The map of material transport mechanism fields as indicated by Criterion 3a and3 b for the NaCl /brine system. Superimposed are the experimental data from Spiers and Schutjens (1990) and Schutjens (1991). The rectangular boxes indicates the stress range of all individual experiments and ρ approximated by the range of values reported for the grain boundary width. Note that both experimental data sets plot in the field of contact healing.

From the combination of experimental data and criteria plotted in Figure 2.8-2.10, several interesting observations are apparent

Criterion 1 All data plot in the solution/precipitation field. In case of the aggregate compaction experiments this is in agreement with the experimental observations. In case of

the Hickman and Evans experiments neck growth was observed. It is however possible that neck growth occurred because the condition for criterion 2a or 2b was met and that the process of neck growth proceeded faster than solution/precipitation creep, leading to contact overgrowth. In order to critically test criterion 1, experiments much closer to, or preferably crossing, the dividing curve are required.

Criterion 2

The Spiers and Brzesowsky data are the only dataset tested for which marginal dissolution was reported for experiments at applied stresses ≥ 4 MPa. As illustrated in Figure 2.9, the data ≥ 4 MPa indeed plot on the marginal dissolution side of criterion 2. However, when crossing the criterion, no change to neck growth was observed but a transition to (wetted) grain boundary diffusion controlled solution/precipitation, i.e. from one compaction mechanism to another. The latter compaction behaviour was also observed in the experiments by Spiers and Schutjens (1990) plotting in the same 'neck-growth' field with respect to Criterion 2. The bi-crystal experimental by Hickman and Evans (1991,1992) are expected to be close to the curve of criterion 2 since these data represent the condition at the onset of neck growth. Instead the data plot well within the neck-growth field (see Figure 2.9).

Criterion 3 was tested using the estimated grain boundary width reported by Spiers and Schutjens (1990) for grain contacts in compacted aggregates, and the grain boundary width reported by Schutjens (1991) for the bi-crystal experiments. The data plot on the neck-growth side of the criterion 3 curve (see Figure 2.9) despite the fact that compaction occurred and rough grain contact structures were observed.

Three possible explanations for the deviating behaviour are shortly addressed. First, the role of mass transfer kinetics and local inhomogenities can be more influential than the driving force criteria, as already mentioned in relation to neck growth in the experiments by Hickman and Evans (1991, 1992). Note, that e.g. for Criterion 3, growth of the islands in the grain boundary can be predicted from a driving force aspect, while local differences in dissolution and mass redistribution within the contact could maintain a rough contact structure. Second, when considering surface stress instead of interfacial free energy, γ_{sl}, the position of the criteria fields could be different. Third, for facetted crystal shapes the effects of surface free energy anisotropy can be significant.

The remarkebly different behaviour observed in the two experimental bi-crystal data-sets of Hickman and Evans (1991, 1992) and Schutjens (1991) is still not adequately explained by the models and criteria described in this chapter. However, it can be explained qualitatively when making use of the general background on interfacial energy and grain boundaries described in Section 2.2 and the above mentioned explanations for deviating behaviour. An important finding by Hickman and Evans (1992) is, that neck growth rates could not be correlated with the applied stress, but were found to be largely dependent on the grain boundary misorientation between the two crystals. Especially experiments with low angle misorientation between the <100> in the plate and <100> in the convex lens tended to have higher neck growth rates (Hickman and Evans, 1992) while a moat formed near grain-to-grain contacts. The moat formation results in a large increase in area (and curvature/unit area), indicating that the growth of the low energy grain boundary is a relatively larger energy reduction than the "cost" in energy for the moat geometry formation. This indicates that this geometry (Geometry B in Table 2.1) is dictated by anisotropy. Another important observation which supports the strong anisotropy influence is the lobate or fingered appearance of the contact region (Hickman and Evans, 1992). It shows an outer rim which has two principle directions perpendicular to eachother. These are likely to be the {100} directions, because a larger reduction in energy can be achieved in these directions than in any other. This shows that an extra driving force term for neck growth is present due to surface energy anisotropy for the two-grain geometry described by Hickman and Evans (1991, 1992). This driving force is not included in the models.

The extra driving force present for neck growth when the grain boundary is a low energy boundary compared to a random high angle (higher energy) grain boundary, will also shift the boundaries of the field where neck growth is dominant, in such a way that the neck growth field will be larger at the expense of marginal dissolution and/or solution/precipitation.

For the bi-crystal experiments of Schutjens (1991), only one crystal face is a non-{100} surface, namely the grain boundary surface of the lower crystal (see Figure 2.1b), and observations show that this surface dissolves under stress while the {100} side of the grain boundary (upper crystal) remains intact. When using the same arguments as for the bi-crystal experiments by Hickman and Evans described above, an additional driving force is present for solution/precipitation as long as a sufficiently high stress is applied, i.e. a

stress high enough to prevent the high energy surface to reconstruct in low energy {100} facets. As a result the field of conditions favouring solution/precipitation is expected to be larger for this geometry compared with random solid/liquid interface- and grain boundary orientations. An alternative explanation for only one of the two surfaces at the contact dissolving, is that the increase in solubility under stress leads to preferential dissolution of the relatively high energy interface as a result of faster dissolution kinetics, or lower activation energy (fewer neighbouring bonds to be broken).

In conclusion, the different behaviour for the two series of bi-crystal experiments is thought to be due to anisotropy effects of interfacial free energy (or surface stress) and/or orientation dependent kinetics of the mass transfer processes.

2.6 Summary and conclusions

A theoretical background including definitions for a thermodynamic surface, surface free energy and surface stress has been described. Against this background, various classes of interfacial boundaries in solid/liquid systems were considered and expressions for the pointwise chemical potential at solid surfaces were reviewed. Subsequently, driving forces for mass transfer in a stressed solid/liquid aggregate were considered, taking both stress and interfacial energy related terms into account.

Building on this basis, models were developed for neck growth at grain-to-grain contacts under the action of surface energy driving forces only, in a purely hydrostatically stressed solid/liquid system. Two-grain geometries, involving just-touching grains, as well as grains having finite contact area before neck growth, were considered. These can be directly compared with previous models by Hickman and Evans (1992). However, in the new models the grain boundary energy, γ_{gb}, is specifically taken into account, in contrast to previous models which neglected this. This extension for the first time describes neck growth towards a realistic, final equilibrium state.

Moving on to solid/liquid systems subjected to a positive effective stress, models for densification of an aggregate where derived in which both an applied stress and surface energy are considered as driving forces. When the surface energy term becomes negligible,

these models reduce to those for compaction by pressure solution obtained previously by Spiers and co-workers and others. However, the models including the surface energy term predict that pressure solution densification will slow down towards sufficiently low stresses and fine grain sizes, finally coming to a halt at/below a strain and grain size dependent " yield stress". The predicted behaviour at low stress and grain size is quite different from previous models describing pressure solution compaction of solid/liquid systems.

In addition, it has been shown that the neck growth models need to be modified for a granular solid/liquid system subjected to a state of positive effective stress. Here too competition between surface energy and stress related driving forces becomes important. New rate models for neck growth in stressed systems were accordingly derived.

Lastly, the models developed for pressure solution and neck growth, including the effects of both stress and surface energy related driving forces, were applied to derive criteria defining the conditions under which pressure solution, neck growth and grain contact healing can be expected to occur.

Three maps were subsequently drawn, substituting material specific data into the criteria for the NaCl/brine system. Experimental data on pressure solution and neck growth in the NaCl/brine system were superimposed on these maps as a first test. The results are not completely explained by the theoretical criteria, however. More data are required, especially lower stress data for Criterion1. In addition, kinetic factors may play a role, as well as driving force factors, in determining the dominant mass transfer processes. To exclude the influence of surface free energy anisotropy as far as possible, aggregate densification experiments seem more appropriate for testing the various criteria, than bi-crystal experiments which indicate a large influence of the grain-to-grain contact orientation.

CHAPTER 3

DENSIFICATION OF $NaNO_3$ AGGREGATES PLUS SATURATED SOLUTION: AN ANALOGUE FOR PARTIALLY MOLTEN SYSTEMS

3.1 Introduction

In order to model large scale deformation and melt segregation/migration phenomena occurring in partially molten regions of the crust and mantle, an understanding of the underlying grain-scale microphysical processes, controlling material behaviour, is needed. Compaction of the solid matrix is recognized as a possible onset-mechanism for solid/melt segregation (McKenzie, 1984; Stevenson, 1986, 1989 and White and McKenzie, 1995). In Chapter 2, models for densification of a solid/liquid system by solution/precipitation creep were derived considering both surface energy and effective stress as driving forces for material transport. The present chapter is concerned with experimentally testing the models derived. In view of the fact that the models assume idealised behaviour in chemical systems, these first experiments are performed on a simple analogue system, namely $NaNO_3$ plus saturated solution. Experimentation can be performed under ambient conditions with such an analogue system, so that high quality data can be far more easily obtained than for silicate/melt systems. In particular, experiments were performed with the aim of investigating possible effects of the solid/liquid interfacial energy as a driving force for material transport and the occurrence of a possible "yield stress" for solution/precipitation creep due to a surface energy forces opposing the effect of applied stress.

The experimental approach adopted, involved room temperature densification creep tests (i.e. 1-dimensional compaction experiments) in which the applied stress and grain size were systematically varied from experiment to experiment. In this way, the dependence of strain rate on stress and grainsize could be determined and compared with the models, which predict an increasing influence of surface free energy, γ, in relation to applied stress, σ, towards low stress and fine grain size. At coarse grain sizes (> 20 μm), the observed behaviour was consistent with conventional diffusion controlled, stress driven solution/precipitation or pressure solution creep. For the finest grain size fractions used (8-

20 μm), evidence was found for a variety of surface energy related effects, including a "yield stress" in the 8 μm material.

3.2 Background data on $NaNO_3$

3.2.1 $NaNO_3$ plus saturated solution as an analogue system

Under conditions where mass transfer results from diffusive transport through the liquid phase, an ionic salt plus saturated-solution system bears close similarities to a simple mineral plus partial-melt system, with respect to the models above, and in this sense can be seen as a suitable analogue for a partially molten system. The main advantages of a salt plus saturated solution system are that experiments can be performed under easily excessible (ambient) experimental conditions.

The choice here of $NaNO_3$ as a suitable salt is based on the fast kinetics of dissolution and precipitation and on its high solubility (0.921 kg/l at room temperature) (Weast, 1970), making it possible to observe significant solution transfer in short times, and at low driving forces, as in the case of NaCl (e.g. Rutter, 1976; Raj, 1982; Pharr and Ashby, 1983; Spiers and Schutjens, 1990; Schutjens, 1991; Spiers and Brzesowsky, 1993). Moreover, at room temperature, $NaNO_3$ is already at an homologous temperature of 0.52 T/T_m so that room temperature experiments at least approach the "high temperature" regime under which deformation of partially molten systems takes place.

Previous work on plastic deformation of $NaNO_3$ single crystals at room temperatures (Hoeffer, 1989), has shown that mechanical twinning is likely to occur at 8 ± 1 MPa, due to glide along the $\{ 10\bar{1}2\}$ mechanical twin planes. In order to avoid twinning it is important to use low applied stresses during experimentation and to study microstructures afterwards for significant increases in mechanically twinned grains.

3.2.2 Physical properties of $NaNO_3$

$NaNO_3$ posseses trigonal symmetry and spacegroup R3c. The crystal structure is thus closely similar to calcite and can be described in terms of a pseudo face-centered rhombohedron containing four $NaNO_3$ molecules. The pseudo face-centered rhombohedron represents the commonly observed cleavage rhombohedron (see Figure

3.1a). Apart from the familiar cleavage rhombohedron $\{10\bar{1}1\}$, some of the most frequently occurring crystal faces for $NaNO_3$, like calcite, are the rhombohedrons e$\{01\bar{1}2\}$ and f$\{02\bar{2}1\}$, the prisms m$\{10\bar{1}0\}$ and a$\{11\bar{2}0\}$ and skalenohedron $\{21\bar{3}1\}$. Some euhedral crystal forms are illustrated in Figure 3.1b. Mechanical twins form on $\{01\bar{1}2\}$ and produce a distinct "striping" on the $\{10\bar{1}1\}$ cleavage rhombohedron (Klockmann's, 1967 and Sammler-Kuluzewsky, 1959).

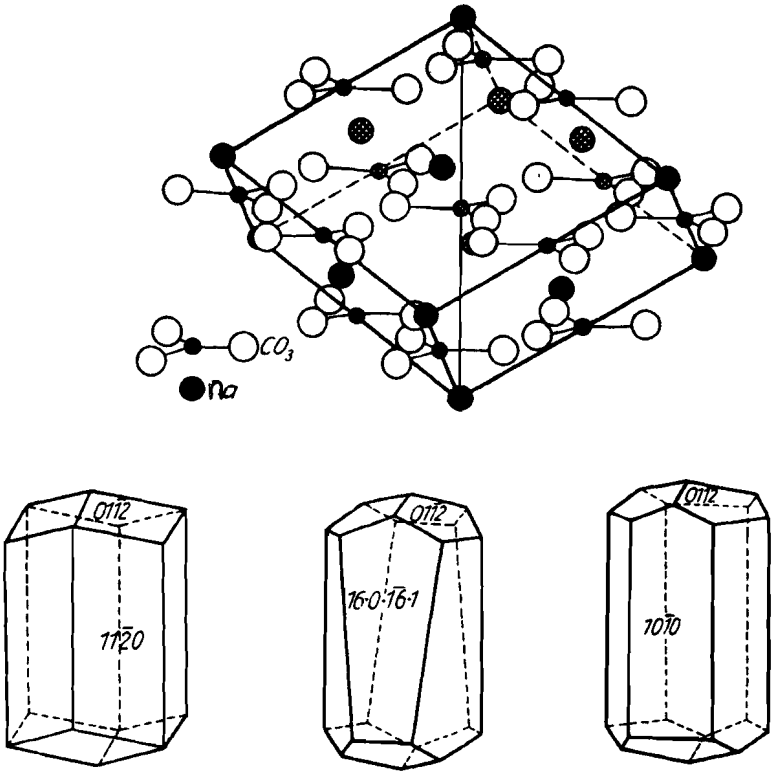

Figure 3.1. a) Schematical drawing of the cleavage rhombohedron $\{10\bar{1}1\}$ representing the most commonly observed $NaNO_3$ crystal shape. b) Schematic drawings of crystal shapes of $NaNO_3$ with some of the more often occuring crystal faces. (After, Klockmann's, 1967; Sammler-Kuluzewsky, 1959 and Hoeffer, 1989).

The surface free energy of crystals always varies with orientation. In highly anisotropic (trigonal) crystals such as $NaNO_3$ or calcite, this orientation dependence is expected to be strong. However, the only available value found for the surface free energy

of $NaNO_3$ is a range from 0.17-0.26 J/m^2 determined by Dzherakov et al (1986), based on a calculation relating surface tension to Young's modulus, Poisson's ratio, a structural coefficient and microhardness. This value can be compared with the surface energy determined for NaCl because ionic materials generally have similar solid/vacuum interfacial energies. The values for NaCl are indeed similar. Because the accuracy of individual surface energy values is low and average values for NaCl are based on far more data, I prefer to use the average value for NaCl as an estimate for $NaNO_3$ instead of relying on the only one literature value for $NaNO_3$. The NaCl data are reviewed by Benson and Yun (1967) and the resulting average solid/liquid interfacial energy value is 0.27 J/m^2 .The ratio of the highest and lowest surface energy of the solid faces, a measure of anisotropy, was concluded to be above 2 for NaCl. This surface energy ratio is however determined by crystallography, and cannot be used for $NaNO_3$. A rough estimate of minimum anisotropy can be obtained from the morphology of large crystals. By measuring the perpendicular distances from the crystal faces to the center of the crystal (Tiller, 1991). Considering the morphology of $NaNO_3$ crystals (Figure 3.1), the ratio of maximum to minimum surface energy is expected to be >3.

3.3 Models to be tested

In chapter 2, a set of models was derived for neck growth processes at grain-to-grain contacts, i.e. mass transport from the positively curved pore regions towards the grain contact due to a surface energy related driving force, in stressed and non-stressed solid/liquid systems. Additional models were derived for the rate of densification, $\dot{\beta}$, by solution/precipitation or pressure solution creep including the effects of both surface energy, γ, and effective stress, σ_e, as possible driving forces. The latter models, which are derived for small volumetric strains ($e_v \leq 20\%$), are written

$$\dot{\beta} = \frac{nI^*\Omega^s}{kTde_v^{\,b}}\left(\frac{a\sigma_e}{e_v} - \frac{4\gamma_{sl}}{d}\right) \quad \text{when interface reactions are rate limiting} \qquad ((2.52))$$

$$\dot{\beta} = \frac{144Z^*\Omega^s}{kT^3e_v}\left(\frac{a\sigma_e}{e_v} - \frac{4\gamma_{sl}}{d}\right) \quad \text{when diffusion is rate limiting} \qquad ((2.51))$$

where $\dot{\beta}$ is the rate of densification (s^{-1}), σ_e is the effective applied stress which is defined as $\sigma_e = \sigma - p_f$, with p_f being the fluid pressure, d is the aggregate grain size, a is a geometrical term dependent on the grain packing geometry (for FCC it is 0.675), k is Boltzmann's constant, T is temperature and Ω^s is the molecular volume. In the interfacial reaction limited case, Γ^* is the rate coefficient for the dissolution or precipitation reaction depending which is rate controlling. For dissolution n = 6 and b = 1 while n= 3 and b=2 for precipitation control. In the equation for diffusion control, Z^* is an effective grain boundary diffusivity parameter defined $Z^* = D_{gb} C S$, where D_{gb} is the intrinsic grain boundary diffusion coefficient, C is the solubility of the solid in grain boundary solution (mole-fraction) and S is the average grain boundary fluid thickness. Note that these models predict a " yield" stress for pressure solution, given $\sigma_e = 4\gamma_{sl}e_v/ad$, corresponding to zero driving force for solution/precipitation creep at the condition $\dot{\beta}=0$. The surface free energy related term in equation (2.51) and (2.52) is then equal and opposite to the stress related term and hence a "yield" stress must be overcome before solution/precipitation creep will occur.

In this chapter an experimental approach is chosen to test the densification models. Although the neck growth models will not be directly tested themselves, they are important in defining limits of the solution/precipiation creep field and a general understanding of microscale processes which can take place. The neck growth models can all be written in the general form

$$\dot{x} = A(T)\, R\, \gamma_{sl} \left[\cos\left(\frac{\theta}{2}\right) - \cos\left(\frac{\theta_{eq}}{2}\right) - \left(\frac{\rho}{\gamma_{sl}\Omega^s}\right)\Delta f^s\right] \frac{d^b}{(x^2 - x_{cr}^2)^c} \quad ((2.63))$$

where A(T) is a temperature dependent term, describing the temperature dependence of solubility and of diffusivity or surface reaction rates, R is a constant incorporating molecular volume and geometry dependent constants, ρ is the radius of curvature at the grain-to-grain neck, and ($\cos\theta/2 - \cos\theta_{eq}/2$) measures the deviation from the equilibrium dihedral wetting angle (θ_{eq}). In addition Δf^s is the change in Helmholz free energy within necks due to elastic or dislocation stored energy (see chapter 2), so that the term ($\rho\Delta f^s/\gamma_{sl}\Omega^s$) is zero when no stress is applied. The exponents b, c are either 0 or 1 depending on the initial contact configuration and detailed diffusion path length. For zero initial contact, x_{cr} is zero.

In general, the equations show that neck growth is favoured when the contact stress is low, i.e. when the applied stress is low and/or the grain-to-grain contacts are large

(large strains or large x_{cr}). Neck growth is also favoured by small grain size and relatively large γ_{sl} values.

3.4 Experimental aspects

The present experiments consist of 1-D compaction experiments performed on granular $NaNO_3$ under both dry and solution-flooded conditions. In the latter case, simple evaporation-proof drainage maintains the fluid pressure at atmospheric level.

3.4.1 Starting Material

The tests were performed on 12 grainsize fractions of fine grained $NaNO_3$, having mean grain sizes (± 1 standard deviation) of 8 ± 2 μm, 11.5 ± 2 μm, 15 ± 3 μm, 20 ± 3 μm, 22 ± 3 μm, 27 ± 7 μm, 39 ± 5 μm, 39 ± 7 μm, 63 ± 8 μm, 71 ± 7 μm, 90 ± 8 μm, 104 ± 9 μm, 163 ± 15 μm, and 250 ± 19 μm. The fractions with a mean grain size ≥39 ± 7 μm were obtained from analytical grade $NaNO_3$ (as received from Merck Chemicals) by sieving. Fractions of 39 ± 5 μm and smaller were prepared by first crushing the unsieved analytical reagent in a ball mill, followed by separation using conventional gravitational settling. The gravitational separation was performed using $NaNO_3$-saturated, high-grade methanol (Baker 99.5% pure) as a medium to bring the milled powder into suspension. The different grain size fractions were then collected over different settling times, calculated using Stokes' law. After filtering, the powder was washed with ultrapure hexane (less than 0.05% water) to remove the last of the saturated methanol. The powder was subsequently dried in an oven at a temperatures of ~ 60°C, and stored in a dry room before use. The true average grainsize of the final fractions was determined from measurements on SEM micrographs of representative samples. The grain shapes characterizing the individual fractions were more or less equiaxed, with material separated using Stokes settling being nearly spherical, while the sieved grain size fractions showed angular grain shapes. Thus, of the 39 μm grain size, both angular (± 7 μm) and a sub-spherical (± 5 μm) grain size fractions were obtained.

3.4.2 Experimental Apparatus and Testing Procedure

The various grainsize fractions were tested at room temperature under both wet and dry conditions, using the small-scale, dead weight, capillary tube set-up illustrated in Figure 3.2. In this set-up, a "gap sensor" transducer (Baumer Electric, type IWA 18U 9001) was used to measure displacement. Five such set-ups were used, so that five experiments could be run simultaneously. The displacement transducers are characterized by a linearity of 0.5 % across a full scale of 1.5 mm (correlating with an output signal of 2-8 volts). The five displacement output signals were logged using a 16 bit A/D converter plus PC, with a logging cycle of 5s. This enabled displacement versus time data to be recorded for each set-up with displacement errors of < 0.01 μm between adjacent readings and time errors < 0.001 s. Using dummy samples of bras, gradual displacements were recorded as an effect of temperature/expansion differences between day and night. The absolute amounts were however very small. Because other error effects such as friction and humidity during dry compaction are much larger, no corrections for temperature variation were performed.

In performing each experiment a dry, 10.0 ± 0.05 mg sample of the selected grain size fraction was first deposited into the glass capillary tube (internal diameter 2.1 ± 0.05 mm, see Figure 3.2) supported in its base and with the lower steel piston ($\pm$ 2.00 mm diameter) in place. The upper piston was then inserted and the sample was loaded with a dead weight of 1500 g. Samples were thus compacted dry for 2 hours at an applied stress of 4.9 MPa to achieve a locked aggregate with a well controlled "starting porosity". After dry compaction, the weights were adjusted to give the desired stress for further testing, the range of stresses being 2 kPa - 4.9 MPa. The samples were then rapidly flooded with $NaNO_3$-saturated solution by adding the liquid to the plastic ring located at the top of the capillary tube (Figure 3.2) and by applying a partial vacuum using the evacuation tube in the brass base. When the whole sample was flooded, the evacuation tube was closed, the remaining liquid in the plastic ring reservoir was removed and a drop of silicone oil was added to the ring to prevent evaporation. Displacement of the dead weight was then measured as a function of time, as described above, typically for a period of 24 hours. Finally the weights were removed, the samples were flush-dried by passing compressed air through the capillary tubes, and then carefully pushed out of the tubes to be dry-stored for thin sectioning and SEM sample preparation.

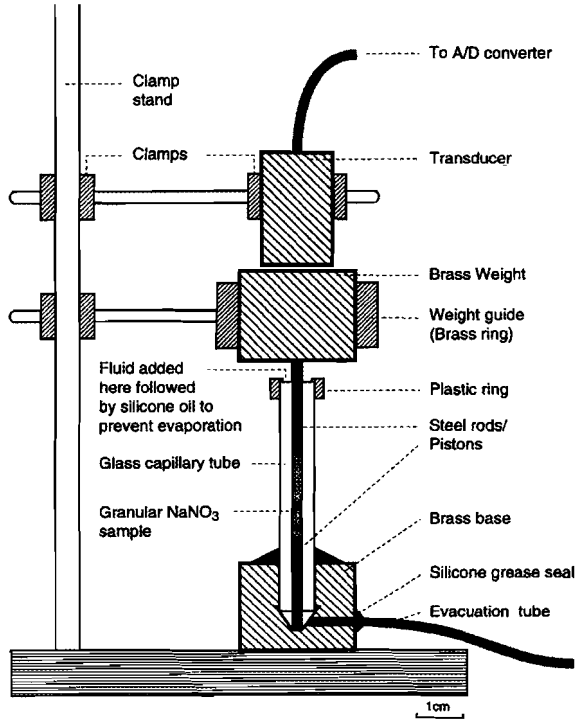

Figure 3.2. Schematic diagram illustrating the set-up of the uniaxial glass tube experiments.

Some experiments were performed under dry conditions for 24 hours. In other cases silicone oil was added after 2 hours instead of $NaNO_3$ solution. These experiments were performed for control purposes. In addition, the following further variations on the standard procedure were carried out with different objectives. Some samples were wet compacted for less than 24, hours or for much longer times (up to 2 months), in order to study the microstructural development over widely varying times. Other experiments were performed using wider capillary tubes (internal diameter 5.0 ± 0.05 mm) plus 55 ± 5 mg samples in order to facilitate experimentation at low applied stresses (down to 2 kPa) using the standard dead weight configuration. In total, more than 150 experiments were performed of which around 120 involved wet compaction using saturated solution. The solution was always saturated with the grain size fraction being tested. As the wet compaction behaviour proved to be very sensitive to the "starting" porosity (i.e. porosity after dry compaction), narrow ranges of starting porosity were chosen. The 5-mm tubes in general produced higher starting porosities (48.5-50 ± 2%), while the 2-mm tubes

produced starting porosities in the range 39-47%. As a result, the data from the 2-mm and 5-mm tube experiments were not mixed when constructing graphs. For the 2-mm tube experiments, a porosity range was chosen in such a way that most experiments could be used while the porosity range stayed within a narrow range, i.e. $40.5 \pm 2.5\%$, $42.0 \pm 2.5\%$ and $45.5 \pm 2.0\%$ (see indications at the graphs). Samples with starting porosities outside the range were rejected.

In practice, one of the more difficult parts of experimentation was to keep the salt sufficiently dry, thus allowing pressure solution-free dry compaction (locking of the aggregate) and avoiding solution transfer microstructures prior to wet compaction. On warm humid days (> 25 °C, relative humidity > ~ 80%) experimentation was because dry compaction could not be performed.

3.4.3 Friction Tests

Since one of the aims of the wet compaction tests was to investigate competition between stress-related and surface-energy-related driving forces for solution-transfer (see models), it was necessary to achieve very low stresses, i.e. of magnitudes comparable with the quantity $4\gamma/d$ (equations 2.51 and 2.52). These low stresses required the application of dead weight loads down to 5 g. The applied loads are so low that the question must be asked whether or not frictional effects at the piston/tube and sample/tube surfaces will introduce significant errors in the applied load. Even capillary forces at the fluid minisci need to be considered. In order to answer these questions, a number of so-called friction experiments were performed.

Sample preparation for the friction experiments was the same as for compaction experiments. After 2 hours of dry compaction, the glass tube, including pistons and sample, was removed from the brass base and placed in a clamp stand positioned over a balance. The tube was clamped in such a way, that the force transmitted through the inner column, i.e. lower piston, sample and upper piston, were measured by the balance, while the weight of the glass capillary tube was not. In this way, frictional forces between the inner column (sample plus pistons) and the glass tube inner wall, and adhesion forces due to the fluid-air menisci at the pistons, could be measured as a reduction in applied dead weight value observed on the balance.

After setting up the dry sample and applying an appropriate dead weight, saturated solution was added to the plastic ring on top of the capillary tube. Fluid filled the porous sample due to capillary action. Only a small excess of fluid was added. The fluid did not run out of the capillary tube at the lower piston side due to capillary action.

The friction experiments were performed using the smallest weights used in the compaction experiments, i.e. 5 and 25 g for the 5 mm tube and 11 and 25 g for the 2mm tube. The influence of grain size was investigated as well, using 25 μm, 104 μm and a mixture of 5-200 μm grain size samples. After fluid infiltration, the mass on the microbalance was recorded with time, taking measurements every 20 seconds at the start and every 10 minutes at the end of the experiment. The largest deviation from the real weight occurred while the sample was still dry, when fluid passed through the sample, and shortly after this. In order to illustrate the effect, the data of three experiments are shown in Figure 3.4. At time zero, the fluid was added. All curves show a sharp increase in the weight measured with time after fluid penetration. Also, every curve shows a rough wave-like pattern after or even during the sharp increase. The wave-like pattern is typical of frictional force versus time experiments (Ravikiran, 1995). The maximum error is at the start of the experiments, when the applied stress can be reduced by as much as 17% for the very low stress experiments (≤ 5 kPa). Because the absolute weight reduction does not vary much with applied weight, the relative error decreases rapidly with increasing applied stress (e.g. 8% for 1.4 10^4 Pa and 4% for 2.5 10^4 Pa). At longer times (> 60-80 minutes for the low stress experiments in Figure 3.3), the remaining error due to friction and adhesion is ~1- 4%. Because relatively high stress experiments (> 1 MPa) can achieve several percent of strain within 1 minute, a window of minimum strain and time can be used to restrict errors due to friction and adhesion. On this basis, it was decided to reject data obtained below 10% unless obtained after more than one hour elapsed time.

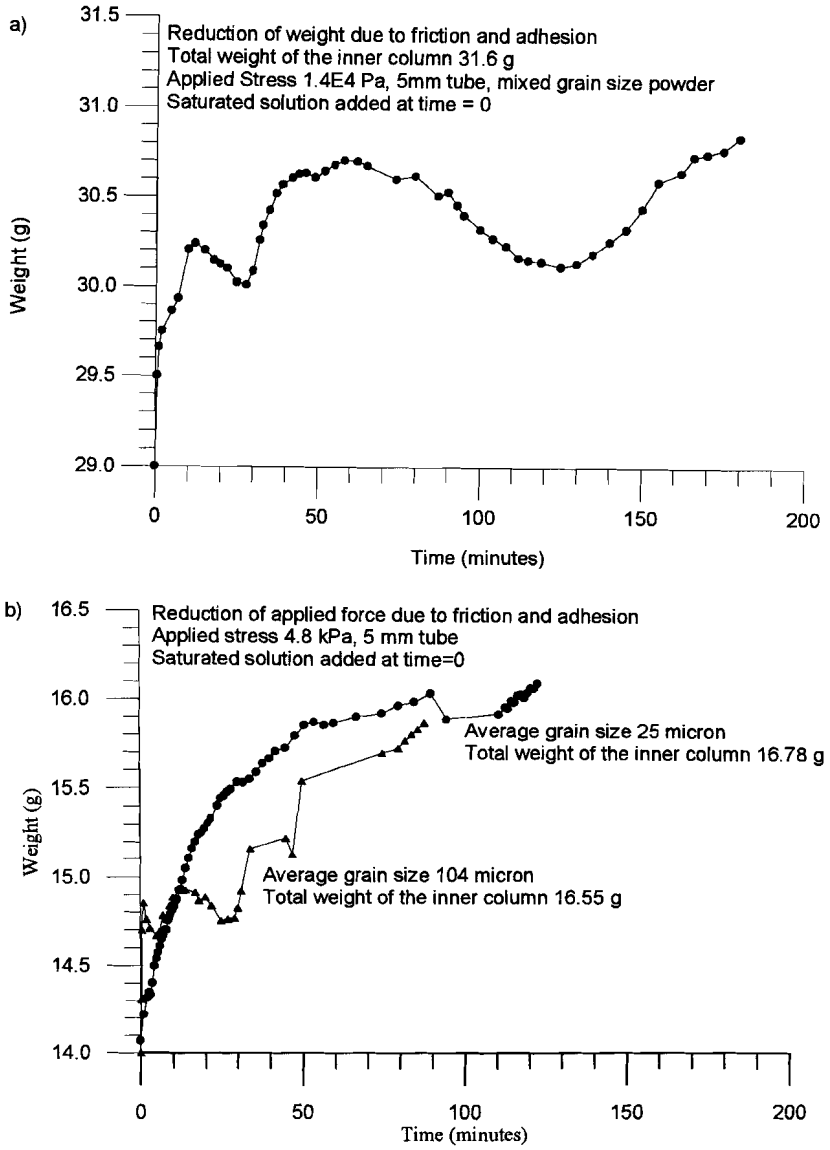

Figure 3.3 Typical creep curves during friction tests, illustrating the reduction in weight due to friction and adhesion with time of compaction. a) Creep curve for mixed of grain sizes (see text at the graph). b) Creep curves for 25 μm and 104 μm grain size fractions.

3.4.4 Data Processing

Volumetric strain versus time data were calculated directly from the displacement versus time records obtained for each experiment. Strain rates were calculated vs. volumetric strain using the 3-point central difference method. For the first and last data points of each test, and for data points where the time interval to the next data point was larger than 7200 s, the strain rate was interpolated using 2 data points only. Taking into account all sources of error in measuring displacement and time, the maximum error in calculating strain rate is estimated to be typically around 4%, reaching 10% at strain rates $< 10^{-7}$ s^{-1}.

3.5 Results

3.5.1 Mechanical data

During initial dry compaction at 4.9 MPa, all samples showed an instantaneous shortening of 0.04-1% followed by minor creep. Samples which were subsequently loaded at lower stresses, either dry or with added oil, also showed little or no creep (see Figure 3.4).

In contrast to dry or oil saturated samples, wet samples showed very rapid creep densification (Figure 3.4 and 3.5). Figure 3.5 shows typical creep curves, obtained at different stresses for material with fixed starting grain size. Note the large range of stresses used (3 orders of magnitude in the case of Figure 3.5). The experiments performed at higher stresses clearly tend to produce more or faster creep, reaching nearly full densification in 24 hours.

The displacement vs. time data recorded from the wet compaction experiments were used to construct plots of compaction rate (β) versus volumetric strain (e_v), applied effective stress (σ_e) and grain size (d). Representative results are shown in Figures 3.6-3.8. From the log-log plot of Figure 3.6, it can be seen that volumetric strain rates decrease with increasing strain, the data showing slopes ranging from -2 to -4 at strains around 10%. Towards higher strains, the strain rates decrease very rapidly with increasing strain, indicating that densification slows down, reaches unmeasurable rates or even stops. For the highest stress experiments (e.g. 4.9 MPa), a steep decrease in strain rate can be observed from ~ 20% strain to nearly full densification (only a few percent porosity left).

At the lower stress curves a similar shape is observed, but with creep slowing down sharply at lower volumetric strains. The experiment at 6.2 10^3 Pa, for example, attained 18.3% strain before it stopped, which is long before full densification.

Figure 3.7a-d show log strain rate vs. log stress plots derived from experimental data similar to those plotted in Figure 3.6 and drawn for constant strains and for various grain sizes. In these diagrams the slopes of the curves represent the exponent (n) in an empirical power law description of the form $\dot{\beta} \propto \sigma^n$. The slopes in Figures 3.7 are roughly 1 at stresses in the range ~3 10^4- 4.9 10^6 Pa, although for the 8 μm grain size experiments shown in Figure 3.7d, the slope is somewhat more than 1, on average $n \approx 1.3$ for stresses downto 2.2 10^4 Pa and for the 104 μm experiments, shown in Figure 3.7a, the slope is less than 1, with $n \approx 0.7$. Towards the lower stresses, the strain rate suddenly decreases for the spherical grain sizes (Figure 3.7b, 3.7c and 3.7d). In Figures 3.7b and 37c (d=15 and 39 μm) this sudden drop is evidenced only by one data point. However at 8μm grain size (Figure 3.7d), the effect is clearly established..

The grain size dependence of strain rate is shown in the log strain rate vs. log grain size plots of Figures 3.8a-d, each drawn for the applied effective stresses indicated. At relatively coarse grain sizes (> ~ 22 μm), an average slope of about -3, demonstrates that the strain rate is roughly proportional to $1/d^3$ in this region. However, towards finer grain sizes, the curves pass through a maximum at around 20 -25 μm, followed by a decrease in strain rate with decreasing grain size.

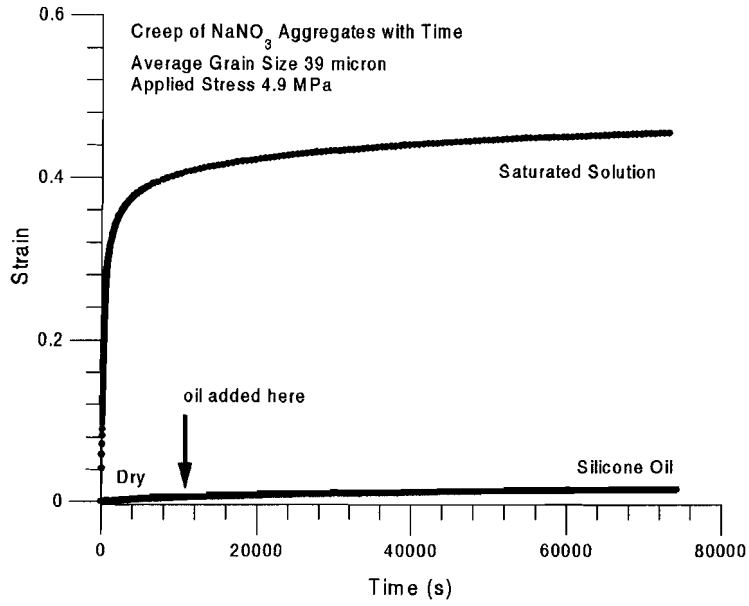

Figure 3.4 Comparison of creep behaviour of granular $NaNO_3$ loaded dry then saturated with oil, versus a sample loaded with saturated $NaNO_3$ solution Applied stress was 4.7 MPa and the average grain size was 39 μm (rounded fraction) for both experiments.

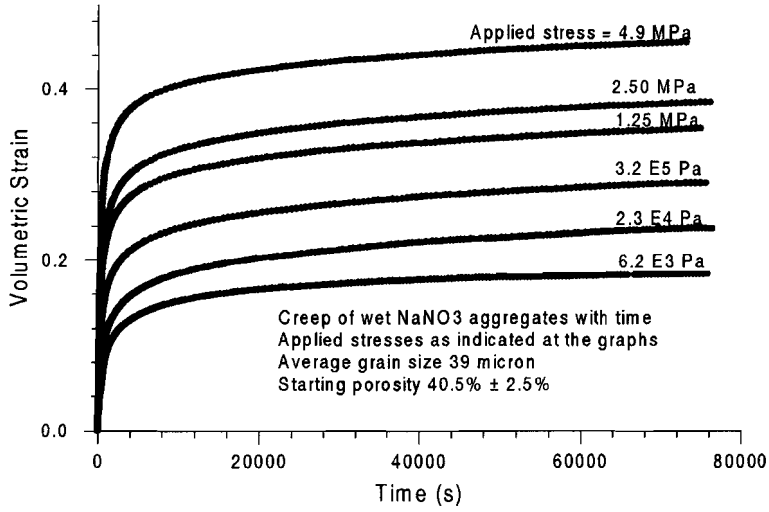

Figure 3.5 Typical creep curves obtained for wet (brine-saturated) $NaNO_3$ powder, showing the effect of increasing stress. Stresses are indicated at the graphs. Average grain size is 39 μm (rounded fraction) for all experiments.

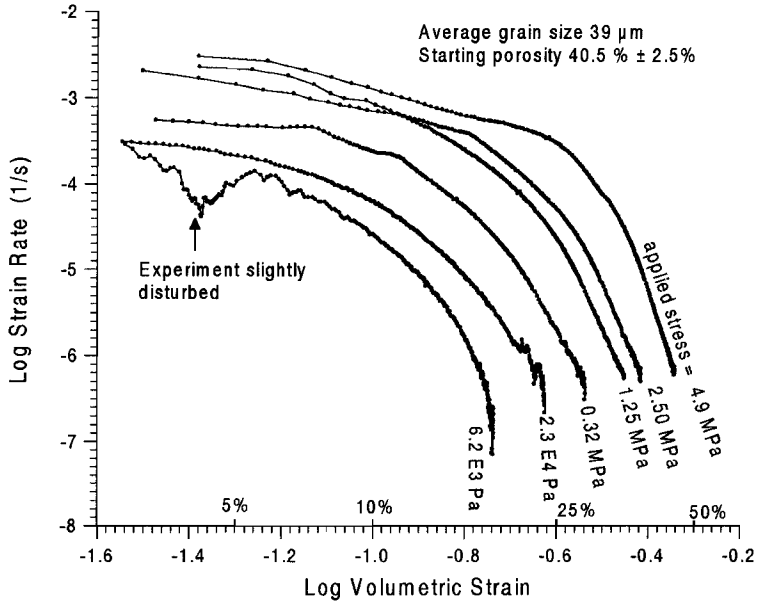

Figure 3.6 Typical log strain rate versus log strain data for wet compacted $NaNO_3$ samples. The different applied stresses are indicated at the curves. The average grain size for all experiments is 39 µm (spherical fraction).

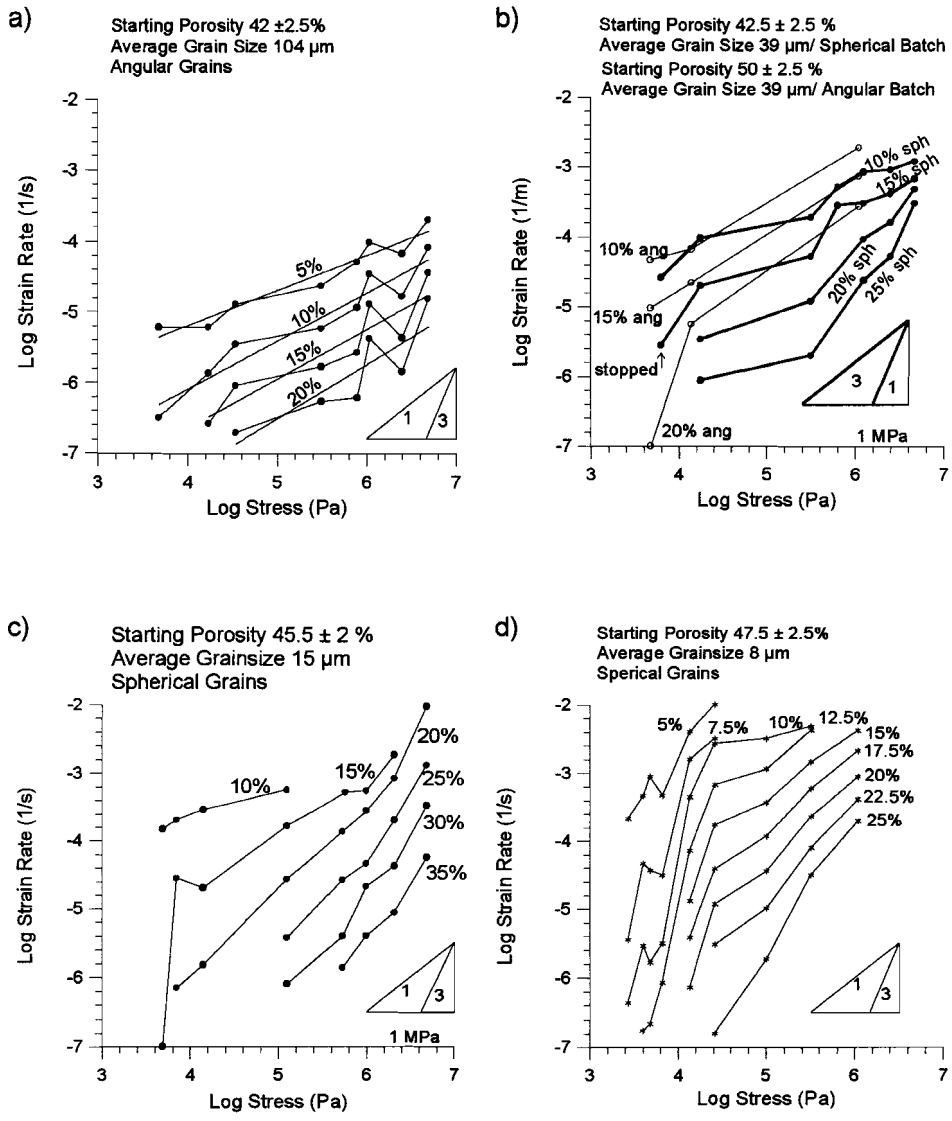

Figure 3.7 Log Strain rate versus Log stress diagrams for wet compacted $NaNO_3$ samples for the various grain size fractions indicated.

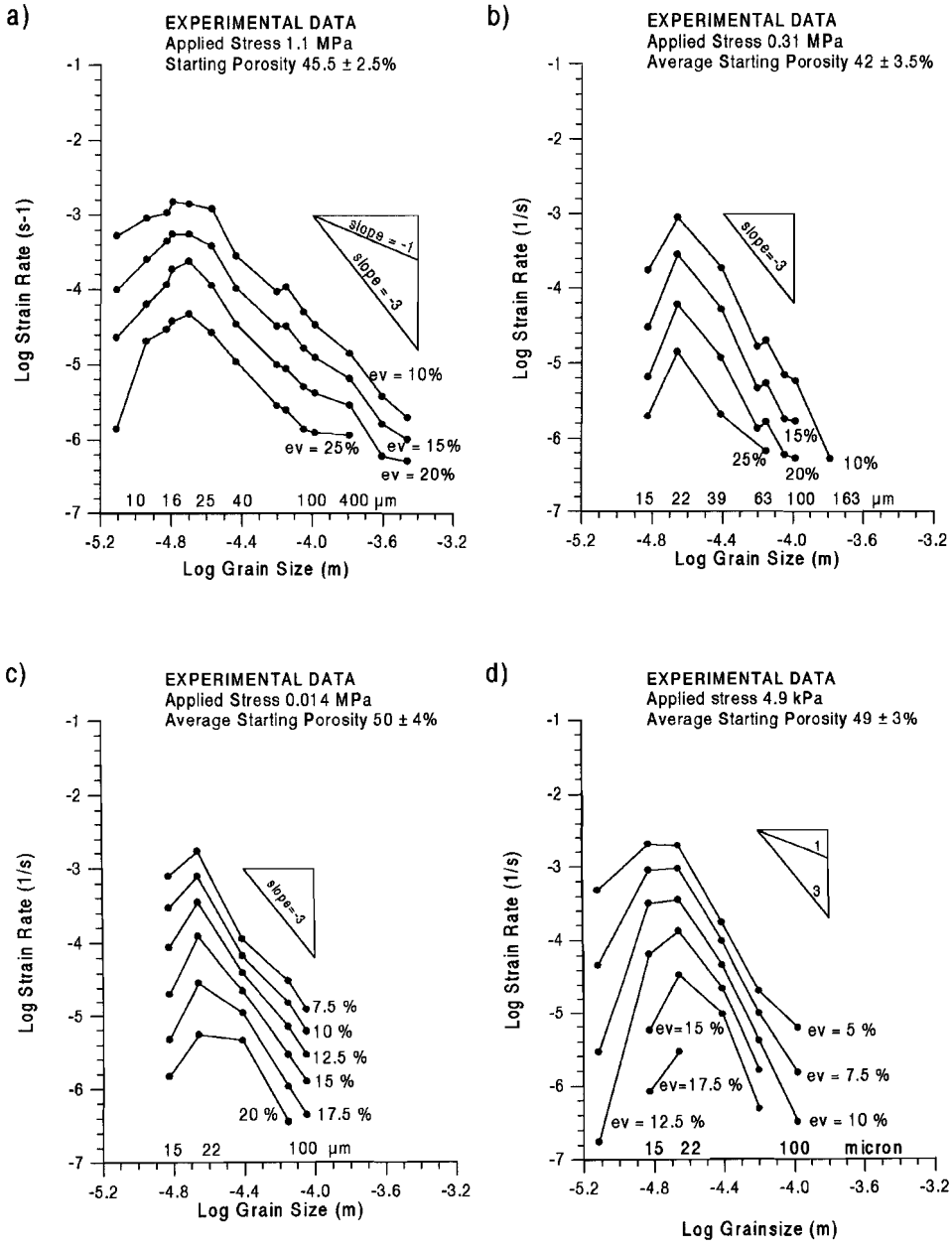

Figure 3.8 Log strain rate versus log grain size diagrams for wet $NaNO_3$ samples for the applied (effective) stresses indicated.

3.5.2 Microstructural Observations

3.5.2.1 Methods

Both the scanning electron microscope (SEM) and transmission optical microscope were used to study the starting material, the dry compacted and the wet compacted samples. For the SEM work on the starting powder, this was distributed on SEM sample-stubs coated with a dry layer of colloidal carbon adhesive (as all "wet" glues affected the starting material) and was then directly gold coated (thus minimizing exposure to the atmosphere). The compacted samples were mounted with colloidal carbon adhesive to SEM-stubs and both carbon and gold coated. For optical microscopy, thin sections of the compacted samples were prepared as follows. First, the compacted samples were cut in half. One half was used for the SEM sample, the other half was impregnated with epoxy resin containing a blue dye and then polished, using Bruers SiC-4000 paper, to a thickness of ~ 8-50 micron (depending on the grain size). Final polishing was done in a low humidity room. For optical microscopy, a cover slip was then glued onto the sample, with epoxy resin, to prevent moisture corrupting the microstructure afterwards. Some thin sections were used for SEM study. Most of these were etched after polishing with Zn-saturated glacial acetic acid for 10-30 seconds (following Van den Hoop et al., 1995) and then rinsed with ultrapure hexane (< 0.05% water). Because zinc is preferentially adsorbed onto the resin surface, the outline of the epoxy/grain surface shows up very clearly.

3.5.2.2 Starting Material

As mentioned in Section 4.1, SEM micrographs of the starting fractions were used to determine the true average grain sizes (8, 11.5, 14.0, 15.0, 19.8, 22.3, 27.0 , 39, 63, 71, 90, 104, 163 and 250 μm). The starting powders consisted of granular aggregates of mostly discrete equiaxed particles with reasonably uniform size. Fractions separated by the Stokes settling method (≤ 39 μm) showed sub-spherical grains whereas the sieved fractions showed angular grain shapes. Rounding apparently occurred by minor dissolution in the methanol settling fluid, although this was saturated (see Figure 3.9a). Some of the grains in the fractions obtained by sieving (≤ 39 μm) can be recognised as cleavage rhombohedra (Figure 3.1a), but otherwise no distinct preferential shapes or orientations

can be recognised (Figure 3.9b). In the "settled" material minor interparticle "welding", neck growth and sintering features are present. Rare "pressure solution" like microstructures (indentations) were also found. The amount of plastic deformation present in the starting material was investigated using an optical microscope to study powdered material immersed in a droplet of paraffin between two glass plates. Very little undulatory extinction was observed. However, deformation twins (i.e. on e{01$\bar{1}$2} twins, Hoefer, 1990) were found in some larger grains. The total proportion of twinned grains was estimated to be ~3%.

3.5.2.3 Dry Compacted Samples

SEM and thin section studies were carried out on dry compacted samples, to find out if deformation mechanisms other than particular sliding and rearrangement occurred. The typical granular/porous microstructure observed is shown in Figure 3.10. No undulatory extinction could be observed. Evidence for grain fracturing or contact crushing was found in only a few grains per sample. With respect to mechanical twinning, no visual difference could be observed between the proportion of twinned grains in the dry compacted sample and the starting material. Like the (sieved) starting fractions, only occasional grains show microstructural features similar to those for solution/precipitation creep.

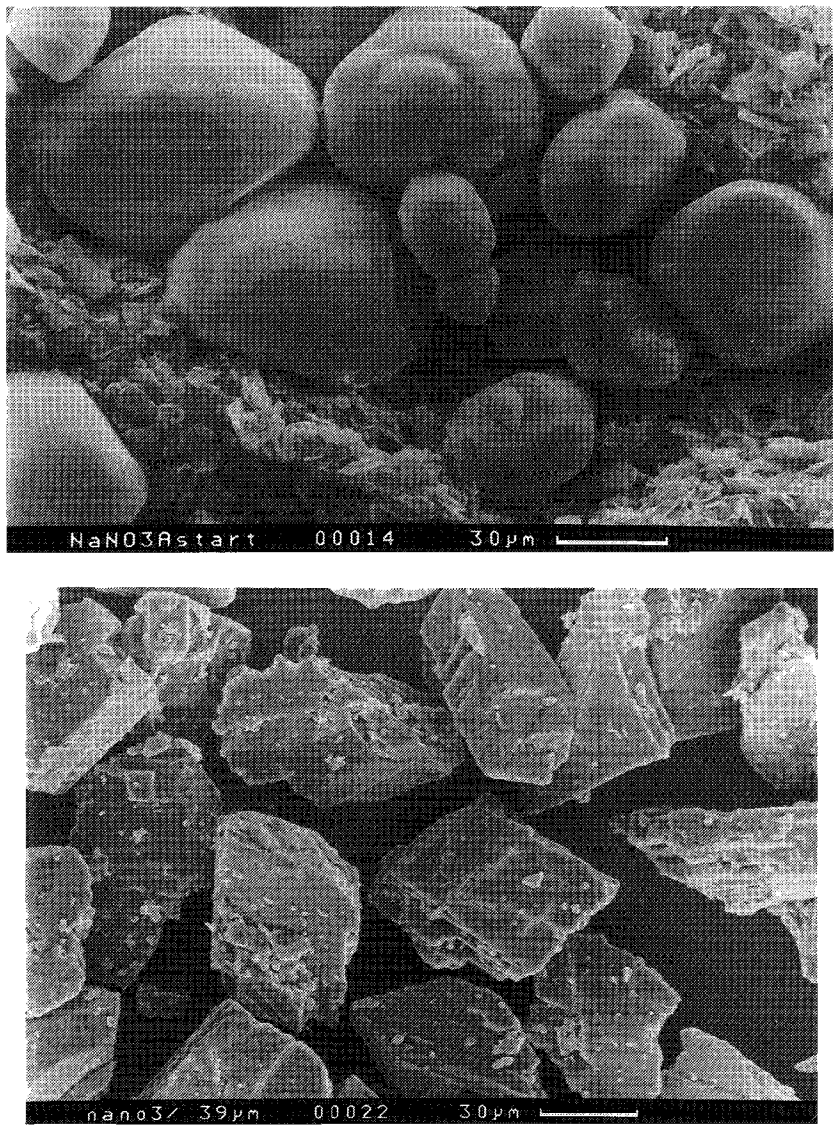

Figure 3.9 SEM micrographs of $NaNO_3$ starting material. A) Typical near-spherical grain shapes obtained by Stokes settling; grain size 39 µm. B) Typical angular grain shapes obtained by sieving grain size 39 µm.

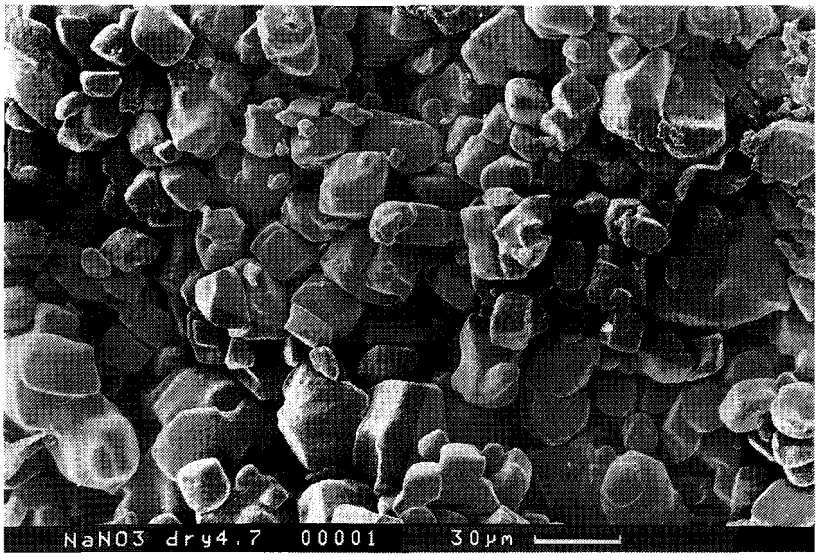

Figure 3.10. SEM micrograph of a dry compacted $NaNO_3$ aggregate. The applied stress during compaction was 4.9 MPa, and the average grainsize of the starting material was 15 micron.

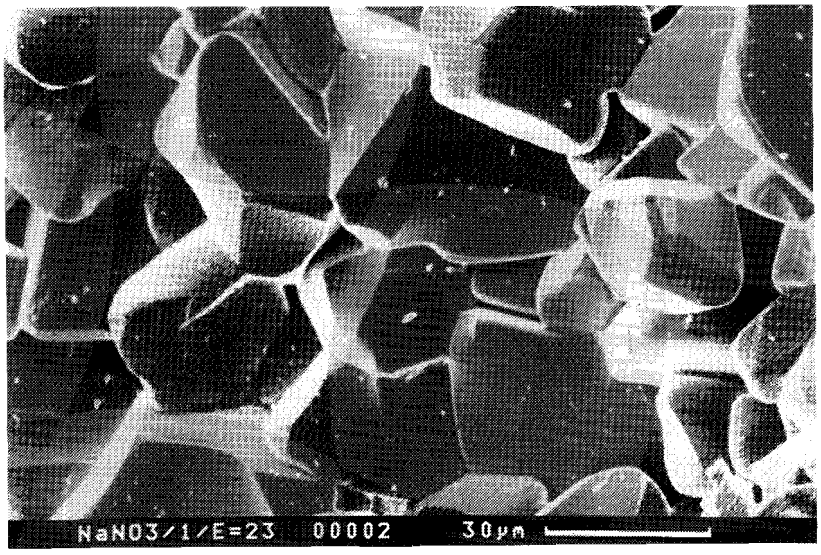

Figure 3.11 SEM micrograph of a 3-D fracture surface showing a dense microstructure after 24 hours compaction at 1 MPa (36% strain, starting porosity 44%, final porosity ~11 %). Average starting grain size 27 μm (rounded).

3.5.2.4 Wet Compacted Samples

Three distinct styles of microstructure were observed in the wet compacted samples depending on applied stress, final strain and grain size.

The highly, fine grained stressed samples (σ_e > 0.3 MPa, d ≤ 39 μm) show high strains (i.e. > 20%) and low porosities within 24 hours of flooding with solution. At stresses ≥ 1 MPa, only 8-12% porosity remains after this period of compaction for grain sizes in the range 20-39 μm. The microstructure which develops is a dense polygonal structure of well fitting grains and often well developed triple junctions are observed (see Figures 3.11 and 3.12). For starting grain sizes < 20 μm, where somewhat less strain is achieved under otherwise similar conditions, the microstructures show more residual pores and increased final grain sizes, indicating that grain growth has occurred during compaction. Often a ring-like structure forms within grain-to-grain contacts (see Figure 3.13).

In the high stress experiments on coarse grain samples (≥ 63 μm at 0.3 MPa and ≥ 104 μm at ≥ 1 MPa), lower final strains (< 20%) are obtained after 24 hours of compaction. Such strains are also obtained for finer grain sizes compacted at high grain stress for shorter compaction times. The microstructures of these high stress/ low to medium strain samples show typical solution/precipitation creep of pressure solution features such as indentations, dissolved contacts and overgrowths in the pores (see figure 3.14). Figure 3.15 shows that at low strain, the grain shape remained sub-spherical for the fine grain sizes. Open ring structures and neck growth features are also present in such samples. Figure 3.16 shows large dissolution pits which were only observed for the highest stress (4.9 MPa) experiments.

The low stress experiments (<1. 10^4 Pa) show distinctly different microstructures. In the finer grain size samples (≤ 39 μm), (sub) euhedral grains developed within 24-48 hours, both from sub-spherical starting fractions (Figure 3.17) as well as from the angular 39 μm grain size fraction (Figure 3.18). For the latter fraction, only shape change occurred, whilst for the subspherical grain sizes < 39 μm grain growth occurred simultaneously. The 8 μm grain size fraction grew to ~ 12 μm and the 15 μm grain size fraction to an average of 24.8 μm within 24 hours. For larger grain sizes (> 39 μm) and shorter compaction times, no extensive grain shape changes were observed. Pressure solution type features, such as contact dissolution and indentation were observed (similar to those of Figure 3.15 and 3.14). Also, in samples subjected to longer compaction times, distinctive rim-structures were observed on former grain contacts (similar to those of

Figure 3.13).

Figure 3.12 SEM micrograph of an impregnated, etched 2-D thick section. Sample is compacted for 24 hours at 1 MPa in which 36% strain was achieved (starting porosity 48%). Starting grain size 39 µm (angular). The white areas are areas with Zn-adsorbed epoxy resin (former porosity).

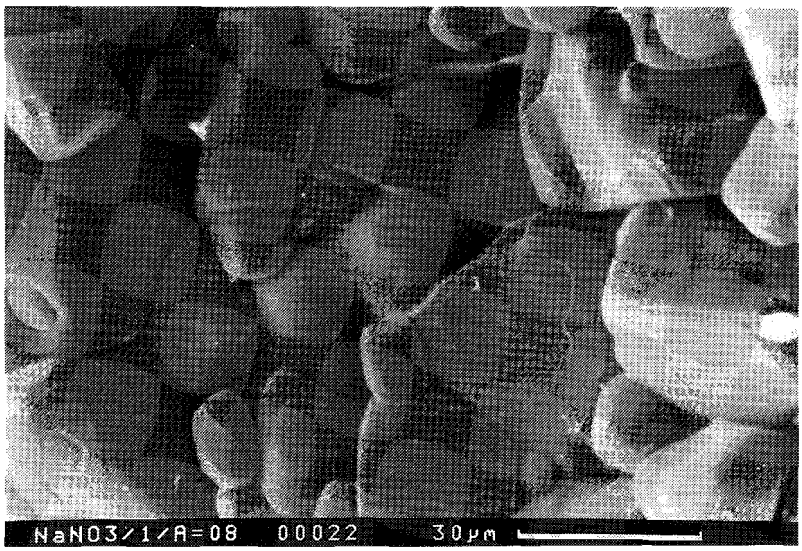

Figure 3.13. SEM micrograph of a sample fracture surface. Wet compacted sample at 1 MPa uniaxial stress with an average starting grain size of 15 µm. Note the ring within grain contacts .

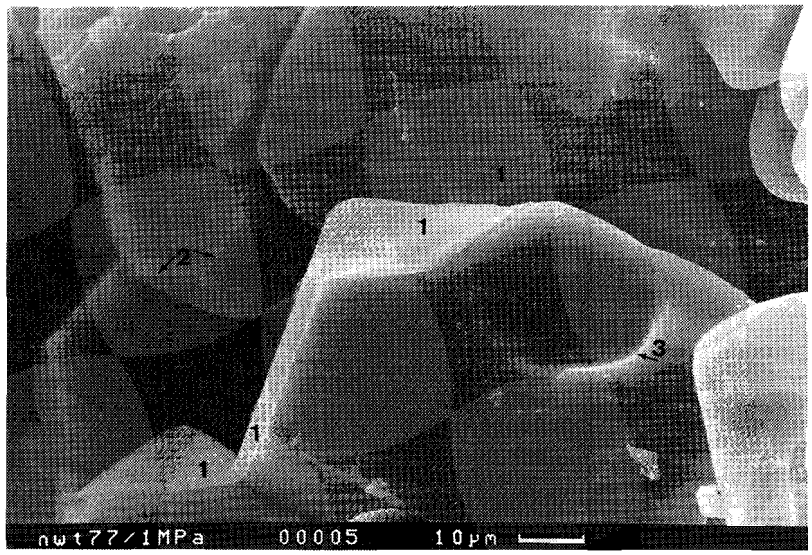

Figure 3.14 SEM micrograph of a sample fracture surface. Wet compacted sample at 1 MPa applied stress and with an average starting grain size of 39 µm (angular). Note the former contact surfaces (1), the overgrowth in the pore region (2) and a "pit" (3) probably resulting from dissolution.

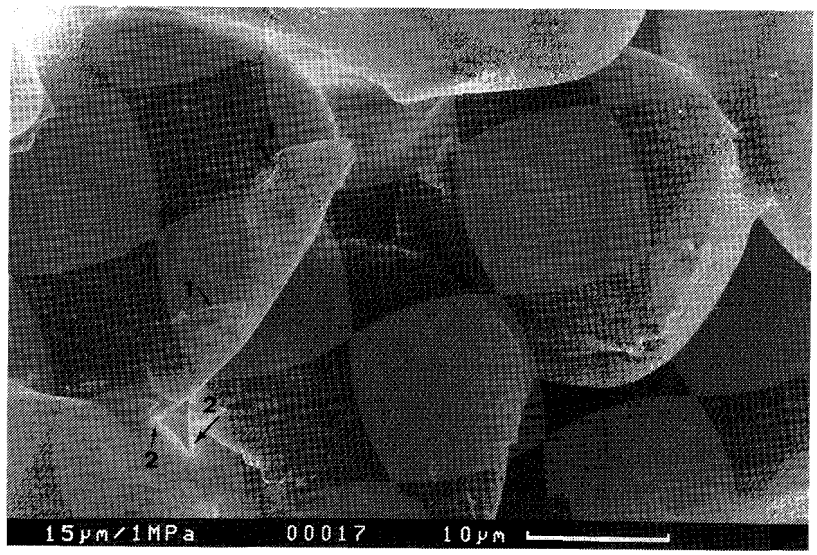

Figure 3.15. SEM micrograph of a sample fracture surface. Wet compacted sample: 1MPa stress applied for 15 minutes (18% strain). Average starting grain size 15 µm. Note that the grain shape is still sub-spherical. Former grain-to-grain contacts show open ring structures (1) and possibly neck growth (2).

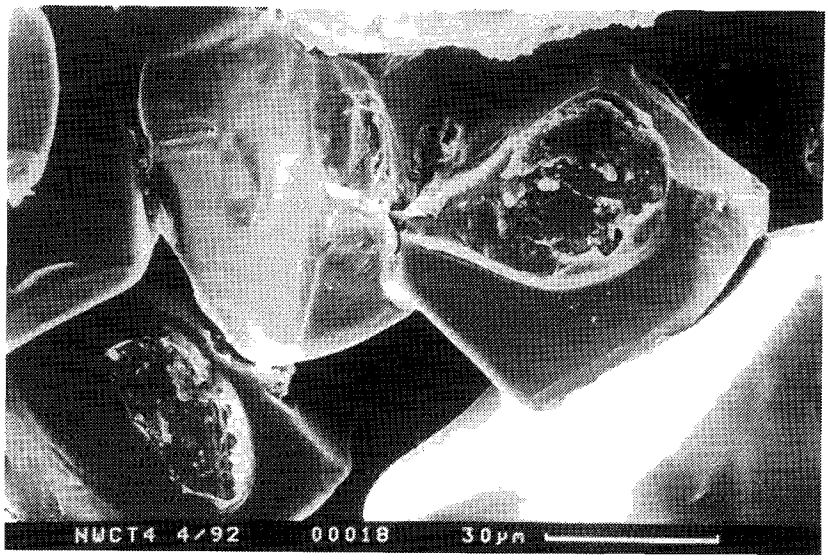

Figure 3.16. SEM micrograph of a sample fracture surface. Note the large dissolution pits. Dissolution phenomena on this scale were only observed for wet compacted samples at an applied stress of 4.7 -4.9 MPa. Starting grain size 39 µm.

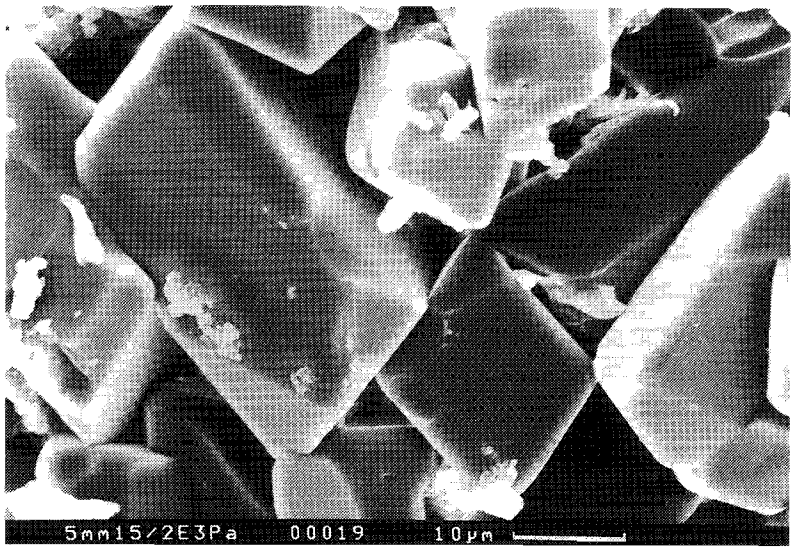

Figure 3.17. SEM micrograph of a fractured sample surface. Note formation of faceted (euhedral) grain shapes from 8 µm starting grain size (sub-spherical). Strain 3% after 48 hours of compaction at 2 10^3 Pa.

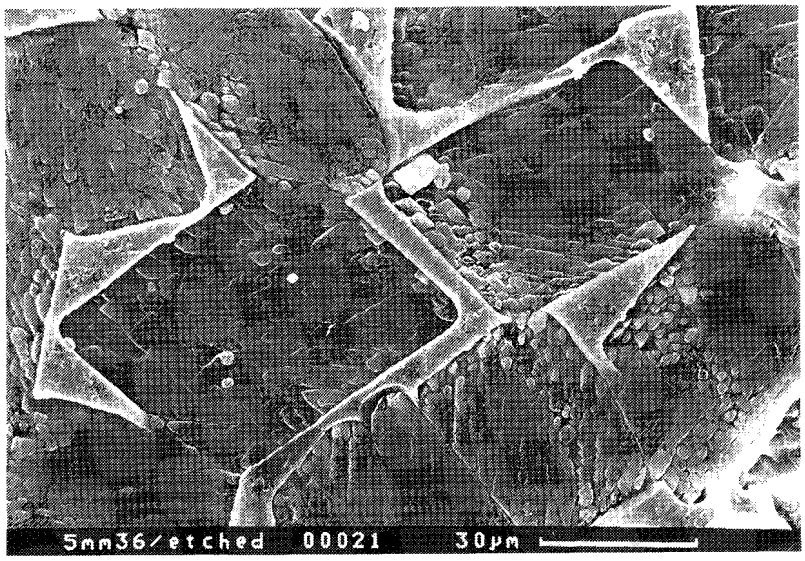

Figure 3.18 SEM micrograph of an impregnated/polished and etched sample surface. Starting grain size 39 µm (angular batch). Compaction for 24 hours at an applied stress of 4.8 10^3 Pa, volumetric strain 21% (starting porosity 52%). White-rimmed surfaces are Zn decorated epoxy resin.

Attention is now foccused on SEM observations of grain boundary structure within former grain-to-grain contacts, in relation to the three microstructural styles of regimes identified above. The observed grain boundary structures can themselves be divided into 3 categories:

1) Grain boundaries or contact characterised by a rough structure (Figure 3.19 and 3.20).
2) Closed rim structures such as illustrated in Figure 3.13.
3) Open rim structures. These are illustrated in Figure 3.15 and 3.21.

The rough grain boundary structure 1), is observed in high stress samples at low/intermediate strains (final porosity >10%). However, occidental rough contacts have also been observed in very low stress experiments on coarser grain size samples. This is illustrated in Figure 3.22. In such cases, the rough structures (Figure 3.22) are associated with small, indenting contact areas, suggesting an association with relatively high contact stresses.

The closed rim structure (2) was observed in the high-stress/ high-strain regime and also in the low stress regime. In both cases, long compaction times were involved (24-48 hours). The amount of obtained strain was however very different.

Contact rims which are open on at least one side (case 3) are observed to occur both together with rough contact structures as well as with closed rim structures. It may

represent an intermediate grain boundary structure (Compare e.g. Figure 3.23 with Figure 3.15, both of the same sample).

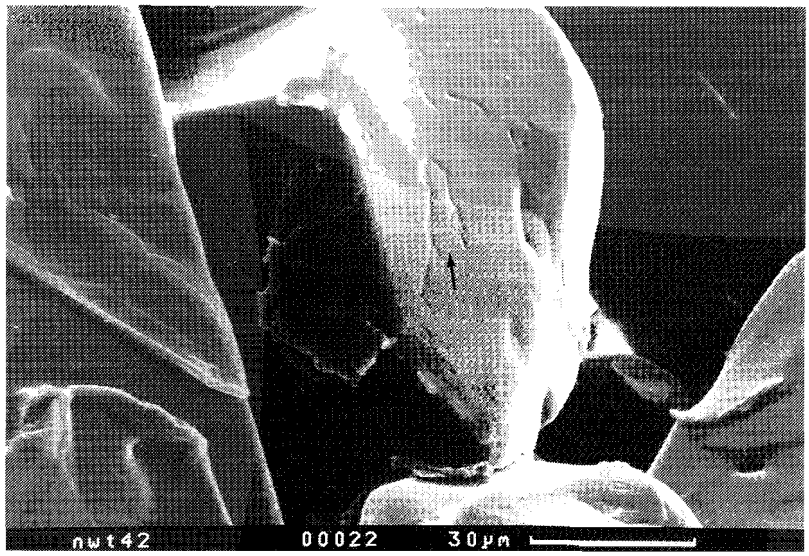

Figure 3.19 SEM micrograph of a fractured sample surface. Wet compaction at 1 MPa applied stress for 24 hours. Starting grain size is 104 µm. Note the roughness on the former contact surface.

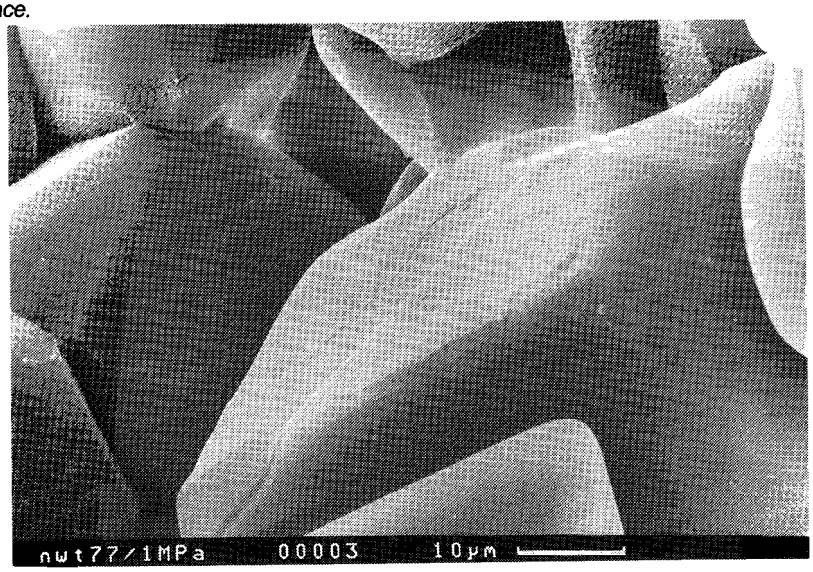

Figure 3.20. SEM micrograph of a fractured sample surface. Wet compaction at 1 MPa applied stress for 24 hours. Starting grain size 39 µm (angular batch). Note the roughness on the former contact surface.

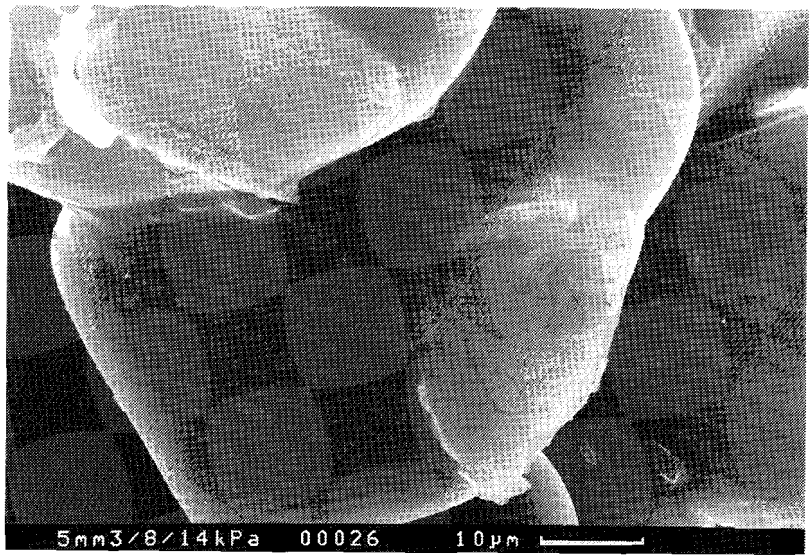

Figure 3.21 SEM Micrograph of a fractured sample surface. Wet sample of 39 µm starting grain size (spherical batch) compacted at an applied stress of 1.4 10^4 Pa. Note the rim-type of structures which are partially open.

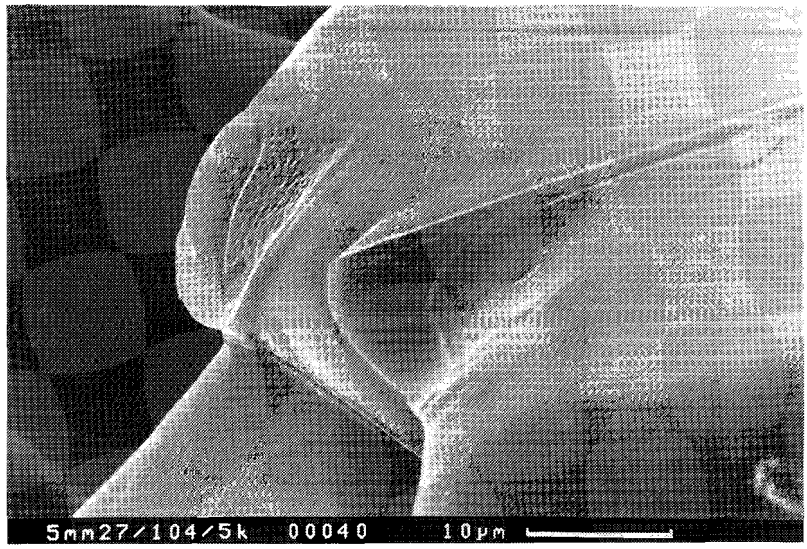

Figure 3.22 SEM micrograph of a fractured sample surface. Wet sample compacted at 5 10^3 Pa for 24 hours. Starting grain size 104 µm, final strain 11.7%. Note the rough contact surface at the indentation sites.

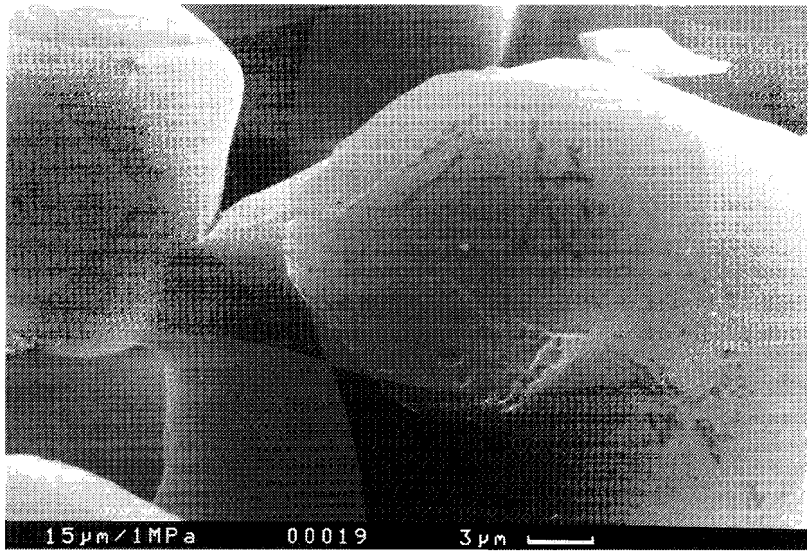

Figure 3.23 SEM micrograph of a fractured sample surface. Wet sample compacted at 1MPa applied stress for 15 minutes. Starting grain size 15 µm, final volumetric strain 18%. Note this is the same sample as in Figure 3.15. Some of the contact surface is rough, but most likely has been open on only one side.

3.6 Discussion

The above uniaxial compaction experiments have demonstrated that fine-grained $NaNO_3$ aggregates, pre-compacted to a fairly constant "starting porosity" (42.5 ± 5% for the 2 mm tubes and 49 ± 3 % for the 5 mm tubes) show little or no densification creep when loaded dry at stresses up to 4.9 MPa. This implies negligible time-dependent deformation by plasticity or intergranular sliding under these conditions. Furthermore, addition of silicone oil to the loaded samples has little effect, ruling out any purely mechanical effect of adding a liquid. However, in the presence of saturated $NaNO_3$ solution, rapid compaction creep was observed, demonstrating the operation of some kind of liquid-enhanced deformation process. The presence of indentations, truncations, dissolution pits and other grain contact roughness structures observed in the microstructures of many samples indicate an important role was played by grain boundary diffusional solution/precipitation creep. The main difference of behaviour which can be distinguished on the basis of both mechanical and microstructural observations, leads to two regimes in applied stress, namely a low stress regime (< 3 10^4 Pa) and an intermediate to high stress regime (> 3 10^4 Pa). The intermediate to high stress regime which can be further divided into low strain and high strain (> 20%) fields. With respect to grain size, some distinctive fields of behaviour can be recognised in combination with applied stress and volumetric strain. To avoid to many divisions, the effect of grain size will be discussed in more detail within the recognised stress regimes described below.

3.6.1 The high stress regime: low and high strain fields.

For low volumetric strains between ~10 and 20%, the wet compacted samples showed strain rates ($\dot{\beta}$) approximately proportional to $\sigma^{0.5\text{-}1.5}$, $1/d^3$, and $1/e_v^{2\text{-}5}$ for d >20 μm and $\sigma_e > 2.5\ 10^4$ Pa. This behaviour is broadly consistent with the diffusion controlled solution/precipitation creep derived in Section 2.4.1, i.e. with the equation

$$\dot{\beta} = \frac{A^* Z^*}{T d^3 e_v} \left[\frac{a\sigma_e}{e_v} - \frac{4\gamma}{d}\right] \qquad ((2.51))$$

for the case that the surface energy related term ($4\gamma/d$) is negligible in comparison with the stress-related driving force term ($a.\sigma_e/e_v$) (the non-equilibrium field of Section 2.4.1).

Notably, evaluation of these two terms using the values $\sigma_e > 2.5\ 10^4$, $0.1 \leq e_v \leq 0.2$, $d > 20$ μm, using $\gamma_{sl} \approx 0.27$ J/m^2 for $NaNO_3$, and taking $a = 0.675$ as the aggregate packing constant shows that for the stress range investigated it is indeed expected that $(a.\sigma_e/e_v) > (4\gamma/d)$. The observed behaviour is associated with indentation/truncation microstructures as well as rough grain boundary structures, suggesting solution/precipitation creep to occur with an island/channel grain boundary structure present at the contacts.

As explained previously, data obtained at strains lower than 10% are not in the present treatment because of the influence of frictional/ adhesive forces on load transmitted to the sample.

For $d < 20$ μm, a decrease of strain rate towards smaller grain size was observed (see Figure 3.8) and less strain was obtained compared to the larger grain size samples under otherwise the same conditions. Microstructural observations indicate some grain growth, but the final grain size can not explain the decrease in strain rate. At former grain contacts often ring-type structures were observed, suggesting some neck growth took place in the small grain size samples, even at medium to high stress conditions.

At high volumetric strains, i.e. > ~20%, the observed wet compaction behaviour for grain sizes > 20 μm still shows a grain size dependence of strain rate with an exponent close to -3. However, the sensitivity of strain rate to stress increases and the sensitivity to e_v deviates strongly from the model of equation (2.51) (see Figure 3.6). Explicitly, the exponent to e_v increases rapidly from 5 to more than 10, and near the end of some experiments it tends to ∞ as the strain rate approaches zero. The rapid decrease in strain rate coincides with the occurrence of closed, ring-type grain contact structures in contrast to the rough contacts observed at low e_v. This suggests that peripheral neck growth processes driven by surface energy forces become significant at these high strains, i.e. become competitive at increased contact area and lower contact stress. Many of the high stress (> 1 MPa) experiments effectively stopped creeping as the porosity approached 10-12%. Experiments at lower stresses stopped at higher porosities (lower strains). This is consistent with the notion that densification will stop ($\dot{\beta} \rightarrow 0$) when the driving force due to the applied stress ($a\ \sigma_e/e_v$) , in equation (2.51), approaches that due to surface forces ($4\gamma/d$). This would correspond to a situation of contact healing as the chemical potential of dissolved solid in the pores approach the mean solid potential within the grain boundary (see Chapter 2). An alternative explanation for the cessation of creep at large strains is simply that grain contact stresses become sufficiently low, peripheral neck- or island growth processes dominate over solution/precipitation creep.

Closed-rim features at former grain contacts were most frequently observed at large e_v (> 25%). Moreover, combinations of both (partly) developed rim or neck structures plus an internal rough grain boundary surface were observed at ~20% e_v, indicating maybe a transition from non-equilibrium solution/precipitation creep at lower strains to a neck-growth type of process at higher strains. However, it is also possible that rapid densification at the start of the experiments deposited material just outside the grain boundary, which subsequently became "accreted" into the contact rim.
For experiments with d< 20 μm, the same deviation from the model is observed as for the low to medium field described above. For experiments with an applied stress ≥ 1 MPa, volumetric strains obtained within 24 hours were > 20%. The microstructures observed are dominated by the closed ring-type of structures at former contacts (see Figure 3.13).

3.6.2 Determining the kinetic coefficient governing creep in the high stress regime

Combining the above points, it is inferred that between 10-25% compaction, deformation of the wet samples almost certainly occurred by grain boundary diffusion controlled solution/precipitation creep as described by equation (2.51), with no significant retarding effect due to the interfacial energy driving force term in the regime d ≥ 20 μm and $\sigma_e > 2.5\ 10^4$ Pa. At higher strains and longer times, however, it seems likely that neck growth and grain growth processes became dominant, pulling the system towards equilibrium, and leading to more complicated mechanical behaviour.

Having inferred that solution/precipitation creep, described by the model expressed in equation (2.51), applies to the experimental data in the range of experimental conditions described above, with the surface energy term being negligible, it is now possible to obtain an estimate of the effective grain boundary diffusivity, $Z^* = CDS$. This has been done by fitting equation (2.51) to the experimental strain rate data to for the region $e_v \leq 20\%$, taking $4\gamma/d = 0$. The data used were for the 25, 39, 63, 104 and 250 μm grain size fractions, at applied stresses of $3\ 10^5$ Pa, 1 MPa and 4.9 MPa and volumetric strains 10% and 20%. Values obtained for Z* are 5.7 ± 4.10^{-20} m^3/s. This agrees well with the value of Z^* of 10^{-19} - 10^{-20} m^3/s obtained for solution/precipitation creep in NaCl (Spiers et al 1990, Schutjens 1991 and Spiers and Brzesowsky, 1993), and increases confidence in the present interpretation. Z* shows no dependence on stress or grain size in the range calculated, but at e_v = 20% is mostly a little smaller (less than a factor two) than at e_v = 10%. The active grain boundary thickness $S = \delta(1-\alpha)$, where δ is the grain boundary width

and α the fraction of islands, is difficult to establish from microstructural observations after densification. Some separated contacts show roughnesses on the scale of a few hundred nm, suggesting an island-channel structure with this thickness. However larger and smaller amplitude roughness also occurs. Therefore further analysis of the kinetic coefficient, Z^* , is not attempted.

3.6.3 The low stress regime

At stresses < 3 10^4 Pa and grain sizes < 27 μm, the observed compaction behaviour shows anomalously low strain rates compared with the high stress behaviour, with a stress exponent rapidly increasing towards low stresses (see Figure 3.7). Moreover, a positive grain size dependence of the strain rate was observed, instead of the exponent of -3, observed for solution/precipitation creep in the high stress regime. Most of the small stress experiments stop (become unmeasurably slow) long before full densification is attained. This type of behaviour is consistent with that predicted by the solution/precipitation model (equation 2.51), when the surface energy term ($4\gamma/d$) approached the stress term (a σ_e/e_v) in magnitude. Indeed calculations of the relative magnitude of the terms, using γ=0.27 J/m^2 shows that the former can not be neglected in this case. On the other hand, neck- or grain growth processes could partially be responsible for the anomalous low creep rates seen at low stress and fine grain size.

The microstructures observed in the low stress samples provide some evidence for solution/precipitation creep. However most sample fracture surfaces show ring-type neck structures at grain contacts (see Figures 3.13, 3.15 and 3.21), both closed and partially open. Furthermore, grain growth was observed, as well as a change of grain shape from sub-spherical to euhedral (faceted) at applied stresses < 5 10^3 Pa. These samples attained very low strains (< 10%). The observed shape changes move the microstructure closer to equilibrium, from a high to low surface energy shape illustrating an important surface free energy contribution to mass transfer and that anisotropy of surface energy has an important influence on microstructure.

3.6.4 Comparison with criteria for pressure solution versus contact healing processes

In an attempt to identify more closely the reason for the anomalous behaviour seen in the low stress regime, the experimental results are now compared with the criteria for solution/precipitation creep and contact healing processes derived in chapter 2. In chapter 2, a map was constructed for the NaCl-brine system plotting these criteria in a space defined by the normal stress at contacts versus surface curvature radius. The criteria can be summarised as follows and are shown in Figure 3.24.

Criterion 1: Driving force for solution/precipitation creep → zero. The limiting condition here obtained from equation (2.51) is given

$$\frac{a\sigma_e}{e_v} = \frac{4\gamma_{sl}}{d} \quad \text{or} \quad \sigma_e = \frac{4\gamma_{sl}e_v}{a\,d} \qquad ((2.64))$$

Thus, when the surface energy term is significant, a yield stress must be overcome to make solution/precipitation creep possible at a finite rate. This yield stress, σ_e, is dependent on strain, on the value of γ_{sl}, and inversely dependent on the packing constant, a, and grain size. Note that replacing the grain size, d, by 2ρ, where in this case ρ expresses the radius of curvature of the grains at the pore walls, and substituting σ_n for $a\sigma_e/e_v$, the criterion can be written in (dimensionless) log form as

$$\ln\left(\frac{\sigma_n\Omega^s}{kT}\right) = \ln\left(\frac{\gamma_{sl}\Omega^s}{\rho kT}\right) + \ln 2 \qquad ((2.65))$$

Criterion 2: Limiting condition for neck growth versus undercutting. This is written

$$\frac{\gamma_{sl}}{\rho kT}\Omega^s\left(\cos\frac{\theta}{2} - \cos\frac{\theta_{eq}}{2}\right) = \frac{\Delta f^s}{kT} \qquad ((2.66))$$

where ρ is now the radius of curvature at the contact margin (Section 2.5.2). Recall that here θ_{eq} is the equilibrium dihedral angle under hydrostatic reference conditions. When Δf^s, the increase in internal energy, is assumed to reflect purely elastic strain energy at the contact margin,

then $$\Delta f^s \approx \frac{\sigma_n^2}{2E}\Omega^s \qquad ((2.67))$$

where E is the Youngs modulus. Criterion 2a for the elastic case can hence be written

$$\ln\left(\frac{\sigma_n \Omega^s}{kT}\right) = \frac{1}{2}\ln\left(\frac{\gamma_{sl}\Omega^s}{\rho kT}\right) + \frac{1}{2}\left[\ln\left(\frac{2E\Omega^s}{kT}\right) + \ln\left(\cos\frac{\theta}{2} - \cos\frac{\theta_{eq}}{2}\right)\right] \qquad ((2.68))$$

For dislocation stored energy being the dominant contribution to Δf^s,

$$\Delta f^s = (\rho_{disl} . W)\Omega^s \qquad ((2.69))$$

with

$$W = \frac{1}{2} G b^2 \qquad ((2.71))$$

where b is the burgers vector, ρ_{disl} is the dislocation density and G is the shear modulus (Humphreys and Hatherly, 1995; Hull, 1975 and Poirier, 1985).

and Criterion 2b for the dislocation case can be written as

$$\ln\frac{\sigma_n \Omega^s}{kT} = \frac{1}{2}\ln\frac{\gamma_{sl}\Omega^s}{\rho kT} + \frac{1}{2}\left[\ln\frac{G\Omega^s}{kT} + \ln\left(\cos\frac{\theta}{2} - \cos\frac{\theta_{eq}}{2}\right)\right] \qquad (2.73)$$

A third Criterion was derived in chapter 2, namely the healing of a grain boundary containing an island/channel structure due to island-growth within the grain boundary. The appropriate radius of curvature is then the curvature of the island/island contacts in the grain boundary, approximated by the grain boundary width. Although no definite conclusion was drawn with respect to the thickness of the island and channel model in the results Section, a range of 0.1-1.0 μm is chosen, based on the rough contacts of the microstructures, to obtain an order of magnitude calculation for the Criteria 3a and 3b. When Δf^s, the increase in internal energy, is assumed to reflect purely elastic strain energy at the contact margin, then using the same approach as for Criterion 2a, Criterion 3a becomes

$$\ln\left(\frac{\sigma_n \Omega^s}{\alpha kT}\right) = \frac{1}{2}\ln\left(\frac{\gamma_{sl}\Omega^s}{\rho_{isl} kT}\right) + \frac{1}{2}\left[\ln\left(\frac{2E\Omega^s}{kT}\right) + \ln\left(\cos\frac{\theta}{2} - \cos\frac{\theta_{eq}}{2}\right)\right] \qquad (2.79)$$

where ρ_{isl} is the radius of curvature of the island-island contacts and the stress is intensified by the fraction of island contacts with respect to the full contact area.

When the dislocation stored energy is the dominant contribution to Δf^s, equation (2.67) is used with the modified contact stress σ_n/α, and following the derivation of Criterion 2b, Criterion 3b can be written

$$\ln\frac{\sigma_n \Omega^s}{\alpha kT} = \frac{1}{2}\ln\frac{\gamma_{sl}\Omega^s}{\rho kT} + \frac{1}{2}[\ln(\frac{G\Omega^s}{kT}) + \ln(\cos\frac{\theta}{2} - \cos\frac{\theta_{eq}}{2})] \qquad (2.80)$$

In Figure 3.24 three regions are plotted (boxes) which represent the experimental conditions defined in terms of grain contact stress, σ_n and radius of curvature ρ for the $NaNO_3$-brine experiments. It is assumed that the map constructed for the NaCl-brine system can be used for the $NaNO_3$-brine system because the material properties (notably the γ-value) and mechanical behaviour are very similar. In theory, if the experimental conditions would satisfy Criteria 1,2 or 3 during the present tests on $NaNO_3$, then densification would come to a halt. In practical terms, the cessation of creep in the present experiments corresponds to the point at which immeasurable strain rates are reached, i.e. $\dot{\beta}$ =8-9 10^{-8} s^{-1}, for this value of $\dot{\beta}$, the corresponding contact stress can be calculated using $\sigma_n \approx a\sigma_o/e_v$, for $e_v < 20\%$. For Criterion 2 the radius of curvature is approximated using $\rho \approx de_v/6$ (see chapter 2), for Criterion 3, ρ is approximated by the grain boundary width, while the radius of curvature for Criterion 1 is d/2. The resulting σ_n-ρ data corresponding to the condition $\dot{\beta} \rightarrow 0$ have been superimposed on the map with the Criteria and illustrated in Figure 2.25. The data are closer to Criterion 1 than Criterion 2 or 3.

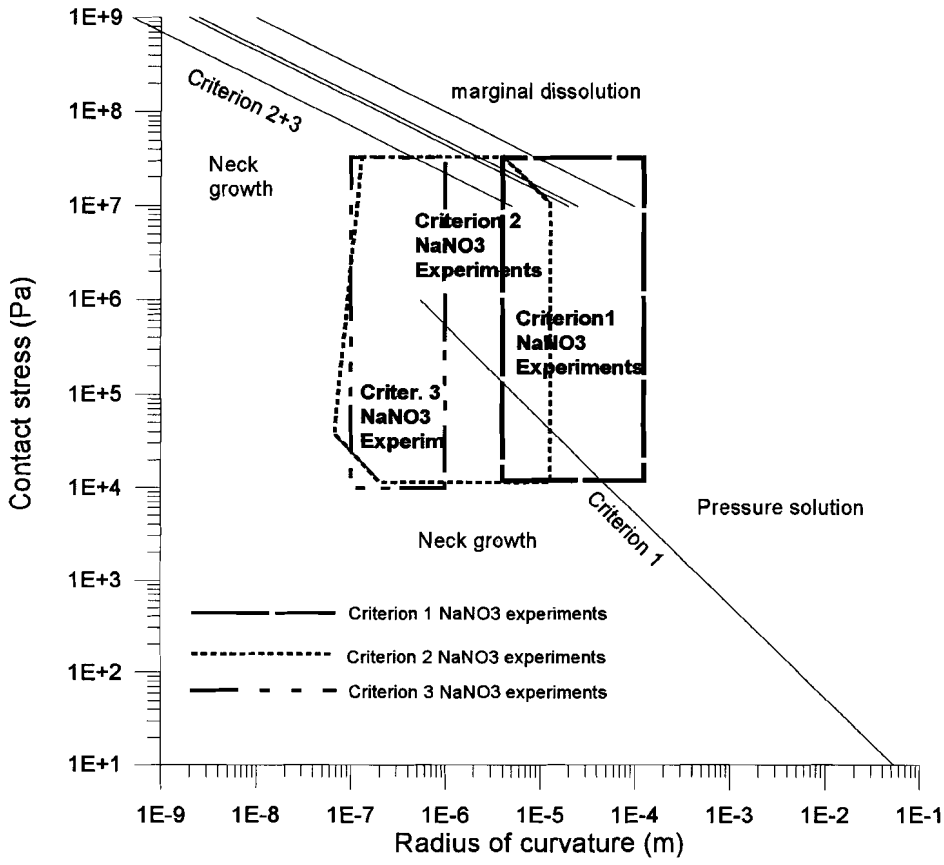

Figure 3.24 The Mass transfer mechanism map for NaCl indicating the Criteria 1and 2a +b and 3a+b. The map is drawn for γ=0.27 J/m^2. Superimposed are three boxes indicating the experimental conditions for the present $NaNO_3$-brine experiments.

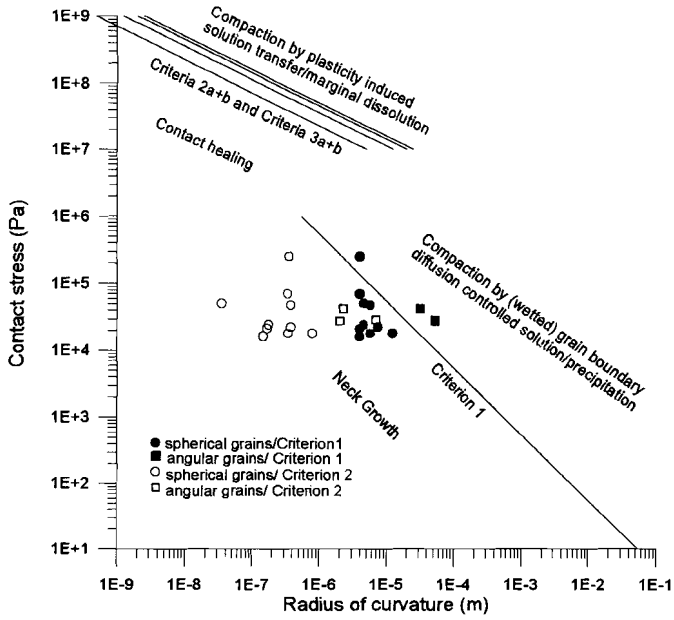

Figure 3.25. The mass transfer mechanism map with data plotted for the $NaNO_3$-brine experiments in which the strain rates decreased below $10^{-7}s^{-1}$. It can be seen that these experiments plot close to the conditions of Criterion 1.

Since Criterion 1 is observed to fit the best, an estimate of the possible yield stress value in Criterion 1, i.e. the stress for which $a\sigma_e/e_v=4\gamma_{sl}/d$ can be obtained. Strain rate vs. stress data obtained for $NaNO_3$ at low stress are plotted on a linear scale (Figure 3.26). The curves are not straight lines, but extrapolations near the origin give values of a finite " yield stress" at $\dot{\varepsilon}=0$. These intersection stress values obtained are plotted in Figure 3.27, drawn for $\gamma=0.27$ J/m^2. The approximate fit to Criterion1 further supports the model described by equation (2.51) for the case when the surface free energy term is no longer neglected. The observed non-linearity of the curves in Figure 3.26 could perhaps be explained by an additional dependence of the "yield term" on stress, suggesting that surface stress instead of surface free energy would be a more appropriate variable in the models. The observed small deviation from Criterion 1 in Figure 3.27 could, apart from non-linearity due to surface stress, be a result of differences in grain shape (sub-spherical $\leq$ 39 μm versus angular $\geq$39 μm grain sizes) or due to influences of some grain growth observed for the smaller grain sizes.

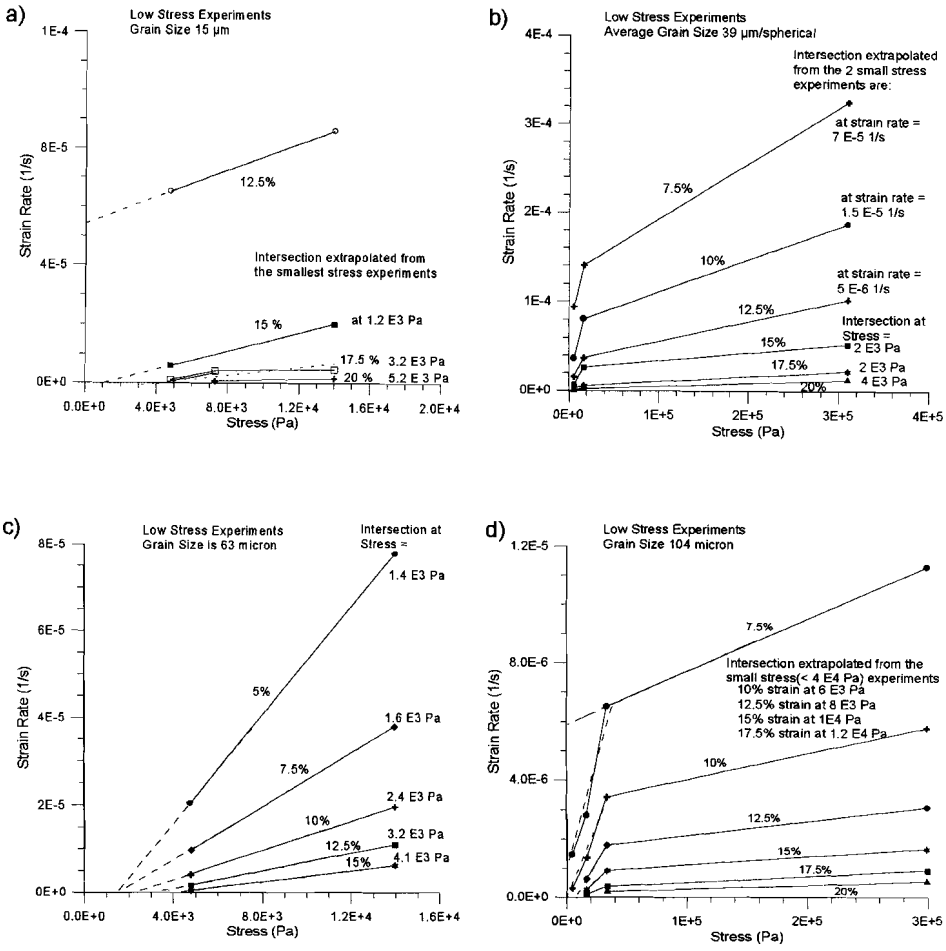

Figure 3.26 Typical linear strain rate versus stress diagrams for wet compacted $NaNO_3$ experiments for 15 (A), 39 (spherical batch)(B), 63 (C) and 104 (D) micron grain size fractions. Extrapolations from low stresses indicate whether the curves intersect the strain rate axis (at zero stress) or the stress axis (at strain rate is zero).

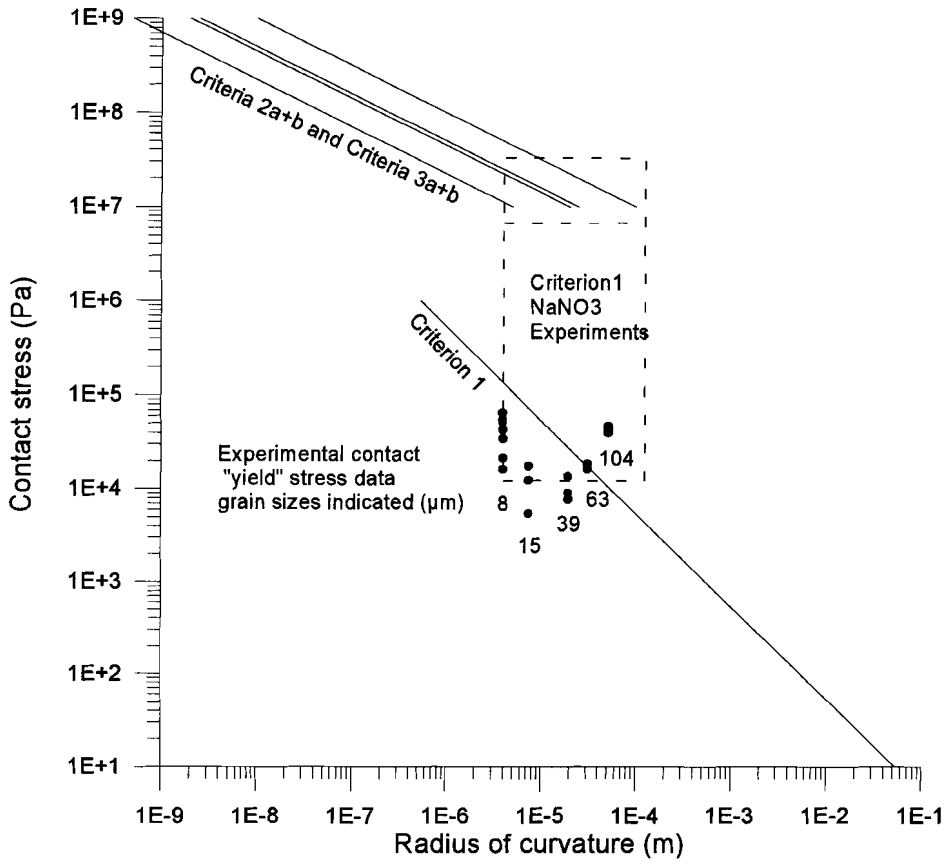

Figure 3.27. Intersection data from Figure 3.26 used for comparison with Criterion 1. A) Determination of γ_{sl} from the slope in the graph for grain size fractions 15, 39, 63 and 104 μm. B) Determination of γ_{sl} from the slope in the graph for grain size fractions 8 μm for the different extrapolation stresses shown in Figure 3.26. C) Determination of γ_{sl} from the slope in the graph for all grain size fractions in A and B, now as a function of 1/d.

3.7 Summary and Conclusions

1) Uniaxial compaction creep experiments have been performed on fine grained (8-250 μm) $NaNO_3$ aggregates. Dry and oil-saturated material showed no significant creep. However, rapid creep occurred in the presence of an $NaNO_3$ solution saturated with respect to the unstressed granular $NaNO_3$ starting material.

2) At volumetric strains, e_v of 10-20 %, grain size, d> 20 μm and applied effective stress, $\sigma_e > 3\ 10^4$ Pa, the wet compacted samples showed compaction rates which were approximately proportional to the applied stress, to one over the cube of the grainsize, and to $1/e_v^{2-5}$ where e_v represents volumetric strain. This is roughly consistent with the solution/precipitation creep model derived in Section 2.4.1 for the case of grain boundary diffusion control when surface energy effects are negligible.

3)Unusual mechanical behaviour is observed for d<20 μm. The rate of densification decreases with decreasing grain size while for experiments with $\sigma_e < 4.10^4$ Pa a rapid increase in the stress sensitivity of strain rate is observed towards lower stresses. Order of magnitude calculations indicate that the surface energy term is no longer negligible.

4)Microstructural study of the wet samples showed evidence for solution/precipitation creep features (indentations, truncations and overgrowths), but also showed neck growth and grain growth suggesting an approach to microstructural equilibrium at long times, i.e. after the initial relatively rapid deformation of 20-30%. Distinct differences in microstructure were observed between samples compacted at high/medium stress (> 0.3 MPa and low volumetric strains (< 20%)) and those compacted at low stress (< 4.10^4 Pa) or high/medium applied stress at high e_v (> 20%).

5) It is inferred that the initial rapid densification of the wet samples occurred by grain boundary diffusion controlled solution/precipitation creep, with neck and grain growth dominating at the low stress, fine grain size conditions and at large strain, described under conclusion (3) above. Estimation of $Z^* = \delta CD$, the effective grain boundary diffusivity associated with grain boundary diffusion controlled solution/precipitation creep in the high stress regime, gives a value of 2.10^{-18} m^3/s, which is in reasonable good agreement with the value of 1.10^{-19} m^3/s found for NaCl (Spiers et al 1990).

6) At low applied stresses (σ_e <4.10^4 Pa) and fine grain sizes (d < 20 μm), the microstructural observations and decelerating strain rates indicate that surface energy related driving forces become dominant. From experiments which became unmeasurably slow as well as from low stress data extrapolated to strain rate = 0 in linear stress versus strain rate graphs, it is inferred that Criterion 1 can be used to describe this behaviour. Criterion 1 describes the conditions when the driving force for solution/precipitation goes to zero due to an opposing surface energy force.

CHAPTER 4

DENSIFICATION OF FORSTERITE AGGREGATES AT LOW STRESSES

4.1 Introduction

An understanding of the high-temperature deformation mechanisms operative in olivine is crucial in constraining the flow behaviour of olivine rocks in the mantle. Much experimental work has been performed on polycrystalline Mg-Fe olivine and dunite rocks (Carter and Ave Lallement, 1970; Post, 1973; Schwenn and Goetze, 1978; Chopra and Paterson, 1981, 1984; Cooper and Kohlstedt, 1984 and Borch and Green, 1989) as well as on pure forsterite (Mg_2SiO_4) (e.g. Relandeau, 1981; Karato et al., 1986 and McDonnell, 1997) under a wide range of temperature, grain size and pressure conditions. However, relatively little rheological data is available under the low differential stress conditions generally thought to prevail in the mantle. Estimates of upper mantle differential stresses obtained from earthquake and gravitational data (see Stocker and Ashby, 1973) and microstructural studies (Mercier, 1980) give global values which fall between 0.1 and 20 MPa. Stocker and Ashby (1973) state that local stresses could be higher, up to 50 MPa, and Mercier's estimates include some higher stresses (up to 45 MPa) associated with specific tectonic settings, e.g. the uppermost mantle beneath continental extension regions (Mercier,1980). However for the bulk of the mantle 0.1-20 MPa is considered the best estimate (Stocker and Ashby, 1973).

Summarising the conclusions of previous experimental studies, dislocation creep is the dominant deformation mechanism in high density olivine materials (porosity < 7%), at grain sizes > 25 micron, differential stresses > 10 MPa, strain rates > 10^{-7} s^{-1} and at temperatures < 1773 K (1500 °C) (e.g. Schwenn and Goetze, 1978; Carter and Ave'Lallement, 1970; Chopra and Paterson, 1986; Borch and Green, 1989 and Hirth and Kohlstedt, 1995a). However, at finer grain sizes, higher porosities or higher temperatures, several studies indicate a change of mechanism towards diffusion dominated creep (Relandeau,1981; Schwenn and Goetze, 1978; Karato et al., 1986 and Hirth and Kohlstedt, 1995). Recently, much attention has been given to the influence of water in olivine systems, with and without melt (Chopra and Paterson, 1984; Hobbs, 1984; Mackwell et al., 1985; Karato, 1986; Rutter and Brodie, 1988; Bai and Kohlstedt, 1992;

Hirth and Kohlstedt, 1996 and McDonnell, 1997). When water is present, both dislocation and diffusion creep are enhanced via accelerated intra-granular- and/or grain boundary diffusion (Karato et al., 1986 and McDonnell, 1997). In this thesis, attention will be restricted to the dry olivine system. Note that experimental data previously available for low differential stresses (e.g. 0.1 - 10 MPa), is limited and insufficient to establish whether diffusion creep would become dominant at these low differential stresses under bulk mantle conditions.

Aside from effects of water, the presence of melt- or vapour-filled porosity in an aggregate can also provide easy pathways for diffusion (e.g. Ramahan, 1995 and Poirier, 1985). Due to enhanced grain boundary and pore diffusion, densification of porous aggregates containing a melt or vapour phase is not directly comparable with deformation of dense aggregates. However, comparison of densification experiments on porous forsterite aggregates with appropriate theoretical models can be regarded as a means of gaining basic knowledge on grain volume-, grain boundary- and pore/surface diffusion (cf. Spiers et al., 1990). This can subsequently be used to predict the behaviour of both fully dense and partially molten olivine materials and corresponding regions of the mantle. Moreover, comparison of experimental data for olivine/melt systems with data for porous olivine/vapour samples (e.g. Cooper and Kohlstedt, 1984, 1986) can provide insight into the effects of a vapour phase compared to a melt phase present in the pores. This would be useful for the interpretation of experimental studies of porous olivine aggregates and their comparison with natural dense olivine rocks. Several earlier studies on diffusion creep in granular synthetic and naturally derived olivine aggregates (e.g. Relandeau,1981; Cooper and Kohlstedt, 1984 and Schwenn and Goetze,1978), have investigated relatively high porosity (> 10%-35%) systems with and without a melt phase. In interpreting the results, the effect of the vapour and surface diffusion in the pores was neglected. However, the role of fast diffusion paths due to the presence of porosity (whether melt-filled or vapour filled) can only be studied by comparison with experiments on fully dense samples or, alternatively, by establishing the relative importance of surface diffusion, evaporation/condensation or solution/precipitation and/or diffusion in the melt phase compared to lattice -plus (solid-solid) grain boundary diffusion.

It was shown in Chapter 3 that, at the low grain sizes and stresses favouring fluid assisted diffusion creep, surface energy can provide a significant driving force influencing the densification behaviour of porous aggregates as well as pore geometry. The results were compared with microphysical models derived in Chapter 2 for densification and grain

contact (neck) growth by solution/precipitation transfer. In the models both surface energy and stress were considered as driving forces. Here, the models will be adjusted for high temperature conditions, taking solid-state diffusion and surface diffusion (previously neglected) into account as possible mass transport mechanisms alongside grain boundary and pore phase diffusion processes. The resulting models are tested against experiments on granular forsterite aggregates without a melt phase being present.

The ultimate aim is to enable a comparison between the dry (no melt) forsterite system to be studied in this chapter with a forsterite plus partial melt system, to be investigated in the next chapter. The main question with respect to this comparison is if and how the presence of a melt phase influences diffusion creep mechanisms and pore microstructure. Some previous work suggests that the direct effect of a melt phase on olivine rheology is minor since it merely occupies the triple junctions, replacing a part of the solid/solid grain boundary diffusion path by a faster melt-filled diffusion path (Cooper and Kohlstedt, 1984,1986; Waff and Bulau, 1982; Watson et al, 1990). However, recent studies have shown the occurrence of melt along flat grain boundaries of olivine, which has been explained by anisotropy of the surface free energy (Waff and Faul, 1992 and Faul, 1997) or by stress-induced wetting (Jin et al, 1994). Also, Hirth and Kohlstedt (1995b) found different mechanical behaviour for samples containing relatively small amount of melt (< 5%) and larger (> 5%) amounts of melt.

In this chapter, uniaxial compaction experiments will be described, performed on fine grained (1-25 μm) granular forsterite aggregates at high temperature (1663 - 1743 K or 1390-1470 °C, i.e. T/T_{melt}= 0.77-0.81) and low applied stresses (0.1 - 6.3 MPa) in the absence of melt. The questions addressed are

1) Is diffusion creep the dominant densification mechanism over dislocation creep under the imposed conditions? If so, what is the detailed mechanism (i.e. the relative importance of solid state diffusion versus faster diffusion path mechanisms) and what are the values of the controlling kinetic parameters?
2) Do surface energy effects become important under the conditions investigated, and if so, do they enhance or inhibit creep (densification versus neck growth processes)?

The mechanical data obtained were found to be fully consistent with diffusion creep as the dominant densification mechanism under the conditions investigated. However, surface energy effects, exert an important influence on densification behaviour and pore-microstructure at stresses < ~2 MPa.

4.2 Theoretical background

4.2.1 Driving force and mass transfer paths at high temperature

Models derived for stress-driven densification, neck growth and pore reconfiguration in a porous aggregate containing a solution phase, described in chapter 2 and tested in chapter 3, must be modified when applying them to a porous aggregate with vapour-filled pores at high temperature. This is because alternative mass transport paths become feasible at high temperature, although the driving forces remain the same. Consider the two-grain geometries illustrated in Figure 4.1. Neglecting the possibility of chemical reactions and assuming gradients in the Helmholz free energy of the solid to become negligible at the high temperatures considered (i.e. $\Delta f^s=0$), the two principal driving forces for mass transfer in such a system are (Coble, 1970):

1) the reduction of total surface free energy, which, assuming the specific surface free energy to be isotropic, results in mass transport from convex solid surfaces (positive curvature) to flat or negatively curved surfaces.
2) when a stress is applied, the stress related driving force ($\Delta\sigma_n\Omega^s$) which results in mass transfer from points of relatively high intergranular normal stress (σ_n) to stress free pore walls (Ω^s being the molecular volume of the solid).

The high temperature mass transfer processes, as indicated in Figure 4.1, are addressed in detail in the materials science literature, especially the sintering and hot-pressing literature which specifically include the role of surfaces. Sintering can be defined as the process by which powders are consolidated into strong polycrystalline aggregates by heating (Coble and Burke, 1963). During sintering many changes such as neck growth occur and under most circumstances fine-grained powders densify to some degree under the action of a reduction in surface free energy. The process of hot pressing involves the surface energy driving force but also the driving force due to an applied stress. For a review of sintering and hot-pressing processes the reader is referred to Rahaman (1995), German (1996) and Kingery et al. (1976).

The five different matter transport paths indicated in Figure 4.1 are described below. Some of the mass transport mechanisms indicated lead only to neck growth (1-3), as a result of surface energy forces related to gradients in surface curvature. Others lead to densification of a polycrystalline sample (4 and 5) under the action of either surface curvature gradients or intergranular stress.

1) Surface diffusion involves the motion of vacancies and ad-atoms on the crystal surface. The process is thought to be confined to a thin surface layer of 1-2 atomic diameters thick (0.3-0.5 nm). The activation energy for surface diffusion is expected to be less than for lattice diffusion (fewer bonds need to be broken) and therefore the relative importance of surface diffusion increases with decreasing temperature.
2) Volume- or lattice diffusion via mass transfer path 2) involves vacancy diffusion due to a gradient in surface curvature, from the negatively curved neck region to positively curved grain/pore interfaces, or the equivalent mass transfer in the opposite direction.
3) Evaporation/condensation occurs at the surface and diffusion of mass now occurs through the vapour phase. The mass transfer rate is not only dependent on the driving force and the activation energy, but also depends on the gaseous environment which determines the equilibrium vapour pressure .
4) Grain boundary diffusion due to a stress- or surface energy related driving force is a densifying mechanism involving mass transfer from the grain boundary area to the pore region. The grain boundary is a region of lattice mismatch and disorder so that the activation energy for grain boundary diffusion is expected to be lower than for lattice diffusion.
5) Densification can also be achieved through volume (lattice) diffusion when the mass transfer is from (or near) the grain boundary to the pore walls. In general, transport through the grain boundary is expected to be faster, but at sufficiently high temperatures the contribution of lattice diffusion can be significant (Rahaman, 1995).

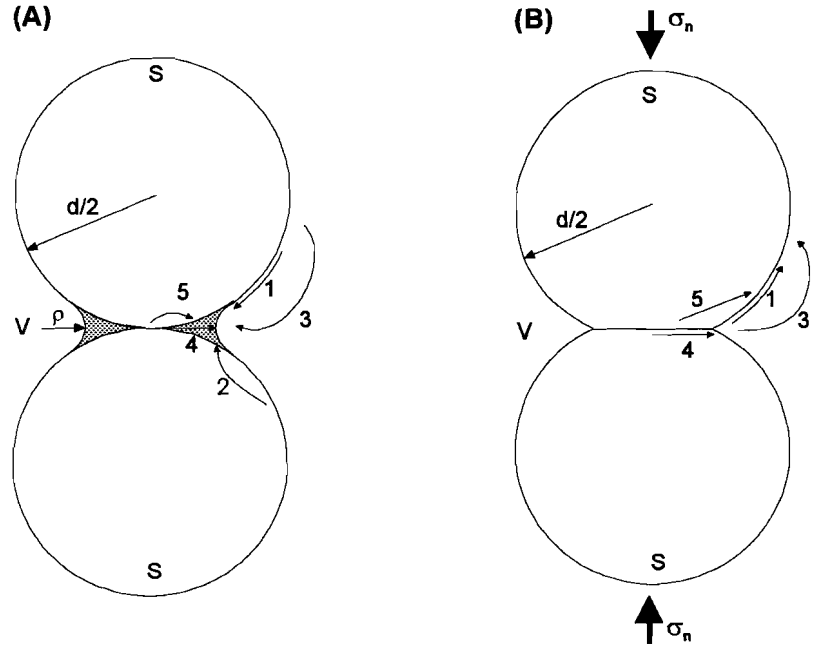

Figure 4.1 Five different matter transport paths are indicated for two different grain-to-grain geometries. (A) Neck growth and densification resulting from the surface energy related driving force due to curvature gradients. (B) Densification resulting from the driving force due to an applied stress. Mass transport paths indicated are 1) surface diffusion 2) lattice diffusion (from the surface) 3) evaporation/condensation (transport through the vapour phase) 4) grain boundary diffusion 5)lattice diffusion (from the grain boundary). In case (A) mechanisms 1-3 lead only to neck growth, while mechanisms 4-5 lead to densification in geometry. In case (B) the mass transport paths indicated all contribute to densification because the applied stress driving force is considered larger than the surface energy driving force, otherwise the mass transfer along path 1 and 3 would be in the opposite direction.

For the above diffusion processes, it is often stated that the diffusion coefficients for lattice diffusion, D_l, grain boundary diffusion, D_{gb}, and surface diffusion, D_s increase in the order $D_l < D_{gb} < D_s$, and that the corresponding activation energies vary as $Q_l > Q_{gb} > Q_s$ (Rahaman, 1995). The rate of evaporation/condensation transport is very much dependent on the type of material and gaseous environment. For most materials, sintered or hot-pressed in air, evaporation/condensation transport is relatively slow compared with the other transfer paths and therefore often ignored. The relative contribution of dislocation creep will mainly depend on the applied stress and grain size, with the activation energy being larger than for grain boundary diffusion mass transfer. Thus, at

high homologous temperatures, low stresses and fine grain sizes, diffusion mechanisms prevail in oxide materials for surface-energy and/or stress-induced driving forces.

All mechanisms shown in Figure 4.1 lead to an increase of the grain-to-grain contact area during sintering and hot-pressing. A very important difference compared with solution phase transport at low temperature is that at high temperature the non-densifying neck-growth processes can occur simultaneously with the densifying mechanisms, without one or the other coming to a halt. This is a direct result of the operation of solid-state diffusion processes (lattice- and grain boundary diffusion) which do not require the grain boundary to contain a second phase (liquid) in order for densification to take place. Although densification at high temperature will not come to a halt when neck-growth processes occur, it will be slowed down because the neck-growth generally reduces the driving force for densification (i.e. reduces curvature gradients and intergranular normal stress) as well as increasing the diffusion path length. Other processes such as grain growth and grain boundary migration are also facilitated by high temperature. Hence the free energy of the system can be reduced by these alternative processes which also reduce the driving force for densification (Rahaman, 1995).

4.2.2 Models

Models will now be developed for sintering and hot-pressing involving high temperature diffusion processes, taking both surface energy related driving forces and stress related driving forces into account. The derivation represents an extension of the models given in Chapter 2, to the high-temperature case. An important difference compared with previous work in the sintering and hot pressing literature (e.g. Coble, 1967; Kingery et al, 1976 and Rahaman, 1995) is that the interfacial energies of both free surfaces and grain boundaries are taken into full account. At the high temperature case considered, it is assumed that gradient in Δf^s (the internal Helmholz free energy) can be neglected.

4.2.2.1 Densification processes driven by stress and interfacial energy

The geometry as given in Figure 4.1a has been used in the derivation of previous models for pressure-less sintering and hot-pressing (i.e. sintering under stress) assuming that grain boundary energy is negligible. Essential is the presence of the negatively curved region, or neck, at the rim of the grain boundary intersecting with the pore. This geometry

has been experimentally verified during the initial stage of sintering (although not always present or heterogeneously developed (Rahaman, 1995)). The resulting driving force for grain boundary and/or volume diffusion of vacancies, hence of solid mass, during hot pressing as first derived by Coble (1967) is given

$$\Delta\mu \approx (\sigma_n + \frac{2\gamma_{sv}}{\rho})\Omega^s \qquad (4.1)$$

where $\Delta\mu$ is the difference in chemical potential between grain contacts and neck margins, σ_n is the intergranular applied stress, γ_{sv} is the solid/vapour interfacial energy, ρ is the radius of curvature of the neck region (Figure 4.1a) and Ω^s is the molecular volume of the solid. Note that when the applied stress tends to zero, a driving force for densification is still present, but this is reduced to the surface free energy related term alone.

When specifically taking the grain boundary energy into account, and allowing a general (non-equilibrium) dihedral angle to be present at the grain boundary/pore intersection, then the driving force for transport from grain contacts to neck margins is reduced. This reduction corresponds to the work which must be done to replace solid/vapour interface by grain boundary with a finite specific energy. Following the derivation of the relevant surface forces employed in Chapter 2, the modified driving force is written

$$\Delta\mu \approx (\sigma_n + \frac{2\gamma_{sv}}{\rho}(\cos\frac{\theta}{2} - \cos\frac{\theta_{eq}}{2}))\Omega^s \qquad (4.2)$$

where θ_{eq} is the equilibrium dihedral angle under hydrostatic conditions. When grain boundary diffusion is the rate controlling process, $\Delta\mu \approx \Delta\mu_{diff}$ where $\Delta\mu_{diff}$ is the potential drop associated with the diffusion mechanism. Inserting this driving force into Ficks law, the flux of material through the grain boundary is obtained and yields for the densification rate:

$$\dot{\beta}_{gb} = \frac{2D_{gb}\Omega^s}{kTx^2d}(\sigma_n + \frac{2\gamma_{sv}}{\rho}(\cos\frac{\theta}{2} - \cos\frac{\theta_{eq}}{2})) \qquad (4.3)$$

Here D_{gb} is the self diffusion coefficient of the rate limiting element of forsterite through the grain boundary times the grain boundary width, δ, $\dot{\beta}$ is the rate of densification, d is the grain size, x the radius of the two-grain contact, k is Boltzmanns constant and T is temperature.

Using the geometrical approximations $\rho \approx x^2/2d$ for small x, where x is the radius of the neck (Coble, 1970) and assuming x to be mainly determined by densification so that employing $x^2 \approx d\, e_v/6$, where e_v is the volumetric strain, we obtain

$$\dot{\beta}_{gb} = \frac{12D_{gb}\Omega^s}{kTd^3e_v}(\sigma_n + \frac{24\gamma_{sv}}{de_v}(\cos\frac{\theta}{2} - \cos\frac{\theta_{eq}}{2})) \qquad (4.4)$$

Note the above approximations for ρ and x are only valid as long as densification is dominant over neck growth and x is small (small strains).

When assuming volume diffusion to be the dominant mechanism and diffusion to be the rate limiting step, then the approach of Coble (1970) is followed, only now inserting the modified driving force (equation 4.2) into the general derivation of the Nabarro-Herring or lattice diffusional creep equation (Coble, 1970). The resulting model for densification rate controlled by volume diffusion is

$$\dot{\beta}_l = \frac{2D_l\Omega^s}{kTd^2}(\sigma_n + \frac{24\gamma_{sv}}{de_v}(\cos\frac{\theta}{2} - \cos\frac{\theta_{eq}}{2})) \qquad (4.5)$$

where D_l is the lattice self diffusion coefficient of the slowest diffusing species in the solid. The same approximations for ρ and x have been used as in the grain boundary diffusion case. Note that in the above models (equation 4.4 and 4.5) the term containing γ_{sv} will be positive when $\theta < \theta_{eq}$ and negative when $\theta > \theta_{eq}$.

4.2.2.2 Neck growth processes

When either surface diffusion or evaporation/condensation is the dominant mass transfer mechanism, no densification can occur and only neck growth will take place. In general surface diffusion, evaporation/condensation and intergranular vacancy diffusion will go on simultaneously at some relative rate. When vacancy diffusion over the surface is much faster, this will be the rate determining step. The chemical potential drop between the free grain surface and the neck margin drives this diffusion, i.e. $\Delta\mu_{diff} \approx \Delta\mu$. Then using Fick's law and assuming an average diffusion path length of (πd/8 - x) the volume flux of material to the neck region can be obtained (Figure 4.1a). Here the diffusion path is assumed to be ¼ of the sphere circumference minus half the contact width, $\rho = x^2/2d$ and the area of precipitation is assumed to be restricted to the neck region (see also Chapter 2). The resulting model for neck growth with surface diffusion control is written

$$\dot{x}_{ng} = \frac{4\gamma_{sv} D_s \Omega}{\pi kT(x^2 - x_{cr}^2)} (\cos\frac{\theta}{2} - \cos\frac{\theta_{eq}}{2}) \qquad (4.6)$$

where D_s is the surface diffusivity, i.e., the self diffusion coefficient of the slowest diffusing species in the solid times δ_s, the surface layer thickness through which surface diffusion takes place. Note that the resulting rate of neck growth is the same as derived for diffusion controlled solution/precipitation transfer (see equation 2.42 in Chapter 2), with the diffusivity for surface diffusion replacing the diffusivity through the liquid phase, and with the solid/vapour interfacial energy used instead of the solid/liquid interfacial energy. Neck growth by evaporation/condensation follows a kinetic law analogue to that for precipitation controlled neck growth in a solid/liquid system (Chapter 2, equation 2.37), but is usually expected to be slower then surface diffusion controlled neck growth.

4.2.2.3 Densification with near equilibrium neck configuration

From examination of micrographs appearing in reviews on sintering and hot-pressing (e.g. Kingery et al., 1976 and Rahaman, 1995), it is questionable whether the negatively curved neck region is maintained after the initial sintering or hot-pressing stage, especially during hot-pressing. I suggest an alternative geometry, namely a near equilibrium neck geometry, be considered and tested experimentally. For the case when densification due to an applied stress dominates, because $\theta \approx \theta_{eq}$ (local equilibrium geometry), the cosine difference term in equation (4.2) falls to zero and the driving force for transport from contacts to pore walls is given

$$\Delta\mu \approx (\sigma_n - \frac{4\gamma_{sv}}{d})\Omega^s \qquad (4.7)$$

as derived for solid/liquid systems in Chapter 2. The resulting models for densification when $\theta \approx \theta_{eq}$ becomes

$$\dot{\beta}_{gb} = \frac{12 D_{gb} \Omega}{kTd^3 e_v} (\sigma_n - \frac{4\gamma_{sv}}{d}) \qquad (4.8)$$

for the case that grain boundary diffusion is the relevant transport mechanism and diffusion

the rate limiting step (cf. equation 4.3). For the case that volume diffusion is the dominant densification mechanism and diffusion the rate limiting step then (cf. Equation 4.5)

$$\dot{\beta}_{gb} = \frac{2D_l\Omega}{kTd^2}(\sigma_n - \frac{4\gamma_{sv}}{d}) \qquad (4.9)$$

Note that in equations (4.8) and (4.9), the γ-related term opposes densification. In equations (4.4) and (4.5) the surface energy term assists densification when $\theta < \theta_{eq}$ and opposes it when $\theta > \theta_{eq}$

4.3 Experimental Aspects

In this study, forsterite powders of grain sizes ranging from 1 to 25 μm were uniaxially hot-pressed (densified) at temperatures between 1390 and 1470 °C and stresses between 0.13 and 6.37 MPa. Of the 16 experiments performed, six were isothermal stress-stepping tests. One experiment was an isothermal constant-load test performed to obtain a reference creep curve over longer times, and three experiments were performed at constant load, cycling the temperature to determine an apparent activation energy. The remaining 6 experiments were performed to obtain samples for microstructural analyses, especially studying porosity and grain growth, at various (early) stages of the stepping procedure employed.

4.3.1 Starting Material and Sample Preparation

Finely powdered Mg-forsterite, typically 99% Mg_2SiO_4, was obtained from Cerac Inc. (Milwaukee, USA). The supplier's analyses of this high purity forsterite show the Mg-content to be 33.9% compared to 34.55 for the theoretical composition of forsterite and an impurity content of roughly 0.15 wt%, of which 0.03 wt% is Fe, 0.04% Al, B 0.01%, Ca 0.02%, Cr 0.02%, Cu 0.01%, Mn 0.003%, Mo 0.01%, Ni 0.02% and Sr 0.001%. The granular forsterite was separated in methanol to obtain different grain size fractions using conventional gravitational settling. The resulting fractions had average grain sizes and standard deviations of 1.5 ± 0.3 μm, 2.9 ± 0.5 μm, 5.1 ± 1 μm, 6.2 ± 1

μm, 8.1 ± 2 μm, 11.0 ± 2 μm, 15.4 ± 3 μm, and 20 ± 5 μm. These average particle sizes were determined by measuring the longest and shortest axes of individual grains on Scanning Electron Microscope (SEM) images. After separation, the various fractions were dried for 48 hours at 60 ^{0}C. In order to prepare individual samples for hot pressing or densification, approximately 1 gram was deposited into a steel die with an internal diameter of 10 mm and uniaxially cold-pressed, using a Carver hand-press. A maximum stress of 200 MPa was applied to the aggregate. The cold pressed samples typically had lengths between 6 and 7 mm, diameters of ~10 mm and porosities from 33 to 39%. The samples thus prepared were subsequently heated for 48 hours at 1300 $^\circ$C in air to anneal out any dislocation damage introduced during cold-pressing. During heating, no measurable changes in dimensions occurred. Examination of the heated samples showed that no grain growth occurred during heat treatment.

4.3.2 Experimental Apparatus

Stress-densification experiments were performed using a small scale set-up consisting of a uniaxial die plus loading pistons , as shown in the inset of Figure 4.2. This assembly was loaded using a programmable Instron Model 8500 testing machine, equipped with its own loading pistons and split furnace (maximum temperature 1773 K/ 1500 °C), all kindly made available at Hoogovens Ceramic Laboratory (IJmuiden, The Netherlands). The die, pistons and other parts indicated in the inset of Figure 4.2, were constructed using high purity alumina (Alsint). The (disposable) die was lined with thin Pt foil and also the pistons were topped with Pt-foil to avoid reaction between the forsterite sample and the alumina parts. The Instron furnace incorporates Super Kanthal 33 heating elements and controlled using a programmable Eurotherm 821 controller. The sample temperature was monitored and the furnace controlled using B-type (Pt30Rh-Pt6Rh) thermocouples, positioned outside and a few millimetres away from the die assembly. Temperature stability is ± 2 °C. No attempt was made to control the atmosphere within the furnace, so that the pores of the samples were air/vapour filled. The displacement of the lower piston into the die is measured remotely using a LVDT located in the water-cooled part of the lower Instron piston (Figure 4.2). This LVDT has a range of ± 5 mm and an accuracy of 0.02%. It was calibrated using a specially designed micrometer fitting placed into the Instron set-up. Stiffness calibration runs were performed using an alumina dummy to determine the distortion versus the force characteristics of the entire apparatus at

operating temperature. No permanent creep of the alumina parts took place and the small elastic strain occurring during loading and unloading were reproducible. Force, displacement and temperature signals were logged using the Instron computer logging/control system and IEEE-488 interface, with a 16-bit resolution and a sampling cycle rate of up to 5.1 kHz.

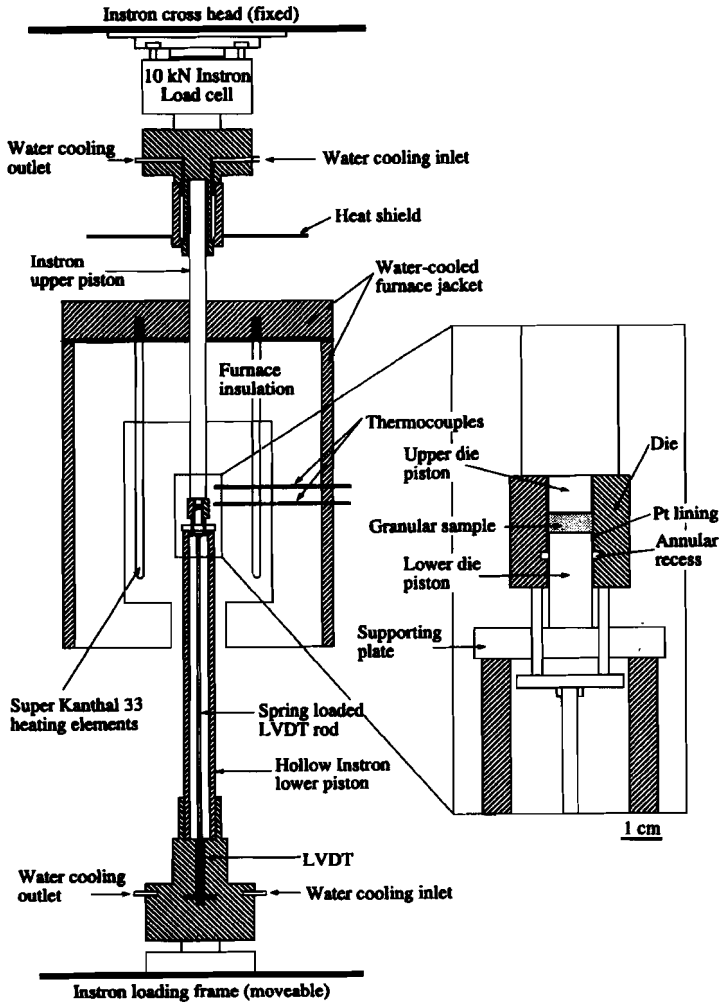

Figure 4.2 Schematic diagram showing the experimental Instron set-up and small scale die assembly. Note that the die assembly is inverted with respect to its orientation during preparation.

4.3.3 Testing Procedure and Data Processing

In each experiment, the sample, prepared as described above, was polished, where necessary, to fit the die diameter of 9.9 mm and the complete die assembly was then placed in the Instron loading frame. The samples were heated to 1743 K (1470 °C), then left at this temperature for 1 hour to equilibrate before any load was applied. The Instron lower piston was then advanced upward until the upper Instron piston was brought into contact with the die assembly. Loading was always performed to an initial compressive stress of 6.3 MPa, under computer control, ramping the load linearly over a 2 minute period. A few experiments were terminated at the end of the first loading stage (achieving the applied stress of 6.3 MPa) to examine grain size, sample length, sample diameter and porosity. No grain growth was observed, and in all cases the sample filled the diameter of the die completely while porosity decreased or increased to a reproducible value of 33 ± 2%. This point, i.e. the point at which the ramping period was completed and 6.3 MPa was applied to the sample, was chosen as starting point of the hot-pressing or densification experiment (t=0). The associated length and starting porosity at this time are subsequently referred to as the starting length and starting porosity of the samples and used as such for further data processing.

After the initial loading stage of each experiment was completed, the compaction creep was monitored as function of time, with the computer logging a datapoint every 6 or 12 seconds. Both constant stress and stress-stepping experiments were performed, using applied stresses in the range 0.1 - 6.3 MPa. Stress stepping was performed in the downward direction from 6.3 MPa to 3.8 MPa, 1.9 MPa, 1.3 MPa, 0.95 MPa, 0.64 MPa, 0.38 MPa and sometimes further to 0.26 MPa and 0.13 MPa, finally stepping up again to 6.3 MPa. Nine stepping tests were done in all. This included three combined stress and temperature stepping tests, performed using three different grain sizes. All stepping-tests performed are listed in Table 4.1, along with the experimental conditions.

Tests were terminated by switching the furnace off and keeping the sample loaded during (unassisted) cooling. More rapid quenching was impossible because both heating elements and ceramic alumina parts are very sensitive to thermal shock. After 3 minutes the temperature had dropped by 150 °C to 1320 °C. After 17 minutes, 1050 °C was reached, and after another 13 minutes (~ 30 minutes cooling under load) at a temperature of about 1000 °C (1273 K), the load was removed and the die set-up was left in place to cool down to room temperature overnight. Finally, the small scale set-up (figure 4.2) was

taken out, the die was sawn open and the final length of the sample was measured for control purposes. The sample was then impregnated with epoxy resin to allow sections to be prepared for optical microscopy as well as SEM (Scanning Electron Microscopy) and TEM (Transmission Electron Microscopy) study.

Volumetric strain versus time data were calculated directly from the displacement versus time records after corrections for apparatus distortion and thermal expansion. A running least squares fitting method was used to smooth the data obtained from each experiment and to reduce the densely spaced data stream to a set of several hundred points. Subsequently, strain rates were calculated for each experiment, and each constant stress-step, using the 3-point central difference method applied to the reduced data-set. This enabled the dependence of the strain rate on stress, strain (hence porosity) and temperature to be evaluated.

4.3.4 Microstructural analysis

Microstructural analysis was carried out on all starting powder fractions, on fractured sample fragments obtained after sintering and hot pressing, and on thin sections of epoxy-impregnated hot pressed samples. This was done using optical microscopy, Scanning Electron Microscope (SEM) and Transmission Electron Microscopy (TEM) performed in combination with detailed chemical analysis by Electron X-ray Diffraction (EDS) under the SEM and TEM, as well as separate X-ray diffraction (XRD) and thermal analysis performed on powdered sample material (DTA/TGA). For the SEM-work, polished thin sections were prepared (10 to 15 μm thick) and studied first by means of transmission optical microscopy. The thin sections were then etched for 1 minute in 10% HF, carbon coated and studied under the SEM. Also, TEM foils were prepared from 4 samples (1ol3 grain size 1.5 μm), 5ol13 (3 μm), 5ol6 (5 μm) and 5ol12 (8 μm)). TEM-sample preparation, involved first ion-beam thinning of slices of material prepared as thin sections, approximately 30 μm thick. After perforation the samples were coated with a thin layer of carbon, to avoid charging during observation.

Experiment porosity (φ)	Grain size (μm) Maximum Strain (e_v)	Temperature	Stress (steps) (MPa)	datapoints (•) at indicated strains (extrapolated (o)) volumetric strain 7.5%	12.5%	20%
1ol3 φ_{start}=0.32 φ_{end}=0.26	1.5 maximum e_v=7.5%	1470 ^{0}C/ 1743 K	6.3 3.8 1.9 1.3 0.95 0.65 0.38 6.3	o o o o o o o o		
5ol13 φ_{start}=0.3 φ_{end}=0.09	3 maximum e_v=22%	1470 ^{0}C/ 1743 K	6.3 3.8 1.9 1.3 0.95 0.65 0.38 0.26 6.3	• • 	o o • o 	 o o o o • •
5ol15 φ_{start}=0.31 φ_{end}=0.10	3 maximum e_v=22.1%	1470 ^{0}C/ 1743 K 1470 ^{0}C/ 1743 K 1430 ^{0}C/1703 K 1390 °C/1663 K 1470 ^{0}C/ 1743 K 1470 ^{0}C/ 1743 K 1430 ^{0}C/1703 K 1390 °C/1663K 1470 ^{0}C/ 1743 K	6.3 3.8 1.3 1.3 0.95 0.64 0.38 0.38	• o 	 • 	 o o
5ol6 φ_{start}=0.338 φ_{end}=0.11	5 maximum e_v=25.0%	1470 ^{0}C/ 1743 K	6.3 3.8 1.9 1.3 0.95 0.64 0.38 0.26 0.13 6.3	o o 	o • o o	 o o o o o o o

Experiment porosity (φ)	Grain size (μm) Maximum Strain (e_v)	Temperature	Stress (steps) (MPa)	datapoints (•) at indicated strains (extrapolated (o)) volumetric strain 7.5%	12.5%	20%
5ol8	6	1470 ^{0}C/ 1743 K	6.3	•	o	
			3.8	o	o	
		1470 ^{0}C/ 1743 K	1.3		o	o
		1430 ^{0}C/1703 K				
φ_{start}=0.33	maximum	1390 °C/1663 K				
φ_{end}=0.15	e_v=20.5%	1470 ^{0}C/ 1743 K	1.3		o	o
		1470 ^{0}C/ 1743 K	0.38			o
		1430 ^{0}C/1703 K				
		1390 °C/1663 K				
		1470 ^{0}C/ 1743 K	0.38			o
5ol2	8	1470 ^{0}C/ 1743 K	3.8	•	•	•
φ_{start}=0.327	maximum					
φ_{end}=0.099	e_v=25.2%					
5ol12	8	1470 ^{0}C/ 1743 K	6.3	o		
			3.8	•		
			1.9	o		
			1.3			
φ_{start}=0.328	maximum		0.95		o	
φ_{end}=0.22	e_v=13.7%		0.65		o	
			0.38		o	
			0.26		•	
			6.3		o	
5ol14	11	1470 ^{0}C/ 1743 K	6.3	o		
			3.8	o		
		1470 ^{0}C/ 1743 K	1.3	•		
		1430 ^{0}C/1703 K				
φ_{start}=0.35	maximum	1390 °C/1663 K				
φ_{end}=0.28	e_v=8.8%	1470 ^{0}C/ 1743 K	1.3	o		
		1470 ^{0}C/ 1743 K	0.38	o		
		1430 ^{0}C/1703 K				
		1390 °C/1663 K				
		1470 ^{0}C/ 1743 K	0.38	o		
5ol11	15	1470 ^{0}C/ 1743 K	6.3			
			3.8	o		
φ_{start}=0.33	maximum		1.9	o		
φ_{end}=0.27	e_v=7.5%		1.3	o		
			0.95	•		

5oil φ_{start}=0.33 φ_{end}=0.24	20 maximum e_v=10.0%	1470 ^{0}C/ 1743 K	6.3 3.8 1.9 1.3 0.95 0.65 6.3	 o o • o o o		

Table 4.1 Densification experiments performed.

4.4 Results

4.4.1 Mechanical data

As already indicated, the initial loading stage (i.e. loading to 6.3 MPa) achieved complete volume filling of the die, resulting in a reproducible "starting" porosity of 33 ± 2%. Figure 4.3 shows the single creep curve obtained at constant stress (3.8 MPa and an average initial grain size of 8 μm at1470 °C (1743 K)). In total, 25% strain was achieved in this run over approximately 8200 s (2 hours and 17 minutes). This is equivalent to a decrease in porosity from 33% to 10%. Figure 4.3b shows the corresponding plot of strain rate as a function of strain, while Figure 4.3c shows log strain rate versus log volumetric strain. In Figure 4.3b, a straight line can be drawn through the data between ~ 5% and 25% strain, suggesting that linear extrapolation of strain rate versus strain data is justified in analysing stepping data covering this range. Clearly the strain rate is not very sensitive to strain, with Figures 4.3b and 4.3c showing a decrease in strain rate of less than 1 order of magnitude in the range 8 - 25% strain. The slope of the log strain rate versus log strain plot in this range is around -1.7, so that the strain rate is proportional to 1/ ($e_v^{1.7}$). At the start of the experiment, the strain rate is less sensitive to strain (the slope being on average -0.6).

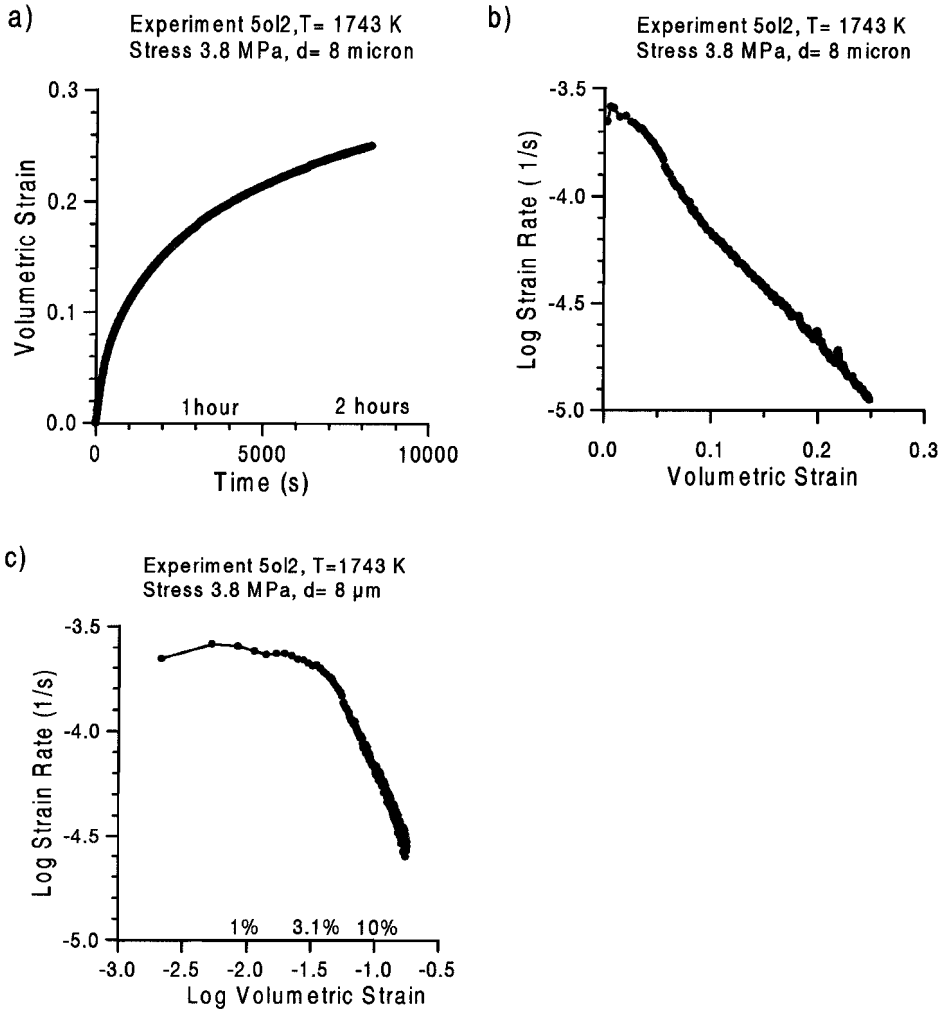

Figure 4.3 a) Compaction creep curve obtained from the single constant stress hot-pressing experiment performed on porous forsterite aggregate at 1743 K. Applied stress 3.8 MPa. Average grain size 8 micron. b) Log strain rate versus volumetric strain diagram for the same experiment as shown in a). c) Log- log plot of strain rate versus strain for the same experiment as illustrated in a) and b).

Figure 4.4 shows two examples of the creep curves obtained from the stress-stepping and temperature-stepping tests. Only data at thermal equilibrium and constant stress are plotted (not plotting relaxation/expansion/compaction during ramping and equilibration periods). For temperature down-stepping, larger periods of time were necessary for temperature equilibration.

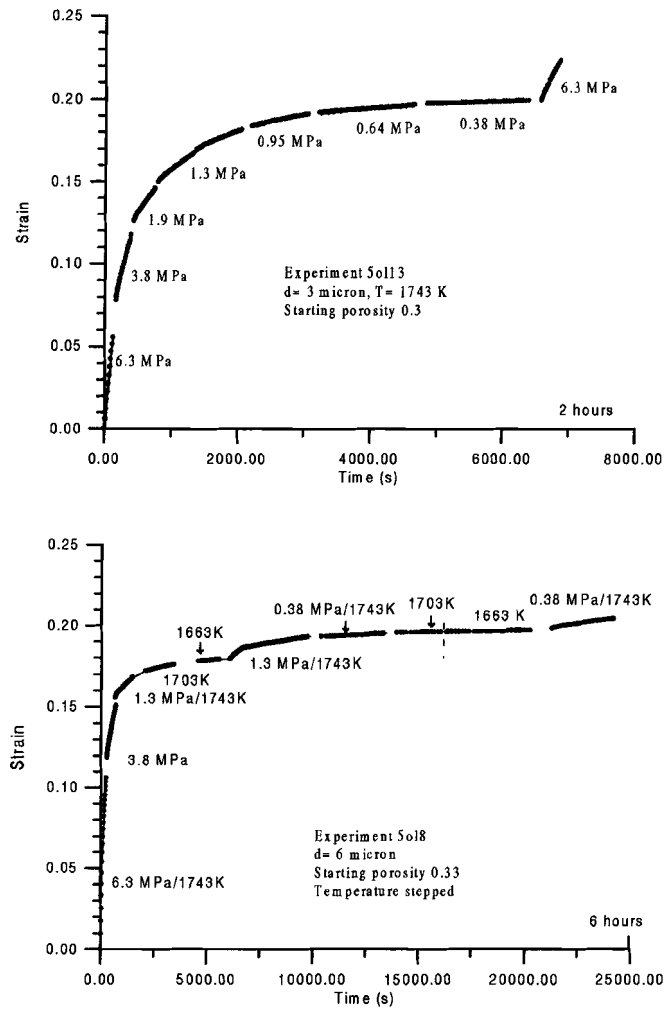

Figure 4.4 Typical creep curves obtained for the forsterite aggregates. a) Stress stepping experiment. b) Combined stress and temperature stepping..

Figure 4.5a-i shows the complete set of strain rate versus strain data obtained from the stepping experiments. In these graphs, vertical lines indicate constant strain values used to construct the following composite diagrams of log strain rate versus log stress and log strain rate versus log grain size. Most of the strain rate data are interpolated or extrapolated to these strains, using the linear trends seen in the log strain rate versus strain data. Table 4.1 shows which stress-steps were extrapolated to these constant strain values.

Extrapolation was performed by extending a best (least squares) fit line through the data points when at least the last 75% of the data-set showed a good linear fit (correlation coefficient, R^2>0.9). Alternatively, when the fit was less good, especially for the low stress steps, two lines were drawn from the centre of the data, one with the maximum slope of other stress steps in the graph and a horizontal line (minimum slope). Extrapolation in this way never extended more than 2% strain and the difference in strain rate indicated by the two lines is used as an error bar in subsequent representation of the strain rate data.

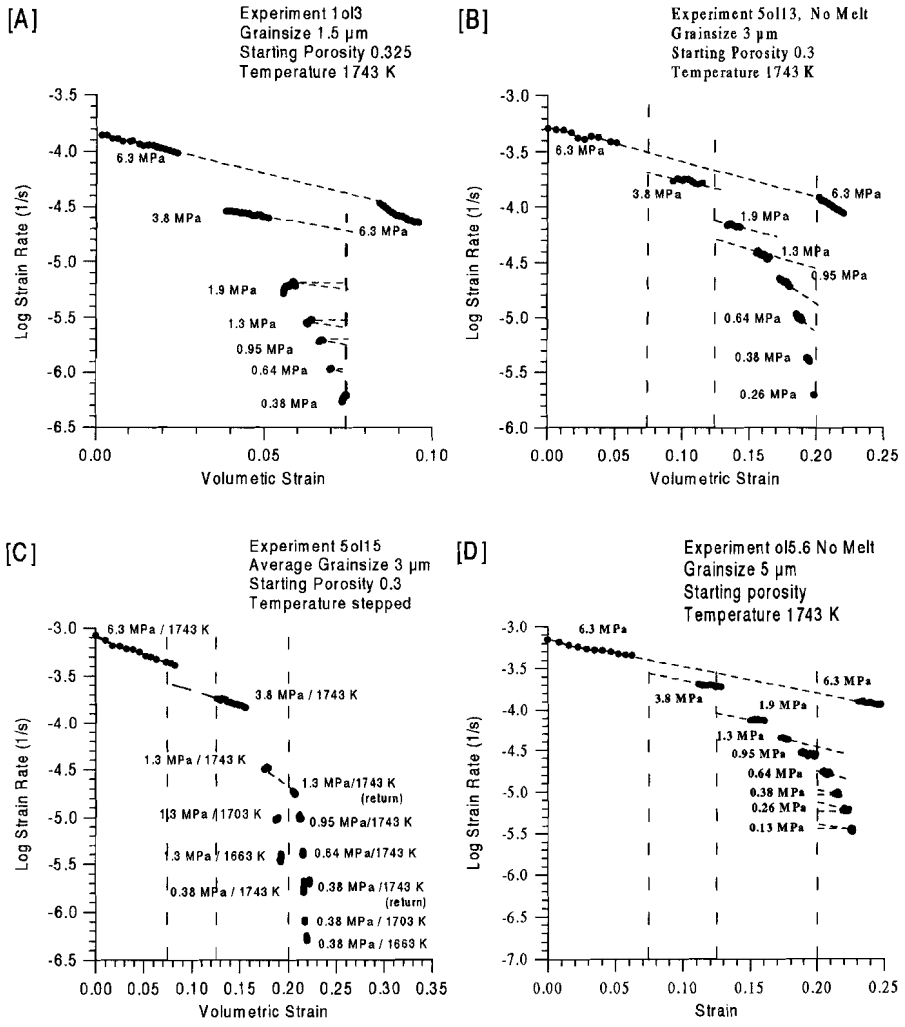

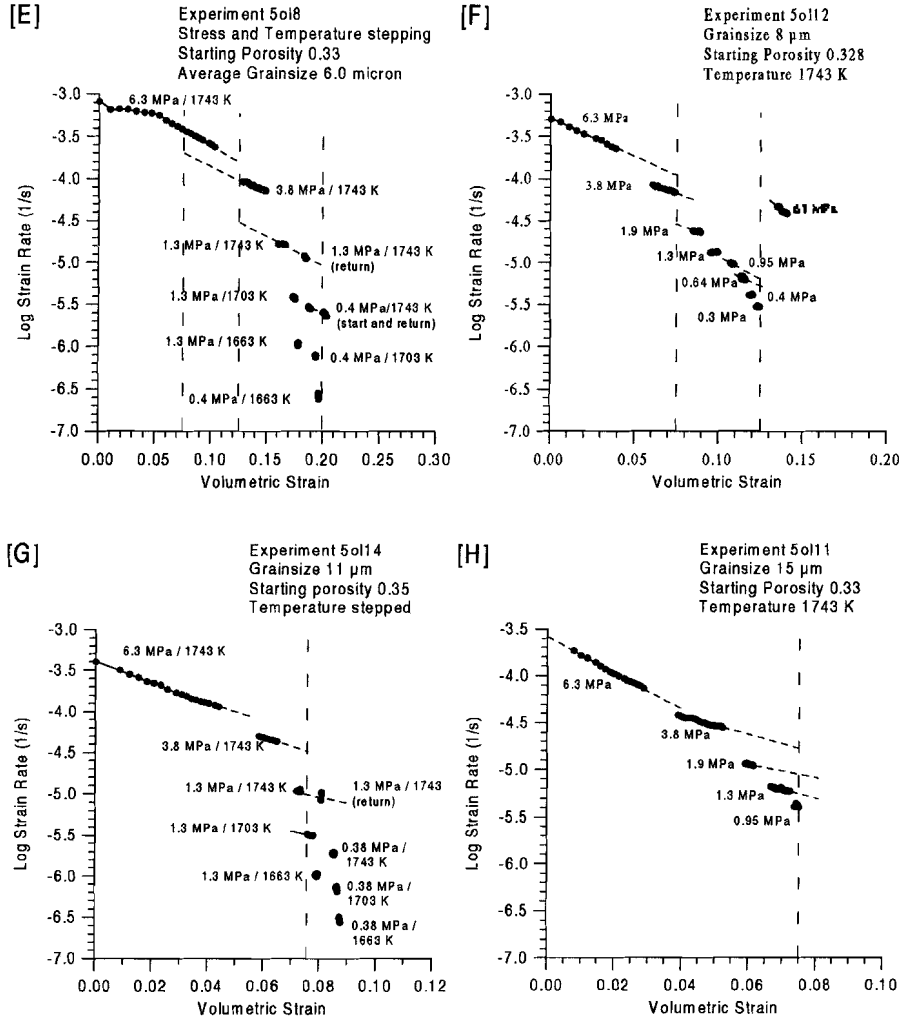
[E]
Experiment 5ol8
Stress and Temperature stepping
Starting Porosity 0.33
Average Grainsize 6.0 micron
6.3 MPa / 1743 K
3.8 MPa / 1743 K
1.3 MPa / 1743 K
1.3 MPa / 1743 K (return)
1.3 MPa /1703 K
0.4 MPa/1743 K (start and return)
1.3 MPa / 1663 K
0.4 MPa / 1703 K
0.4 MPa / 1663 K
Log Strain Rate (1/s)
Volumetric Strain
[F]
Experiment 5ol12
Grainsize 8 µm
Starting Porosity 0.328
Temperature 1743 K
6.3 MPa
3.8 MPa
1.9 MPa
1.3 MPa
0.95 MPa
0.64 MPa
0.4 MPa
0.3 MPa
Log Strain Rate (1/s)
Volumetric Strain
[G]
Experiment 5ol14
Grainsize 11 µm
Starting porosity 0.35
Temperature stepped
6.3 MPa / 1743 K
3.8 MPa / 1743 K
1.3 MPa / 1743 K
1.3 MPa / 1743 (return)
1.3 MPa / 1703 K
0.38 MPa / 1743 K
1.3 MPa / 1663 K
0.38 MPa / 1703 K
0.38 MPa / 1663 K
Log Strain Rate (1/s)
Volumetric Strain
[H]
Experiment 5ol11
Grainsize 15 µm
Starting Porosity 0.33
Temperature 1743 K
6.3 MPa
3.8 MPa
1.9 MPa
1.3 MPa
0.95 MPa
Log Strain Rate (1/s)
Volumetric Strain

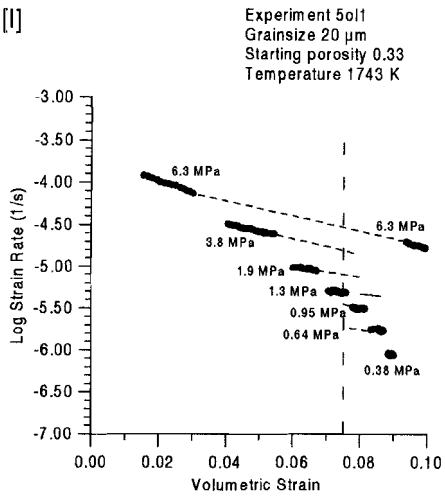

Figure 4.5 (A)- (l). Log strain rate versus volumetric strain diagram for all stepping experiments. Dashed lines indicate the strain values to which the strain rate data per step were extrapolated or interpolated for comparison at constant strain (i.e. constant porosity or structure).

Figure 4.6a-c shows strain rate versus log stress data plotted for constant volumetric strains of 7.5%, 12.5% and 20% using the extrapolated data from Table 4.1. All data, except those of the 6 µm experiment at 7.5% strain and the 1.5 µm experiment, which show slopes of 1.5 ± 0.1, give slopes within the range of 1.0 ± 0.3, down to applied stresses as low as 0.13 MPa. Note however, that the lines of constant grain size are not completely in sequence from course to fine.

Figure 4.7 shows the strain rate dependence on grain size at constant stress and strain. At 7.5% strain, the strain rate versus grain size data show a maximum strain rate around 5 µm. From 5 to 15 µm, the average slope of the data is between -2 to -3 for the stresses indicated. However for smaller grain sizes (< 5 µm) the slope approaches zero and becomes positive between 1.5 and 3 µm demonstrating a marked slowing down of densification rate towards the finest diameters. The data sets at 12.5% and 20% are too few to show such a clear trend, thought do suggest similar behaviour.

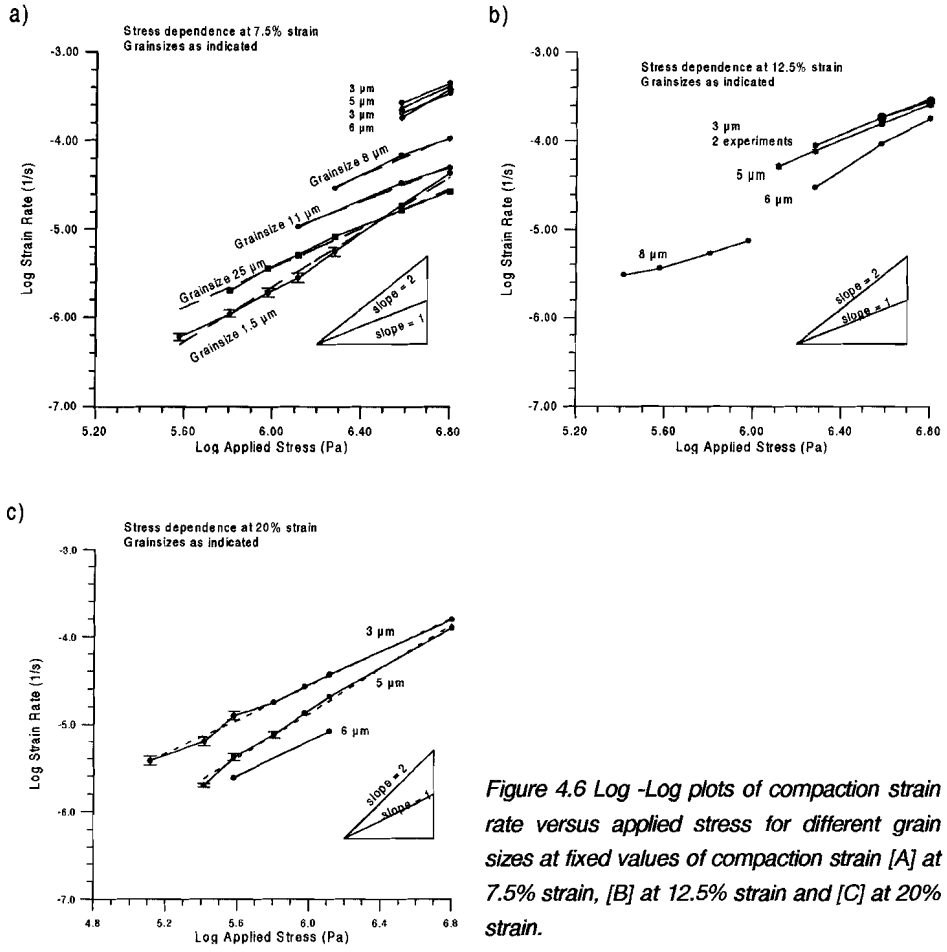

Figure 4.6 Log -Log plots of compaction strain rate versus applied stress for different grain sizes at fixed values of compaction strain [A] at 7.5% strain, [B] at 12.5% strain and [C] at 20% strain.

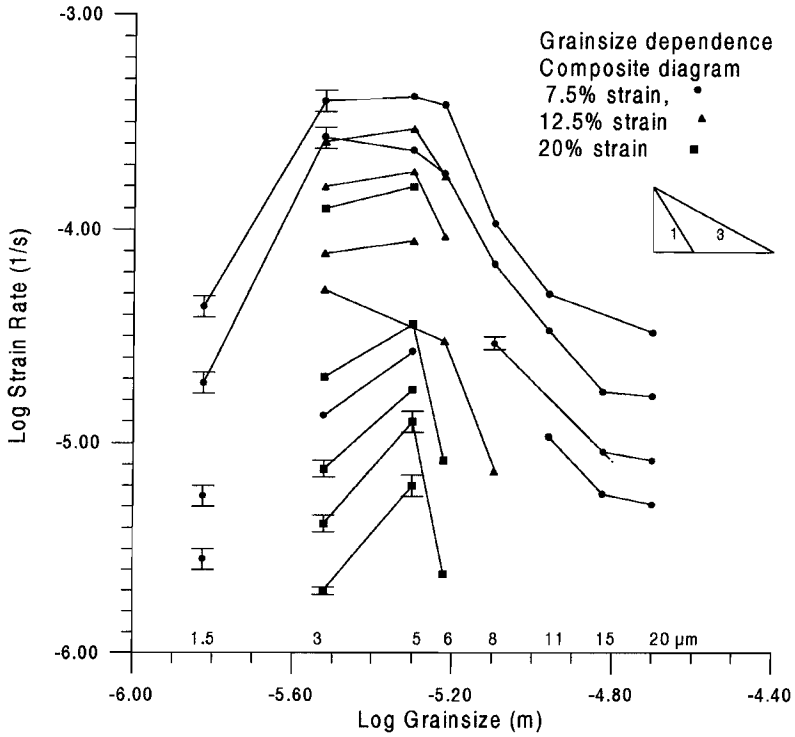

Figure 4.7 Log-Log plot of strain rate versus grain size at 1743 K illustrating graphs of constant applied stress and strain.

The strain rate data obtained in the three temperature stepping tests (Table 4.1) will now be used to illustrate the strain rate dependence on temperature. Assuming an Arrhenius type of dependence of strain rate on temperature, the slopes of the data sets plotted in the log strain rate versus 1/RT diagram, shown in Figure 4.8, give the apparent activation energy (Q) for densification creep of samples of fixed grain size. The Q values obtained range from 380-756 kJ/mol. As shown in Figure 4.5, the three temperature stepping tests were cycled at two stresses, first at 1.3 MPa then at 0.38 MPa. The grain size of the experiment, and the average strain during the temperature cycling are indicated at the curves in Figure 4.8. Note that for all three experiments, the apparent activation energy is systematically lower for temperature cycling at 0.38 MPa than at 1.3 MPa, despite the only minor differences in volumetric strain. The average values for Q at constant grain size are, 492 kJ/mol for d= 3 µm, 725 kJ/mol for d= 6 µm and 610 kJ/mol for the 11 µm grain size fraction.

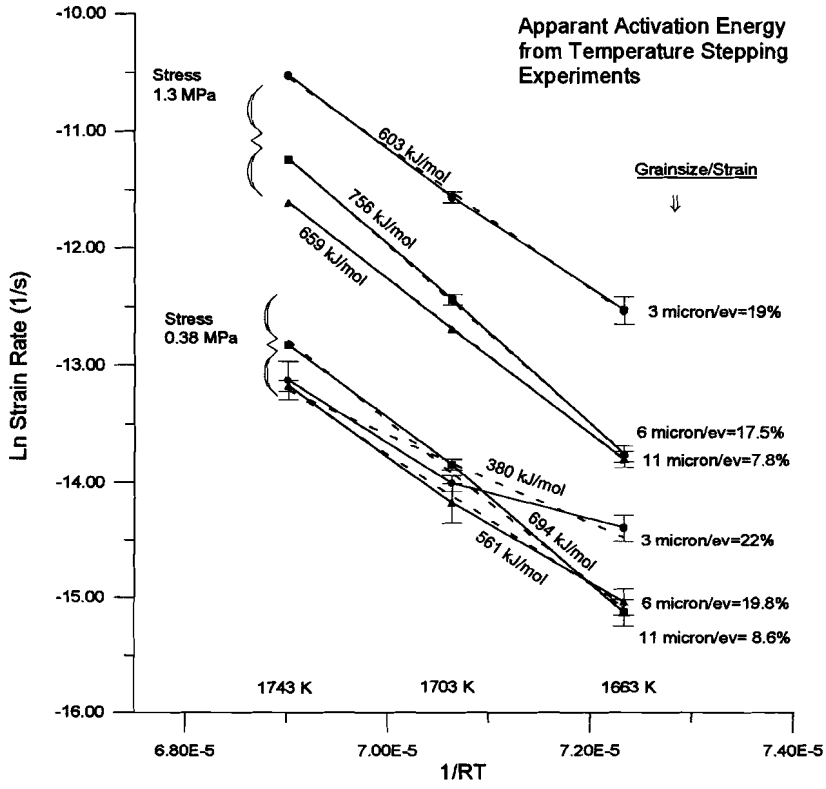

Figure 4.8 Ln strain rate versus 1/RT diagram showing the apparant activation energies obtained from the forsterite densification experiments for 2 applied stresses and for the 3, 6 and 11 μm grain sizes fractions (experiments 5ol15, 5ol8 and 5ol14).

4.4.2 Microstructural Observations

Study of the loose granular starting fractions, showed that all grain size batches consisted of nearly equiaxed, rounded grains. Only the 15 and 20 μm grain size fractions contained a small percentage of somewhat elongated grains.

Sintering effects during the annealing heat treatment of cold pressed material, prior to deformation, produced rounded necks between grain contacts and occasionally faceting of poor walls, but no grain growth was observed. Figure 4.9 shows a typical microstructure after sintering but before deformation. A similar mircostructure persisted through the first phase loading procedures.

After densification (hot-pressing), a decrease in porosity was apparent as well as an enlargement of grain contact areas (see Figure 4.10). Grains remained nearly equiaxed (no grain flattening). "Well-fitting" grains indicate intergranular redistribution of material (see Figure 4.11) and indentations can be recognised as shown in Figure 4.12. In a few grains, some local microcracking was observed. Grain growth during main phase densification was only observed in two samples. In the 1.5 μm grain size sample (figure 4.10), grains grew to 2.2 μm on average (after 5.5 hours of densification at 1743 K), and in the 5 μm grain size sample some inhomogeneous grain growth took place with a small fraction (~ 5%) growing to 20-25 micron (figure 4.11).

TEM was used to study whether or not grain boundaries the densified samples contained a glassy film and to determine dislocation densities in the grains. This work was performed with the help of T. Fliervoet. Small voids were observed at the grain boundaries, but only in the finest grain size (1.5 μm) sample. HRTEM showed lattice fringes of ~10 Å terminating at the grain boundary. At a magnification of 20.000 times, no evidence was found for glassy phase. Dislocation densities were found to be very low in all 4 samples studied and were inhomogeneously distributed, both with respect to individual grains and with respect to the sample (see Figure 4.13). Some systematic variation in dislocation density was observed between the samples, ranging from the finest grain size sample, which is virtually dislocation free, to an rough calculated density of $\sim 2.10^{11}/m^2$ in the 8 μm grain size sample, based on the total area investigated, an estimate of the thickness of the sample and the total amount of dislocations. Even at the highest density, in the 8 μm sample, at least 30% of the grains were free of dislocations.

Let us consider now the grain boundary and pore geometries observed among the various samples. The only samples which show a large fraction of grain boundary/ pore intersections having a negative curvature at the neck are the samples studied after sintering but before hot-pressing (Figure 4.9). Sample 5ol11 which was densified for a short period of time (~ 1 hour) and cooled without an applied stress also showed rounded necks and negative curvature at the neck margins (Figure 4.14). A rough estimate for ρ (the radius of negative curvature) in these samples is 0.5- 1 μm. For all other samples studied the majority of grain contacts show straight or positively curved solid/vapour surfaces, even at the highest magnifications using TEM (see Figure 4.15a and b).

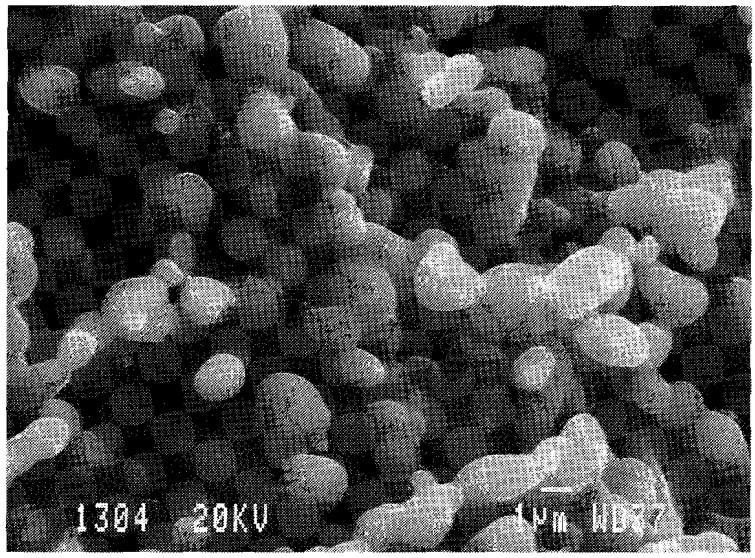

Figure 4.9 Typical microstructure after sintering but before hot-pressing. Fragment of sample 5ol13 after sintering for 48 hours at 1300 °C. The average grain size is 3 μm.

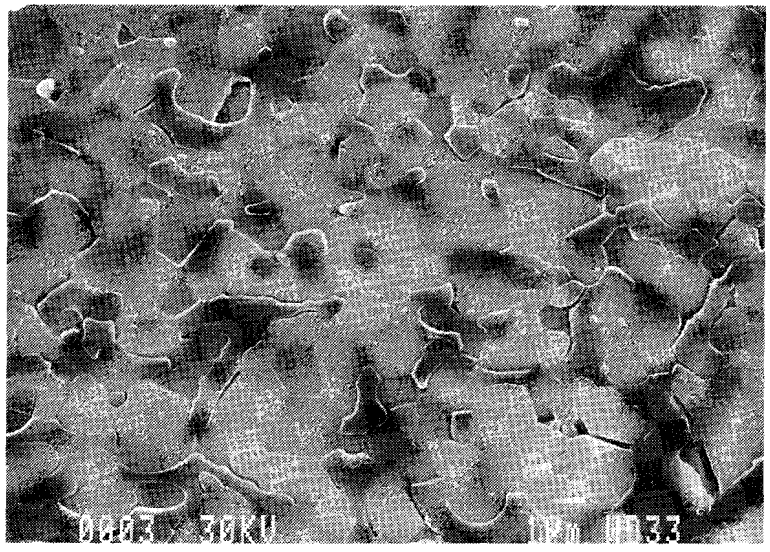

Figure 4.10 SEM micrograph of a polished and etched thin section of sample 1ol3. Dark areas are epoxy resin. Starting grain size was 1.5 μm and final grain size after densification is 2.2 μm, final porosity 0.26.

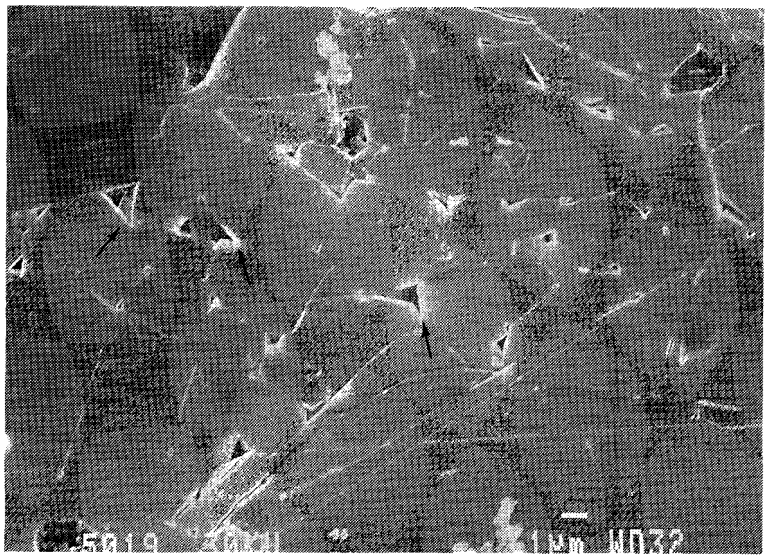

Figure 4.11 SEM micrograph of a polished and etched thin section of sample 5ol6 after hot pressing. Starting grain size was 5 μm and in the final sample illustrated, some abnormal grain growth can be observed (top left and bottom right) final porosity 11%. Note the small dihedral angles and the straight pore surfaces.

Figure 4.12. SEM micrograph of a polished and etched thin section of sample 5ol11 after hot pressing (average grain size 15 μm). Note the indented grain filled with epoxy resin (darker grey). Remaining porosity 27% (7.5% strain).

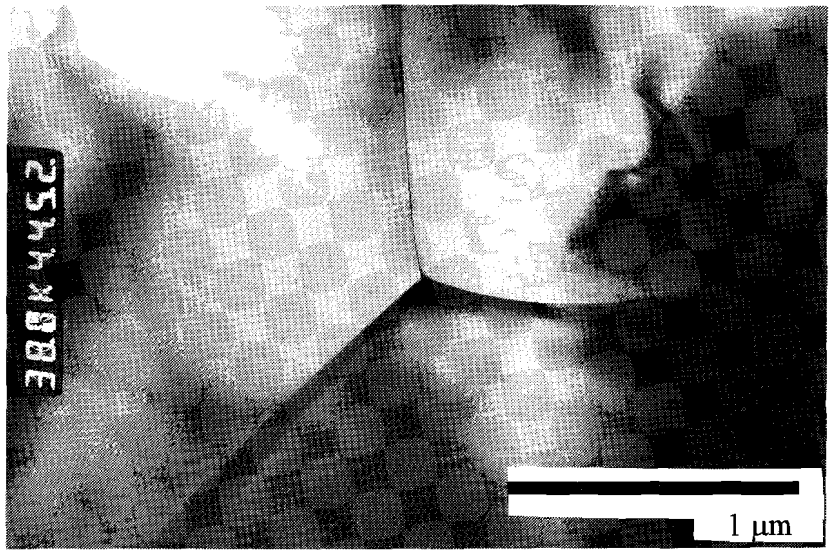

Figure 4.13 TEM micrograph of hot pressed sample 1ol3. Dislocations are present in the top right grain, the other two grains are free of dislocations Dislocation density is representative for samples 1ol3, 5ol3 and 5ol6.

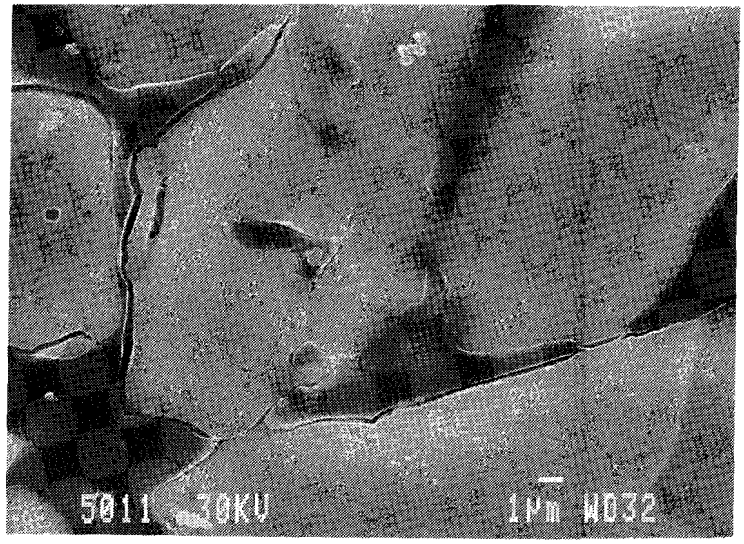

Figure 4.14 SEM micrograph of a polished and etched thin section of sample 5ol11 (average grain size 15 μm) after hot pressing for 1 hour and cooling in the load free condition. Note some of the grain boundary pore/ intersections have a negative solid/vapour curvature (dark grey is epoxy resin). Remaining porosity 27% (7.5% strain).

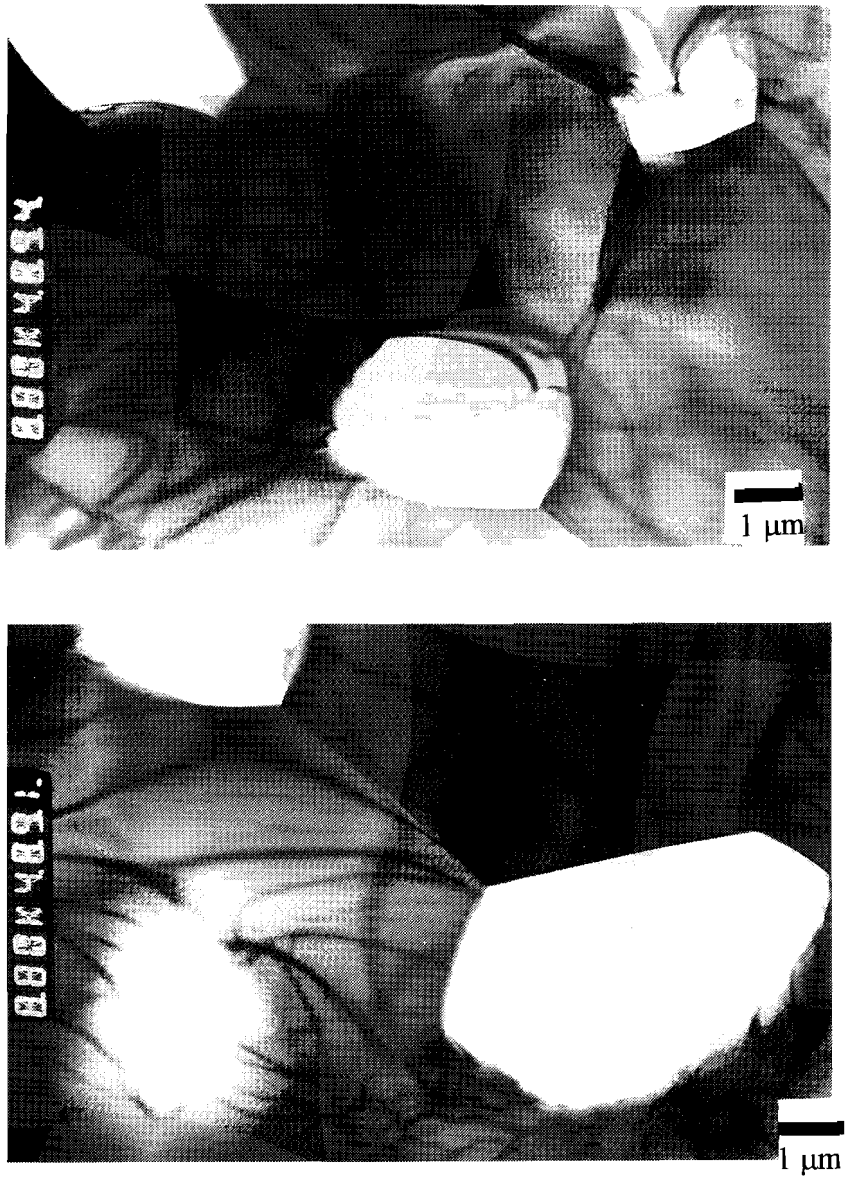

Figure 4.15. TEM micrographs of a) sample 5ol6 (5 μm average grain size) and b) 5ol12 (8 μm average grain size). Note the relatively straight solid/vapour surfaces in the pores near to the intersection with the grain boundaries. Also note the relatively large dislocation density in sample 5ol12 (lower part of micrograph b) compared with the other samples.

4.5 Discussion

The above experiments show that porous forsterite aggregates, hot pressed with initial grain sizes of 1.5 -20 μm, at applied stresses of 0.13-6.3 MPa and temperatures of 1643-1743 K (1370-1470 °C), undergo densification at volumetric strain rates of the order of 10^{-3}-10^{-7} s^{-1}.

In all experiments, a closely similar strain dependence of strain rate was observed. Moreover, the dependence of strain rate on strain changed very little during stepping (for example, see Figure 4.5 where extrapolation of the first 6.3 MPa step data connects to the 6.3 MPa step at the end of the experiment). This justifies the use of the stepping procedure and the associated extrapolation to asses the dependence of strain rate on applied stress and grain size. It is evidently not important if individual stress steps are performed at the beginning or the end of the experiments.

For grain sizes ≥ 5 μm a systematic decrease in strain rate was observed with increasing grain size, as is expected for all diffusion mass transfer creep processes. However, the finer grain size experiments (1.5 - 3 μm experiments) mostly show slower densification behaviour than the larger grain sizes (Figure 4.7). Nonetheless all experiments showed finite creep rates. Based on the mechanical data obtained, two regimes can thus be distinguished, namely the experiments with grain sizes ≥ 5 μm (Regime A) and < 5 μm (Regime B).

4.5.1 Regime A (average grain size ≥ 5 μm).

For volumetric strains in the range 7.5-12.5% strain, applied stresses ≥ 1 MPa and grain sizes ≥ 5 μm, the compacted samples showed strain rates approximately proportional to, σ^{1},$1/d^{2\rightarrow4}$ and $1/e_v^{0.2\rightarrow1}$. This behaviour is broadly consistent with the grain boundary diffusion creep models described in Sections 4.2.2.1 (equation 4.4) and 4.2.2.3. (equation 4.8) when surface energy related terms are neglected, in which case both equations are reduced to the densification rate model

$$\dot{\beta}_{gb} = \frac{12 D_{gb} \Omega^{s} \sigma_n}{kTd^3 e_v} \qquad (4.10)$$

The observed microstructural data are also consistent with this model, since dislocation

densities were observed to be very low. Furthermore, indentations and tightly fitting grains suggest that microstructural development was dominated by diffusion mass transfer under the action of the applied stress. The data obtained in experiments at 1.3 MPa , using 6 and 11 μm material at $e_v < 20\%$ provide the only data on apparent activation energies available in Regime A and give on average Q=707 kJ/mole. Looking at the data in Regime A in more detail, the grain size dependence at 7.5% strain suggests that $\dot{\beta} \propto 1/d^{2-3}$ with the exponent to e_v being smaller than 1. This might reflect a contribution from volume diffusion ($1/d^2$ dependence and independent of e_v) alongside grain boundary diffusion. However, it could also be due to any other less grain size dependent mechanism than grain boundary diffusion. For $e_v = 12.5\%$, the grain size dependence is $1/d^{3-4}$ (although based on few data). This could indicate grain boundary or lattice diffusion to be dominant, though with some additional contribution from the surface energy related term (equation 4.4). Overall however, the data for Regime A at 7.5%-12.5% strain are consistent with densification creep being dominated by grain boundary diffusion.

For the 20% strain data in the log strain rate versus log grain size plot of Figure 4.7 (data available only for grain sizes of 5 and 6 micron), the seems to increase to a value no longer consistent with any of the models (slope ≈7). Note however that the remaining porosity in the samples is reduced to ~15% and grain growth can be expected to become important when densification slows down (Rahaman, 1995). Some grain growth was indeed observed for the 5 micron sample (11% porosity at the end of the densification test) and will effect the slope in Figure 4.7.

4.5.2 Kinetic coefficient in Regime A

In view of the above, rough fitting of the theoretical model

$$\dot{\beta} = \frac{12 D_{gb} \sigma_n \Omega^s}{kTd^3 e_v} \qquad ((4.10))$$

for the data of Regime A obtained at $\sigma \geq 1$MPa, $d \geq 5$ μm and $7.5 \leq e_v \leq 12.5\%$ strain, allows calculation of $D_{gb}=\delta D_{gb,self}$ yielding a value of 2.10^{-20} m^3/s. The value for the apparent activation energy from the Arrhenius diagram is Q= 707 kJ/mol, averaged for the 6 and 11 μm.

When comparing the activation energy and diffusion data with literature values, the difficulty arises that independent values for grain boundary diffusion are rare. The only value for the apparent activation energy for grain boundary diffusion found is for Mg-

diffusion in synthetic forsterite (100) aggregates by Farver et al. (1994). This yields 343 ± 47 kJ/mol, which is only slightly lower than the activation energy for lattice diffusion in forsterite (390 kJ/mol (Chakraborty et al., 1994) at similar conditions, e.g. temperatures ~ 1300 °C). Assuming grain boundary diffusion is characterised by an activation energy approximately 2/3 of the lattice diffusion value (as in metals; following Stocker and Ashby, 1973 and Karato et al., 1986), the expected Q-values should thus around ~ 240 ± 40 kJ/mol (Jaoul et al., 1980; Jaoul et al, 1981; Andersson et al., 1989 and Chakraborty et al., 1994).

To asses whether the diffusivity estimated for Regime A is of the right order for grain boundary diffusion and to asses which might be the rate limiting species in the diffusion creep mechanism, a comparison with available grain boundary diffusion data for Mg, Si and O species can be made. When extrapolating the trend in the data for Mg grain boundary diffusion described by Farver et al. (1994) to 1470 °C, then $\delta D_{gb,Mg} \approx 10^{-20}$- 10^{-21} m^3/s (10^{-22} m^3/s at 1250°C). Farver et al. (1994) performed an additional experiment to estimate the effective grain boundary width, δ, which was found to be ~3 nm. Hence $D_{gb,Mg}$ would be ~5.10^{-11} m^2/s. For volume diffusion data (D_l) in forsterite (Chakraborty et al., 1994 and Andersson et al., 1989), extrapolated to 1470 °C, $D_{l,Mg} \approx 10^{-15} m^2/s$, indicating that for Mg, diffusion through the grain boundary is ~3- 4 orders of magnitude faster than volume diffusion.

For O, a study by Condit et al (1985) for grain boundary diffusion of oxygen in forsterite aggregates yields a value for $\delta D_{gb,O} \approx 10^{-21}$- 10^{-22} m^3/s for 1470 °C (and about 3 order of magnitude lower for 1250 °C). The only other diffusion data for O species which might give an indication of diffusion along a fast diffusion path in synthetic Fo100, single crystals comes from Yurimote et al. (1992). The authors describe diffusion along dislocations, within a core of 0.1 nm surrounding the dislocation, to be 4 orders of magnitude faster than volume diffusion rates, i.e. at 1200 °C, D_O through the fast diffusion path yield 10^{-17} m^2/s while experimental data for lattice diffusion yield 10^{-21} m^2/s. Other data for lattice diffusion yield $D_{l,O} \approx 10^{-18} m^2/s$ at 1470 °C and ~10^{-20} m^2/s at 1200 °C (Jaoul et al., 1980 and Andersson et al., 1989). Note that when assuming $\delta \approx 1$ nm, then at ~1200 °C, all data above show a consistent $D_{gb,O}$ being 3-4 order of magnitude faster than $D_{l,O}$.

For Si diffusion, no grain boundary or fast diffusion path data are available for a solid/solid boundary. Lattice diffusion data at 1470 °C yield $D_{l,Si} \approx 10^{-21}$ m^2/s (Jaoul et al, 1981 and Andersson et al., 1989). For lattice diffusion, Si is the slowest diffusing species in forsterite.

Note that the obtained value for δD_{gb} in the present work (2.10^{-20} m^3/s) can only be directly compared with the above values for δD_{gb} in forsterite aggregates. From the extrapolated trends of the data by Farver et al. (1994) and Condit et al. (1985) to 1470 °C, it can concluded that $\delta D_{gb,Mg} \approx 10^{-20}$-$10^{-21}$ m^3/s and $\delta D_{gb,O} \approx 10^{-21}$- 10^{-22} m^3/s not differ much at 1470 °C and δD_{gb} obtained form the present work shows reasonable agreement with the independent Mg and O diffusivity data. No direct comparison can be made with independent grain boundary diffusivity data for Si. However, when assuming the grain boundary width to be similar to recent estimates of grain boundary width in other ceramic and oxide aggregates, i.e. 1-3 nm (Joesten, 1991 and Farver, 1994), the value of D_{gb} implied by the present data for Regime A gives $D_{gb} \approx 10^{-11}$ m^2/s. When comparing the obtained D_{gb} with the lattice diffusion data for Mg, O and Si, described above, it can be concluded that the order of magnitude of the obtained diffusivity in this work is consistent with the idea that grain boundary diffusion is the dominant mass transport mechanism. The experimentally determined diffusivity is consistent with the grain boundary diffusion value of Mg, as obtained from independent diffusivity studies, however, grain boundary diffusion data for O are also within an order of magnitude from the obtained value.

4.5.3 Regime B (average grain size < 5 μm)

The mechanical data for grain sizes < 5 μm show a log β versus log σ trend with a slope of ~1 indicating a diffusion dominated densification mechanism for this regime too (figure 4.6). However the 1.5 μm experiment is significantly slower than all other (coarser) grain size experiments. Indeed, the grain size dependence of the strain rate is reversed (positive dependence) for grain sizes < 5 μm, in comparison with the slopes seen in the log β versus log d diagram (Figure 4.7) for grain sizes ≥ 5 μm and expected for grain boundary diffusion dominated processes. The apparent activation energies obtained for the 3 μm grain size show a similar trend as the 6 and 11 μm experiments (see Figure 4.8) although the values are lower (603 kJ/mol for the 1.3 MPa and 380 kJ/mol for the 0.38 MPa experiments). The microstructural observations of low dislocation densities in Regime B are consistent with a diffusion creep process. Moreover, tight-fitting grains, low porosity and absence of grain flattening, observed in Regime B indicate densification via surface and grain boundary mass redistribution. The straight pore/grain boundary intersection geometries observed suggest Geometry B in Figure 4.1 is a closer approximate geometry than Geometry A, which has a negatively curved neck region (see

Figure 4.1). A small amount of grain growth was observed for the 1.5 μm experiments to an average grain size of 2.2 μm,

Possible reasons for the decrease in strain rate towards finer grain sizes (see Figure 4.7) could be

1) The smaller positive radius (grain radius) of curvature. In this case the opposing driving force term $-4\gamma_{sv}/d$ in equation 4.8 becomes more important for smaller d.

2) Grain growth. This can be eliminated, because the strain rates for the final grain size are still lower than for experiments with larger grain sizes.

3) Neck growth may reduce the term $(\cos\theta/2-\cos\theta_{eq}/2)/\rho$, hence reducing the driving force for densification (equation 4.4). However, the additional driving force due to the cosine-difference term is more important for smaller grain sizes and therefore it can (partly) explain differences with time or increasing strain for the experiments in Regime B, however, it is unlikely to explain differences observed between Regime A and Regime B experiments.

4) The term $(\cos\theta/2-\cos\theta_{eq}/2)/\rho$ in equation (4.4) may become negative, thereby becoming an opposing rather than an additional driving force term. Although being a possible explanation for the observed mechanical behaviour, microstructural observations indicate negatively curved regions to have disappeared after a short period of densification. Therefore it can be considered a possibility for small volumetric strain data only.

Hence, during densification, the negative contribution due to the $(-4\gamma_{sv}/d)$ term described at 1) above, seems the most likely reason for the observed decrease in strain rate in Regime B, although contributions (positive or negative) due to the negatively curved region at the neck can not be ruled out at low volumetric strains, i.e. at short times of densification.

4.5.4 Determining the surface energy related contribution

In order to test the idea that the anomalous grain size effect seen in Regime B may be caused by a reduction of the driving force for densification due to surface energy effects (possibilities 1 or 4 above) linear graphs of the strain rate versus stress have been constructed (Figure 4.16). Only data obtained from experiments and stresses $\leq$ 1.3 MPa are used. Extrapolating linear best fits towards the origin yields intersection values (intercepts) on the stress or strain rate axis, which are indicated at the curves. In general it was found that most extrapolation intercept the stress axis at small positive values

indicating that a threshold force or "yield stress" has to be overcome before compaction occurs. At 7.5% strain, for example, both the curves for 20 μm and 1.5 μm intersect the stress axis. However, for the 3 μm data at $e_v \leq 12.5\%$ and for all 5 μm graphs, intersection was on the strain rate axis, although close to the origin (see Figure 4.16b). When extrapolations from higher stress data points (> 1.3 MPa) are used, the extrapolations all intersect on the stress axis and at higher "yield stress" values. Possible explanations for this rough "yield stress" type of behaviour are

a) that a frictional force must be overcome within the apparatus to initiate compaction, and

b) that some additional driving force opposes to the effect of stress on densification, such as a negative surface energy term of the type mentioned under points 1 and 4 in section 4.5.3. or contributes to densification as mentioned under 3). Frictional forces are believed to be too low to explain the observed behaviour because an independent experiments using a pill of glass instead of a solid aggregate sample showed that the melt was squeezed out of the die at an applied stress of 2.10^4 Pa. Moreover, frictional forces could not explain the grain size effect seen in Figure 4.7. Therefore, an order of magnitude calculation can be made to investigate whether the apparent yield stress values are at least consistent with a surface energy related driving force term acting in opposition to the applied stress. The first calculation is made to test if the yield stress values (the intersection stress values) are of the order of $4\gamma_{sv}/d$ (see Equation 4.8). The results for the calculated γ_{sv} yield ~6 J/m^2, for the highest intersection value of the 1.5 μm curve, which is of the same order as the expected γ_{sv} value of 2.7 J/m^2 (Watson, 1997). For the 20 μm curve the γ_{sv} value calculated is 50 J/m^2 which is roughly a factor 20 to high. Note that in the order of magnitude calculations no dependence of stress for the interfacial energy term is incorporated. From the order of magnitude calculations it is thus suggested that the deviation from equation (4.8) for the low stress data is consistent with the possible opposing effects of surface energy versus stress. However, some positive contribution of surface energy to densification can not be ruled out for the low strain 3 μm and for the 5 μm data. The observed stress dependence of the intersection data can possibly be explained by surface stress being more appropriate for use in the models than surface energy.

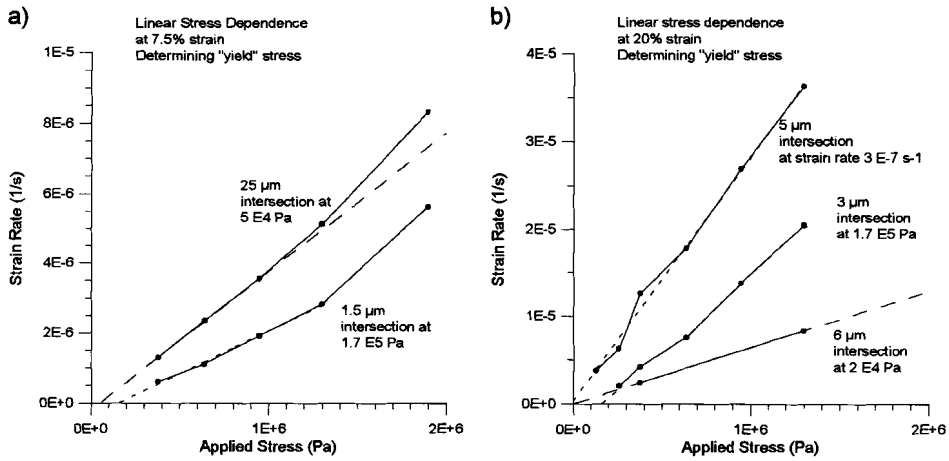

Figure 4.16 Strain rate versus applied stress data obtained in experiments at stresses ≤ 1.3 MPa: Data plotted for strains of [A] 7.5% and [B] 20%. Note linear scales and intercepts on σ-axis suggesting that critical stress must be overcome to cause densification creep.

4.5.5 Comparison with previous work on olivine aggregates.

Generally good agreement exists in terms of stress and grain size dependence between the densification data obtained in this work and previous densification and deformation experiments on fine grain size material at high temperatures (Schwenn and Goetze, 1978; Relandeau, 1981; Cooper and Kohlstedt,1984; Karato et al., 1986 and Hirth and Kohlstedt, 1995). In the present work, for grain sizes ≥ 5 µm and temperatures between 1390-1470 °C, and applied stresses ≥ 1 MPa the average values are ~1 for the stress exponent and -3 for the grain size exponent, consistent with densification by grain boundary diffusion creep. Both densification and deviatoric creep data can be fit to equation (4.8) or more general to the equation

$$\dot{\beta} = \frac{A\sigma^n \Omega}{kTd^p} e^{-Q/RT} \qquad (4.10)$$

where A is a porosity or strain dependent term (see Spiers et al., 1990).

In Table 4.2 typical data are listed from previous studies in which diffusion (grain size sensitive) creep was obtained for forsterite aggregates ($Fo_{90\text{-}100}$), nominally melt free and without added water. For studies where equation 4.10 has been fitted to the data set, the determined exponents n, p and the apparent activation energy are listed in Table 4.2.

Authors Data	Schwenn and Goetze (1978)	Relandeau (1981)	Cooper and Kohlstedt (1984,1986)	Karato et al., (1986)	Hirth and Kohlstedt (1995)
Material system	San Carlos Fo92	Synthetic Fo100	San Carlos Fo92	San Carlos Fo92	San Carlos Fo92
Temperature range (°C)	1429	1600	1300-1400	1300	1200-1300
Confining Pressure	0.1 MPa	0.1 MPa	0.1 MPa	300 MPa	0.1 MPa
Applied stresses (MPa)	16.6-17.0	3-8	5-30	20-160 deformation experim.	10-100 deformation experim.
Grain size (μm)	5-25	60-132	3-13	7-30	8-20
Sample Starting (S) and Final (F) porosity	S 15-35% F 27-1%	S 7%	S 26-34% *[2]	S 0-2%	< 1% melt
Best fit model data (equation 4.11or 4.10)					
n	1.5 ± 0.4	1.5 ± 0.5	1.1 ± 0.3	1.4 ± 0.3	1.1
p	-	-	3	2-3	~3 *[5]
Q (kJ/mol)	355 ±121 *[1]	-	380 ± 105 *[3]	290 *[4]	315
δD_{gb} (m^3/s)		-			2.10^{-21}
Comments	*[1] for a combination of dislocation and diffusion creep. Recalculated Q values in Figure 4.16	Transition to dislocation creep observed at Temp. < 1600 °C	*[2] strain rates normalized for 15% and some at 5% porosity at 20 MPa *[3] Recalculat. Q values in Figure 4.16	*[4]Q value based on 2/3 of Si and O volume diffusion coefficient for olivine	*[5] After correction of the grain sizes by a grain growth law?? 3-5% enstatite.

Table 4.2 Data from previous studies on forsterite aggregates (Fo_{90-100}) in which diffusion creep was obtained. Samples nominally melt free and without added water.

Apparent activation energies for diffusion creep of olivine aggregates containing no melt, water or second phase minerals are scarce. The values of the apparent activation energies determined by Cooper and Kohlstedt (1984) and Schwenn and Goetze (1978) vary over a wide range of conditions showing a wide scatter in activation energy values. The value by Karato et al. (1986) is an estimate based on 2/3 of the lattice diffusion values. The above average values for Q differ significantly from the values determined in the present work. However, when restricting the data in the densification work of Schwenn and Goetze (1978) and Cooper and Kohlstedt(1984) to those stress and grain size conditions for which a grain boundary diffusion creep model (Coble creep) was found to be applicable, a more consistent picture is apparent. In the framework of a Coble creep type equation (Equation 4.11 with n=1, p=3), the slope of a diagram of $\log(\beta d^3/\sigma)$ versus 1/RT plotted for fixed structure (fixed porosity) yields is the apparent activation energy. Such a diagram is plotted in Figure 4.17 for the present data (Regime A) and diffusion creep data of Schwenn and Goetze (1978) and Cooper and Kohlstedt (1984, 1986). Only data points of the same microstructural characteristics (same e_v or porosity) are connected. From Figure 4.17 it is evident that a consistent picture arises for the activation energy assuming a Coble mechanism. A division is clear for grain size data < 15 μm and grain size data ≥ 15 μm. The average activation energy for the data in the range 15-25 μm is 250 kJ/mol while for the grain size range 6-15 micron the average apparent activation energy is 620 kJ/mol. The latter value is very high when comparing it with (2/3 of) the activation energies known for lattice diffusion of Si and O species in olivine, but consistent for the three different studies. An explanation due to different experimental or material parameters is not very likely since within the data set of Schwenn and Goetze (1977) the same division is present between small and larger grain size data. At present no adequate explanation is found for the observed difference.

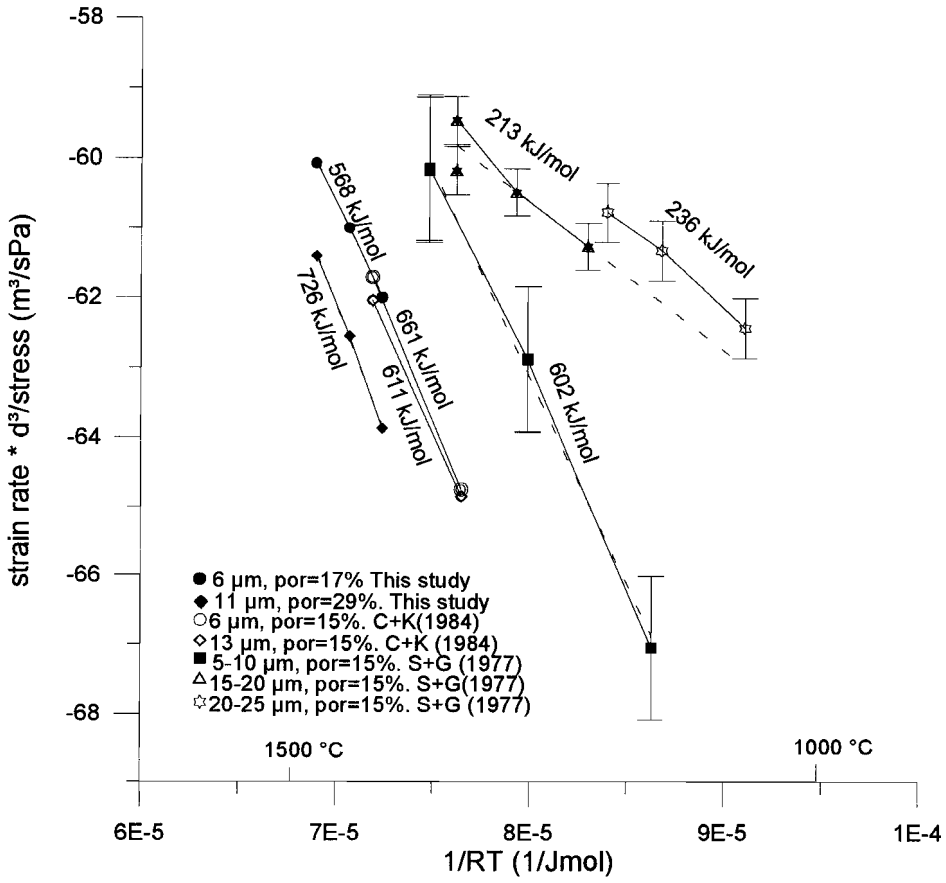

Figure 4.17 Diagram illustrating the apparent activation energies recalculated from two previous studies fitting experimental diffusion data to the Coble creep equation and the activation energy data obtained from the present work.

Lastly, some comparison between fully dense and porous samples must be made. In all studies described above, for small grain sizes (< 25 µm), high temperatures (≥ 1573 K) and low to moderate stresses (< 100 MPa), Coble creep was inferred to be the dominant creep mechanism both in densification experiments as well as in dense samples. Therefore, no distinction can be made in terms of stress or grain size dependence. Apparent activation energies reported show a wide range of values, roughly between 200-700 kJ/mol, with no distinction being apparent between porous and dense samples in terms of temperature dependence. The diffusivity obtained by Hirth and Kohlstedt for dense samples (< 1% melt), δD_{gb} is $2.10^{-21} m^3/s$ and suggested by the authors to be due to rate

limiting diffusion of Si in the grain boundary. The value obtained for δD_{gb} reported in this work is $\sim 2.10^{-20}$ m^3/s for porous samples. Although the values differ by an order of magnitude, no direct comparison can be made because the diffusion coefficients are obtained at different temperatures. In conclusion it can be stated that not enough data are available to make a comparison between the mechanical behaviour of porous and dense samples.

4.6 Summary and conclusions

1)Stress densification experiments have been performed on fine grained (1.5-20 μm) forsterite (Fo_{100}) aggregates. At strains < 20%, stresses > 1 MPa, for grain sizes > 5 μm and temperatures of 1470 °C, compaction rates are approximately proportional to the applied stress and to one over the grain size cubed, which is consistent with Coble or grain boundary diffusion controlled creep (Regime A).

2) For grain sizes < 5 μm, the grain size dependence of the strain rate is reversed, implying a significant reduction in densification rate compared with Coble creep and a retardation becoming larger for smaller grain sizes. It is suggested that this effect may be due to the action of surface energy related forces (Regime B).

3) Microstructural study of the samples shows very low dislocation densities, no grain flattening and few mircofractures to be present. These features plus tightly fitting grains and reduced porosity support the dominance of diffusion creep as the main densification mechanism.

4) When studying the possible contribution of surface energy forces, then for samples densified and cooled under stress, mainly straight solid/vapour surfaces near the grain boundary were observed. Intersection data obtained in linear stress versus strain rate diagrams were in general consistent with the presence of a "yield stress" which has to be overcome before densification occurs, according to

$$\dot{\beta}_{gb} = \frac{12 D_{gb} \Omega}{kTd^3 e_v}(\sigma_n - \frac{4\gamma_{sv}}{d}) \qquad ((4.8))$$

However, an additional contribution to the densification rate at small volumetric strains (≤ 12.5%) is not excluded This could be consistent with the surface energy effect in

$$\dot{\beta}_{gb} = \frac{12 D_{gb} \Omega}{kTd^3 e_v}(\sigma_n + \frac{24\gamma_{sv}}{de_v}(\cos\frac{\theta}{2} - \cos\frac{\theta_{eq}}{2})) \qquad ((4.4))$$

5) Fitting the data in Regime A to the Coble creep equation, the diffusivity δD_{gb} was determined to be 2 $10^{-20} m^3/s$ and broadly consistent with literature data for the diffusion rate of Mg in the grain boundary. Comparison with previous studies on diffusion creep of forsterite aggregates shows good agreement in terms of stress and grain size dependence of the strain rate. Values determined for δD_{gb} and the apparent activation energy (Q) for creep, also show good agreement with other studies when taking temperature differences into account and when comparing data under similar microstructural conditions.

CHAPTER 5

DENSIFICATION OF PARTIALLY MOLTEN FORSTERITE AGGREGATES AT LOW STRESSES

5.1 Introduction

The densification and deformation behaviour of partially molten systems is of direct relevance to geodynamic settings where melt generation and/or transport play a role. Of all such settings, the best known and the most simple with respect to chemistry and tectonics is the case of mid-ocean ridges. These are sites where basaltic melt wells up through a relatively uniform crystalline solid mantle in which olivine is the most abundant mineral.

Despite the fact that mid-ocean ridges are the simplest large-scale setting where partial melting occurs, many processes at depth, such as segregation and migration of the melt, remain poorly understood. Considerable effort has been made to quantitatively model melt extraction and segregation beneath mid-ocean ridges (Sleep, 1988; Stevenson, 1989; Sparks and Parmentier, 1991; Turcotte and Morgan, 1992; White and McKenzie, 1995; Kelemen et al., 1995; Aharonov et al., 1995 and Richardson et al., 1996). However, some of the essential input parameters are poorly constrained. Essential information for realistic dynamic models involving partial melts include an understanding of the melt distribution on the grain scale, whether or not a connected network of grain-scale melt channels exists and the effect of the melt on bulk rock rheology (Waff and Bulau, 1979; Cooper and Kohlstedt, 1982; Faul et al., 1994 and Hirth and Kohlstedt, 1995).

In order to establish the solid/liquid phase distribution under controlled (hydrostatic and non-hydrostatic) conditions, numerous experimental studies have been performed (Waff and Bulau, 1979; 1982; Von Bargen and Waff, 1986; Cooper and Kohlstedt, 1982; Riley and Kohlstedt, 1991; Faul et al., 1994; Hirth and Kohlstedt, 1995a, b and Faul, 1997). Recently Faul and co-workers (1994, 1997) and Hirth and Kohlstedt (1995) found that surface energy anisotropy has a large effect on the melt topology in olivine aggregates. Instead of equilibrium dihedral wetting angles, which determine that for olivine/basalt the melt is present in triple junction networks only, many

wetted grain boundaries were found. If this is indeed the case at depth, it may have major implications for seismic velocities and other geopysical parameters, but also for the rheological behaviour of the partially molten rock (see also Chapter 1). Another important contribution to understanding the behaviour of partially molten regions of the earth is provided by experimental deformation studies on olivine/melt samples. Cooper and Kohlstedt (1984 and 1986) and Hirth and Kohlstedt (1995 and 1996), studied the dependence of densification and deformation rates on stress and melt content, compairing the results with the rheological behaviour of olivine rock in the absence of a melt phase.

When trying to combine information from equilibrium (hydrostatic) melt distribution studies and densification or deformation studies on partially molten samples, the difficulty arises that little or no information is available under conditions where both stress-related and surface-energy-related driving forces for diffusive mass transfer are comparable in magnitude. Rather, in work on solid/melt geometries in partially molten mantle rocks, small non-hydrostatic stresses are neglected and interfacial energies are considered to determine the melt distribution (Faul et al., 1994 and Waff and Bulau, 1982). Similarly, no systematic densification studies have been performed under the low stress conditions where surface energy forces become significant. In all previously reported deformation studies of olivine/melt samples, surface energy was, when considered at all, found to be negligible compared to stress-related driving forces. However, applied stresses are usually > 10 MPa in the experiments reported (except for a few individual experiments excluded from curves and/or conclusions). Although surface forces are small and usually neglected, they could become significant in the differential stress range from 0.1 - 10 MPa, which is the differential stress range thought to prevail under bulk mantle conditions (Stocker and Ashby, 1973). Therefore, taking both interfacial energy and low stresses into account in trying to understand diffusive mass transfer processes is a necessary step in investigating the rheological behaviour and solid/melt topology of partially molten systems under low stress conditions.

It is the aim of this chapter to derive diffusion creep models for partially molten aggregates densifying under high temperature conditions, taking both stress and surface energy related driving forces into account. It is important to find out at what applied stresses the surface forces become important, and how the different driving forces for mass transport interact. Are they complementary or competitive? After derivation of the models, densification experiments on aggregates of pure Mg-forsterite containing a basaltic analogue melt are described and compared with the models. A comparison is also made

with the results obtained for densification of melt-free, forsterite/vapour aggregates at similar temperatures (Chapter 4) and for salt/solution systems at room temperature (Chapter 3). In particular, the effects of the relative contribution of surface energy related forces will be compared as a function of applied stress. Finally, the findings for the forsterite/melt system will be applied to discuss the consequences for our present understanding of melt segregation and migration in partially molten mantle material under mid-ocean ridges.

5.2 Theoretical Considerations

5.2.1 Driving forces and mass transfer paths in partially molten aggregates

In Chapter 4, mass transfer paths were identified and models were derived for neck growth and diffusion creep processes in solid/vapour systems under high temperature conditions. Here, the grain scale driving forces and mass transfer paths relevant to neck growth in and stress densification of a solid plus partial melt system are considered.

Following the approach adopted in Chapter 4, consider the two-grain geometry represented in Figure 5.1. Neglecting chemical reactions, the two main driving forces for mass transfer in such a system are

I) Reduction of surface free energy. When assuming surface free energy to be isotropic, this results in mass transfer from convex solid surfaces (positive curvature) to flat or negatively curved surfaces and/or from flat to negatively curved surfaces (Figure 5.1A).

II) Stress-related driving force. When a stress is applied to grain contacts (Figure 5.1B), this results in transfer of mass from points of relatively high normal stress (grain to grain contacts) to points of relatively low normal stress (pore walls).

The corresponding transport paths for the high temperature solid/melt case are indicated in Figure 5.1 and are briefly described below:

1)Surface diffusion can occur on pore walls as in the case of solid/vapour systems (see Chapter 4). However the interaction of the solid surface with the liquid is likely to have an effect on this transport mechanism and in practice the mechanism will be indistinguishable from a solution/precipitation process.

2) Volume or lattice diffusion via mass transfer path (2) involves vacancy diffusion through the solid, therefore this mass transfer mechanism and path is exactly the same as in a high temperature solid/vapour system. The only difference may be in the relative contribution to the total mass transport rate.

3) Solution/precipitation at grain surfaces is a process comparable to solution/precipitation in a low temperature solid/solution system (Chapter 3), but also to the evaporation/condensation process in a high temperature solid/vapour system (Chapter 4). For the latter system, however surface diffusion is usually considered more important than evaporation/condensation, i.e. it is a faster parallel process.

4) Grain boundary diffusion due to a stress- or surface energy related driving force is a densifying mechanism with mass transfer from the grain boundary region to the neck margin. Under high temperature conditions grain boundary diffusion does not critically depend on the presence of a fluid in the grain boundary, as for the low temperature case described in Chapter 3.

5) Densification can also be achieved through volume (lattice) diffusion when the mass transfer is from (or near) the grain boundary to the pore walls. In general, transport through the grain boundary is expected to be faster, but at sufficiently high temperatures the contribution of lattice diffusion can be significant (Rahaman, 1995).

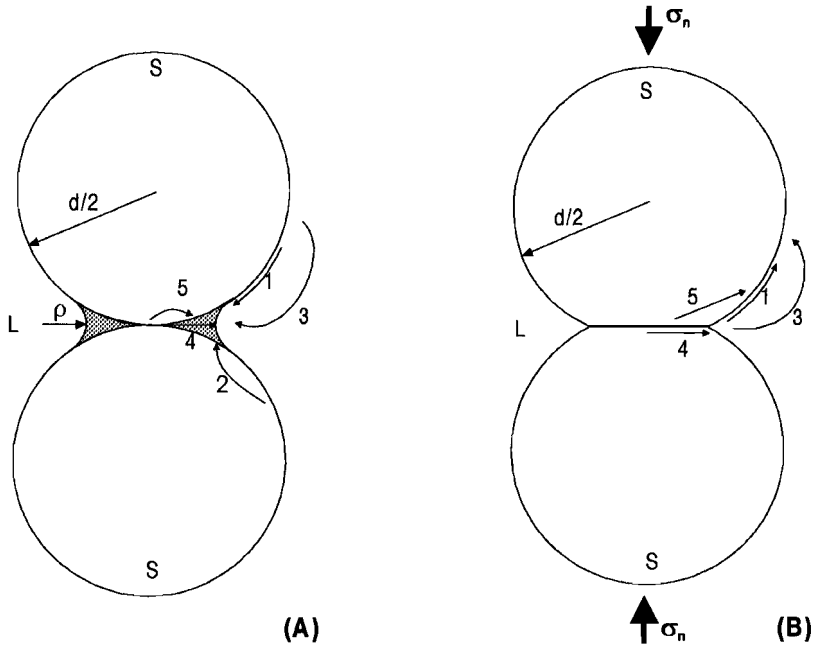

Figure 5.1 Five different matter transport paths are indicated for two different grain-to-grain geometries. (A) Neck growth and densification resulting from the surface energy related driving force due to curvature gradients. (B) Densification resulting from the driving force due to an applied stress. Mass transport paths indicated are 1) surface diffusion 2) lattice diffusion (from the surface) 3) solution/precipitation (transport through the liquid phase) 4) grain boundary diffusion 5)lattice diffusion (from the grain boundary). In case (A) mechanisms 1-3 lead only to neck growth, while mechanisms 4-5 lead to densification in geometry. In case (B) the mass transport paths indicated all contribute to densification because the applied stress driving force is considered larger than the surface energy driving force, otherwise the mass transfer along path 1 and 3 would be in the opposite direction.

5.2.2 Models

In the following, models will be described for densification by diffusion creep, taking both surface free energy and applied stress into account as driving forces. For the present case of solid/melt systems, a distinction has to be made between the cases of 1) non-wetted grain boundaries, whereby the melt phase is restricted to the pores, and 2) wetted grain boundaries, whereby the grain-to-grain contacts are fully penetrated by melt either in a stable equilibrium configuration (stable thin film - Weyl, 1959 and Rutter, 1976) or via dynamic wetting (non-equilibrium island/channel configuration - Raj, 1982 and Lehner,1990).

5.2.2.1 Non-wetted grain boundaries.

For the case when grain boundaries are not penetrated by the melt phase, no island/channel structure or thin film exists within the grain boundary and the grain contact is a solid state boundary. For the case of a 2-grain geometry with a negatively curved grain boundary/pore intersection, as shown in Figure 5.1a, the driving force $\Delta\mu$ for transport of mass from the solid/solid contact to the curved neck region is analogous to that obtained in Chapter 4, for the solid/vapour case. Following the derivation of the relevant surface forces employed in Chapter 2, the modified driving force for the high temperature case is written

$$\Delta\mu \approx \left(\frac{2\gamma_{sl}}{\rho}\left(\cos\frac{\theta}{2} - \cos\frac{\theta_{eq}}{2}\right)\right)\Omega^s \qquad (5.1a)$$

when no stress is applied to the contact, and by

$$\Delta\mu \approx \left(\sigma_n + \frac{2\gamma_{sl}}{\rho}\left(\cos\frac{\theta}{2} - \cos\frac{\theta_{eq}}{2}\right)\right)\Omega^s \qquad (5.1b)$$

when the contact supports a normal stress σ_n. Here $\Delta\mu$ is the difference in chemical potential between source and sink sites, σ_n is the applied stress perpendicular to the contact, γ_{sl} is the solid/liquid interfacial energy, ρ is the radius of curvature of the neck region, θ is the dihedral angle at the pore/grain boundary intersection, θ_{eq} is the equilibrium dihedral angle under hydrostatic conditions and Ω^s is the molecular volume of the solid. Two driving forces can be recognised in equation 5.1b to contribute to the gradient in

chemical potential, i.e. the applied stress and the surface energy related driving force (second term on the right hand side of equation 5.1). When the latter term is positive ($\theta<\theta_{eq}$), these driving forces each contribute to driving self diffusion through the grain boundary and the volume of the crystal (lattice diffusion) from the contact to the negatively curved pore region. Following the same arguments used in Chapter 4, the resulting equation for densification rate ($\dot{\beta}$) when diffusion through the grain boundary is rate controlling is given

$$\dot{\beta} = \frac{12D_{gb}\delta\Omega^s}{kTd^3e_v}(\sigma_n + \frac{24\gamma_{sl}}{de_v}(\cos\frac{\theta}{2} - \cos\frac{\theta_{eq}}{2})) \qquad (5.2)$$

where d is the grain size, T is temperature, k is Bolzmann's constant, e_v is volumetric strain, D_{gb} is the self diffusion coefficient of the rate limiting element through the grain boundary, δ is the grain boundary width. Similarly when diffusion through the lattice is rate controlling, then

$$\dot{\beta}_l = \frac{2D_l\Omega^s}{kTd^2}(\sigma_n + \frac{24\gamma_{sl}}{de_v}(\cos\frac{\theta}{2} - \cos\frac{\theta_{eq}}{2})) \qquad (5.3)$$

where D_l is the lattice self diffusion coefficient of the rate limiting element. Both equations apply for small e_v only, i.e. for $e_v \leq 0.2$.

Note that when the normal stress is zero and $\theta < \theta_{eq}$, densification occurs due to the surface energy term only and 5.1b reduces to 5.1a. In that case, the strain rate dependence on grain size is $\dot{\beta} \propto d^{-4}$ when grain boundary diffusion is rate limiting and $\dot{\beta} \propto d^{-3}$ when volume diffusion is rate limiting. When $\sigma_n \geq 0$ and $\theta > \theta_{eq}$, the surface energy related term is negative and will oppose the stress related driving force, reducing the total driving force for densification.

For the case when densification due to an applied stress is dominant because $\theta \approx \theta_{eq}$, the driving force for transport from contacts to pore walls (see Figure 5.1b), is given

$$\Delta\mu = (\sigma_n - \frac{4\gamma_{sl}}{d})\Omega^s \qquad (5.4)$$

by analogy with the solid/vapour result obtained in Chapter 4. Similarly, the resulting strain rate for densification by grain boundary diffusion, when diffusion is rate limiting is given

$$\dot{\beta} = \frac{12 D_{gb} \delta \Omega^s}{kTd^3 e_v} (\sigma_n - \frac{4\gamma_{sl}}{d}) \tag{5.5}$$

For the same geometry, but with lattice diffusion being rate controlling, the compaction strain rate is given

$$\dot{\beta}_l = \frac{2 D_l \Omega^s}{kTd^2} (\sigma_n - \frac{4\gamma_{sl}}{d}) \tag{5.6}$$

When comparing the equations (4.5) with (5.3) and equation (4.4) with (5.2) for the solid/vapour and the solid/melt systems, since only the phase in the pore changes the relative densification rate is expected to change by a factor

$$\frac{\dot{\beta}_{sol/vap}}{\dot{\beta}_{sol/meltpores}} = \frac{(\sigma_n d e_v + 24\gamma_{sv}(\cos\frac{\theta}{2} - \cos\frac{\theta_{eq}}{2}))}{(\sigma_n d e_v + 24\gamma_{sl}(\cos\frac{\theta}{2} - \cos\frac{\theta_{eq}}{2}))} \tag{5.7}$$

With γ_{sl} = 0.5 ± 0.2 J/m ^{2} (Cooper and Kohlstedt, 1982) and γ_{sv} for high energy interfaces being ≈ 2.7 J/m ^{2} (Watson, 1997), then typically $\gamma_{sv} \approx 5\gamma_{sl}$. Hence it can be seen that for the same applied stress, strain, grain size and cosine difference-term, the densification rate is faster for the solid/vapour case than for the solid/melt case with unwetted grain boundaries. This is simply because γ_{sv} is larger than γ_{sl}.

When microstructural equilibrium is approached (i.e. $\theta \approx \theta_{eq}$) or when neck curvature effects are negligible, so that equation (5.5) and (5.6) apply, the ratio of strain rates becomes

$$\frac{\dot{\beta}_{sv}}{\dot{\beta}_{sm}} = \frac{(\sigma_n d - 4\gamma_{sv})}{(\sigma_n d - 4\gamma_{sl})} \tag{5.8}$$

Since $\gamma_{sv} > \gamma_{sl}$, (Watson, 1997 and Cooper and Kohlstedt, 1982) this implies that $\dot{\beta}_{sm} > \dot{\beta}_{sv}$ when $\theta \approx \theta_{eq}$. Moreover, the condition of zero driving force, $\sigma_n d=4\gamma_{sv}$, requires larger stresses- and/or grain sizes than for $\sigma_n d=4\gamma_{sl}$, so that the regime for densification versus neck growth processes will be somewhat larger for the solid/melt case then for the solid/vapour case.

An important conclusion from the above, is that densification in a solid/melt system is not necessarily faster than densification in a solid/vapour system, as often assumed, see e.g. equation 5.7 (e.g Kohlstedt, 1992).

5.2.2.2 Wetted grain boundaries

When the grain boundary is assumed to contain melt in an island/channel structure or thin film, then the models derived in chapter 2 for low-temperature solution/precipitation creep processes can be applied. To allow direct comparison with the model for non-wetted grain boundaries, the diffusion path length is taken the same as for the non-wetted model derived in Section 5.2.2.1. For the case where grain boundary diffusion is the rate limiting step, the rate of densification of a partially molten aggregate is accordingly given

$$\dot{\beta} = \frac{12Z^*\Omega^s}{kTd^3e_v}(\sigma_n - \frac{4\gamma_{sl}}{d}) \qquad (5.9)$$

where $Z^* = CD_{gbf}\delta(1-\alpha)$, C is the concentration of the solid in the liquid phase, δ is the grain boundary width, α is the fraction of islands within the grain contact, and D_{gbf} is the diffusion coefficient through the grain boundary fluid. When the melt is expelled from the grain boundary, then equation (5.9) reduces to equation (5.5). Thus the densification rate for the wetted and non-wetted grain boundary cases differs only by the kinetic factor $Z^* = CD_{gbf}\delta(1-\alpha)$, for the melt-filled grain boundary, versus $\delta D_{gb(sol/sol)}$, the kinetic factor for the solid/solid grain boundary. Following the same approach as for non-wetted boundaries in Section 5.2.2.1, the ratio of strain rates for the solid/vapour and the solid/melt systems is given

$$\frac{\dot{\beta}_{sv}}{\dot{\beta}_{sm}} = \frac{\delta D_{gb}(\sigma_n d - 4\gamma_{sv})}{Z^*(\sigma_n d - 4\gamma_{sl})} \tag{5.10}$$

Accordingly, it is clear that whether densification in a solid/melt system is faster than in the corresponding solid/vapour system at the same stress, strain, temperature and grain size conditions, depends not only on the relevant kinetic parameters but also on the differences in the relevant interfacial energies and whether or not the melt phase wets the grain boundaries (dynamically or stably). This must be taken into careful account when interpreting experimental results.

5.3 Experimental Methodology

In this study, samples of Mg-forsterite powder infiltrated with a simulated basaltic melt, were uniaxially hot-pressed at applied axial stresses between 0.13 and 6.37 MPa. The starting grain sizes of the forsterite samples ranged from 1.5 to 20 μm. Six isothermal stress-stepping experiments were performed in all, but some additional tests were done in order to study the melt infiltration and grain growth behaviour. Moreover, for the 1.5 μm grain size material, two experiments were performed at different temperatures to obtain an estimate of the apparent activation energy for compaction creep.

5.3.1 Starting material and sample preparation

The starting material for these experiments was finely powdered forsterite, typically 99% pure Mg_2SiO_4, obtained from Cerac Inc. (Milwaukee, USA) and idential to that used for the experiments on melt-free forsterite reported in Chapter 4.

Analysis of the forsterite powder (as delivered) by powder x-ray diffraction (XRD) has shown that apart from the forsterite only a minor amount of MgO is present. McDonnell (1997) has investigated the same forsterite powder in more detail using standardised mixtures and found the amount of MgO to be ~ 1%. No other crystalline phases were found to be present. Inductively-coupled plasma atomic emission spectroscopy (ICP-AES) performed on the forsterite powder showed good agreement with the element analysis by Cerac BV given in Chapter 4.

Following the procedure employed for the solid/vapour experiments of Chapter 4, the granular forsterite was first separated gravitationally in methanol to obtain grain size fractions with average grain sizes and standard deviations of 1.5 ± 0.3 μm, 2.9 ± 0.5 μm, 8.1 ± 2 μm, and 20 ± 5 μm, determined by measuring the longest and shortest axes of typically 100-150 individual grains on Scanning Electron Microscope (SEM) images. To prepare individual samples for cold-pressing, approximately 1 gram of material was loaded into a steel die, with an internal diameter of 10 mm, and uniaxially cold-pressed at 200 MPa. The resulting samples typically had lengths between 6 and 7 mm.. They were subsequently heated, unconfined, for 48 hours at 1300 °C to anneal out any dislocation damage introduced during the cold-pressing stage and to lightly sinter into a cohesive sample. The final porosities were in the range from 33 to 39%. No grain growth occurred during the heat treatment stage.

The powder used to make the basaltic melt phase was prepared separately. The composition used was of 51% SiO_2, 29% MgO and 20% Al_2O_3. This composition represents a chemically-simplified analogue for a natural MORB (mid-ocean ridge basalt) melt which is chemically in equilibrium with Mg-forsterite and molten at a temperature corresponding to the mid-ocean ridge melt source region (~1300-1550 °C, Chapter 1). To achieve these requirements, the composition of the melt must be in the forsterite primary field (Figure 5.2). For all mixtures falling within the limits of the primary field, forsterite will be the first phase to crystallise on cooling from the molten condition. Conversely, assuming chemical equilibrium is always maintained, forsterite will be the last phase to disappear from the melt on heating the mixture from the solid condition. The fact that forsterite is soluble in the melt (i.e. melt composition in the forsterite primary field), is necessary to allow the study of solution/precipitation processes. For the experiments and the result analyses the following (practical) conditions had to be taken into account. The necessary creep resistance of Al_2O_3 parts of the experimental set-up under stress determined the upper temperature limit that could be used to be ~ 1470 °C. Further, chemically restricting the melt phase to the ternary phase diagram, in the way described, allows detection of the melt phase by the presence of alumina when using EDS analyses on polished (SEM) samples. While determining the composition of the melt phase (by EDS), and comparing it with the expected composition in the phase diagram is used to monitor whether chemical equilibrium is achieved and/or whether the melt phase in the samples after densification has been quenched sufficiently fast.

The powder with the desired melt composition was prepared via a sol-gel method, consisting of a variant of the sol-gel route for preparing forsterite and/or basalt given by Kazakos et al (1990). In the method finally adopted, first tetra-ethyl orthosilicate (TEOS) is mixed with ethanol in a closed glass container to render the TEOS soluble. Mg-nitrate and Al-nitrate are then mixed with double-distilled water in a Teflon (PTFE) beaker,. The resulting solution is added after 10 minutes to the container with TEOS and stirred for 24 hours. Ammonium hydroxide is subsequently added, stirring the solution continuously while a fast gelling process takes place. After 3 hours of stirring, the gel is placed in an oven at 85 °C to dry. After 20 hours, the dried gel is ground, transferred to a porcelain crucible and placed in a small furnace to be fired for 24 hours at 650 °C.

Preparation of melt for infiltration into individual samples, from the basaltic powder, was carried out by heating a few grams of powder in a small Pt crucible, several times, for a few hours at 1470 °C and/or 1500 °C. This was done using an electrically heated box-furnace, cooling rapidly between the heating stages. For fast cooling, the Pt crucible was transferred from the hot furnace to ambient conditions. Several heating cycles were required to remove the gas-bubbles from the melt phase, releasing minor volumes of volatile components (e.g. water and CO_2).The bubbles must be removed for successful subsequent infiltration of the melt phase into the porous solid sample. After a total heating period of ~ 8 hours, in 3 or 4 cycles, all bubbles, except those attached to the bottom of the crucible had been removed and no visible crystallisation occurred during cooling, so that a clear glass was produced.

In order to infiltrate basaltic melt into the individual forsterite samples, the box-furnace was pre-heated to 1470 °C or 1500 °C. Each sample was then placed in the appropriate Pt-crucible on top of the basalt glass, without it touching the crucible walls, and the crucible transferred to the furnace for 0.5 (1500 °C) to 2-2.5 hours (1470 °C). After the allotted time, the Pt crucible was removed from the furnace and left to cool to room temperature. Due to pervasive infiltration of the melt into the sample, the cooled samples show dilation in all directions but remain intact (for the heating periods used). Samples to be stress-densified were polished to form cylinders of 9.9 mm diameter, thus fitting the die set-up used in the densification tests.

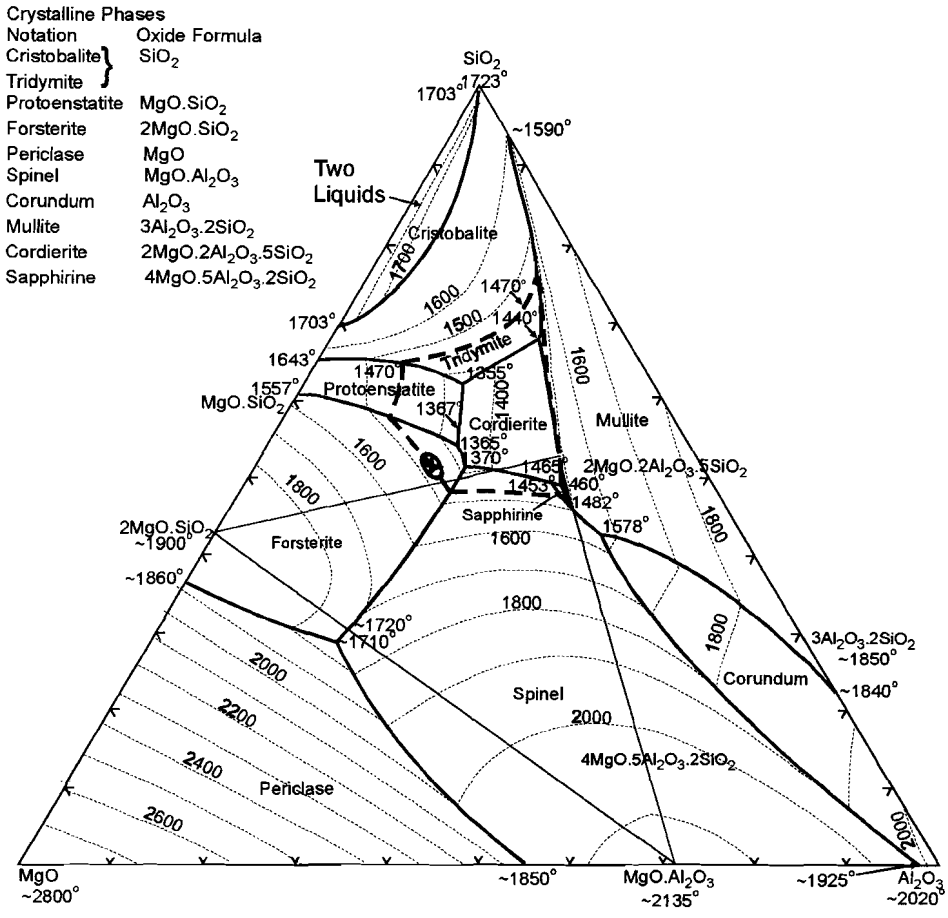

Figure 5.2 Phase diagram for the system SiO_2, MgO, Al_2O_3, after Osborn and Muan (1960). Of the sub-solidus triangles, only Forsterite-Cordierite-Spinel is drawn. The 1470 °C isotherm is indicated by the dashed line, indicating the area (inside the closed line) of equilibrium melt compositions at this temperature. The composition of the basaltic melt (before infiltration) is indicated by the circled cross.

Analysis of the basaltic glass by XRD, at the pre-infiltration stage showed no crystalline phases, indicating that if any crystallites are formed during cooling, the amount is less than 0.5-1%, the detection limit of the XRD-technique. Two differential thermal analysis (DTA) experiments were performed on the glass at Hoogovens Ceramic Laboratory (see Figure 5.3). The apparatus used was a Setaram type tag24. The sample mass was 53.6 mg, the container Al_2O_3, the atmosphere is oxygen and the heating and the cooling rate was 10°C/minute. The principal properties of the glass emerging from the DTA are listed in Table 5.1.

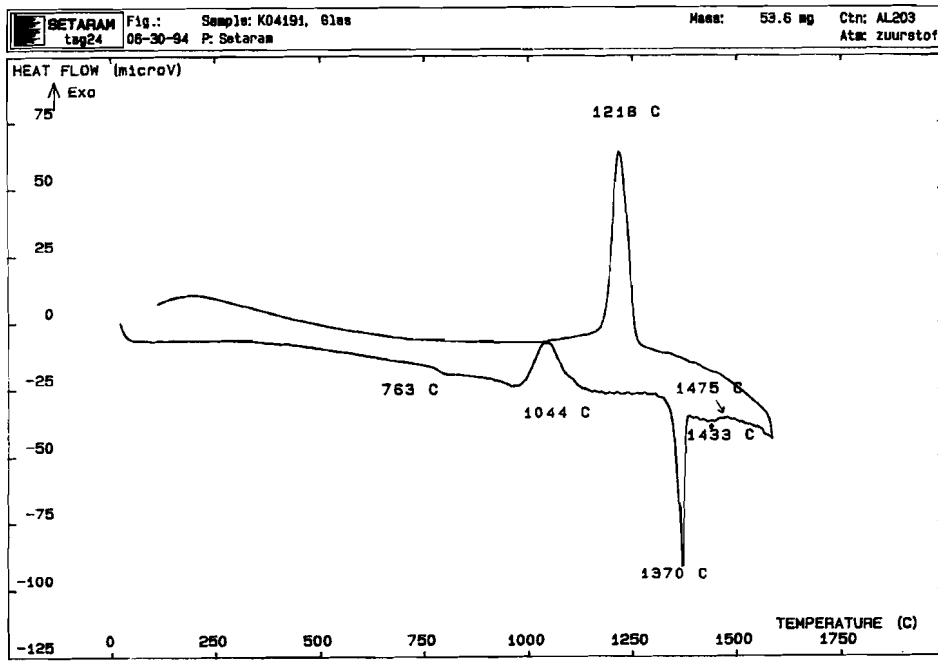

Figure 5.3 Differential thermal analyse (DTA) experiment on basaltic glass. Heating and cooling rate at 10°C/minute up to 1550 °C. Indicated are peak temperatures of which the significance is indicated in Table 5.1.

Analysis Technique	Observation/Analysis	Implications
SEM/EDS	Average chemical composition of the melt 0.525 SiO_2, 0.295 MgO and 0.18 Al_2O_3	Close to aimed composition Within forsterite stability field. Variations in composition below detection limit of SEM/EDS using standards (~ ±1%)
SEM	No crystals observed in the "glass"	Liquid is indeed quenched to a glass
DTA (heating)	Glass transition temperature at 760-780 °C	During preparation liquid was quenched to a glass
DTA (heating)	Devitrification at 970-1125 °C	Ordering/crystallization of the liquid at a heating rate of 10°/minute
DTA (heating) (Compare with phase diagram)	Melting trajectory from 1350-1475 °C with the main peak at 1370 °C	Note that if no crystalline ordering had occurred, no melting would be observed. Main peak of melting coincides with invariant reaction point of the forsterite, spinel, cordierite triangle in the phase diagram (see Figure 5.2). Onset of melting within 5 °C from (SiO_2, MgO, Al_2O_3) ternary eutectic. Everything molten at 1475°C
DTA (cooling)	Large exothermic peak around 1218 °C (reverse of melting reaction, i.e. crystalline ordering). No reverse of the glass transition	Cooling with 10°C/minute is insufficient to cool liquid to a glass.

Table 5.1 Summary of the observations and analyses using DTA and SEM/EDS techniques on the rapidly cooled liquid. In preparation of the glass, the Pt-container with the liquid was placed from 1470 °C to room temperature. From the data in the table in can be concluded this was sufficient to quench the liquid to a glass. Note also the good agreement between the melting trajectory by DTA and the expected values from the phase diagram which indicates a negligible presence/influence of impurities (including a possible influence of water).

XRD analysis of a melt infiltrated sample (infiltration at 1470 °C for 1 hour) shows forsterite as the only detectable crystalline phase. The minor amount of MgO has disappeared. No other crystalline phase has appeared after rapid cooling of the infiltrated sample. No crystals were observed in the melt phase after inspection with the SEM.

5.3.2 High temperature densification apparatus

Stress-densification experiments were performed using a small-scale set-up consisting of a uniaxial die plus loading pistons (see inset of Figure 5.6). This itself was loaded using a programmable Instron Model 8500 testing machine, equipped with its own loading pistons and split furnace (maximum temperature 1773 K/ 1500 °C), all kindly made available at Hoogovens Ceramic Laboratory (IJmuiden, The Netherlands). The die, pistons and other parts, indicated in the inset of Figure 5.4, were constructed using high purity alumina (Alsint). The die is lined with thin Pt foil and also the pistons were topped with Pt-foil plates to avoid reaction between the forsterite/basalt sample and the alumina parts. In contrast to the solid/vapour experiments, reported in Chapter 4, the die for the solid/melt experiments has an annular recess machined into the inner surface of the die, close to the lower piston, to create an extra volume to receive excess melt squeezed out of the sample during hot-pressing (Figure 5.4). From this extra volume the melt can be squeezed out of the die, along the lower piston.

In order to test if the melt could be squeezed out of the die set-up without requiring a significant stress to be applied, an specially designed test was performed. A solid volume of glass was machined and polished to the same dimensions as the forsterite samples and loaded into the small die set-up. This was placed in a (box) furnace at 1470 °C and a dead weight of 150 grams was placed on the top piston, i.e. a stress of ~ 2.10^4 Pa was applied. After 1 hour the set-up was taken from the furnace and it was observed that the top piston had advanced into the die, while all melt had been squeezed out (the die was sawn open for control purposes). Hence, it is inferred that the melt phase is maintained at atmospheric pressure during the hot-pressing experiments and that effects due to frictional forces are $<2.10^4$ Pa.

The split furnace within the Instron machine is heated by Super Kanthal 33 heating elements and operated by a programmable Eurotherm 821 controller. The sample temperature was monitored and the furnace controlled by B-type (Pt30Rh-Pt6Rh) thermocouples, positioned outside and a few millimetres away from the die assembly. Temperature stability is ± 2 °C. The displacement of the lower die piston into the die is measured remotely using an LVDT located in the water-cooled part of the lower Instron piston. This LVDT has a range of ± 5 mm and an accuracy of 0.02%. It was calibrated using a specially adapted micrometer fitting into the Instron set-up (Figure 5.4). Several calibration runs were performed using an alumina dummy to determine the stiffness of the

set-up. No permanent creep of the alumina parts took place and the small elastic relaxations during unloading were reproducible. Force, displacement and temperature signals were logged automatically by the Instron computer logging/control system throughout the test, with a 16-bit resolution and a sampling rate of up to 5.1 kHz over 8 possible channels.

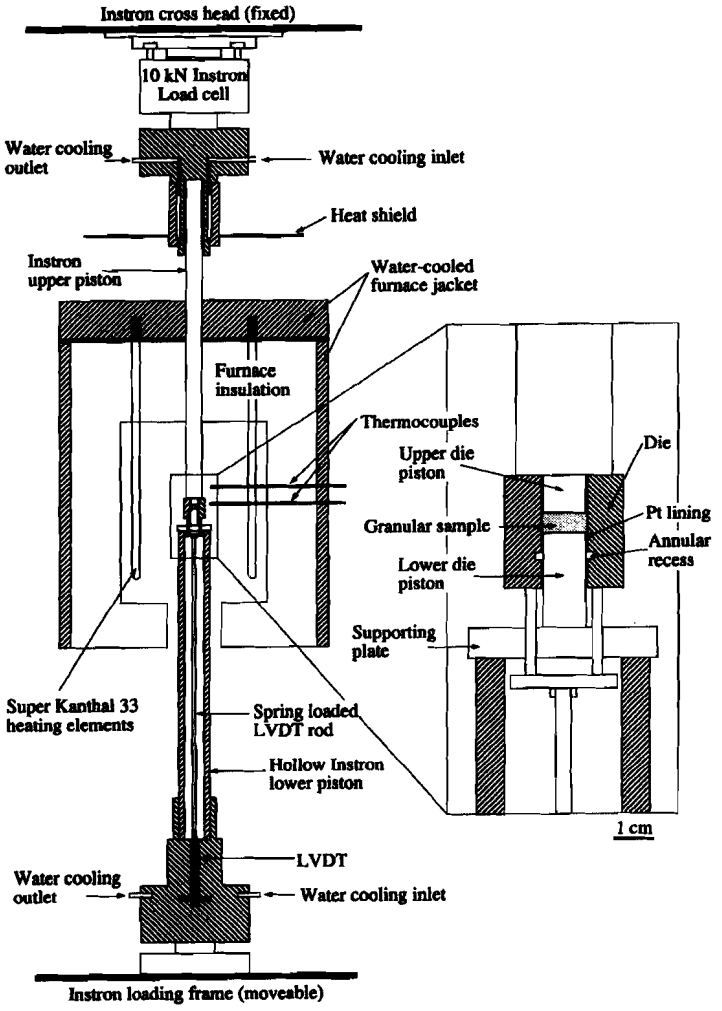

Figure 5.4 Schematic diagram showing the experimental hot-pressing set-up located within the Instron loading frame.

5.3.3 Testing Procedure and Data Processing

In each experiment, the infiltrated sample, prepared as described above, was inserted into the die (diameter of 9.9 mm) and the complete die assembly was then located on the lower Instron piston within the Instron furnace. The samples were heated to 1743 K (1470 °C), or 1663 K in case of one experiment, then left at this temperature for 1 hour to equilibrate before any load was applied. The Instron lower piston was then advanced upward to bring the upper Instron piston into contact with the die assembly. Initial loading was always performed to reach a compressive stress of 6.3 MPa, ramping the load linearly over a 2 minute period under computer control. A few experiments were terminated at the end of this first loading stage (i.e. on achieving the applied stress of 6.3 MPa) to examine grain size, sample length, diameter and porosity. In all cases, the sample filled the diameter of the die completely while porosity decreased or increased to a closely reproducible value of 33 ± 2%. At the point where ramping was terminated (6.3 MPa), the samples studied showed that the excess melt had been squeezed out of the sample, establishing a load-bearing framework of grain-to-grain contacts. This point was chosen as the starting point of the hot-pressing experiment (time=0). The associated length and starting porosity at this time are subsequently referred to as the starting length and starting porosity of the sample and used as such for further data processing.

After completing the initial loading stage of each experiment, compaction creep was monitored as function of time, with the computer logging the various data channels every 6 or 12 seconds. Stress-stepping experiments were performed using applied stresses in the range 0.1 - 6.3 MPa. Stress stepping was performed in the downward direction from 6.3 MPa to 3.8 MPa, 1.9 MPa, 1.3 MPa, 0.95 MPa, 0.64 MPa, 0.38 MPa and sometimes further to 0.26 MPa, finally stepping up again to 6.3 MPa in four experiments. Six stress stepping tests were performed using three different starting grain sizes. All tests performed are listed in Table 5.2, along with the corresponding experimental conditions. Maximum strain achieved in the tests ranged from ~10-16%.

Tests were terminated by switching the furnace off and keeping the sample loaded during unassisted cooling. More rapid quenching was impossible because the heating elements and the ceramic parts are highly sensitive to thermal shock. After 2.5 minutes the temperature had dropped from 1470 °C degrees to 1350 °C and after a total of 17 minutes 1100 °C was reached. After further 11 minutes cooling, and on reaching a temperature of about 1000 °C (1273 K), the load was removed and the die set-up was left in place to cool

down to room temperature overnight. Finally, the die was taken out of the Instron, sawn open, and the final length of the sample was measured. The sample was subsequently impregnated with epoxy resin to allow sectioning for optical microscopy, SEM (Scanning Electron Microscopy) and TEM (Transmission Electron Microscopy).

Volumetric strain versus time data were calculated directly from the displacement versus time records obtained for each sample, after applying corrections for apparatus distortion and thermal expansion. A running least squared fitting method was used to smooth the data obtained from each experiment and to reduce the densely spaced data stream to a set of several hundred points. Subsequently, strain rates were calculated for each experiment, and each constant stress-step, using the 3-point central difference method applied to the reduced data-set. This enabled the dependence of the strain rate on strain and stress to be evaluated.

5.3.4 Grain growth experiments and grain size estimation

Any dependence of the strain rate on grain size could not be directly determined in the present experiments, because of grain growth during infiltration as well as during the equilibration period of 1 hour at 1470 °C (1743 K) before densification. Therefore 6 extra tests were performed in order to calculate (or estimate) the grain size reached at different stages of sample preparation and experimentation (Table 5.2). Two different temperatures (1470 °C and 1500 °C) and two different initial grain sizes (1.5 μm and 8 μm) were used. The samples were infiltrated with melt and then subjected to different heating periods (Table 5.2). Thereafter, they were rapidly cooled by removing them to room temperature, as in the standard procedure. The samples were then analysed and grain sizes measured, taking the average of the longest and shortest axis on SEM micrographs. To calculate grain growth, the same procedure was used as by Hirth and Kohlstedt (1995). These authors corrected their grain size values according to a grain growth law, in order to determine the dependence of strain rate on grain size in creep experiments on dense olivine (Fo 91)/enstatite/melt samples.

Experiment	Grain size (μm) (d_{start}, d_{infil}, d_{equil} ,d_{end})	Temperature/ time (Infiltration/ deformation)	Stress (steps) (MPa)	datapoints (•) at indicated constant strains (extrapolated (o))		
				7.5%	10%	12.5%
1ol2			6.3	o		
	d_{start}=1.5	$Temp_{infilt}$=1743K	3.8	o		
		$Time_{infilt}$= 2 hours	1.9	o		
Max. e_v	d_{infilt}=13.3		1.3	•		
10%	(calc)	$Temp_{deform}$=	0.95	o		
	d_{equil}=**16.5**	1743 K	0.65	o		
Min.	(calc)	$Time_{deform}$= 6.2	0.38	o	o	
porosity		hours	0.26		o	
26%	d_{end}=**25.2**					
1ol4			6.3	•	o	
	d_{start}=1.5	$Temp_{infilt}$=1743 K	3.8	o	•	
Max. e_v		$Time_{infilt}$=2.5	1.9		o	•
14.5%	d_{infilt}=14.9	hours	1.3			o
	(calc)		0.95			o
Min.	d_{equil}=19.3	$Temp_{deform}$=	0.65			o
porosity	(calc)	1663 K				
23%	d_{end}=**15**	$Time_{deform}$=2.5 hours				
1ol6			6.3	o		•
	d_{start}=1.5	$Temp_{infilt}$=1773 K	3.8	•	o	
Max. e_v		$Time_{infilt}$=0.5 hour	1.9	o	o	
13.4%	d_{infilt}=6.3		1.3		•	
	(calc)		0.95		o	o
Min.	d_{equil}=**11.4**	$Temp_{deform}$	0.64		o	o
porosity	(calc)	1743 K	0.38			o
24%	d_{end}=**17.7**	$Time_{deform}$=2.9 hours				
5ol3			6.3	o	o	o
	d_{start}=3	$Temp_{infilt}$=1743 K	3.8	•	•	o
Max. e_v		$Time_{infilt}$=0.5	1.9		o	o
16.2%	d_{infilt}=6.8	hours	1.3		o	o
	(calc)		0.95			•
Min.	d_{equil}=**11.7**	$Temp_{deform}$=	0.64			o
porosity	(calc)	1743 K				
21%	d_{end}=**14**	$Time_{deform}$=2.4 hours				

Experiment	Grain size (μm) (d_{start}, d_{infilt}, d_{end})	Temperature	Stress (steps) (MPa)	data (•) at indicated constant strains (extrapolated (o))		
				7.5%	10%	12.5%
5ol10	d_{start}=8		6.3	o		
		$Temp_{infilt}$=1773 K	3.8	•	•	o
Max. e_v	d_{infilt}=15.6	$Time_{infilt}$= 2 hours	1.9	o	o	o
11.3%	(calc)		1.3		o	•
	d_{equil}=**18.3**	$Temp_{deform}$=	0.95			o
Min.	(calc)	1743 K	0.64			o
porosity	d_{end}=**19**	$Time_{deform}$= 2.2	0.38			o
26%		hours				
5ol9			6.3	o	o	o
	d_{start}=20	$Temp_{infilt}$=1773 K	3.8	•	o	
Max. e_v		$Time_{infilt}$=0.5 hour	1.9	o	o	o
14.6%	d_{infilt}=20.9		1.3	o	•	o
	(calc)	$Temp_{deform}$=	0.95		o	o
Min.	d_{equil}=22.9	1743 K	0.65		o	•
porosity	(calc)	$Time_{deform}$=3.2	0.38			•
22%	d_{end}=**22.3**	hours	0.26			o
1ol1	d_{start}=1.5	$Temp_{infilt}$=1743 K				
	d_{infilt}=10.6	$Time_{infilt}$= 1 hour				
1ol5	d_{start}=1.5	$Temp_{infilt}$=1743 K				
	d_{infilt}=19	$Time_{infilt}$=2.5 hours				
5ol5	d_{start}=8	$Temp_{infilt}$=1773 K				
	d_{infilt}=14	$Time_{infilt}$=1.5 hours				
5ol5b	d_{start}=8	$Temp_{infilt}$=1773 K				
	d_{infilt}=16	$Time_{infilt}$=3 hours				
5ol7	d_{start}=8	$Temp_{infilt}$=1773 K				
	d_{infilt}=15	$Time_{infilt}$=3 hours				

5ol7b	d_{start}=8 d_{infilt}=18.5	$Temp_{infilt}$=1773 K $Time_{infilt}$=6 hours				

Table 5.2 Overview of experiments performed and experimental conditions. Indicated in the grain size column is whether the grain size data were measured or were calculated using the grain growth law. Indicated on the right of the table are the combinations of stress step and constant strain for which the strain rates were used constructing the composite graphs on mechanical data (see experimental results).

5.3.5 Microstructural analyses

Microstructural analysis was carried out on all starting powder fractions, on fractured sample fragments and on thin sections of all epoxy impregnated samples, deformed and heated only. This was done using optical microscopy, Scanning Electron Microscope (SEM) and Transmission Electron Microscopy (TEM) performed in combination with detailed chemical analyses by scanning electron (x-ray energy) dispersion (EDS) under the SEM and TEM, as well as separate X-ray diffraction (XRD) and thermal analysis (DTA/TGA) performed on powdered sample material. For the SEM-work, polished thin sections were prepared (10 to 15 μm thick) and studied first by means of transmission optical microscopy. The thin sections were then etched for 1 minute in a 10% HF solution, carbon coated and studied under the SEM. Also, TEM foils were prepared of hot pressed samples 1ol2 and 1ol4. TEM-sample preparation, involved first ion-beam thinning followed by carbon coating.

5.4 Experimental Results

5.4.1 Mechanical data

As described above, the initial loading stage (i.e. loading to 6.3 MPa) achieved complete lateral filling of the die, resulting in a reproducible "starting" porosity of 33 ± 2% and establishing a load-supporting grain framework from which the excess melt was expelled.

Figure 5.5 shows representative densification or compaction creep curves obtained from the stress-stepping tests. Only data obtained at thermal equilibrium and constant stress are plotted (not plotting relaxation/expansion/compaction during ramping and equilibration periods). Figure 5.6a-f shows the corresponding strain rate versus strain data obtained from the stepping experiments. Clearly, strain rate tends to decrease with increasing strain and constant stress. In these graphs, vertical lines indicate constant strain values used to construct composite diagrams of log strain rate versus log stress at constant volumetric strain. Most of the strain rate data are extrapolated or interpolated to these strains using the linear trends seen in the log strain rate versus strain data segments associated with each stress step (Table 5.2). Extrapolation was performed by extending a best (least squares) fit line through the data points when at least the last 75% of the data-set showed a good linear fit (correlation coefficient, R^2 >0.9). Alternatively, when the fit was less good, two lines were drawn from the centre of the data segment, one with the maximum slope shown by other stress steps in the same test and a second, horizontal line (minimum slope). Extrapolation in this way never extended more than 2% strain and the range in strain rate obtained at fixed strain is represented by error bars in subsequent handling.

Figures 5.7a-c show the log strain rate versus log stress data obtained for constant volumetric strains of 7.5%, 10% and 12.5% using the extrapolated data from Figure 5.6 and Table 5.2. All experiments at 7.5% strain show slopes in the range 0.5-1.0, except for the 2 data points of experiment 5ol3. At 10% strain, 5ol3 shows a slope of 1.3 while for the other 5 experiments the slope is in the range 0.8-1.1. At 12.5% strain, experiments 5ol9 and 5oll0 show best fit slopes of 1.0 (linear stress dependence of the strain rate), while for the other experiments the average slopes are in the range 1.1-1.3. Here, the deviation from ~1.0 occurs mainly below ≤ 1.9 MPa. Note that 50l9 and 5oll0 are the

experiments with the largest initial grain sizes. Summarising, a minor increase in slope can observed from 7.5% to 12.5% strain, however, deviations from 1.0 are small (-0.5, +0.3), demonstrating a broadly linear dependence of strain rate on stress.

As seen in table 5.2, three stress-stepping experiments with the same starting grain size of 1.5 μm were performed at two different temperatures, in order to obtain a first estimate of an apparent activation energy for densification. However, experiment 1ol4 performed at 1390 °C shows faster densification then experiment 1ol2 and 1ol6 performed at 1470 °C, contrary to expectations for an Arrhenius type of temperature dependence. As already mentioned, any dependence of strain rate on grain size could not be directly determined because of grain growth effects.

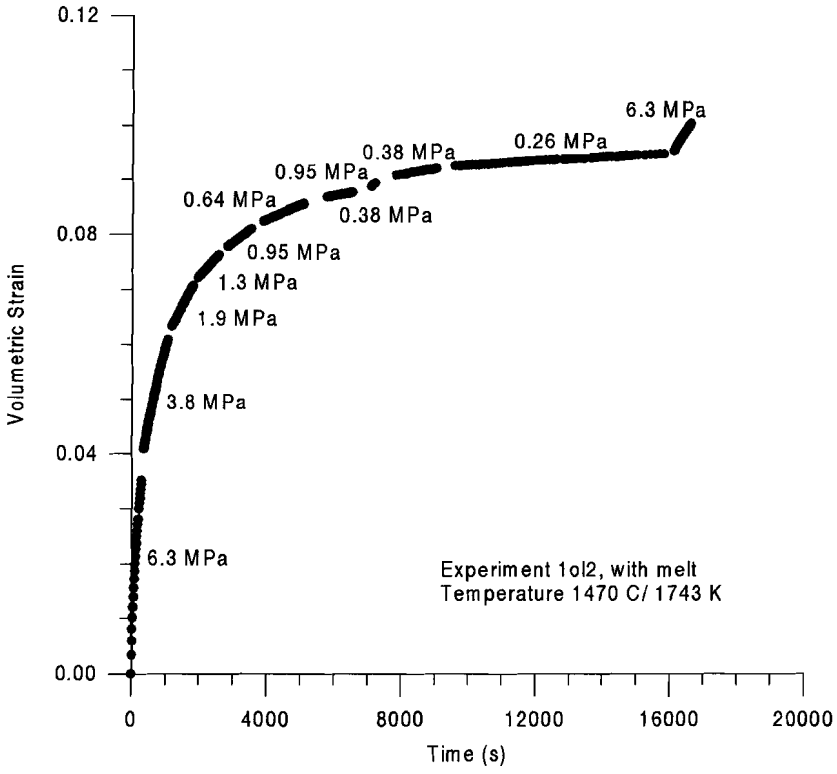

(A)

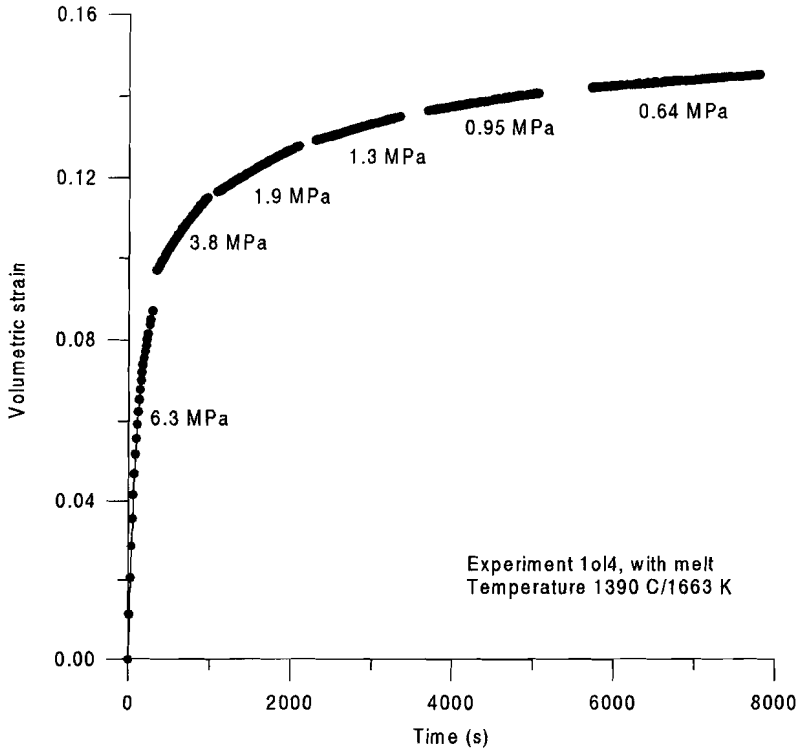

(B)

Figure 5.5 Typical creep curves obtained for the forsterite aggregates plus basaltic melt.a) at 1470 °C b) at 1390 °C

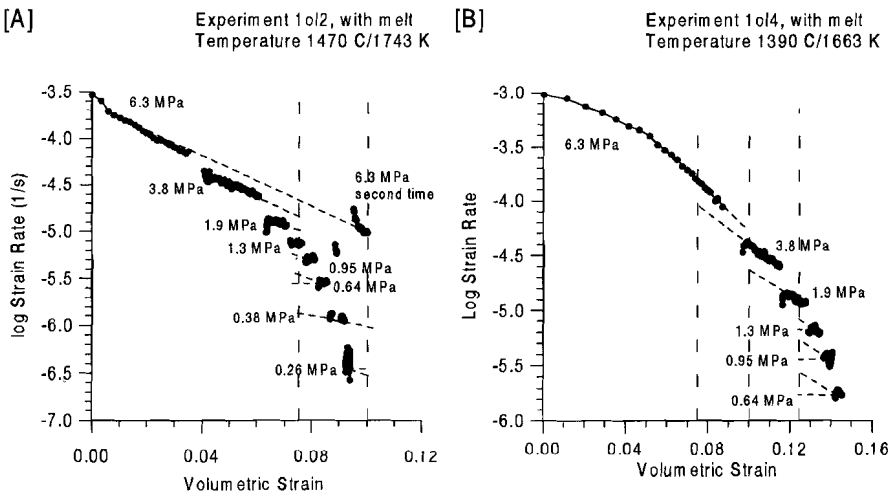

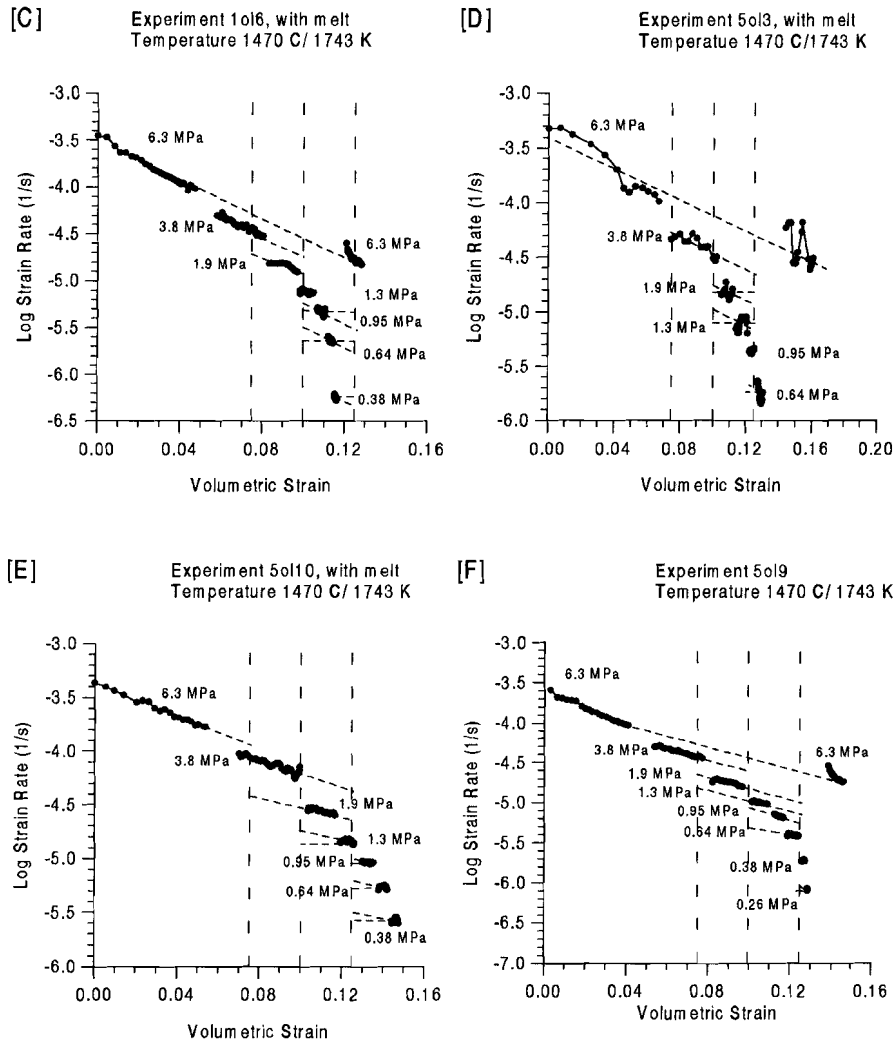

Figure 5.6 A -F. Log strain rate versus volumetric strain diagram for all stepping experiments. Vertical dashed lines indicate the strain values to which the strain rate data per step were extrapolated for comparison at constant strain (i.e. constant porosity or structure).

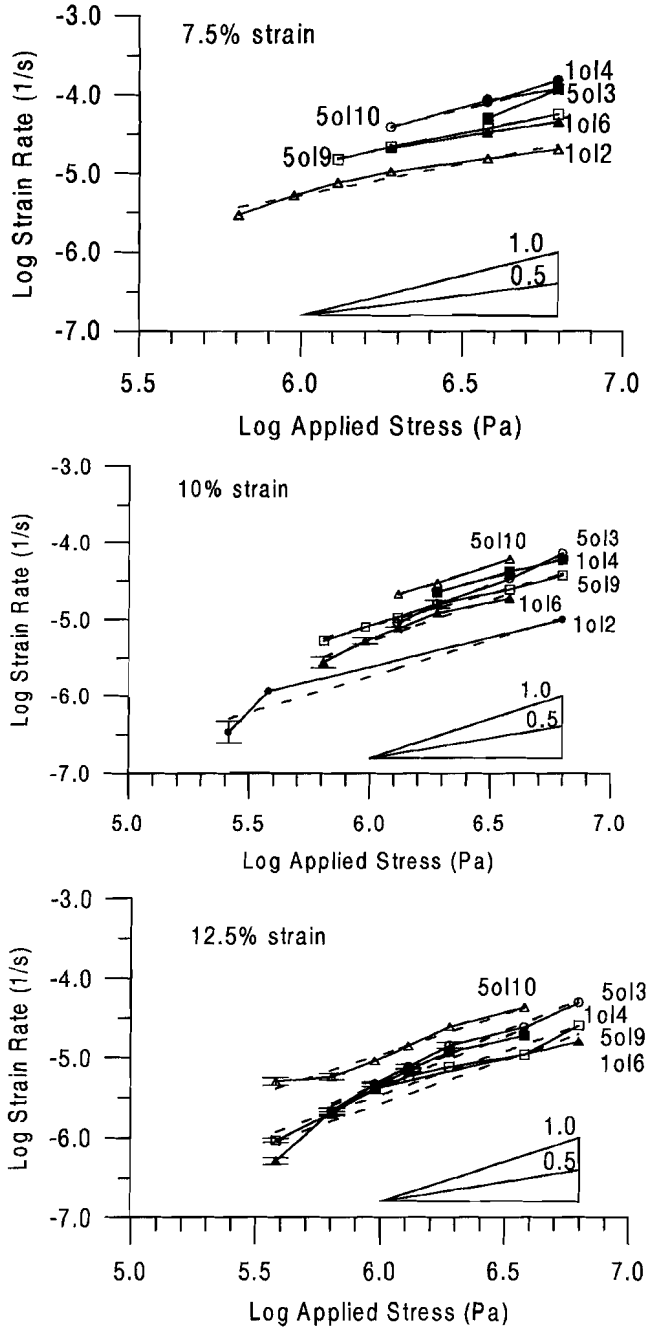

Figure 5.7 a - c. Log-Log plots of compaction strain rate versus applied stress for different grain sizes at fixed values of compaction strain. (A) at 7.5% strain, (B) at 10% strain and (C) at 12.5% strain.

5.4.2 Microstructural and microchemical analyses

Study of the granular starting material fractions showed that all grain size fractions consisted of nearly equiaxed, rounded grains of forsterite. Only the 20 μm grain size fractions contained a small percentage (<10%) of somewhat elongated grains. Sintering effects during the annealing heat treatment at 1300 °C, prior to melt infiltration and deformation, produced small necks between grain contacts, but no grain growth was observed. Figure 5.8 shows a typical microstructure after heat treatment (annealing/sintering) but before melt infiltration and deformation. Average grain sizes are indicated in Table 5.2 as d_{start}.

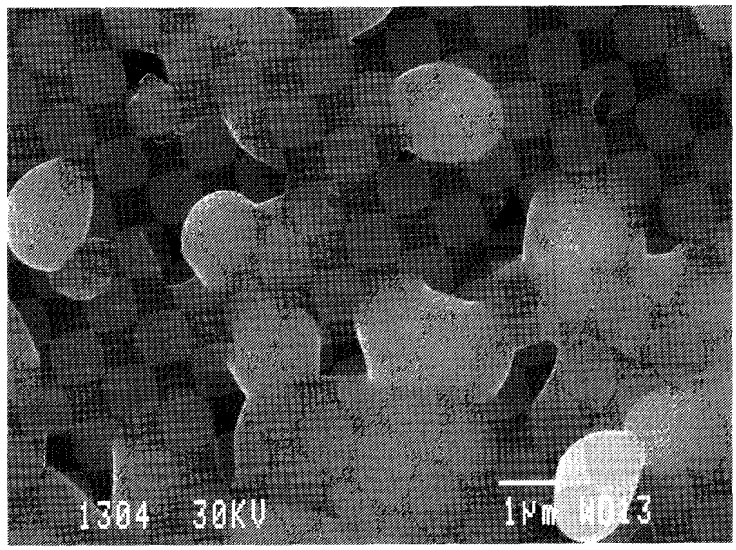

Figure 5.8 SEM micrograph of a forsterite aggregate sintered for 24 hours at 1300°C. Sample 5ol3 prior to melt infiltration

After melt infiltration at 1470 or 1500 °C, grain shapes changed quickly from fairly rounded grains to faceted or euhedral crystal shapes (Figure 5.9) while grain growth occurred simultaneously. The grain size data obtained from growth experiments are given in Table 5.2 as d_{infilt}. Figure 5.9a shows the microstructures after 1 hour infiltration/heat treatment at 1470 °C of a 1.5 μm starting material sample (1ol1). Some smaller grains can still be observed but most are faceted and grains have grown from 1.5 to ~11 μm on average. Figure 5.9b shows the microstructure of sample 5ol5b after infiltration with melt/heat treatment at 1500 °C for 3 hours. This shows euhedral grains which have grown

from an initial average grain size of 8 μm to 16 μm. Less spread in the grain size distribution was observed in samples heat treated for 3-6 hours compared with those treated for 1 hour (cf. Figure 5.9a and 5.9b). In general, no necks at grain-to-grain contacts are left after infiltration, and all grains are surrounded by melt.

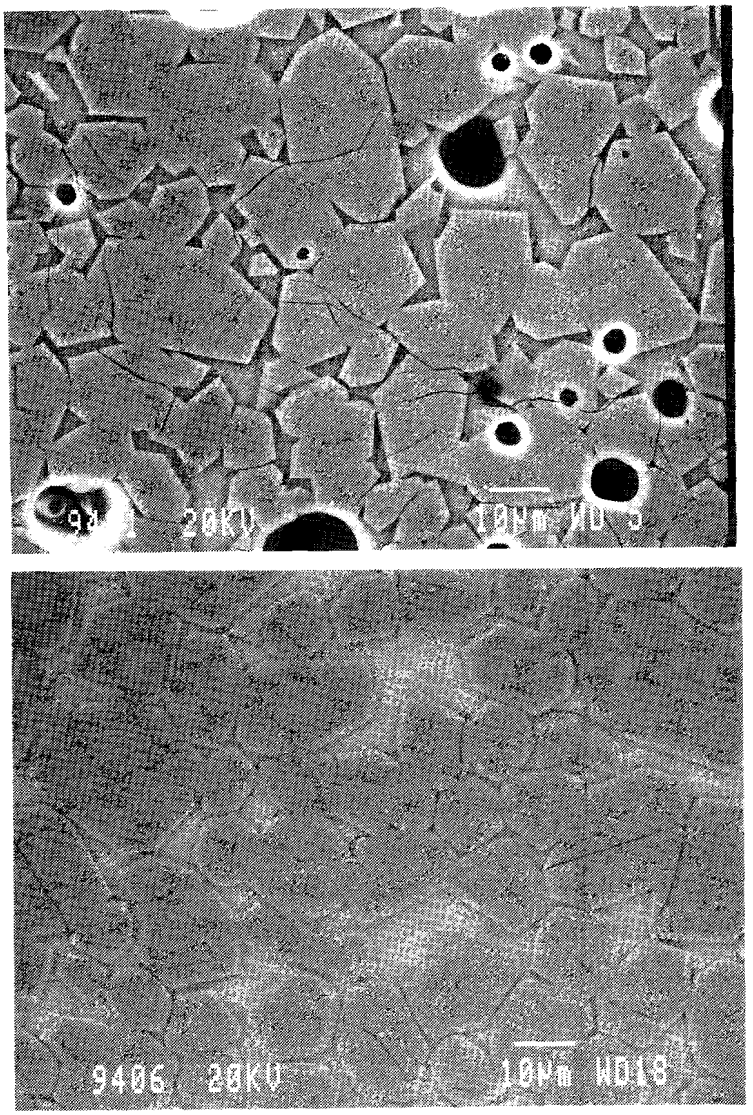

Figure 5.9a) SEM micrographs of A) sample 1ol1 after melt infiltration (1hour at 1470 °C). b)sample 5ol5b after melt infiltration (3 hours at 1500 °C) Note the near euhedral faceted grain morphology in both samples. In sample 5ol5b less spread in the grain size is present compared to sample 1ol1.

After densification (hot-pressing), a decrease in porosity was apparent as well as an increase in grain contact areas (See Figure 5.10a). Vapour-filled porosity decreased from a maximum of 10% to a maximum of 5%. Melt-filled porosity decreased depending on the amount of strain achieved and on the decrease in open porosity. For example, 16.2% strain was achieved in experiment 5ol3, while the amount of melt-filled porosity decreased from ~ 25% to 10.5% at the end of the experiment. Some grain growth occurred during the period of heating, equilibration and densification in the Instron set up (note the difference between d_{infilt} and d_{end} in Table 5.2). The final grain sizes measured are indicated in Table 5.2 as d_{end}. Grain shapes remained roughly equiaxed during hot-pressing, i.e. no significant grain flattening occurred. "Well fitting grains" suggest material redistribution from contacts into pores. Solid/melt interfaces in the pores are more "rounded" than the faceted interfaces present after infiltration, although, as can be seen in Figure 5.10b, small sections of faceted interfaces are present in the microstructure of the hot-pressed samples. With respect to the melt distribution, both melt-filled grain boundaries as well as melt free grain boundaries are present in samples after densification. Illustrative in this respect is a broken (not polished or etched) fragment of sample 5ol9 shown in Figure 5.11, where in 3 D a glass-filled triple junction network is seen, but also a melt layer can be observed on a former grain contact, indicating that some grain boundaries were fully wetted. When maximising contrast in SEM-images at relatively low magnification, small crystals (mostly spinel and occasionally a small forsterite crystal) can be observed within the melt areas but also as inclusions in larger crystals (Figures 5.12 and 5.13). These small crystals are observed only after densification, not after the melt infiltration stage. The SEM micrograph and the associated chemical mapping of the area indicated in Figure 5.12 and 5.13, show substantial differentiation of the elemental concentration in the melt phase. In general, relative element concentrations in the melt which decreased with respect to the starting composition correspond to the chemical species present in spinel, suggesting that crystallisation of spinel is the main reason for chemical changes in the melt. Further it was observed that experiment 1ol4, equilibrated (chemically and thermally) and densified at 1390 °C, contained more (9.5% compared to 4.8% for 1ol2) and larger spinel crystals (on average 5-8 μm compared to 1-3 μm crystals for 1ol2).

TEM studies of hot pressed samples 1ol2 and 1ol4, performed with the help of T. Fliervoet, were used to study, whether or not apparently unwetted grain boundaries in the densified samples contained a glassy film and to determine dislocation densities in the

grains. Only 9 olivine/olivine/melt intersection geometries could be found in the 2 samples studied (probably due to preferential milling of the molten areas) and the olivine/olivine contacts studied did not contain a melt phase at the (centre of the) grain boundary visible at 200000 times magnification (HRTEM), suggesting no glassy phase to be present. Overall dislocation densities were found to be very low (< 2 $10^{11}/m^2$). Dislocations were inhomogeneously distributed and mostly associated with grain boundaries. Roughly 70-80% of the grains were free of dislocations.

Using both the SEM and microprobe, the chemical composition of the melt was measured after infiltration into the porous samples (1ol1, 1ol2 and 5ol5b) and after densification (all densified samples). The sample analysis techniques were EDX (with a forsterite standard) and WDX (wave length dispersive x-ray analyses) respectively. In Figure 5.14, the theoretical equilibrium melt/forsterite composition is indicated and at 1470 °C the composition of the melt is expected to be in equilibrium with forsterite (see Figure 5.2). In contrast to the expected single melt composition aimed at, local melt compositions measured in samples 1ol1, 1ol2 and 5ol5b, after infiltration, show a range in the SiO_2, MgO, Al_2O_3 phase diagram (Figure 5.14a). All compositions, however, can be observed to be within the 1470 °C molten region and all are roughly on the sub-solidus triangle Forsterite-Cordierite line (see Figure 5.14a). Chemical analyses of samples after densification also deviate from the starting melt compositions (see Figure 5.14b for the case of 1ol2) and from the average composition after infiltration.

A)

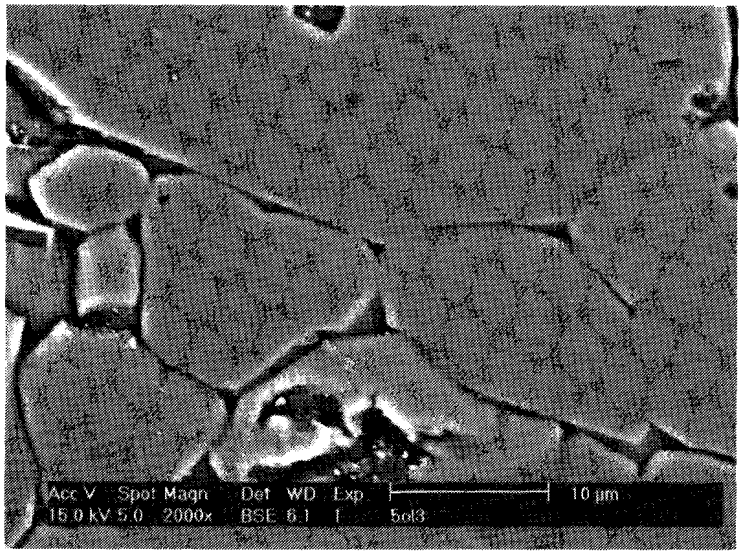

B)

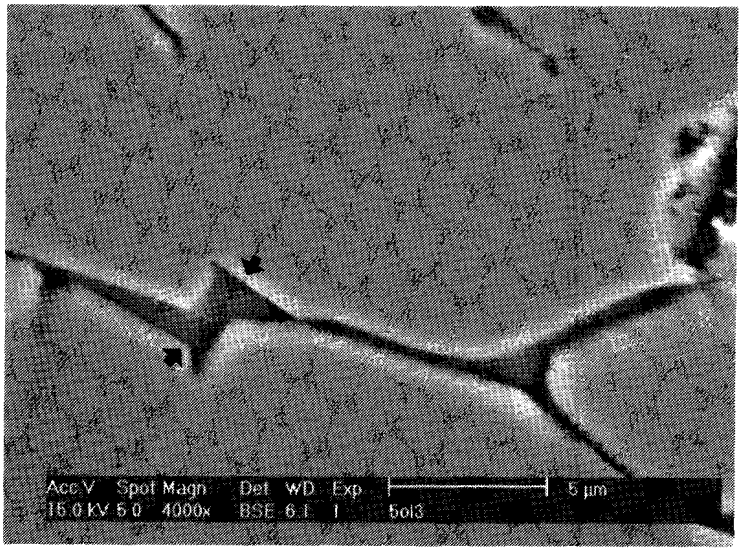

Figure 5.10 SEM micrographs of sample 5ol3, densified in the presence of a melt phase. B) illustrates a detail of the micrograph illustrated under A). Note the general rounded grain shapes in the pore areas, but also some small facets (indicated by the arrows).

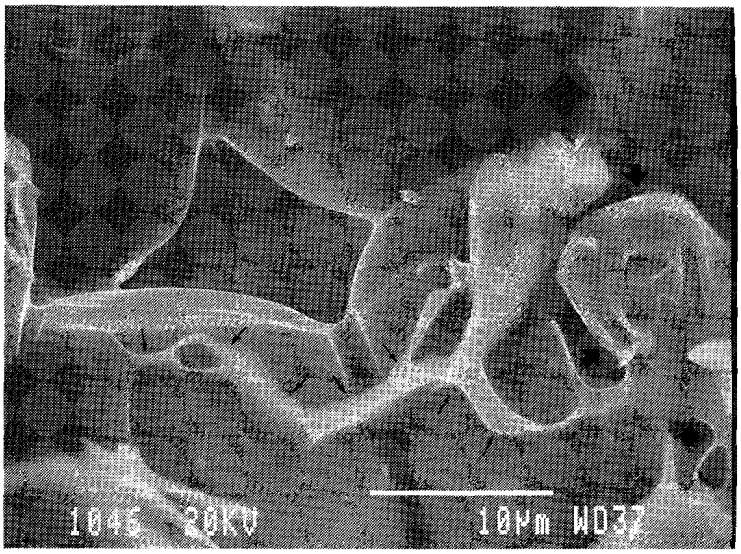

Figure 5.11. SEM micrograph of a fractured sample surface (5ol9) after densification. Note the 3D melt triple junction indicated by the small arrows. Note also the melt layer at a former grain-to-grain contact on the right side of the micrograph, indicated by the bold arrows.

(A)

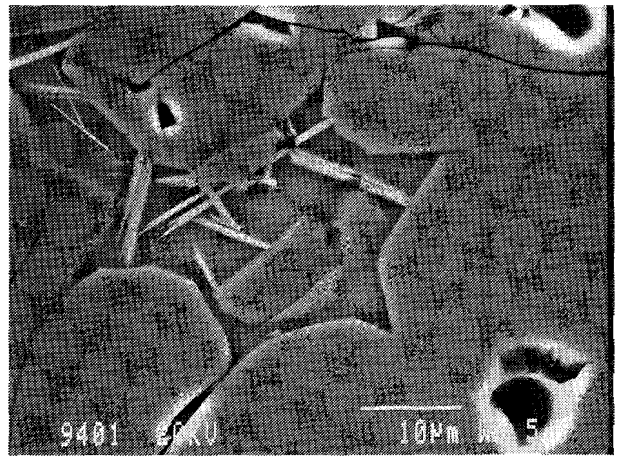

(B)

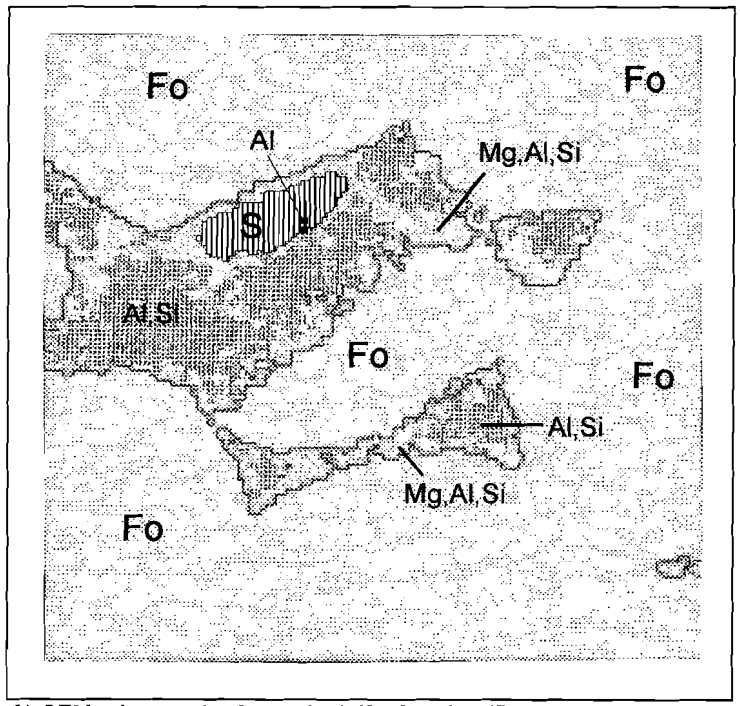

Figure 5.12.A) SEM micrograph of sample 1ol2 after densification. Chemical mapping with EDS) of a large area of the image shown in (A) is illustrated in (B). Fo is forsterite, S is spinel, also indicated by vertical lines. Mg, Al,Si indicates the elements present in the melt phase. Note the segregation that has occurred.

(A)

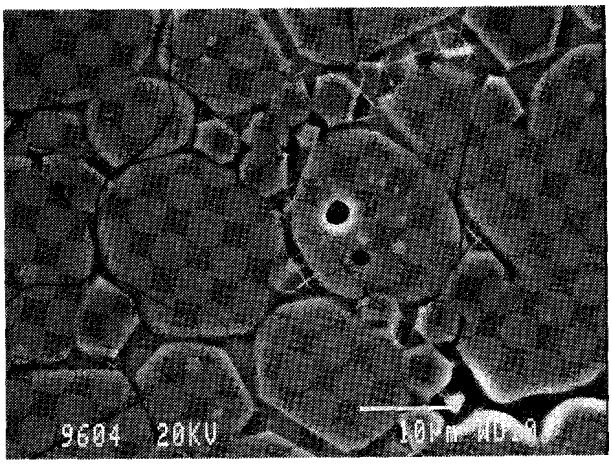

(B)

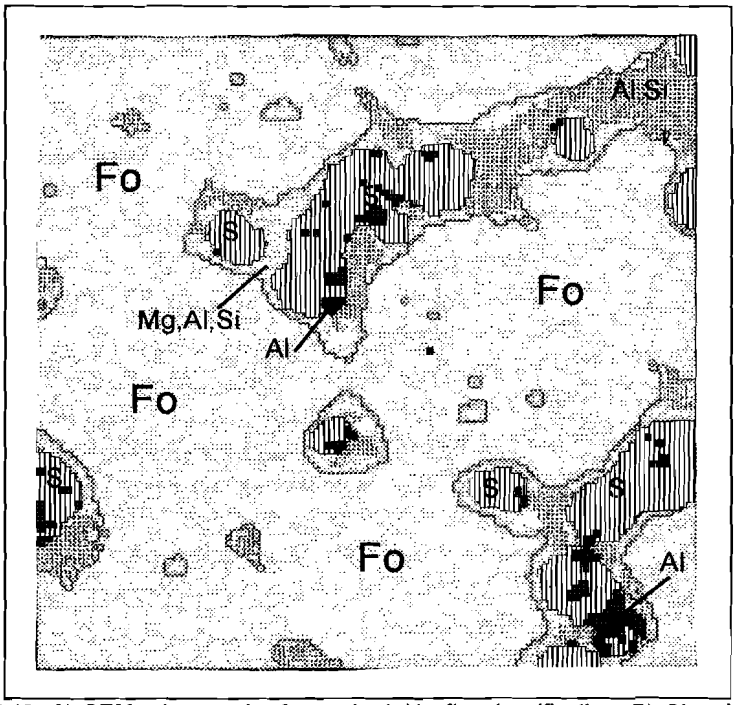

Figure 5.13. A) SEM micrograph of sample 1ol4 after densification. B) Chemical mapping using EDS of an area on the right hand side of (A). Note the large number of spinel crystals, indicated by S and vertical lines. Fo is forsterite and Al,Si, Mg indicate the elements present in the melt phase.

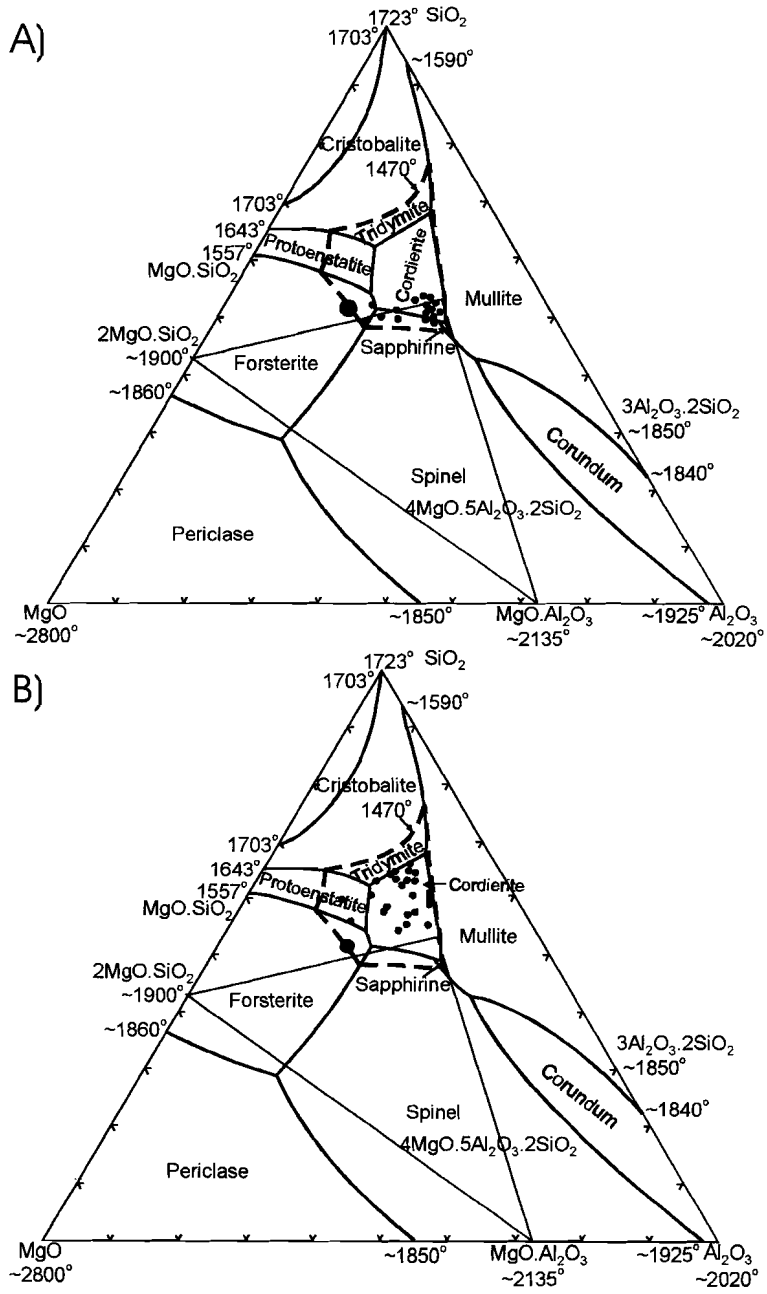

Figure 5.14. A)Melt compositions measured on the SEM and microprobe for samples 1ol2, 1ol1 and 5ol5b after infiltration but prior to densification (filled circles). B) Melt compositions in sample 1ol2 after densification. In both phase diagrams, the original melt composition is indicated by the large filled dot and the super-solidus area (area of molten compositions) at 1470 °C is the region within the closed dashed line.

5.5 Discussion

5.5.1 Grain growth and mechanical behaviour

The above heat treatment and densification experiments show that grain growth occurs during both the melt infiltration stage and the heating / equilibration / densification stage. The present densification data showed that at stresses in the range 0.26-6.3 MPa and at temperatures of 1663-1743 K, forsterite samples infiltrated with melt undergo rapid compaction with the strain rate decreasing with increasing strain. A procedure was developed to extrapolate the individual strain rates during stress steps over a limited range, based on the trends with strain. In this way strain rate values at fixed strains, i.e. 7.5%, 10% and 12.5%, could be compared for the various stresses. On average, a linear dependence was established between strain rate and stress at fixed strain. However, the 7.5% and 10% strain data show that many experiments in this range show strain rate to be proportional to σ_e^n with $0.5 \leq n \leq 1.0$. This cannot be attributed to an effect of grain growth on a grain size sensitive diffusion creep process, since the experiments in this study are mainly down-stepping in stress. Such an effect would then lead to n>1 as observed predominantly at 12.5% strain. Effects of a surface energy driving force becoming more significant at low stress may offer an explanation.

In order to determine the strain rate dependence on grain size, a grain growth law was used, following Hirth and Kohlstedt (1995), to correct grain sizes to obtain an average grain size value just before densification started. The grain growth law used is

$$d(t)^m - d_i^m = kt \qquad (5.11)$$

where d_i is the average initial grain size and d(t) is the average grain size at time t. The term k has an Arrhenius form with

$$k = k_o \exp(-Q_{gg} / RT) \qquad (5.12)$$

where Q_{gg} is the activation energy for grain growth and k_0 is a material parameter. Values of m=2 and Q_{gg}=160 kJ/mol were used, based on an olivine grain growth study by Karato (1989). Using the present grain growth data (d values and times for experiments 1ol1, 1ol5, 5ol5, and 5ol7 see Table 5.2), k_0 was calculated by taking the average from the individual grain growth experiments. A consistent value for k_0 was found to be 4.0 ± 2.10^{-19}

m^2/s. With this empirically determined constant, the grain sizes for each densification experiment were calculated after infiltration (d_{infilt}) and after an additional 1 hour equilibration before densification started (d_{equil}). These calculated values together with the measured values after densification (d_{end}) are listed in Table 5.2. Note that the d_{equil} grain sizes vary between 11.5 - 22.3 μm and are used as the starting grain size for the densification experiments. For experiments 1ol4 and 5ol9, the calculated d_{equil} is larger than the measured d_{end} (see Table 5.2) therefore the value of d_{end} is used.

With the calculated average grain sizes after equilibration and at the start of densification, a log strain rate versus log grain size plot can be constructed for the 1470 °C experiments. However, some grain growth is expected to have occurred during densification as well. Grain growth measured after densification experiments is less than expected when applying the grain growth law for the total heating period. Therefore the grain sizes in the log strain rate versus log grain size graph are plotted as $(d_{equil} + d_{end})/2$ with error bars representing the total range during experimentation $(d_{equil} - d_{end})$ - see Figure 5.15. The slope in the log strain rate versus log grain size diagram of Figure 5.15, for the two largest grain sizes is around -3, while the linear fit for the 3 initially finest grain size fractions shows an average slope of -1.5 to -3. Extrapolating trends to the same volumetric strain of 7.5, 10 or 12.5%, indicates that strain rates for the finest grain size experiments are approximately an order of magnitude slower. In general it was observed in Figure 5.15 that experiments with relatively more grain growth before densification resulted in relatively lower strain rate during densification (5ol3, 1ol6 and 1ol2). The experiments with larger starting grain sizes and less grain growth, i.e.5ol9 (20-22.3 μm) and 5oll0 (8-18.3 μm) densify relatively fast compared to the smaller starting grain size experiments described above.

Summarising the mechanical data obtained from the densification, it can now be concluded that the higher stress data are roughly consistent with models for densification by diffusion controlled solution/precipitation or Coble creep when surface energy effects are negligible, i.e. strain rate proportional to $\sigma^{\sim 1}$, e_v^{1-4}, d^{-3} under the conditions $d_{start} \geq 8$ μm, $\sigma_n \geq 6.3\ 10^5$ Pa, melt-filled porosity > 10% and e_v=7.5-12.5%. The decreased sensitivity of strain rate to stress (n<1) at low applied stresses may reflect an influence of other driving force terms, or variations in driving force or kinetics with varying stresses.

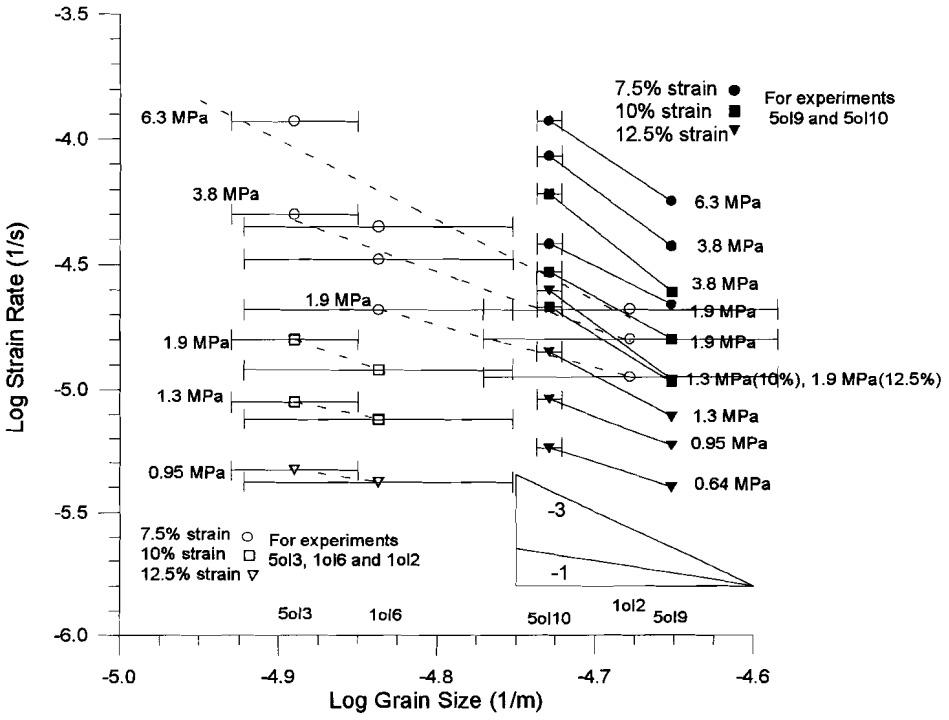

Figure 5.15 Log grain size versus log strain rate graph, using grain size values obtained after correction with the grain growth law, described by equations (5.11 and 5.12). The grain sizes indicated by symbols are $(d_{equil} + d_{end})/2$, *while the error bars indicate the total range from* d_{equil} *to* d_{end}. *Two data sets are plotted, the original small grain size samples (open symbols) and the larger grain sizes which showed almost no grain growth (closed symbols).*

5.5.2 Microstructural and chemical analyses

Combining microstructural observations with the chemical analyses some important constraints can be placed on the active mass transfer processes.

It was observed that samples with initially smaller grain sizes and a larger amount of grain growth before densification showed relatively low densification rates. In combination with the microstructural observations, it is evident that the samples showing major grain growth coincide with the experiments with low densification rates. A possible explanation can be that due to different crystal morphology, different surface energy effect can be expected for faceted grains compared to the samples with relatively more spherical grains (experiments 5ol9 and 5ol10).

From the chemical analyses performed on the samples after melt infiltration, the range of measured local melt compositions shows a general enrichment toward cordierite (see Figure 5.14), compared to the original melt composition. Comparing the microstructure before and after infiltration, a substantial amount of grain growth (Ostwald ripening) has occurred and the grain shapes have changed from rounded to euhedral/faceted shapes. In view of the high temperature (1470 °C), and hence the high rate at which transport through the melt will take place, it seems unlikely that the observed range of composition seen in Figure 5.14 can exist due to local (spatial) concentration differences. Besides, all local melt compositions lie on one side of the original composition, away from forsterite. The infiltrated samples show no crystalline phases other than forsterite. When analysing the forsterite crystals, the composition has not changed, taking the error margins of the analyses into account (~ ± 0.5% per element).The maximum deviation from pure forsterite measured was the presence of ~ 1% Al_2O_3. This therefore excludes solid solution as a possibility for changes in the melt phase composition. Furthermore, no visual evidence exists for segregation in the melt phase (2 liquids) nor would this be expected from the phase diagram. Therefore, the most likely explanation for the range of compositions observed is that precipitation of forsterite has taken place during cooling, after infiltration. This seems to have shifted the average melt composition away from forsterite. This process must have occurred rapidly and hence equilibrium is not expected to have been reached. The implication is that although the points shown in Figure 5.14 are a good graphical representation of the melt composition, these points need not be associated with the equilibrium isotherms in the phase diagram. Comparing the original melt composition

with the infiltrated melt composition at the same distance from the forsterite phase (no forsterite crystallisation), a small deviation in composition still exists and a small shift has occurred away from the SiO_2 apex. A possible explanation is that some evaporation of the most volatile component, SiO_2, has occurred.

The fact that quenching a melt infiltrated samples from 1470 °C to room temperature was evidently not fast enough to preserve the microstructure has important implications. Not only has the melt composition changed, but by precipitating forsterite, the solid/melt distribution and morphology has changed as well.

When studying compositions of the melt after densification, a shift has occurred (compared to both the composition after infiltration and original melt composition), (see Fig 5.14b for 1ol2). These measured compositions plot on isotherms which are generally below 1470 °C and compared to the original melt composition. Compared to the original composition the range of measured compositions has shifted away from forsterite, while compared with the average composition after infiltration see Figure 5.14a, the melt composition after densification has shifted towards the SiO_2 apex, or in other words, away from the spinel composition. This is in agreement with the observation that spinel was precipitated in the densified samples and in combination with the plotted chemical compositions it can be concluded that the samples were not adequately quenched. Since only a few small (newly precipitated) forsterite crystals are found in contrast to the large amount of small spinels, it is concluded that most of the forsterite (as in the infiltration experiments) precipitated on the existing crystals. Based on the above, it must be concluded that the solid/melt morphology observed after densification does not represent the morphology during the experiments and the question of whether or not a melt phase was present at the grain boundary during densification cannot be answered. It must be seriously questioned whether this point can be answered in studies by other authors (e.g. when using a solid medium apparatus), since quenching the samples by taking it from the hot zone at 1470 °C to room temperature was not fast enough to prevent precipitation (approximate time to reach room temperature ~ 15 minutes).

Making use of the phase diagram for the system investigated (see Figure 5.2) it can it is determined that at 1470 °C, this original melt composition lies in the Fo + L (liquid) field. However at 1400 °C it is on the boundary of the Fo + L and the Fo + Sp + L fields. The 1ol4 experiment, equilibrated at 1390 °C before densification,

therefore must have had spinel present during the experiment while the experiments equilibrated at 1470 °C started with only forsterite and melt present. Comparing microstructures and chemical element mapping after densification (Figures 5.14 a and b), the 1ol4 sample has much more spinel and also larger size spinel crystals. The presence of spinel during densification can also explain why relatively little grain growth occurred, and the fact that although the temperature was 90 °C lower, the densification was generally faster than the 1470 °C experiments under the same stress conditions. The faster deformation can be (partly) attributed to the smaller grain size.

Comparing the densification experiments performed at two different temperatures, but otherwise the same experimental conditions, shows that numerous differences in mechanical and microstructural observations are present. An apparent activation energy, calculated from these two experiments was considered to provide little useful information on the kinetics of the densification process.

5.5.3 Comparison with models

For the two densification experiments performed on the coarsest material (5ol9 and 5ol10, Table 5.2), which showed limited grain growth, the compaction behaviour showed strain rates approximately proportional to $\sigma^{\sim 1}$, e_v^{1-4}, d^{-3} under the conditions $d_{start} \geq 8$ μm, $\sigma_n \geq 6.3\ 10^5$ Pa, melt fraction > 10% and e_v=7.5-12.5%. This is consistent with diffusion controlled grain boundary diffusion (Coble) or solution/precipitation creep. The increase in sensitivity of strain rate to stress at low applied stresses (< 1.3 MPa) may reflect an influence of other driving force terms.

In order to further compare the data with the models given in section 5.2.2, graphs were constructed for linear strain rate versus stress data for all experiments. These are shown in Figure 5.17a-c. Experimental data are plotted for stresses < 2 MPa and from extrapolated linear fits to these data the intersection on the axes are determined. Except for the two largest grain size experiments, 5ol9 and 5ol10, all curves intersect on the σ-axis, indicating that a "yield" stress must be overcome. The curve of the 5ol9 experiment changes from an intersection on the strain rate axis at 7.5% to intersection of the stress axis at 10% and 12.5% strain but the intersection stress value remains small, i.e. between $1\text{-}4.10^4$ Pa. All other curves intersecting the stress axis give intersection values > 1.10^5 Pa up to $5.4\ 10^5$ Pa. All curves show a

linear best fit at stresses < 2 MPa, except for experiment 5ol10 which clearly shows a dependence on stress. For the latter experiment at average applied stresses > 8.10^5-10^6 Pa, the intersections are on the stress axis when extrapolated from the higher stress region, while for smaller applied stresses the interaction shifts to the strain rate axis. The intersection stress values are consistent with the stress steps for which no densification was observed and visa versa, i.e. all experiments with stresses above the intersection values were observed to densify.

As already inferred, the experiments with the smallest initial grain size and largest grain growth before densification (1ol2, 1ol6 and 5ol3) behave differently than the coarser grain size experiments. The two coarsest grain size experiments are broadly consistent with the grain boundary diffusion creep models described in Section 5.2.2 (equation 5.5 and 5.9) in which, for the experimental applied stresses used, the surface energy related term can be neglected so that the relations are reduced to

$$\dot{\beta} = \frac{12 D_{gb} \delta \Omega^s \sigma_n}{kTd^3 e_v} \quad \text{for non wetted grain boundaries} \qquad (5.11)$$

$$\dot{\beta} = \frac{12 Z^* \Omega^s \sigma_n}{kTd^3 e_v} \quad \text{for grain boundaries wetted by a melt phase} \qquad (5.12)$$

When using the above equations, then from the experimentally determined strain rates a rough estimate for the kinetic factors Z* or δD_{gb} can be obtained. The average value calculated for Z* or δD_{gb}, from all stress steps of experiments 5ol9 and 5ol10, between 7.5% and 12.5% strain, is 8 ± 3.10^{-21} m^3/s. This is now compared with literature values on diffusivities in melts and solid grain boundaries.

Multi-component diffusion experiments in MgO-Al_2O_3-SiO_2 (MAS) and CaO-MgO-Al_2O_3-SiO_2 (CMAS) silicate melts were performed by Kress and Ghiorso (1993) and Richter et al. (1998) at 1470-1500 °C. All coefficients of the diffusion matrix, in both studies, are in the order of 10^{-11} m^2/s ($2\text{-}7.10^{-11}$ m^2/s), despite the fact that compositions were varied over a wide range. Observation show that the rate of cation diffusion seems to be a function of silica content (Kress and Ghiorso, 1993; McCallum and Barrett, 1952 and Yoder, 1973). This suggest that the rate of diffusion of all melt species may be governed by the same rate limiting step (Kress and Ghiorso, 1993). It supports the hypothesis that the rate limiting step is the rate of exchange of bridging Si-O-Si bonds in the melt structure (Walker and Mullins, 1981). If a silicate

melt phase penetrates the grain boundary, the question is if the bulk values for diffusion in the melt remain unchanged. This question can at present not be answered. Unfortunately no grain boundary diffusion values are known for Si, not for solid/solid nor for melt-filled grain boundaries. When considering the kinetic factor obtained in the present study, then when assuming the grain boundary width to be in the range 1-100 nm, the obtained experimental diffusivities would be in the range 10^{-11}-5.10^{-14} m^2/s. This range of diffusivity values does not indicate whether or not a (large fraction of) grain boundaries was wetted by the melt during densification. A comparison of the kinetic factors from the experiments with and without melt will be made in the next Section.

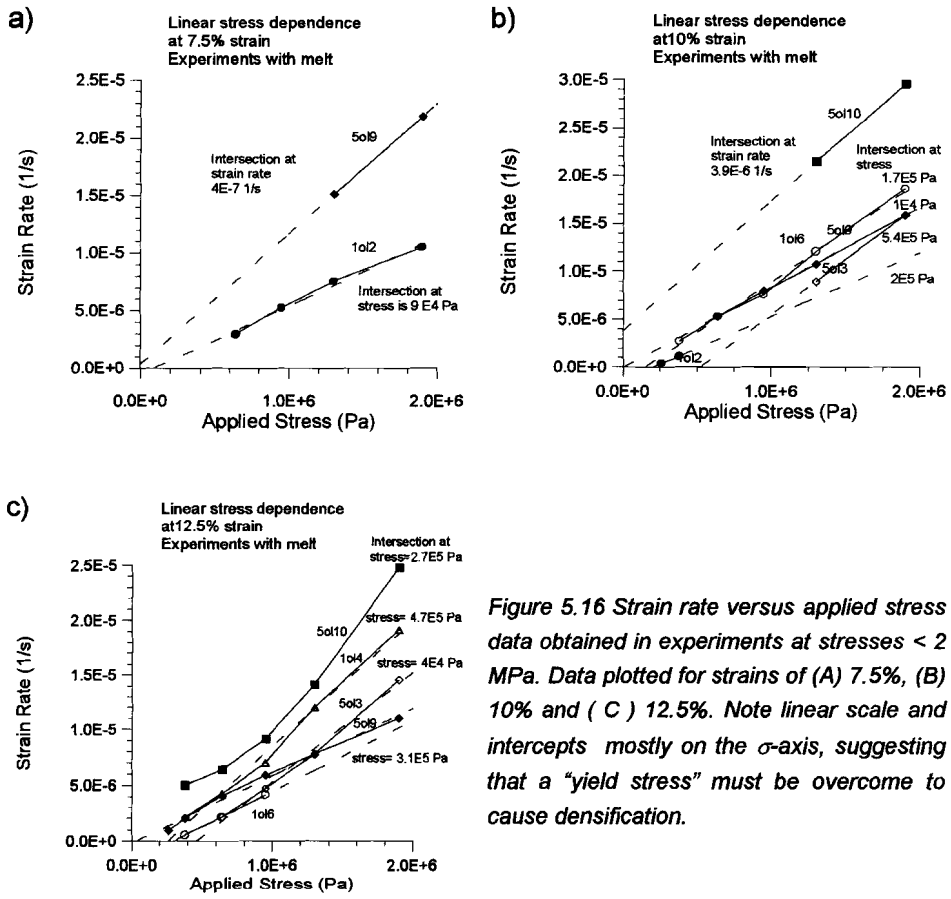

Figure 5.16 Strain rate versus applied stress data obtained in experiments at stresses < 2 MPa. Data plotted for strains of (A) 7.5%, (B) 10% and (C) 12.5%. Note linear scale and intercepts mostly on the σ-axis, suggesting that a "yield stress" must be overcome to cause densification.

5.5.4 Comparison of forsterite experiments with and without melt

A comparison can now be made between the forsterite densification experiments performed with and without synthetic basaltic melt present in the pores. At the high temperatures employed (1390-1470 °C) solid state diffusion processes are expected to be rapid and hence grain boundary diffusion does not critically depend on the presence of the liquid (melt) phase in grain boundaries. Indeed, grain boundary diffusion was found to be the dominant mass transfer mechanism in both sets of experiments (with and without melt) under conditions where surface energy effects were unimportant. Furthermore, in both cases grain boundary diffusion was inferred to be the rate limiting step. What remains to be investigated, is whether the absolute rates of densification are different for the experiments performed with and without melt.

The models described in Section 5.2.2, predict that whether densification in a solid/melt system is faster than in the corresponding solid/vapour system for the same stress, strain (or porosity), temperature and grain size, depend on the relevant kinetic parameters, on differences in interfacial energies (when these terms are significant) and whether or not the melt phase wets the grain boundaries (dynamically or stably). Based on theory a comparison of the two data sets can be made using the relation

$$\frac{\dot{\beta}_{sv}}{\dot{\beta}_{sm}} = \frac{(\sigma_n d - 4\gamma_{sv})}{(\sigma_n d - 4\gamma_{sl})} \qquad ((5.8))$$

when the grain boundaries of the forsterite/melt experiments are non-wetted, and with

$$\frac{\dot{\beta}_{sv}}{\dot{\beta}_{sm}} = \frac{\delta D_{gb}(\sigma_n d - 4\gamma_{sv})}{Z^*(\sigma_n d - 4\gamma_{sl})} \qquad ((5.10))$$

when the grain boundaries in the forsterite/melt experiments are fully wetted by the melt phase. These comparisons assume identical aggregate structure (e.g. pore/contact geometries). Note that where the surface energy terms are negligible compared to the stress term, equation (5.8) predicts $\dot{\beta}_{sv}=\dot{\beta}_{sm}$ while equation (5.10) predicts, $\dot{\beta}_{sv}=\delta D_{gb}/Z^*\dot{\beta}_{sm}$, where the kinetic factor δD_{gb} is the diffusion coefficient

through the solid/solid grain boundary and $Z^*=CD\delta(1-\alpha)$ is the diffusion coefficient through the wetted grain boundaries.

A problem for comparison of the absolute experimental rates of densification is that initially identical grain size fractions showed rapid grain growth and pore wall faceting in the presence of the melt phase but not in the absence of melt. In the forsterite plus melt experiments, samples with major grain growth showed anomalously low densification rates. As a result, only two experiments can be used to make a direct comparison of absolute densification rates for samples with and without melt. These are the coarsest (~ 20 μm) grain size experiments which showed no grain growth in the forsterite/vapour case and only minor grain growth and faceting in the forsterite/melt experiment. Comparing compaction rates at constant strain (similar porosity), the experiment with melt is only a factor ~3 faster, over the total range of stresses investigated (see Figure 5.17).

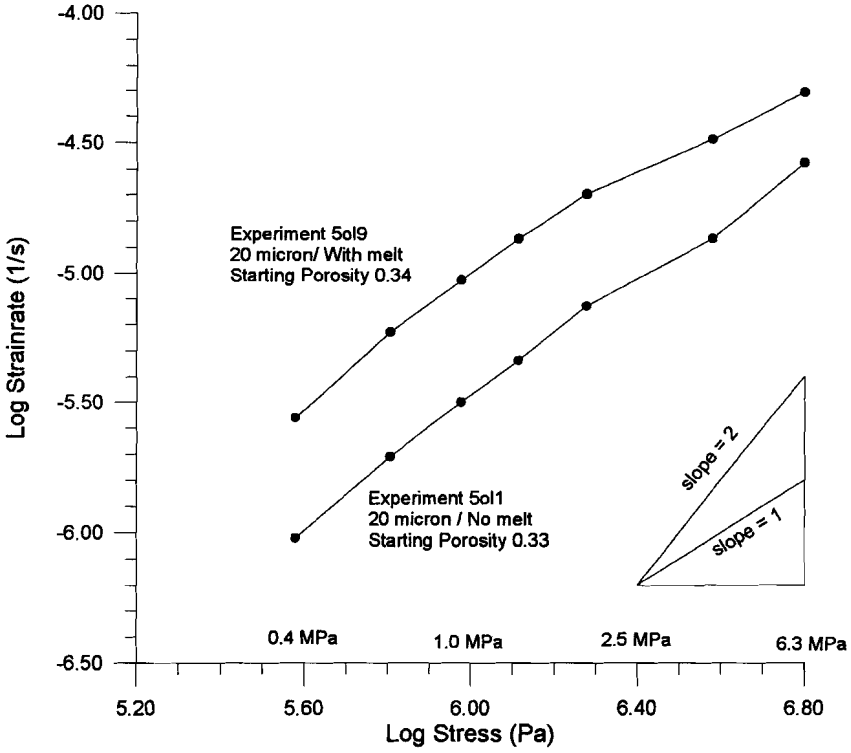

Figure 5.17 Log strain rate versus log stress diagram indicating the absolute rates of two experiments using ~20μm grain size forsterite, one with and one without a melt phase present. Recall that the experiments are down-stepped in applied stress. Experiment 5ol9 obtained 12.5% strain at 0.38 MPa while, experiment 5ol1 obtained 10% strain at 0.38 MPa.

For the differences observed in Figure (5.17), the following explanations are considered. If equation (5.10) applies, provided surface forces and microstructural differences are small, then δD_{gb} for the experiments without melt would be smaller than Z* for the experiments with melt by a factor 3. If equation (5.8) applies, the implication is that there must be some difference in aggregate structure between the samples with and without melt (e.g. smaller grain contacts in the melt bearing experiments) or that the $4\gamma_{sv}$-term significantly retards creep in the melt free experiments. Alternatively, most grain boundaries could be non-wetted while a smaller fraction could be fully wetted and densify at a faster rate due to a higher diffusion coefficient. An additional possibility is that in the samples containing a melt phase, diffusion is enhanced due to the presence of some chemical driving force as a result of impurities concentrated in the melt. The obtained intersection stresses in the linear stress versus strain rate graphs show that for the 20 μm experiments the surface energy contribution can be neglected. Hence for the 20 μm experiments, the difference in kinetic factor (effective diffusion coefficient) seems the most likely explanation. For smaller grain sizes, the intersection values for the forsterite/vapour and forsterite/melt experiments mostly intersect the stress axis suggesting a "yield stress" must be overcome for densification to occur. However, the range of "yield stress" values for the two datasets are broadly similar. Since samples containing a melt phase could not be adequately quenched, no conclusions can be drawn based on the solid/melt geometry. As a result of the arguments above, and in view of the small differences in strain rate observed between porous forsterite aggregates in the presence of only a vapour phase and forsterite aggregates with melt-filled porosity, it is concluded that both systems densify at similar compaction rates under similar conditions.

Comparing the experimental results of the present study with the densification data of Cooper and Kohlstedt (1984, 1986) obtained for Fo_{92} under similar conditions (only at somewhat lower temperatures, i.e. 1300-1400 °C), good agreement is observed in terms of the ratio of densification rates for experiments with and without melt. Samples with medium/high porosities (> 10%) in the experiments of Cooper and Kohlstedt also showed only a modest difference in densification rate between vapour filled and melt-filled pores, the latter densifying faster by a factor 2. They inferred, grain boundary diffusion to be the dominant mechanism with the solid state grain boundary diffusion step of the mass transfer process being rate limiting in both cases.

The explanation for the minor difference in densification rate given by the authors is that the solid/solid diffusion path becomes shorter for experiments performed with melt due to partial penetration of the melt phase into the grain boundaries (Cooper and Kohlstedt, 1982 and 1984). Considering the results of this study, this is considered one of several possibilities which remain open.

Let us now compare the various densification experiments with forsterite deformation experiments by Hirth and Kohlstedt (1995) who studied the dependence of deformation rate on stress and melt content at temperatures 1200-1300°C, applied stresses in the range 10- ~100 MPa and grain sizes < 20 μm. They showed that for deviatoric deformation, grain boundary diffusion is also the dominant mechansim with grain boundary diffusion the rate limiting step. At melt fractions > 5%, the effect of the melt phase becomes increasingly more important, the strain rate being a factor 10 faster for samples containing 7.2% melt compared with nominally melt-free samples. The authors state that the explanation of Cooper and Kohlstedt (1984) for melt-enhanced creep would significantly underestimate the effect of melt fraction on strain rate (Hirth and Kohlstedt, 1995). From microstructural observations they conclude that the melt enhanced creep observed for melt fractions > 5% is the result of complete wetting of a critical number of two-grain boundaries. The fact that grain boundaries are wetted is attributed to the melt topology being controlled by anisotropy of the interfacial energies in the olivine/basalt system. Although the wetting of some grain boundaries was also observed in the present work and it provides an explanation for the faster creep observed in the presence of a melt phase, there is no obvious reason why the same argument would not apply for the experiments with higher (melt-filled) porosities, such as the experiments by Cooper and Kohlstedt and the experiments performed in this study. The samples in the experiments by Hirth and Kohlstedt (1995) contain ~5% enstatite and are perfomed on average at higher streses compared with the densification studies. Considering the effect of the presence of spinel in this study (sample 1ol4) which densified faster than samples without spinel and showed less grain growth, the presence of a second solid phase can possibly explain the difference between the factor 10 increase in strain rate observed by Hirth and Kohlstedt and the factor 2 or 3 increase in strain rate due to the presence of melt, as observed by Cooper and Kohlstedt and in the present work. Alternatively, considering the argument of a fraction of grain boundaries being wetted, the effect of

applied stress could be important, suggesting more grain boundaries are wetted at higher stress.

From the above it is concluded that for both densification and deformation experiments perfomed on forsterite aggregates consisting of fine grain sizes (≤ 20 μm) at high temperatures (~1100-1500 °C) and low stresses (~1-100 MPa), grain boundary diffusion creep is the dominant mechanism with diffusion through the grain boundary being the rate limiting step. In view of the limited accuracy of the data and the small differences observed, it is concluded that porous forsterite aggregates compacted in the presence of only a vapour phase, and forsterite aggregates with melt-filled porosity, densify at similar compaction rates under similar conditions. The presence of porosity, either vapour-filled or melt-filled seems of significant importance when comparing the results of densification experiments with those of deformation experiments on dense material. The faster rates seen in densification are believed to be due to a shorter diffusion path length through the grain boundary when porosity is present. The similarity in densification rates obtained when the porosity is melt-filled versus can be explained by the fact that in both cases the grain boundary diffusion path length is reduced in comparison to dense samples and by rapid transport in the pores (by surface diffusion or diffusion through the melt). The fact that the melt-bearing samples densify slightly faster can be explained by a number of possibilities, including chemical gradient effects due to impurities in the melt, a lower solid/fluid interfacial energy and hence dihedral angle for the melt-bearing material (futher reducing the diffusion path length within the solid/solid grain boundaries) or fully wetting of a certain fraction of the grain boundaries in the melt-bearing samples.

5.6 Conclusions

1. Stress densification experiments have been performed on fine grained (1.5-20 μm) forsterite (Fo_{100}) aggregates in the presence of a synthetic basaltic melt (51% SiO_2, 29% MgO and 20% Al_2O_3). At strains between 7.5%-12.5%, stresses > 1 MPa, grain sizes > 8 μm and temperatures of 1470 °C, compaction rates are approximately proportional to the applied stress and to one over the grain size cubed, which is consistent with Coble or grain boundary diffusion controlled creep.
2. For grain sizes < 8 μm, the grain size dependence of the strain rate shows anomalously slow densification rates compared with the Coble creep type behaviour observed for the coarser grain sizes. This anomalous behaviour coincides with relatively large amounts of grain growth. Grain growth and grain faceting make assessment of a possible role of surface forces, at d< 8 μm very difficult for the present experiments. Linear stress versus strain rate graphs suggest an apparent yield stress for densification creep, except for the 2 largest grain size experiments. This indicates that for d< 8 μm (initial grain size) a significant surface energy driving force may be present acting in opposition to the applied stress.
3. Microstructural study of the samples shows very low dislocation densities, no grain flattening and only very minor grain fracturing to be present. Tightly fitting grains and reduced porosity support diffusion creep as the main densification mechanism. Both triple junction networks of melt as well as melt-wetted grain boundaries were observed. However, comparison of melt compositions measured under the SEM and microprobe with the expected compositions in the phase diagram shows that samples were not adequately quenched.
4. By fitting the data of the two largest grain sizes to the Coble creep equation, the effective grain boundary diffusivity was determined to be $8.10^{-21} m^3/s$.
5. Based on the strain rates of the 20 μm experiments with and without melt (Chapter 4) the experiment with melt is a factor 3 faster, while based on the kinetic factors determined, the experiment without melt would be roughly a factor 2 ½ faster under otherwise similar conditions. Since the kinetic coefficient has been calculated based on the experimental strain rates, no independent information can be obtained from the observed difference. In view of the limited accuracy of the data and the small differences in strain rate observed, it is concluded that porous forsterite aggregates compacted in the presence of only a vapour phase,

and forsterite aggregates with melt-filled porosity densify at similar compaction rates under similar conditions.

CHAPTER 6

GENERAL CONCLUSIONS AND SUGGESTIONS FOR FURTHER RESEARCH

This thesis has investigated grain scale mass transfer phenomena in porous crystalline aggregates in the presence of a fluid phase. A theoretical framework has been provided in which both surface energy and intergranular stresses were taken into account as driving force for mass transfer. The microphysical/thermodynamical models derived, have been tested by means of densification experiments on $NaNO_3$/brine, forsterite/vapour and forsterite plus synthetic basalt melt systems, and an attempt has been made to establish the relative importance of surface energy related driving forces compared to an applied stress.

The purpose of this final chapter is to draw together general conclusions based on findings presented in the preceding chapters and to examine the implications for large scale modelling of melt segregation/migration and expulsion phenomena beneath mid-ocean ridges. In addition, questions which remain unanswered are identified and suggestions are made for further research.

6.1 Theoretical developments

A thermodynamic treatment has been applied to solid/fluid systems under fully hydrostatic and compaction loading conditions to develop expressions for the rate of mass transport in the fluid phase and of 1-D densification. Applied stress and surface energy related driving forces have been taken into account. The rate of densification is controlled by the kinetics of the three serial steps of dissolution, diffusion and precipitation. By coupling the driving force for solution transfer with kinetic rate equations, constitutive equations for mass transfer and densification by solution/precipitation creep were obtained.

Models were developed for neck growth at grain-to-grain contacts under the action of surface energy driving forces only, in a purely hydrostatically stressed solid/liquid system. In contrast to previous models, the new expressions developed take both the grain boundary energy, γ_{gb}, as well as the interfacial solid/liquid energy, γ_{sl}, specifically into

account. The new models therefore allow the prediction of non-equilibrium and equilibrium states. The expressions obtained take the general form,

$$\dot{x} = A(T)\ R\ \gamma_{sl}\ (\cos\frac{\theta}{2} - \cos\frac{\theta_{eq}}{2})^a\ \frac{d^b}{(x^2 - x_{cr}^2)^c} \qquad ((2.42))$$

where $\dot{x}$ is the rate of neck growth, θ_{eq} is the equilibrium dihedral wetting angle under hydrostatic conditions, θ is the dynamic wetting angle, γ_{sl} is the interfacial free energy, x is the contact radius, x_{cr} is the initial contact radius at the start of neck growth, d is the grain diameter, A(T) is a temperature dependent term, describing the temperature dependence of solubility and of diffusivity or surface reaction rates, R is a constant incorporating molecular volume and geometry dependent constants. The exponents a is 1, b is either 0 or 1 and c is 1or 2 depending on the initial contact configuration and on the chosen diffusion path length. At zero initial contact x_{cr} is zero.

Expressions have been developed for 1-D densification by solution/precipitation creep in which driving force effects of grain surface curvature (i.e. curvature of grain/pore interfaces) have been taken into account. The resulting modified expressions for solution/precipitation creep take the general form

$$\dot{\beta} = \frac{A}{d^p\ e^c_v}\left(\frac{a\sigma^n_e}{e_v} - \frac{4\gamma_{sl}}{d}\right) \qquad (6.1)$$

where $\dot{\beta}$ is the rate of densification, A is a temperature dependent term describing the temperature dependence of solubility and of diffusivity or surface reaction rates and incorporates molecular volume of the solid, σ_e is the effective applied stress on the aggregate, e_v is volumetric strain, γ_{sl} is the interfacial free energy, d is the aggregate grain size and a is a geometrical term dependent on the grain packing geometry. The models including the surface energy term (c.f. equation 6.1) predict that solution/precipitation densification will slow down towards sufficiently low stresses and fine grain sizes, finally coming to a halt at/below a strain and grain size dependent " yield stress". The predicted behaviour at low stress and grain size is quite different from previous models describing solution/precipitation compaction of solid/liquid systems.

In addition, it has been shown that the neck growth models need to be modified for a granular solid/liquid system subjected to a state of positive effective stress. Here too competition between surface energy and stress related driving forces becomes important.

New rate models for neck growth in stressed systems were accordingly derived taking the excess Helmholz free energy, Δf^s, due to elastic or defect stored energy into account.

The models developed for pressure solution and neck growth, including the effects of both stress and surface energy related driving forces, were subsequently applied to derive criteria defining the conditions under which solution/precipitation, neck growth and grain contact healing can be expected to occur. Finally, the models were extended in Chapter 4 and 5 to allow solid state mass transfer processes to occur in parallel with liquid or vapour phase transport at high temperatures.

6.2 Densification behaviour at relatively high stresses

The mechanical and microstructural results obtained in the three material systems investigated demonstrated, in all cases, a relatively high stress regime in which rapid densification takes place. The behaviour in this regime roughly fits a grain boundary diffusion creep model in which surface energy effects can be neglected. The relevant creep model takes the form

$$\dot{\beta}_{gb} = \frac{12aD_{gb}\Omega^s\sigma_e^n}{kTd^p e_v^c} \qquad (6.2)$$

where β_{gb} is the rate of densification, k is Boltzmanns constant, T is temperature, Ω^s is the molecular volume of the solid, d is grain size, D_{gb} is the effective grain boundary diffusion coefficient, a is the aggregate packing constant , σ_e is the effective applied stress and e_v is the volumetric strain. Recall that the contact stress $\sigma_n=a\sigma_e/e_v$.

For the $NaNO_3$/brine system, investigated at room temperature, the conditions for which equation (6.2) applies are e_v= 10-25%, d> 20μm and $\sigma_e > 3.10^4$ Pa and the exponents in equation (6.2) fall in the ranges n=0.5-1.5, p≈3 and c=2-5. Starting porosities were in the range 40-54%. Rapid densification was observed to slow down when porosities → 10-12%. Microstructural observations were consistent with solution/precipitation creep and roughness developed in grain-to-grain contacts suggests that a large fraction of the grain boundaries was wetted by the liquid phase. The kinetic coefficient D_{gb} for the solution/precipitation case, expressed as $Z^*=CD\delta(1-\alpha)$ (where C is the solubility of the solid in solution, D is the diffusion coefficient through the grain boundary fluid, δ is the grain boundary thickness and α is the fraction of island-island contacts in the grain boundary), was estimated by comparing the experimental results with

equation (6.2). This yielded $6.10^{-20}m^3/s$ which is similar to values determined for densification of NaCl/brine aggregates (Spiers et al, 1990 and Spiers and Schutjens, 1990).

For the forsterite/vapour experiments, conducted at T= 1390-1470 °C, the conditions for which the data approximately fit the theoretical densification model expressed in equation (6.2) are $\sigma_e \geq 1$ MPa, $d \geq 5$ μm and e_v in the range 7.5-12.5%. The exponents in equation (6.2) fall in the range $n \approx 1$, p=2-4 and c=0.2-1.0. Temperature stepping tests under these conditions gave an apparent activation energy of ~700 kJ/mol. The kinetic coefficient at 1470 °C, $D_{gb}=\delta D_{gb,self}$, was $\sim 2.10^{-20}m^3/s$ and was found to be consistent with the expected value for the Mg grain boundary self diffusion coefficient at this temperature, and to be within 1 order of magnitude for the expected grain boundary self diffusion coefficient of oxygen. Unfortunately no grain boundary diffusion data for Si are available. Experiments with average grain sizes of 5 and 6 μm at applied stresses > 1 MPa attained the largest strain and were observed to slow down sharply when approaching porosities of 11-15%.

For the forsterite with melt experiments, performed at T= 1470 °C, the conditions for which the data roughly fit the theoretical model expressed in equation (6.2) are $\sigma_e \geq$ 0.63 MPa, $d \geq 8$ μm, e_v = 7.5-12.5% and melt fractions (porosity) > 10%. The exponents in equation (6.2) took values in the range n= 0.5-1.3, $p \approx 3$ and c=1- 4. The kinetic coefficient calculated at 1470 °C, δD_{gb} or Z* was $\sim 7.10^{-22}m^3/s$. The values obtained for the diffusion coefficient are clearly lower than the value found for the solid/vapour system. When assuming the grain boundary thickness to be in the range 1-100 nm, then the value obtained for D_{gb} would be in the range 10^{-11}-5.10^{-14} m^2/s. Multi-component diffusion experiments in bulk MgO-Al_2O_3-SiO_2 melts at 1470-1500 °C show all coefficients to be of the order 10^{-11} m^2/s, with the rate limiting step suggested to be the rate of exchange of bridging Si-O-Si bonds in the melt structure (Kress and Ghiorso, 1993 and Richter, 1998). However, grain boundary diffusion coefficients δD_{gb} for Mg through solid grain boundaries, were concluded in Chapter 4 to be in the same range as the values obtained from the forsterite/melt data and no grain boundary diffusion coefficients are known for Si diffusion, so that based on the diffusion coefficient data no definite conclusions can be drawn with respect to wetting or non-wetting of the grain boundaries.

6.3 Densification behaviour at low stresses

For the three systems tested, deviations from the model described by equation (6.2) occur towards low stresses and/or finer grain sizes. The observed behaviour resembles models for densification extended to include effects of surface energy. For solution/precipitation creep at low temperatures, where grain boundary diffusion critically depends on the presence of a fluid phase within the grain boundary, a driving force term due to the positively curved grain surface in the pores was included in the microphysical model, leading to the result

$$\dot{\beta}_{gb} = \frac{12 D_{gb} \Omega^s}{kT d^p e_v^c} \left(\frac{a \sigma_e^n}{e_v} - \frac{4\gamma}{d} \right) \qquad (6.3)$$

where γ is the interfacial free energy. Here the surface energy term $4\gamma/d$ opposes the action of the applied stress. For high temperatures, where solid state diffusion processes must be taken into account in microphysical modelling, an additional driving force for densification was recognised, namely in the zones where grain contacts show a sharp, negative, neck curvature, ρ, and/or a deviation from the equilibrium dihedral wetting angle, θ_{eq}, in such a way that $\theta < \theta_{eq}$. The resulting model takes the form

$$\dot{\beta}_{gb} = \frac{12 D_{gb} \Omega^s}{kT d^p e_v^c} \left(\frac{a \sigma_e^n}{e_v} + \frac{2\gamma}{\rho} \left(\cos\frac{\theta}{2} - \cos\frac{\theta_{eq}}{2} \right) \right) \qquad (6.4)$$

For the high temperature case when no negative radius of curvature is present at the grain boundary /pore intersection, when the dynamic dihedral angle θ is close to the equilibrium dihedral angle or when $\theta > \theta_{eq}$, an opposing force to densification can be described by equation (6.4) or (6.3). Note that in general $\rho << d$, therefore when a negative radius of curvature is present, equation (6.4) applies and the positive radius of curvature of the grains is neglected. Otherwise, the positive radius of curvature of the grains is taken into account.

The mechanical and microstructural data obtained for the $NaNO_3$/brine system show that at stresses $< 3 \cdot 10^4$ Pa and grain sizes < 27 μm, the observed compaction behaviour gives anomalously low strain rates compared with the high stress behaviour, with the stress exponent, n, rapidly increasing towards low stresses. Moreover, a positive grain size dependence of the strain rate was observed instead of the $1/d^3$ dependence

observed for solution/precipitation creep in the high stress regime. Most of the low stress experiments stop (become unmeasurably slow) long before full densification is attained. This type of behaviour is consistent with that predicted by the solution/precipitation creep model (equation 6.3), when the surface energy term ($4\gamma/d$) approaches the stress term ($a\sigma_e/e_v$) in magnitude. Indeed calculations of the relative magnitude of the terms, using γ=0.27 J/m^2 showed that the $NaNO_3$/brine data roughly fit the criterion $a\sigma_e/e_v=4\gamma/d$. Microstructural observations showed both solution/precipitation features as well as peripheral ring/neck structures developed within and around former grain-to-grain contacts, indicating that contact healing or neck growth type processes occurred. These may have been associated with or responsible for slowing down densification at low grain size. Grain growth and grain shape changing processes could also be partially responsible for the anomalously low creep rates seen at low stress and fine grain size.

The mechanical data produced for the forsterite/vapour system show, a log β versus log σ trend with a slope of ~1 for grain sizes < 5 μm, indicating a diffusion dominated densification mechanism for this regime. However the 1.5 μm experiment is significantly slower than all other (coarser) grain size experiments. The grain size dependence of the strain rate is again reversed (positive dependence) for grain sizes < 5 μm, in comparison with the slopes seen in the log β versus log d diagram for grain sizes ≥ 5 μm. Note the similar nature of the grain size dependence of the strain rate to that observed in the salt/brine system described above. From linear stress-strain rate graphs, the extrapolated trends at low stresses (≤ 1.3 MPa) show that for the 3 and 5 μm grain size experiments, the curves intersect the strain rate axis at zero stress, indicating an additional driving force for densification to be present (see equation 6.2). However, at higher strains the curves intercept the stress axis at zero strain rate suggesting that a "yield" stress has to be overcome. Order of magnitude calculations suggest a very rough fit to the criterion $a\sigma_e/e_v=4\gamma/d$, as obtained from equation (6.3). Microstructural observations indicate the negatively curved neck regions were present only in samples which densified during the sample preparation procedure (when no stress was applied) and in a single sample which was densified under stress for an unusually short time. Samples densified under stress for longer periods showed straight solid/vapour interfaces near the contacts. From the above, it is inferred that the deviations from equation (6.1) can be explained in terms of equation (6.2).

In the forsterite/melt system, experiments with initially fine grain sizes were observed to densify at relatively low rates. However, grain faceting and Ostwald ripening

(both surface energy related processes) dominate the experimental differences observed. No reversed dependence of strain rate on grain size was observed, of the type seen in the other two systems studied, only a substantial lower densification rate, deviating from equation (6.2) is observed in comparison with the grain sizes originally > 8 μm. An increase in the stress dependence of the strain rate was observed at 12.5% strain for stresses < 1.3 MPa. An increase in stress exponent towards lower stresses in the $NaNO_3$/brine experiments was found to be consistent with an opposing driving force and similar behaviour was observed for the forsterite/melt system.

6.4 Conclusions regarding the influence of a liquid phase on densification creep

In the present compaction/ densification experiments performed on granular $NaNO_3$ aggregates, the presence of saturated solution results in fast (diffusion controlled) solution/precipitation creep while for time dependent behaviour could be measured in dry or oil-flooded samples. Clearly, the grain boundary diffusion controlled creep seen in the $NaNO_3$/brine system critically depends on the solubility of the solid in solution and on the penetration of the liquid phase into grain boundaries. In addition, the presence of the solution phase resulted in grain growth due to Ostwald ripening for grain sizes < 39 μm. Moreover, at fine grain sizes and low stresses (< 5.10^3 Pa) faceting of free grain surfaces occurred. Like solution/precipitation creep the latter processes also depend on the solubility of the solid in the liquid but are driven by differences in surface energy, indicating the relatively more important role of surface energy at low stresses and fine grain sizes.

Making a comparison between the forsterite densification experiments performed at high temperature with and without simulated basaltic melt, is more difficult than the above comparison made for granular $NaNO_3$ with and without saturated solution. At high temperatures, solid state diffusion processes occur and hence grain boundary diffusion no longer depends on the presence of the liquid (melt) phase. In fact, solid state grain boundary diffusion creep was found to be the dominant mechanism in the experiments performed with and without melt under conditions where surface energy effects were negligible, with diffusion being the rate limiting step.

An additional problem in comparing the forsterite/vapour and forsterite/melt experiments is that initially equal grain sizes showed rapid grain growth and faceting of

free surfaces in the presence of the melt phase. In the melt bearing samples, as in the $NaNO_3$/brine system, the smallest grain sizes showed the largest grain growth rates, as expected from grain growth laws for Ostwald ripening (see Section 5.5.1). In the forsterite plus melt experiments, samples with extensive grain faceting showed anomalous low densification rates. As a result, only two coarse grain size (~20 μm) experiments could be used to make a direct comparison of the absolute densification rates of samples with and without melt. Comparing compaction rates at constant strain (similar porosity), the experiment with melt is only a factor ~3 faster, over the total range of stresses investigated. The fact that the melt containing samples densify slightly faster can be explaned by a number of possibilities, including effects due to impurities in the melt, partial penetration of the melt into the grain boundaries which futher reduces the diffusion path length through the solid/solid grain boundaries or fully wetting of a fraction of the grain boundaries.

6.5 Implications for large scale modelling of melt segregation/migration

As described in Chapter 1, essential input parameters for large scale modelling of melt segregation and migration, such as the melt distribution on the grain scale and whether or not a continuous network of (grain-scale) melt channels exists, are poorly constrained. So is the effect of melt on the rheological behaviour of the mantle rock. Furthermore, up to now no information on densification was available under conditions where both stress-related and surface-energy-related driving forces for diffusive mass transfer are comparable in magnitude. Rather, in previous work on solid/melt geometries in partially molten mantle rocks, small differential stresses have been neglected and interfacial energies considered to determine the melt distribution (Faul et al., 1994 and Waff and Bulau, 1982). Similarly, no systematic densification studies had been performed on partially molten aggregates under the low effective stress conditions where surface energy forces become significant. This is despite the fact that surface energy effects could become significant at the low effective pressure and differential stress range from 0.1 - 10 MPa, which is the range thought to prevail under bulk mantle conditions (Stocker and Ashby, 1973). As explained in Chapter 1, for large scale modelling of melt migration/segregation it is important to find non-vertical driving forces which can attribute to focusing of the melt phase at depth to the very narrow neo-volcanic zone at the Earth's

surface. Such a driving force can be provided by the deviatoric stress, when it is relatively more important than the opposing surface free energy effects.

The theoretical models derived in the present work, in which both interfacial energy and low stresses were taken into account, contribute to understanding diffusive mass transfer processes and rheological behaviour of partially molten systems under low stress conditions. Experimental testing of the models verified the predicted importance of the applied stress as the dominant driving force for mass transfer when high, while surface energy effects become important towards lower stresses. Assuming that effective grain contact stresses can be approximated by differential stresses under natural conditions, where effective pressures are presumable very low, the present experiments on forsterite plus melt indicate that the transition between fully stress dominated creep and stress plus surface energy dominated fields for grain sizes < 20μm and a temperature 1470°C is roughly in the range 3-7 MPa (using $\sigma_n = a\sigma_e/e_v$). This falls within the differential stress range thought to prevail in the mantle. Experimental conditions where surface energy effects dominate, and microstructural textures evolve towards equilibrium correspond to zero applied stress (fully hydrostatic case) for the forsterite plus melt system studied. For the analogue $NaNO_3$/brine system, the γ dominated field comes in for applied stresses < 5.10^3 Pa. The lowest applied stress conditions used for the forsterite and forsterite plus melt systems indicates that at contact stresses of ~1 MPa, surface energy effects are thought to be present, however densification and microstructural development are still dominated by the applied stress. This is broadly consistent with the theoretical models for densification in which surface energy effects are taken into account. In general, densification by diffusion controlled grain boundary diffusion was observed to be the dominant mechanism in both the forsterite/vapour and forsterite/melt systems under the generally low stress and fine grain size conditions investigated. The models derived show good agreement between the predicted and observed rate of densification down to porosities of 10-12%. Below these porosities, densification slows down, and the models which are derived assuming strain <20% break down. At present it is not possible to predict whether surface energy effects become relatively more important at these low porosities. Adapted models and associated experimental research will be required for this.

Extending the present results to predictions for larger grain sizes is not straightforward, since both the dominant densification/ deformation mechanism as well as the relative contribution of surface energy are dependent on grain size. Order of magnitude calculations by Karato et al. (1986) indicate that for dry dense forsterite material at

T/T_m=0.8 a transition is expected, above grain sizes in the range 1-10 mm and stresses in the range 0.1-10 MPa, from diffusion to dislocation creep. However, Hirth and Kohlstedt (1995) indicate that in the presence of > 5% melt diffusion creep becomes significantly faster, which would expand the diffusion creep field accordingly. Based on the present work, it can be expected that surface energy effects become relatively less important for larger grain sizes, due to larger ρ or d in the models above. Moreover, differential stress effects will be dominant over surface energy effects under most of the stress and grain size conditions thought to prevail in the partially molten upper mantle. For example, when taking grain sizes in the range 0.1-1 mm, then the condition σ_n=4 γ/d would for the partially molten system (taking $\gamma \approx 0.5$ J/m^2) indicate the dominance of the stress term above grain contact stresses > 10^3-10^4 Pa.

The expected dominance of differential stress over surface energy effects has major implications for the modelling of melt migration/segregation beneath mid-ocean ridges. The following implications can be envisaged:

1) When microstructural solid/melt distributions develop under non-equilibrium conditions, wetting of grain boundaries by the melt phase may be possible and melt distributions deviating from the triple junction networks predicted by equilibrium dihedral wetting angles may become possible. This can have major implications for the permeability of the rock material.
2) The dominance of differential stresses over surface energy effects will provide an additional driving force for melt migration/segregation in additional to buoyancy forces if small gradients in stress exist, resulting in mass transfer from regions of relatively high to relatively low stress conditions. Thus, a driving force for melt focussing towards the ridge axis can be envisaged when relatively larger extensional forces are present close to the ridge axis compared to positions further away, e.g. due to differences in temperature (Ceulenaar and Rabinowicz, 1992) and/or porosity as suggested in the model by Sparks and Parmentier (1991). Stress gradients within the range 1-10 MPa are expected to be large enough to overcome opposing surface energy effects, based on the criterion σ_n=4 γ/d.
3) On the basis of the foregoing arguments, within the total range of 0.1-10 MPa differential stress thought to prevail in the upper mantle, transitions from surface energy dominated mass transfer to differential stress dominated diffusional creep (and visa versa) and from diffusional creep to dislocation creep mechanisms seem to be possible. As a result, small variations in differential stress conditions in space and time could lead to concomitant, coupled changes in deformation behaviour, transport

properties and melt distribution. This can result then in melt extraction being episodically faster and slower (or non-existent), depending on a relatively high permeability, stress dominated, or relatively low permeability, surface energy dominated (i.e. moving back to equilibrium) variations with time.

6.6 Suggestions for further research

The present work can be considered a establishing insight into competition between stress and surface energy driven mass transfer processes. More research is required, especially for low porosity conditions, i.e. < 10-12%, where the current models are no longer applicable and densification rates are observed to slow down.

Similar experimental studies on forsterite and forsterite plus melt, using a wider range of grain sizes, could establish whether the observed trend of decreasing importance of surface energy related mass transfer processes towards larger grain sizes is continuous, or if other surface energy related processes become important. Also, the departure in densification behaviour from conventional Coble type behaviour at fine grain size could be better verified.

Measurements on Si-diffusion in grain boundaries in forsterite could help establish the rate limiting species in the dominant grain boundary diffusion process, active in the experiments reported here. This would help whether or not the kinetic coefficients in mass transfer models for vapour and melt-filled porous aggregates are indeed governed by diffusion of the same species.

In general the concept of a simple synthetic forsterite/melt system which can be controlled with a triangular phase diagram was considered very useful in this work. In particular, differences due to chemical reactions and those due to mechanical changes can be monitored. For example, the fact that samples were not adequately quenched, i.e. that crystallisation occurred during cooling and therefore microstructures observed can not be confidently considered present during densification could be established only using this technique. Since the presence or absence of melt at grain boundaries during deformation/densification is an important parameter, it is suggested that this tool should be

used in future studies to prove adequate quenching of the microstructure present during experimentation.

In large scale modelling solid/melt geometries should no longer be considered to be dominated by the dihedral wetting angle. Non-equilibrium melt topologies and the dominance of small differential stresses should be included instead.
A first indication, from the presence of spinel in experiment 1ol4 that the presence of a second solid phase has a large effect on the rate of densification and on the extend of grain growth is considered an important effect worthwhile introducing into models and experimental studies when considering the competition between small stresses and surface energy effects in future research.

The present experiments on forsterite and forsterite plus melt should be repeated with Fo_{92} including the simplified basaltic melt, under well controlled fO_2 and fH_2O conditions. The models derived in this work could then be tested on this system, more closely resembling natural systems. Performing densification experiments with melt at the low stress conditions used in this work could elucidate the role of (melt-filled) porosity versus the faster diffusion creep due to grain boundary wetting.

REFERENCES

Aharanov E., J.A. Whitehead, P.B. Kelemen and M. Spiegelman. Channeling of upwelling melt in the mantle, J. Geophys. Res., vol. 100, 20433-20450, 1995.

Ahern J.L. and D.L Turcotte. Magma migration beneath an ocean ridge. Earth Planet. Sci. Lett., vol. 45, 115-122, 1979.

Andersson K., G. Borchardt, S. Scherrer and S. Weber. Self-diffusion in Mg_2SiO_4 (forsterite) at high temperature. Fresenus Z. Anal. Chem., vol. 333, 383-385, 1989.

Ashby M.F., G.H. Edward, J. Davenport and R.A. Verrall. Application of bound theorems for creeping solids and their application to large strain diffusional flows, Acta Metall., vol. 26, 1379-188, 1978.

Aksay I.A., C.E. Hoge and J.A. Pask. Phase distributions in solid/liquid-vapour systems. In: Surfaces and interfaces of glass and ceramics. Ed:. V.D. Frenchette, W.C. Lacourse and V.L. Burdick. Plenum Press, New York, 299-321, 1974.

Aksay I.A., C.E. Hoge and J.A. Pask. Wetting under chemical equilibrium and non-equilibrium conditions. J. Phys. Chem., vol. 78, 1178-1183, 1974.

Andersen D.L. and H. Spetzler. Partial melting and the low-velocity zone. Phys Earth Planet. Interiors, 4, 62-64, 1970.

Bai Q. and D.L. Kohlstedt. Substantial hydrogen solubility in olivine and implications for water storage in the mantle. Nature, vol. 357, 672-674, 1992.

Balmer R.T., Mechanics and energetics of macromolecular interfaces. Surface Sci., 52, 174-194, 1975.

Bennon W.D. and F.P. Incropera. A continuum model for the momentum, heat and species transport in binary solid-liquid phase change systems. I Model formulation, Int. J.Heat Mass Transfer, 30, 2161-2170, 1987.

Benson G.C. Recalculation of the surface energies of alkali halide crystals. J. Chem. Phys., vol. 35, 2113-2116, 1961.

Benson G.C and K.S. Yun. Surface energy and surface tension of crystalline solids, 203-269. In: The solid/gas interface, Ed. E.A. Flood, vol. 1, Edward Arnold Publishers LTD., London, 1967.

Blakely J.M. Introduction to the properties of crystal surfaces. Pergamon Press, Oxford, 1973.

Brown M., Y.A. Averkin, E.L. McLellan and E.W.Sawyer. Melt segregation in migmatites, J. Geph. Res. vol. 100, B8, 15655, 1995.

Bulau J.R., H.S. Waff and J.A.Tyburczy. Mechanical and thermodynamic constraints on fluid distribution in partial melts. J. of Geoph. Res., vol. 84, B11, 6102-6108, 1979.

Borch and Green. Deformation of perioditite at high pressure in a molten salt cell: comparison of traditional and homologous temperature treatments. Phys. Earth Planet. Inter., vol. 55, 269-276, 1989.

Cannon R.M. and W.C. Carter. Interplay of sintering microstructures, driving forces and mass transport mechanisms. J. Am. Ceram. Soc., vol. 72, 1550-1555, 1989.

Carter N.L. and H.G. Ave'Lallement. High Temperature Flow of Dunite and Peridotite, Geol. Soc. Am. Bull., 81, 2181-2202, 1970.

Carter N.L. High temperature flow of rocks. Rev. Geoph. Space Phys., vol.13, 44-381, 1975.

Ceulenaar G. and M. Rabinowicz. Mantle flow and melt migration beneath ocean ridges: Models derived from observations in ophiolites. In: Mantle Flow and Melt Generation at Mid-Ocean Ridges, Geophysical Monograph 71. Ed: J.P Morgan, D.K Blackman and J.M. Sinton, 155-182, American Geophysical Union, 1992.

Chadwick P. Continuum mechanics. Wiley, New York, 1976.

Chakraborty S., J.R. Farver, R.A. Yund and D.C. Rubie. Mg tracer diffusion in synthetic forsterite and San Carlos olivine as a function of P, T and O_2. Phys. Chem. Mineral. 1994

Chopra, P.N. and M.S. Paterson. The Experimental Deformation of Dunite, Tectonophysics, 78, 453-473, 1981.

Chopra, P.N. and M.S. Paterson. The role of water in the deformation of dunite. J. Geophys. Res., vol. 89, 7861-7876, 1984

Chopra, P.N. The plasticity of some fine-grained aggregates of olivine at high pressure and temperature. In: Mineral and rock deformation : Laboratory studies. Geoph. Monogr. Vol 36 Eds: B.E. Hobbs and C. Heard, Am. Geoph. Union, 25-33, 1986

Coble R.L. Initial sintering of Alumina and Hematite. J. Am. Ceram. Soc., vol. 41, p 55 - 61, 1958.

Coble R.L. Sintering crystalline solids. Appl. Phys. vol. 32, 787-793, 1961.

Coble R.L. and J.E. Burke. Prog. Ceramic Sci. vol. 3, Ed: J.E. Burke, 1963

Coble R.L. Mechanisms of densification during hot pressing. In: Sintering and related phenomena. Gordon and Breach, New York, 329, 1967.

Coble R.L. Diffusion models for hot pressing with surface energy and pressure effects as driving forces. J. Applied Physics, 41, 4798, 1970.

Condit R.H., H.C. Weed and A.J. Piwinskii. A technique for observing oxygen diffusion along grain boundary regions in forsterite. In: Point defects in minerals. Geophys. Monogr. Ser., vol. 31, 97-105. Ed: R.N. Schock, 1985.

Cooper, R.F. and D.L. Kohlstedt. Interfacial energies in the olivine-basalt system. In: high-pressure research in geophysics, Adv. Earth Planet. Sci., vol. 12, Eds: S. Akimota and M.. Manghnani, 217-228. Centre for Academic Publications Japan, Tokyo, 1982.

Cooper, R.F. and D.L. Kohlstedt. Solution-Precipitation Enhanced Diffusion Creep of Partially Molten Olivine-Basalt Aggregates During Hot-pressing, Tectonophysics, 107, 207-233, 1984.

Cooper, R.F. and D.L. Kohlstedt. Rheology and structure of olivine-basalt partial melts. J. Geoph. Res., vol. 91, 9315-9323, 1986.

Daines M.J. and F.M. Richter, An experimental method for directly determining the interconnectivity of melt in partially molten systems, Geoph. Res. Lett., 15, 1459-1462, 1988.

Defay R. and I. Prigogine (with the collaboration of A. Bellemans). Surface tension and adsorption, translated from french by D.H. Everett, Longmans, 1966.

Drury S. and H.L.M. van Roermund. Fluid assisted recrystallization in upper mantle peridotite xenoliths from kimberlites, J. Petrol., 30, 133-152, 1989.

Dzerhakhov N., I. Drobilov and I. Popov. Determination of surface energies of carbonates with a calcite structure. God. Vissh. Minno-Geol. Inst. Sofya, 31, 201-206, 1986.

Farver, J.R., R.A. Yund and D.C. Rubie. Magnesium grain boundary diffusion in forsterite aggregates at 1000°-1300°C and 0.1 MPa to 10 GPa.. J. Geopys. Res., vol. 99, 19809-19819, 1994

Faul, U.H.., D.R. Toomey and H.S. Waff. Intergranular basaltic melt is distributed in thin, elogated inclusions, Geoph. Res. Lett., 21, 29-32, 1994.

Faul U.H. Permeabiliteit of partially molten upper mantle rocks from experiments and percolation theory. J. Geoph. Res., vol. 10, 1997

Forsyth D.W. Geophysical constraints on mantle flow and melt generation beneath mid-ocean ridges. In: Mantle Flow and Melt Generation at Mid-Ocean Ridges, Geophysical Monograph 71, Eds: J.P Morgan, D.K Blackman and J.M. Sinton, 155-182, American Geophysical Union, 1992.

Forsyth D.W., D.S. Scheirer, S.C. Webb, L.D. Dorman, J.a. Orcutt, A.J. Harding, D.K. Blackman, J.P. Morgan, R.S. Detrick, Y. Shen, C.J. Wolfe, J.P. Canales, D.J. Toomey, A.F. Sheehan, S.C. Solomon and W.S.D. Wilcock. Science 280, 1998.

Frost, H.J. and M.F. Ashby. Deformation-Mechanism Maps, Pergamon Press, Oxford, UK, 1982.

Gel'perin N.I., B.M. Gurovich and K.Kh. Dubinchik. Concentration and temperature dependence of the surface tensions of some inorganic substances. Zh. Prikl. Khim., 42, 214-216, 1969.

De Gennes P.G., Dynamics of wetting. In: Les Houches summer school 1988, Liquids at interfaces. Eds. J. Charvolin, J.F. Joanny and J. Zinn-Justin. North Holland, Amsterdam, 1990.

German R.M., Liquid Phase Sintering. Plenum Press, NY, 1985.

German R.M. , Sintering theory and practice. Plenum Press, NY, 1996.

Gibbs J. W. 1906. On the equilibrium of heterogeneous substances. In: The scientific papers of J. Willard Gibbs, vol. 1, 55-353, Toronto: Longman (New York; Dover, 1961).

Goetze C.A. A brief summary of our present day understanding of the effect of volatiles and partial melt on the mechanical properties of the upper mantle. In: High pressure Research, Eds: Maghnani M.H. and Akimoto S.I., Academic Press, New York, 1977.

Green H.W. Pressure solution creep: some causes and mechanisms. J. Geoph. Res. 89, 845-856, 1984.

De Groot S.R. and P. Mazur. Non-equilibrium Thermodynamics. North Holland, New-York, 1962.

Guggenheim E.A. Mixtures. Clarendon, Oxford, 1952.

Guggenheim E.A. Thermodynamics, 5th ed, North Holland, Amsterdam, 1967

Hay R.S.and B. Evans , Intergranular distribution of pore fluid and the nature of high angle grain boundaries in limestone and marble. J. Geoph. Res. Vol 93, 8959-8974, 1988

Heidung W.K. A thermodynamic analysis of the conditions of equilibrium at non-hydrostatically stressed and curved solid-fluid interfaces. J. of Geoph. Res. vol. 96, 21909-21921, 1991.

Herring C. Some theorems on the free energy of crystal surfaces. Phys. Rev., 82, 87-93, 1950.

Herring C. Surface tension as a motivation for sintering. In: The physics of powder metallurgy, 143-213. Eds: W.E. Kingston. McGraw-Hill Book Inc. New-York, 1951

Herring C. The use of classical macroscopic concepts in Surface energy problems. In: Structure and properties of solid surfaces. 5-81. Eds: Gomer R. and C.S. Smith. The University of Chicago press, Chicago, 1952.

Herz H.R., Ueber die Beruerung fester elastischer Koerper and ueber die Haerte Verhandlung des Vereins zuer Bfoerderung des Gewerbefleisses, Berlin, 1882.

Hess P.C. Phase equilibria constraints on the origin of ocean floor basalts. In: Mantle Flow and Melt Generation at Mid-Ocean Ridges, Geophysical Monograph 71, Eds: J.P Morgan, D.K Blackman and J.M. Sinton, 155-182, American Geophysical Union, 1992.

Hickman S.H. and B. Evans. Experimental pressure solution in halite: the effect of grain/interphase boundary structure. J. Geol. Soc. London., 148, 549-560, 1991.

Hickman S.H. and B. Evans. Growth of grain contacts in halite by solution transfer: Implications for diagenesis, lithification and strength recovery. In: Fault mechanisms and transport properties of rocks. Eds: B. Evans and T.-F. Wong, Academic, San Diego, California, 253-280, 1992.

Hickman S.H. and B. Evans. Kinetics of pressure solution of halite-silica interfaces and intergranular clay films. J. Geoph. Res., vol. 100, 13113-13132, 1995.

Hirth G. and D.L. Kohlstedt. Experimental constraints on the dynamics of the partially molten upper mantle: Deformation in the dislocation creep regime. J. Geoph. Res. vol. 100, 1995a.

Hirth G. and D.L. Kohlstedt. Experimental constraints on the dynamics of the partially molten upper mantle: Deformation in the diffusion creep regime. J. Geoph. Res., vol. 100, 1995b.

Hirth G. and D.L. Kohlstedt. Water in oceanic upper mantle: implications for rheology, melt extraction and the evolution of the lithosphere. Earth Planet. Sci. Lett., 144: 93-108, 1996.

Hobbs B.E., Point defect chemistry of minerals under a hydrothermal environment. J. Geoph. Res., 89, 4026-4038, 1984.

Hoefer H., Deformation von Natriumnitrat-Einkristallen. Ph.D. Thesis, Universitaet zu Koeln, Germany, 1989.

Hull D., Introduction to dislocations, 2nd edition. International series on materials science and technology; vol. 16. Pergamon Press, Oxford, 1975.

Israelachvili J.N., Intermolecular and surface forces with applications to colloidal and biological systems. Academic Press, London, 1985.

Jaoel O., C. Froidevaux, W.B. Durham and M. Michaut. Oxygen self-diffusion in forsterite: implications for high temperature creep mechanism. Earth Planet Sci. Lett, vol. 47, 391-397, 1980.

Jaoel O., M. Poumellec, C. Froidevaux and A. Havette. Sillicon diffusion in forsterite: a new constraint for understanding mantle deformation. In: Anelasticity in the Earth. Geodyn. Ser. vol. 4, 95-100. Eds: F.D. Stacey, M.S. Peterson and A. Nicolas, 1981.

Jin Z.H., H.W. Green and Y. Zhou. Melt topology in partially molten mantle peridotite during ductile deformation. Nature vol. 372, 1994.

Joesten R. Grain boundary diffusion kinetics in silicate and oxide minerals. In: Diffusion, atomic ordening, and mass transport: selected problems in geochemistry. Ed: J. Ganguky, 345-395, 1991.

Jurewicz S.R. and E.B. Watson. The distribution of a partial melt in a granitic system: The application of liquid sintering theory. Geochim. Cosmochim. Acta, vol. 49, 1109-1121, 1985.

Johnson K.L. Contact Mechanics. Cambridge University Press, New York, 1987.

Karato, S.-I. Does partial melting reduce the creep strength of the upper mantle. Nature, vol. 319, 309-310, 1986

Karato, S.-I., M.S. Paterson and J.D. Fitzgerald., Rheology of systhetic olivine aggregates: influence of grainsize and water. J.Geoph. Res., 91, 8151-8176, 1986.

Kazakos A., S. Komarneni and R. Roy. Preparation and densification of forsterite (Mg_2SiO_4) by nanocomposite sol-gel processing. Materials Letters, vol. 9 , 1990.

Kelemen P. and H. Dick. Focused melt flow and localised deformation in the upper mantle: Juxtaposition of replacive dunite and ductile shear zones in the Josephine perioditite, SW Oregon. J. Geophys. Res. vol. 100, 1995.

Kelemen P.B., J.A. Whitebread, E. Aharanov and K.A. Jordahl. Experiments on flow focusing in soluble porous media, with applications to melt extraction from the mantle, J. Geoph. Res., vol.100, 475-496, 1995.

Kingery W.D. Densification during sintering in the presence of a liquid phase. I. Theory. J. Appl. Phys., 30, 301-306, 1959.

Kingery W.D., H.K. Bowen and D.R. Uhlman. Introduction to Ceramics. 2nd. ed., Wiley, NY, 1976.

Klein E.M. Ocean Ridge magmatic and hydrothermal geochemical processes. Rev. Geoph. (IUGG quadrennial review), 1991.

F. Klockmann. Klockmann's Lehrbuch der Mineralogie. Ed: P. Ramdohr and H. Strunz. Ferdinand Enke Verlag, Stuttgart, 1967.

Kohlstedt D.L. Structure, rheology and permeability of partially molten rocks at low melt fractions. In: Mantle Flow and Melt Generation at Mid-Ocean Ridges, Geophysical Monograph 71. Eds: J.P Morgan, D.K Blackman and J.M. Sinton, 155-182, American Geophysical Union, 1992.

Kress V.C. and M.S. Ghiorso Multicomponent diffusion in MgO-Al_2O_3-SiO_2 and CaO-MgO-Al_2O_3-SiO_2 melts. Geochim. Cosmochim. Acta., vol. 57, 4453-4466, 1993.

Kuczinski G.C. Study of sintering of glass. J. Applied Physics, vol. 20, 1160-1163, 1949.

Kwon O-H. and G.L. Messing. Gas diffusion during containerless hot isostatic pressing of liquid phase sintered ceramics. J. Am. Ceram. Soc. 72, 1011-1015, 1989.

Kwon O-H. and G.L. Messing. A theoretical analysis of solution/precipitation controlled densification during liquid phase sintering. Acta Metall. Mat., 39, 2059-2068, 1991.

Lehner F.K. and J. Bataille. Non-equilibrium thermodynamics of pressure solution. Pure Appl. Geophys. 122, 53-85, 1984.

Lehner F.K. Thermodynamics of rock deformation by pressure solution. In: Deformation processes in minerals ceramics and rocks. Eds: Barber D.J. and Meredith P.G. Unwin Hyman, 1990.

Lehner F.K. A model for intergranular pressure solution in open systems. In: Influence of fluids on deformaton processes in rocks. Eds: Spiers C.J. and T. Takeshita, Tectonophysics, vol. 245, 153-170, 1995.

Levy, B.G. New measurements constrain models of mantle upwelling along a midocean ridge. Physics today, july 1998.

Lister J.R. and R.C. Kerr. Fluid-mechanical models of crack propagation and their application to magma transport in dykes. J. Geophys. Res., vol. 96, 10049-10077, 1991.

MacDonald K.C. Mid-ocean ridges: fine-scale tectonic, volcanic and hydrothermal processes within the plate boundary zone. Ann. Rev. Earth Planet. Sci., 10, 155-190, 1982.

Mackwell S.J., D.L. Kohlstedt and M.S. Paterson. The role of water in the deformation of olivine single crystals. J. Geophys. Res., vol. 90, 11319-11333, 1985

Martin J.W. and R.D. Doherty. Stability of microstructure in metallic systems. Cambridge university press, 1976.

Mavko G.M. Velocity and attenuation in partially molten rocks. J. Geoph. Res., vol. 85, 5173-5189, 1980.

McCallum N. and L.R. Barrett . Some aspects of the corrosion of refractories. Trans. Brit. Ceram. Soc., vol. 51, 523-548 , 1952.

McDonnell R. D. Deformation of fine-grained synthetic peridotite under wet conditions. Ph.D. thesis, Published number 152 in series Geologica Ultraiectina, 1997.

McKenzie D. The generation and compaction of partially molten rock. J. Petrol. 25, 713-765, 1984.

McKenzie D. The compaction of igneous and sedimentary rocks. J. Geol. Soc. London, 1987.

McKenzie D. Some remarks on the movement of small melt fractions in the mantle. Earth and Planet. Sci. Lett., 95, 53-72, 1989.

McLellan E.L. Melt segregation in migmatite complexes. Proc. Geol. Congr., 28th, 2, 402-403, 1989

Mercier, J.-C.C. Magnitude of the Continental Lithospheric Stresses Inferred From Rheomorphic Petrology. J. Geoph. Res., vol. 85, 6293 - 6303, 1980.

De Meer S. and C.J. Spiers. Creep of wet gypsium aggregates under hydrostatic loading conditions. Tectonophysics, vol. 245, 171-184, 1995.

De Meer S. and C.J. Spiers. Uniaxial compaction creep of wet gypsium aggregates. J. Geophys. Res. vol. 102, 875-891, 1997.

Van der Molen I. and M.S. Paterson. Experimental deformation of partially molten granite. Contrib. Mineral. Petrol., 70, 299-318, 1979.

Osborn E.F. and A. Muan. Phase equilibrium diagrams of oxide systems, Plate 3, the system MgO-Al_2O_3-SiO_2. Am. Ceram. Soc. And the Edward Orton, Jr., Ceramic Foundation, 1960.

Nur A. Seismic rock properties for reservoir descriptions and monitoring. In: Seismic tomography; with applications in global seismology and exploration seismics. Ed: Nolet G., Reidel Publ. Comp., Dordrecht, Holland, 1987.

Park H.H. and D.N. Yun. Effect of dihedral angle on the morphology of grains in a matrix phase. Metall., Trans., A, 16A, 923-928, 1985.

Petford N. Porous media flow in granitoid magmas: An assesment. In: Flow and creep in the solar system: Observations, modelling and theory. Eds: D.B. Stone and S.K. Runcorn, Kluwer Academic, Norwell, Mass., 1993

Pharr G.M. and M.F. Ashby. On creep enhanced by a liquid phase. Acta Metall., 31, 129-138, 1983.

Poirier J.P. Creep of crystals. High-temperature deformations processes in metals, ceramics and minerals. Cambride Earth Science Series, 1985.

Porter D.A. and K.E. Easterling. Phase transformations in metals and alloys. Chapman and Hall, London, 1992.

Post, R.L. Jr. The flow laws of of Mount Burnett Dunite. Ph.D. Thesis, 1973.

Post, R.L. Jr. High Temperature creep of Mt. Burnet dunite. Tectonophysics, 42, 75-110. 1977.

Rahaman M.N., Ceramic processing and sintering. Marcel Dekker Inc., NY, 1995.

Raj R. and C.K. Chyung. Solution-precipitation creep in glass ceramics. Acta Metall., 29, 159-166, 1981.

Raj R. Creep in polycrystalline aggregates by matter transport through a liquid phase. J. Geoph. Res. vol. 87, 4731-4739, 1982.

Ravikiran J. Effect of speed and pressure on dry sliding interactions of Alumina against steel. Am Ceram. Soc., vol. 78, no 2, 356-365, 1995.

Relandeau, C. High Temperature creep of forsterite polycrystalline aggregates. Geoph. Res. Lett., 9, 733-736, 1981.

Ribe N.M. Theory of melt segregation- A Review. J. Volcanol. Geotherm. Res., 33, 241-253, 1987.

Richardson C.N., J.R. Lister and D. McKenzie. Melt conduits in a viscous porous matrix. J. Geoph. Res., vol. 101, 20423-20432, 1996.

Richter F.M., Y. Ling and G. Minarik. Multicomponent diffusion and convection in molten MgO-Al_2O_3-SiO_2, Geochim. Cosmochim. Acta, vol.62, 1885-1991, 1998

Riley G.N. Jr. And D.L. Kohlstedt. Kinetics of melt migration in upper mantle-type rocks. Earth Planet. Sci. Lett. 105, 500-521, 1991.

Ringwood A.F. Composition and Petrology of the Earth's Mantle. McGraw-Hill, NY, 1975.

Robin P.Y.F. Pressure solution at grain to grain contacts. Geochim. Cosmochim. Acta 42, 1383-1398, 1978.

Robin P.-Y.F. Theory of metamorphic segregation and related processes. Geochim. Cosmochim. Acta, 43, 1587-1600, 1979.

Rutter E.H and K.H. Brodie. Experimental 'syntectonic' dehydration of serpentinite under conditions of controlled water pressure. J. Geophys. Res., vol. 93 (B5), 4907-4932, 1988.

Rutter E.H., The kinetics of rock deformation by pressure solution. Phil Trans R. Soc. London. A 283, 203-219, 1976.

Salters V.J.M. and S.R. Hart. The hafnium paradox and the role of garnet in the source of mid-ocean ridge basalts. Nature, 342, 420-422, 1989.

Sammler-Kuluszewsky Ch. Specielle Mineralogie 5. Lehrbrief. Bergakademie Freiberg-Fernstudium, 1959.

Sato H., I.S. Sacks and T. Murase. The use of laboratory velocity data for estimating temperature and partial melt fraction in the low-velocity zone: Comparison with heat flow and electrical conductivity studies. J. Geoph. Res., vol. 94, 5689-5704, 1989.

Schutjens P.M.T.M. Intergranular pressure solution in halite aggregates and quartz sands:an experimental investigation. Ph.D. thesis. Published number 76 in series Geologica Ultraiectina, 1991.

Schwenn, M.B. and C. Goetze. Creep of olivine during hot-pressing, Tectonophysics, vol. 48, 41-60, 1978.

Scott D.R.and D.J. Stevenson. A self-consistent model of magma melting, magma migration and buoyency-driven circulation beneath mid-ocean ridges. J. Geoph. Res., vol. 94, 2973-2988, 1989.

Shankland T.J. R.J. O'Connell and H.S. Waff. Patial melting and electrical conductivity anomalies for the upper mantle. Rev. Geophys., 19, 394-406, 1981.

Shuttleworth R. The surface tension of solids. Proc. Phys. Soc. (London), A 63, 444-457, 1950.

Sleep N.H. Tapping of melt by veins and dikes. J. Geophys. Res., vol. 93, 10255-10272, 1988.

de Smet J.H., Evolution of the continental upper mantle: numerical modelling of thermo-chemical convection including partial melting. Ph.D. thesis. Published number 172 in series Geologica Ultraiectina, 1999.

Sparks D.W.and E.M. Parmentier. Melt extraction from the mantle beneath spreading centers. Earth Planet. Sci. Let., 16, 105, 368-377, 1991.

Sparnaay M.J. Thermodynamics (with an emphasis on surface problems). Surface Science Reports (A review journal) No 4, 101-270, 1985.

Spiegelman M.and P. Kenyon. The requirement for chemical disequilibrium during magma migration. Earth Planet. Sci. Lett., 109, 611-620, 1992.

Spiers C.J., P.M.T.M. Schutjens, R.H. Brzesowsky, C.J. Peach, J.L. Liezenberg and H.J. Zwart. Experimental determination of constitutive parameters governing creep of rocksalt by pressure solution. In: Deformation Mechanisms. Ed: Knipe R.J. and Rutter E.H. Rheology and Tectonics. Geological Soc. Spec. Public. 54, 215-227, 1990.

Spiers C.J. and P.M.T.M. Schutjens. Densification of crystalline aggregates by fluid phase diffusional creep. In: Deformation processes in minerals, ceramics and rocks. Eds: Barber D.J. and Meredith P.G. Unwin Hyman, 1990.

Spiers C.J. and R.H. Brzesowsky. Densification behaviour of wet granular salt:theory versus experiment. Seventh Symposium on Salt, vol. 1, Elsevier Science Publishers, Amsterdam, 83-92, 1993.

Stevenson. D.J. On the role of surface tension in the migration of melts and fluids. Geoph. Res. Lett., vol. 13, 1149-1152, 1986.

Stevenson. D.J. Spontaneous small-scale melt segregation in partial melts undergoing deformation. Geophys. Res. Let., 16,1067-1070, 1989.

Stocker, R.L. and M.F. Ashby. On the Rheology of the Upper Mantle. Rev. Geoph. Phys., 11, 391-426, 1973.

Swalin R.A. Thermodynamics of solids. John Wiley, New York, 1962.

Swinkels F.B., D.S. Wilkinson, E. Arzt and M.F. Ashby. Mechanisms of hot-isostatic pressing. Acta Metall., 11, 1829-1840, 1983.

Tiller W.A. The science of crystallography: Microscopic interfacial phenomena. Cambridge University Press, 1991.

Toomey D.R., W.S.D. Wilcock, S.C. Solomon, W.C. Hammond and J.A. Orcutt. Science 280, 1998

Toramaru A. and N.Fujii. Connectivity of melt phase in a partially molten peridotite. J. Geoph. Res., vol. 91, 9239-9252, 1986.

Turcotte D.L. and G. Schubert. Geodynamics: Applications of continuum physics to geological problems. John Wiley & Sons, 1982.

Turcotte D.L. and J.P Morgan. The Physics of Magma Migration and Mantle Flow beneath a Mid-Ocean Ridge. In: Mantle Flow and Melt Generation at Mid-Ocean Ridges, Geophysical Monograph 71, Eds: J.P Morgan, D.K Blackman and J.M. Sinton, 155-182, American Geophysical Union, 1992.

Vaughan P.J., D.L. Kohlstedt and H.S. Waff. Distribution of the glass phase in hot-pressed olivine-basalt aggregates: An elctron microscope study. Contrib. Miner. Petrol., 81, 253-261, 1982.

Vlaar N.J., P.E. van Keken and A.P. van den Berg. Cooling of the Earth in the Archaean; consequences of pressure release melting in a hotter mantle. Earth Planet. Sci. Let., 121, 1-16, 1994.

Von Bargen N. and H.S. Waff. Permeability, interfacial areas and curvatures of partially molten systems: Results of numerical calculations of equilibrium microstructures. J. Geophys. Res., vol. 91, 1986.

Waff H.S. Introduction to special section on partial melting phenomena in earth and planetary evolution. J. Geophys. Res., vol. 91, 9217-9221, 1986.

Waff. H.S. and J.R. Bulau. Equilibrium fluid distribution in an ultramafic melt at 1350 °C and 1.0-2.5 GPa pressure. J. Geophys. Res. vol. 84, 6109-6114, 1979.

Waff. H.S. and J.R. Bulau. Experimental determination of near-equilibrium textures in partially molten silicates at high pressures, From: High pressure research in geophysics. Earth and Planet. Sci., 12, 229-236, 1982.

Waff H.S. and U.H. Faul. Effect of crystalline anisotropy on fluid distribution in ultramafic partial melts. J. Geophys. Res, vol. 97, B6, 9003-9014, 1992.

Walker D. and O. Mullins Jr. Surface tension of natural silicate melts from 1200°-1500°C and implications for melt structure. Contr. Min. Petrol., vol. 76, 455-462, 1981

Watson E.B. and J.M. Brenan. Fluids in the lithosphere 1. Experimentally-determined wetting characteristics of CO_2-H_2O fluids and there implications for fluid transport, host-rock physical properties and fluid inclusion formation. Earth and Planet. Sci. Lett., 85, 497-515, 1987.

Watson E.B., J.M. Brenan and D.R. Baker. Distribution of fluids in the continental mantle. In: Continental Mantle, Ed. M.A. Menzies, Clarendon Press, Oxford, 111-124, 1990

Watson G.W., P.M. Oliver and S.C. Parker. Computer simulation of the structure and stability of forsterite surfaces. Phys. Chem. Minerals, vol25, 70-78, 1997.

Weast R.C.., CRC Handbook of chemistry and physics. CRC Press, Cleveland. Ohio, 1970.

Weyl P.K. Pressure solution and the force of crystallisation - a phenomenological theory. J. Geophys. Res., vol. 64, 1959

White R.S. and D. McKenzie. Mantle plumes and flood basalts. J. Geoph. Res., 100, 17543-17585, 1995.

Wulff G. Zeits. F. Kristallog. 449, 1901.

Yoder H.S. Jr., Contemporaneous Basaltic and Rhyolitic magmas. Am. Mineral., 58, 153-171, 1973.

Young T., Phil. Trans. Roy. Soc. London, 95, 65, 1805.

Yurimote H., M. Morioka and H. Nagasawa. Oxygen self-diffusion along high diffusivity paths in forsterite. Geochem. J., vol. 26, 181-188, 1992.

SAMENVATTING

Het begrijpen van massatransportprocessen in kristallijne aggregaten in aanwezigheid van een vloeibare fase is van groot belang voor het modelleren van gedeeltelijk gesmolten gebieden in de aard-mantel zoals onder mid-oceanische ruggen. Ondanks het feit dat mid-oceanische ruggen beschouwd kunnen worden als de eenvoudigste grootschalige setting waar een gedeeltelijke smelt aanwezig is, worden veel van de processen die op diepte onder deze ruggen plaatsvinden nog maar slecht begrepen. Belangrijke informatie voor grootschalige modellering zijn bijvoorbeeld de verdeling van de smelt op korrel-schaal en of de smelt op deze schaal een continue netwerk van kleine kanaaltjes vormt. Ook over het reologisch gedrag van mantelgesteenten in aanwezigheid van een smelt is nog weinig bekend. Wanneer wordt geprobeerd om informatie van evenwichtsstudies en vaste stof/smelt-systemen te combineren met informatie uit verdichtings- en vervormingsstudies, dan blijkt dit vrijwel onmogelijk omdat infomatie ontbreekt onder condities waar spannings-gerelateerde en oppervlaktekrachten-gerelateerde drijvende krachten van vergelijkbare grootte zijn. Deze condities worden echter wel gedacht aanwezig te zijn in gedeeltelijk gesmolten gebieden van de aard-mantel. In dit proefschrift is zowel theoretisch als experimenteel werk beschreven aan massatransportmechanismen in vaste stof/ fluide fase systemen, onder condities van lage effectieve spanningen waarbij oppervlaktekrachten significant worden.

In hoofdstuk 1 zijn de problemen geïntroduceerd en de doelstellingen beschreven. In hoofdstuk 2 is een theoretische basis gegeven met betrekking tot oppervlakken, grensvlakken en massatransportmechanismen op korrel-schaal in vaste stof/vloeistof systemen waarbij zowel spanning- als oppervlaktekrachten gerelateerde termen in bechouwing worden genomen. In dit hoofdstuk zijn modellen afgeleid voor verdichting en voor "nek-groei", een proces waarbij massatransport plaatsvindt van de poriën naar het contactopppervlak tussen twee korrels, waardoor het contactoppervlak tussen de korrels groeit. Na afleiding van de modellen voor bovenstaande processen, zijn criteria opgesteld om te bepalen onder welke condities welk proces dominant is.

In hoofdstuk 3 zijn uni-axiale verdichtingsproeven beschreven voor het systeem $NaNO_3$/verzadigde oplossing. Dit systeem kan als een eenvoudig analoog systeem worden beschouwd voor een vaste stof/ smelt systeem. De experimenten zijn bij kamertemperatuur verricht waardoor veel en kwalitatief goede data makkelijk worden verkregen voor een eerste test van de modellen. De resultaten laten zien dat verdichting alleen plaatsvindt bij

aanwezigheid van de verzadigde oplossing, niet onder droge omstandigheden en ook niet in aanwezigheid van siliconenolie (waarin het zout niet oplost). De verdichting vind plaats door een oplossing/neerslag proces op de korrelgrenzen waarbij diffusie de snelheidsbeperkende factor is. Echter bij lage spanning en kleine korrelgroottes wijkt het gedrag af van de modellen voor verdichting onder spanning. Bij spanningen $< 3.10^4$ Pa en korrelgroottes < 20 μm geven zowel mechanische als microstructurele data aan dat oppervlaktekrachten belangrijk (niet langer verwaarloosbaar) worden. Dit is conform de modellen die een tegenwerkende kracht door oppervlaktekrachten voorspellen tijdens verdichting onder een lage spanning.

In hoofdstuk 4 zijn uni-axiale verdichtingsexperimenten beschreven bij hoge temperatuur (1390-1470 °C) van forsteriet aggregaten waarbij alleen een dampfase in de poriën aanwezig is. Bij deze hoge temperaturen kan vaste-stof-diffusie plaatsvinden waardoor de verdichting niet meer afhankelijk is van de aanwezigheid van een vloeibare fase op de korrelgrenzen. Mechanische en microstructurele data geven aan dat korrelgrens-diffusie het belangrijkste massatransportmechanisme is met diffusie als snelheidsbeperkende stap. Ook bij deze hoge temperatuur experimenten wordt een afwijking van het model geconstateerd bij lage spanningen en kleine korrelgroottes. Deze afwijking wordt net als bij de $NaNO_3$ experimenten toegeschreven aan de oppervlaktekrachten die verdichting tegenwerken.

In hoofdstuk 5 worden verdichtingsexperimenten beschreven van forsteriet aggregaten in aanwezigheid van een smeltfase bij temperaturen tussen 1390-1470 °C. Korrelgrensdiffusie is wederom het belangrijkste massatransportmechansime, echter, noch de mechanische data, noch de microstructurele data kunnen definitief uitsluitsel geven omtrent de vraag of de smeltfase ook aanwezig is op de korrelgrenzen tijdens de verdichting. Met behulp van chemische puntanalyses op de monsters en met gebruik van een fasediagram is vastgesteld dat er nog kristallisatie heeft plaatsgevonden tijdens de afkoelingsperiode, waardoor de vaste stof/smelt verdeling veranderd kan zijn. Het verschil in snelheid van forsteriet-aggregaatverdichting tussen experimenten met en zonder smelt is gering, waarbij de experimenten met een aanwezige smelt slechts een factor 2-3 sneller zijn.

Tenslotte in hoofdstuk 6, worden de conclusies samengetrokken en suggesties gedaan voor verder onderzoek.

NAWOORD

Hierbij wil ik iedereen bedanken die bijgedragen heeft aan de totstandkoming van dit proefschrift.

In de eerste plaats wil ik de mensen van Koninklijke Hoogovens Groep bedanken, met name de heer J. de Boer maar ook L. Bol, S. Sinnema en R. de Jong. Niet alleeen heeft Hoogovens dit onderzoek gefinancierd maar ook heeft het Keramisch Research Centrum mij alle gelegenheid en gastvrijheid geboden om experimentele- en analyseapparatuur te gebruiken waardoor ik de experimenten zoals beschreven in hoofdstuk 4 en 5 heb kunnen verrichten. De mensen van ECN, en met name Jan Prij wil ik vriendelijk bedanken voor de ruimhartige steun en geduld die ik heb ondervonden bij het afronden van mijn proefschrift naast mijn gewone werkzaamheden.

Mijn enthousiasme voor experimenteel onderzoek werd al tijdens mijn studie ingegeven door mijn promotor Chris Spiers. Vooral het bedenken van elegante, simpele maar doeltrefffende experimenten om moeilijke theoretische onderwerpen te leren begrijpen zijn een voorbeeld geweest waar ik veel van heb geleerd. Ook wil ik hem bedanken voor de moeite en inzet in de laatste maanden toen, na al die tijd, de afronding van dit proefschrift toch nog een wedloop tegen de klok werd. Voor de uitvoering van experimenten in het HPT laboratorium ben ik veel dank verschuldigd aan Colin Peach en aan de technici Gert Kastelein, Peter van Krieken en Eimert de Graaf. Magda wil ik hartelijk bedanken voor alle organisatorische en morele steun.

Speciale dank gaat uit naar de vrienden die mijn verblijf op het IVA vooral tot een zeer gezellige tijd hebben gemaakt waardoor "gewoon doorgaan en niet opgeven" bij tegenvallers en moeilijke perioden toch een stuk gemakkelijker werd gemaakt. Het is onmogelijk om iedereen te noemen. Toch wil ik Siese, Rob, Coen, Patrick en Timon speciaal bedanken, ook voor de (morele) ondersteuning, inhoudelijke bijdrage aan dit proefschrift en het organiseren van de festiviteiten.

Tenslotte, maar niet in de laatste plaats wil ik mijn ouders bedanken die me onvoorwaardelijk hebben gesteund en gemotiveerd tijdens al mijn jaren van school en studie. Jeanette, die veel van de plaatjes heeft gemaakt in dit proefschrift en in de loop der jaren al heel wat blunders uit mijn vergelijkingen heeft gehaald, ook ontzettend bedankt. En natuurlijk Toar, wat heb jij een berg werk en vervelende klussen verzet en ellendige volle dagen mee doorstaan, en wat gaan we ontzettend genieten van heel veel vrije tijd.....

CURRICULUM VITAE

09-11-1964	Geboren te Godenstedt, Duitsland
1977-1983	VWO, Jeroen Bosch College, Den Bosch
1990	Doctoraal examen Geologie, Universiteit Utrecht Hoofdvak Structurele en Toegepaste Geologie, Bijvakken: Economische Geologie, Exploratie Geofysica en Petrologie
1990-1995	Assistent In Opleiding, vakgroep Geologie, Universiteit Utrecht
Vanaf 1996	Onderzoeker bij Energieonderzoek Centrum Nederland, ECN Unit Brandstoffen, Conversie en Milieu